IJHSR International Journal of High School Research

December 2022 | Volume 4 | Issue 6

ijhighschoolresearch.org

ISSN (Print) 2642-1046

ISSN (Online) 2642-1054

Marine Biology Research at Bahamas

Unique and exclusive partnership with the Gerace Research Center (GRC) in San Salvador, Bahamas to offer marine biology research opportunities for high school teachers and students.

- Terra has exclusive rights to offer the program to high school teachers and students around world.
- All trips entail extensive snorkeling in Bahamian reefs as well as other scientific and cultural activities.
- Terra will schedule the program with GRC and book the flights from US to the GRC site.
- Fees include travel within the US to Island, lodging, meals, and hotels for transfers, and courses.
- For more information, please visit terraed.org/bahamas.html

Terra is a N.Y. based 501.c.3 non-profit organization
dedicated for improving K-16 education

Table of Contents

February 2023| Volume 5| Issue 1

1 **The Relationship between Insulin Resistance and Neutrophil to Lymphocyte Ratio**
Alicia Shin

6 **Naturalistic Neuroimaging: From Film to Learning Disorders**
Asha Dukkipati

12 **A Quantitative Analysis of the Active Ingredients of Broad-leaved Bamboo and Study on Its Skin Condition Improvement Effect**
Christine Yuna Jang

18 **Aberrant Human Gut Microbiome Composition in COVID-19 Patients: A Systematic Review**
Cindy H. Lu

22 **Effect of Temperature on the Purity and Yield of Aspirin**
Dhiman Roy

28 **An Examination of Habitability in Exoplanet Systems**
Divya Kumari

34 **Discovery of Novel Genetic Alteration Using Meta-analysis of Colorectal Cancer**
Haryeong Eo

38 **Unveiling the Role of MicroRNA-132 on Alzheimer's Disease Brain Cells**
Hannah Kim, David Kim

43 **Design and Development of an Economic and Effective Hybrid Space Suit**
Hridyanshu, Madhav Sharma

49 **Livestock Manure Recycling for Vegetable Farms in Hong Kong**
Lauren Hsu

56 **Multi-functional, Bioresorbable Stent Technology for Real-time Diagnosis**
Jason Kim, Sunny Kim

60 **Modeling Socioeconomic, Demographic, and Chronic Medical Conditions correlated with COVID-19 Incidence**
Jenna Chuan

68 **High Glucose Transglutaminase 2 Promotes YAP/TAZ and Fibroblast Proliferation in Pulmonary Hypertension**
Jennifer Wu

72 **The Effect of Steering Effort on the Simulated Rollover Dynamics Behavior of Cars**
Lee Yoonsu

77 **Small Molecule-Drug Conjugates: Targeted Tunable Therapy for Cancer Treatment**
Lucy L. Wang

83 **AI-Based Power Demand Forecasting of California Counties**
Maxwell Y. Chen, Shourya Bose, Yu Zhang

86 **Novel Multipurpose Air Purification and Distribution Robot with AI-Based Anomaly Detection**
Mikul Saravanan

93 **The Association of the 'Hide Like and View Counts' Feature with Disordered Eating, Self Esteem, and Self Image**
Naisha Agarwal

99 **Skin Disease Classification Using Privacy-Preserving Federated Learning**
Brian J. Nam

105 **Helmet Modifications and Policy Changes to Mitigate Chronic Traumatic Encephalopathy in Professional Football**
Nikhil H. Vallikat

110 **The Aggregation of Tau Protein in Alzheimer's Disease**
Tanvi Chichili

116 **Therapeutic Potential Targeting Cancer Stem Cells to Treat Breast Cancer**
Tianyue Yu

Editorial Board

International Journal of High School Research

IJHSR
ijhighschoolresearch.org
RESEARCH ARTICLE

The Relationship between Insulin Resistance and Neutrophil to Lymphocyte Ratio

Alicia Shin

Torrey Pines High School, 3710 Del Mar Heights Rd, San Diego, CA 92130, USA; alicia.hs1110@gmail.com

ABSTRACT: There is increasing interest in the role of chronic inflammation on the pathogenesis of various diseases, and one of its markers, high Neutrophil-to-Lymphocyte Ratio, is associated with multiple mortality and morbidity risk, suggesting Insulin Resistance might be one potential associate factor. However, epidemiological studies on the association between NLR and IR are scarce, and they only included diabetes mellitus patients, excluding the general population. This study aims to determine if there is a direct correlation between NLR and IR in the US general population. The Homeostatic Model Assessment for Insulin Resistance value was calculated to evaluate the IR of the 3,307 samples provided by the NHANES. As insulin usage could result in inaccurate HOMA-IR estimation, we excluded them and ran a subgroup analysis. The relationship was shown when insulin users were included, having a beta coefficient value of 0.010 (95% confidence interval [CI] of 0.003-0.017). However, without insulin users, the beta value decreased to 0.004 (95% CI of -0.006-0.015). The statistical significance wasn't reached when age, sex, and BMI were adjusted for in the multivariate analyses. Therefore, IR might not explain the variation of NLR value in healthy people, and further studies are needed to reveal the associated factor of high NLR.

KEYWORDS: Neutrophil-to-Lymphocyte Ratio, Insulin Resistance, HOMA-IR, Diabetes Mellitus.

Introduction

There has been an increase in the study of Neutrophil-to-Lymphocyte Ratio (NLR) and its correlation to various health issues among the human population. NLR is a new biomarker of chronic inflammation, calculated by dividing the Neutrophil count by the lymphocyte count in the blood.[1] Neutrophil is a type of White Blood Cell (WBC) that supports the healing process of damaged tissues and the process of resolving infections. Their role is to recognize phagocytose microbes, kill pathogens through mechanisms that produce reactive oxygen species, release antimicrobial peptides, and expulse their nuclear content to form traps.[2] Lymphocytes are also a type of WBC for the immune system, including the B-Cells and the T-Cells. NLR, therefore, reflects the balance of acute and chronic inflammation (neutrophil count) and adaptive immunity (lymphocyte count).[1] It is a popular marker for medical examinations because NLR calculations are more straightforward and cheaper than other biomarkers.[3] Previous studies have found that an increase in NLR is associated with an increase in mortality[4], diabetes mellitus[5], ischemic stroke[4], cerebral hemorrhage[6], major cardiac events[7], sepsis, and infectious diseases.[4-8]

Insulin resistance (IR) is regarded as crucial pathophysiology of diabetes mellitus, when the target tissue of the insulin does not respond to the stimulation, prohibiting blood glucose levels from decreasing.[9] In normal circumstances, as the glucose level increases in the bloodstream, the pancreas releases insulin to stimulate a series of receptors in muscle cells, enabling glucose to enter the cells. Through this process, glucose is converted to a form of energy reserved for long-term storage. IR, which prevents this process from happening, is also associated with inflammation, obesity, CVD, nonalcoholic fatty liver disease, metabolic syndrome, and polycystic ovary syndrome.[9-11]

Several studies suggested a linkage between NLR and metabolic syndrome.[3,12] However, while NLR is highly correlated with metabolic syndrome, it is a cluster of risk factors and does not directly mean insulin resistance. In one previous study with diabetes patients, IR and NLR were associated. The two comparison groups they had were DM patients without IR and DM patients with IR. Patients without IR showed lower NLR values than patients with IR, and the logistic regression analysis also revealed significance in the correlation between IR and NLR.[3] As a result, the study concluded that NLR could play a role as an important biomarker when predicting IR in diabetic patients.[3] A limitation of this study was that they did not consider insulin usage, which might affect the calculation of the Homeostasis Model Assessment of Insulin Resistance (HOMA-IR), the indicator of insulin resistance.[13]

To current knowledge, no study has investigated the relationship between NLR and IR in the general population and with the consideration of insulin use. A new study of the general population and examining the specific DM and insulin usage would be essential to discover the correlation between IR and NLR.

Hypothesis and Aim:

This study will examine the association between NLR and IR in the general population, considering DM and insulin treatment status. It was hypothesized that increasing IR would affect the increase of NLR.

Methods

Data source:

For the study participants, the general data was collected in The National Health and Nutrition Examination Survey

DOI: 10.36838/v5i1.1

(NHANES), a cross-sectional study conducted by the National Center for Health Statistics (NCHS) to obtain a sample representing the United States population, was used. It has constantly been releasing updated data since 1959 to the public; however, it stopped in March 2020 due to the COVID-19 breakout. The NHANES website contains information on physical examination, questionnaire data, webinars, and surveys that portray the US population's health and nutrition status at 2-year intervals.[14] The data used in this study was obtained through a pre-pandemic community-based survey between 2017 and March 2020.

Study population:

Of the 15,560 people in the data who completed the physical examination between 2017-March 2020, samples over the age of 19 and those who have completed data on insulin usage, BMI, and CBC were included. To establish a more accurate analysis, the following were excluded: participants with a fasting glucose level that exceeds 140 mg/dL, as the normal range of fasting blood glucose level, is below 140mg/dL; participants with more than 10,000 WBC in the collected blood sample, because healthy individuals show values between 4,500-10,000 WBC and >10,000 suggest acute inflammatory status; participants with NLR over 9, as it becomes an outlier considering that normal NLR value in adults is between 0.78 and 3.53, and >9 might mean critically ill status.[15-17] NLR values were calculated by dividing the absolute count of neutrophil by the absolute count of lymphocytes. These factors were eliminated due to the possibility of the data being altered as they showed abnormal figures and could be possible outliers. After all the eliminations, 3,375 samples remained.

During the analysis, 68 insulin users were removed as they could be a confounding variable in the overall analysis. This decision was made due to the HOMA-IR used in this study to measure how much insulin the pancreas creates to regulate blood glucose levels. The HOMA-IR values were calculated by multiplying fasting insulin and fasting glucose levels and dividing by 22.5.

Data collection:

Final data collection was done on the individual's gender, race, height, weight, fasting glucose level, BMI, WBC level, and NLR. (Figure 1) Body measurements were collected in the Mobile Examination Center (MEC). General information, such as age, gender, disease status, etc., was collected through surveys, and experts performed body measurement data with the individual's consent. Overnight fasting blood samples were obtained for fasting glucose, insulin, and other laboratory values.

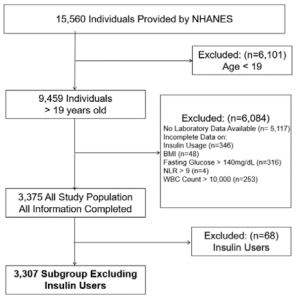

Figure 1: Shows the process of exclusion.

Statistical analyses:

Descriptive statistics (mean, standard deviation (SD) for continuous variables and number and percentage for categorical variables) were used to describe the study population. The distribution of NLR and HOMA-IR level was visualized by a histogram. They showed right skewness for both.

Statistical analyses were performed to see how NLR levels related to HOMA-IR and insulin status. The correlation between NRL and HOMA-IR was displayed in a scatter plot and a line of best fit (regression line). Due the right skewness of the NLR and HOMA-IR, the relationship was also displayed after logarithmic transformation, calculating the values of Log HOMA-IR and Log NLR. We also showed it in three groups: non-DM (Diabetes Mellitus), DM not on insulin, and DM on insulin.

DM and insulin status were considered in our analyses with an a priori hypothesis. The means SD of HOMA-IR and NLR by DM and insulin status were shown by a bar graph. It showed that HOMA-IR and NLR were significantly higher when the subjects were on insulin treatment. Therefore, insulin users were excluded from the additional data analysis. Bivariate and Multivariate linear regression analyses were performed to examine the statistical significance of the relationship between NLR and HOMA-IR. As done in previous studies, multivariate linear regression analyses were performed controlling for age, sex, and BMI, as they could be confounding variables that influence NLR values.[12] BMI was controlled because a high BMI is linked to an increase in insulin resistance and NRL, which may also alter the relationship overall.[17,18] We took HOMA-IR as an independent variable and NLR as a dependent variable, as we hypothesized that insulin resistance would induce chronic inflammation. While several studies suggested a bidirectional relationship, the most recent knock-out mice model suggested such a direction.[3,19]

All statistical analyses were made using STATA 14.0 (College Station, TX), and considering that p-values<0.05 are statistically significant.

Results and Discussion

Study population :

Table 1 shows the participants' characteristics with the sample including insulin users and the sample excluding insulin users. Among the 3,307 participants, 1,731 (52.3%) were female, and the mean age was 49.4 (SD 17.8). 298 (8.83%) were diabetes mellitus patients, and 68 (2.01%) used insulin.

Table 1: Analysis of all participants (N=3,375) and participants without insulin users (N=3,307).

	All participants (N=3,375)			Excluding insulin user (N= 3,307)	
	N or mean	% Or SD		N or mean	% Or SD
Age	49.35	17.83		49.02	17.79
Sex, Female	1762.00	52.21		1731.00	52.34
Diabetes Mellitus	298.00	8.83		230.00	6.95
On insulin	68.00	2.01		-	-
Hypertension	1187.00	35.17		34	0.48

Asthma	518.00	15.35		503.00	15.21
Arthritis	945.00	28.00		910.00	27.52
Heart failure	99.00	2.93		84.00	2.54
Coronary heart disease	119.00	3.53		111.00	3.36
Stroke	150.00	4.44		140.00	4.23
Chronic obstructive pulmonary disease	267.00	7.91		257.00	7.77
BMI (kg/m2)	29.41	7.32		29.35	7.31
Fasting insulin (μU/mL)	13.25	17.63		12.41	11.20
HOMA-IR	3.30	4.73		3.06	3.05
ALT (IU/L)	21.81	20.56		21.9.	20.73
AST (units/L)	21.90	15.63		21.93	15.72
ALP (units/L)	76.41	24.60		76.17	24.37
Albumin (g/dL)	4.03	0.33		4.03	0.33
Blood urea nitrogen (mg/dL)	14.54	5.57		29.35	7.31
Sodium Bicarbonate (mg/dL)	25.59	2.38		25.59	2.36
Creatinine (mg/dL)	0.89	0.50		0.88	0.44
Gamma-glutamyl transferase (units/L)	30.75	56.13		14.39	5.31
Total cholesterol (mg/dL)	184.37	40.31		184.89	40.25
Triglyceride (mg/dL)	117.65	87.53		117.40	87.86
Uric acid (mg/dL)	5.44	1.44		5.42	1.42

Figure 2A shows the distribution of baseline NLR values according to the general population information from NHANES. The graph suggests that the general population (3.307 samples in this study) has a mean of 2 ± 0.02 and a median of 1.82. Also, the range between the 25th and 75th percentile was 1.08 for neutrophil and lymphocyte count. **Figure 2B** shows the distribution of baseline HOMA-IR values in the general population. The graph suggests a mean of 3.3 ± 4.73 and a median of 2.23. Also, the range between the 25th and 75th percentile was 2.48 for HOMA-IR.

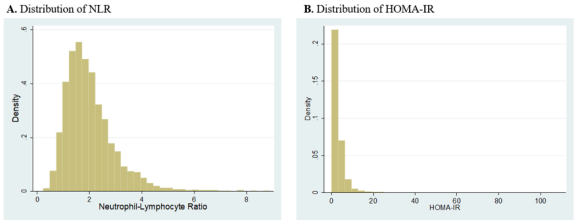

Figure 2: The distribution of neutrophil-to-lymphocyte ratios (A) and HOMA-IR (B) among individuals. The x-axis is truncated at an NLR of 9.

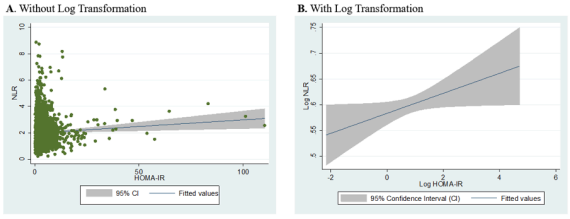

Figure 3: The regression line and 95% Confidence Interval of the relationship between Log HOMA-IR and Log NLR before (3A) and after log transformation (3B).

Figure 3 presents a weak positive correlation between HOMA-IR and NLR. This graph went through a logarithmic transformation due to the skewness, representing the relationship between Log HOMA-IR and Log NLR. The regression line showed a weak, positive correlation. As the Log HOMA-IR slightly increased, the Log NLR value would also increase.

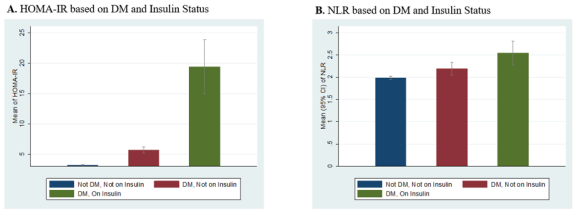

Figure 4: Bar graph comparing the mean (95% Confidence Interval) HOMA-IR (A) and NLR level (B) of individuals: not Diabetes Mellitus (DM) and not on insulin, DM and not on insulin, and DM and on insulin.

Figure 4A shows the different mean HOMA-IR value for each criterion. With the inclusion of insulin users, the data on HOMA-IR will show an abnormally large number when compared to individuals who are not on insulin treatment (for detail, see **Figure 4A**) and offer an unsteady insulin concentration in blood depending on when they receive the treatment.[13] Individuals without DM and insulin had a mean HOMA-IR value of 3.24 ± 0.07, individuals with DM but no insulin treatment had a mean of 5.76 ± 0.27, and individuals with both DM and insulin treatment had a mean of 19.42 ± 2.27. Here, the effect of the insulin treatment on HOMA-IR was evident, suggesting the need to exclude this group in additional analysis.

Figure 4B describes the different NLR value depending on the individual's current DM and insulin status. The results showed each criterion's mean 95% confidence interval (CI). Individuals without DM and insulin had a mean NLR value of 2.06 ± 0.02, individuals with DM but no insulin treatment had a mean of 2.32 ± 0.59, and individuals with both DM and insulin treatment had a mean of 2.65 ± 0.10.

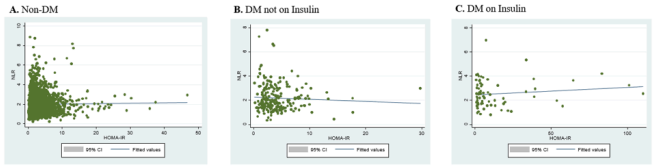

Figure 5: Scatterplot for each criterion, comparing HOMA-IR distribution.

Figure 5 suggests the difference in HOMA-IR - NLR association by DM and insulin status. The non-DM groups showed nearly no significant correlation. Also, DM not in the Insulin group showed a weak, negative correlation. However, the DM in the Insulin group showed a drastically increased HOMA-IR value; therefore, the group individuals were eliminated for further analysis.

Bivariate and Multivariate Linear regression analyses:

Table 2 shows the difference in the linear regression and significance of all study subjects (n=3,375) and the subjects after excluding insulin users (n=3,307). Bivariate linear regression analysis showed a significant positive relationship between

DOI: 10.36838/v5i1.1

HOMA-IR and NLR (beta-coefficient 0.010, 95% CI 0.003-0.017, P-value 0.004). After adjusting age, sex, and BMI, it lost statistical significance due to the altered values (beta-coefficient 0.004, 95% CI -0.006-0.014).

With the exclusion of insulin users, the beta value changed from 0.01 to 0.004, and the 95% CI interval drastically changed from 0.003-0.017 to -0.006-0.015, indicating no significance. This suggests that there is no true association between HOMA-IR and NLR.

Table 2: Univariate and Multivariate Linear Regression Model of HOMA-IR on NLR

All study subjects (N=3,375)						
	β	SE	t	P>t	95% CI	
Bivariate						
HOMA-IR	0.010	0.003	2.880	0.004	0.003	0.017
Constant	1.982	0.020	98.200	0.000	1.942	2.022
Multivariate						
Age	0.010	0.001	10.670	0.000	0.008	0.012
Sex	0.033	0.033	1.010	0.315	-0.031	0.097
BMI	0.004	0.002	1.820	0.069	0.000	0.009
HOMA-IR	0.006	0.004	1.720	0.086	-0.001	0.013
Constant	1.371	0.084	16.290	0.000	1.206	1.536
Excluding Insulin Users (N=3,307)						
Bivariate						
HOMA-IR	0.004	0.005	0.770	0.439	-0.006	0.015
Constant	1.992	0.024	84.510	0.000	1.945	2.038
Multivariate						
Age	0.010	0.001	10.360	0.000	0.008	0.011
Sex	0.028	0.033	0.850	0.396	-0.037	0.093
BMI	0.006	0.003	2.460	0.396	0.001	0.011
HOMA-IR	-0.003	0.006	-0.550	0.584	-0.015	0.009
Constant	1.352	0.085	15.860	0.000	1.185	1.519

BMI: Body mass index; HOMA-IR: Homeostasis model assessment of insulin resistance; β: coefficient; SE: standard error; 95% CI: 95% Confidence Interval

Summary:

In this study using the US general population data, the observation showed a weak, positive association in the relationship between NLR and IR in the overall population but a null association when insulin users were excluded.

Previous Studies/ Mechanism:

We hypothesized that a high HOMA-IR value, indicative of insulin resistant state, could predict high NLR because previous preclinical studies suggested a relationship between the two. Some studies found that chronic inflammations can induce systemic insulin resistance: for example, Uysal *et al*. revealed that proinflammatory cytokine TNF-alpha could generate IR by showing protection from obesity-induced insulin resistance in mice lacking TNF-alpha function; in addition, Talukdar *et al*. showed neutrophil mediate insulin resistance by using mice without neutrophil elastase, an enzyme that responses to tissue injury, in high-fat diet-fed mice via secreted elastase.[20, 21]

Others examined the relationship opposite: Simobayashi used Knockout mice, genetically modified to lack mTORC2 gene (causing mice to have IR), to observe the relationship between IR and inflammation.[19] mTORC2 is a protein complex that regulates glycolysis and the pentose phosphate pathway.[22] These mice were also on a high-fat diet (HFD) and were observed for ten weeks. Simobayashi found that insulin resistance caused macrophage numbers to increase while B and T cell numbers remained consistent.[19] In addition, the increase in macrophages in the KO mice, was disproportionate to other variables, indicating that IR promotes inflammation.[19]

In line with those studies, an epidemiological study done by Lou *et al*. showed a positive relationship between NLR and IR. They collected data from diabetic patients regardless of their insulin usage status and had an additional 130 healthy subjects for comparison.[3] They found that the NLR values were significantly higher in patients with diabetes than in healthy control subjects, interpreted their results as NLR being a marker for IR, and discovered that T2DM patients were in a state of low-degree chronic inflammation that induces inflammatory factors, elevating neutrophil counts.[3] Luo concluded that NLR has a direct relationship with IR and suggested that NLR can be a biomarker to predict IR in diabetic patients.

However, this study showed results that differ from the above studies because there was no significant correlation between NLR and IR after controlling for potential confounders and considering insulin use. A difference in Uysal's and Simobayashi's studies was that they used KO mice while this study focused on human subjects. Since the human subjects did not undergo a gene deletion process, it could have shown a less definite relationship than the correlation shown in mice samples. Also, a difference between Lou's study is that they were focused on patients with diabetes while this study observed the general population. They also included insulin users (insulin-deficient individuals) who dramatically increased the HOMA-IR value. Due to these differences, this study, which focused on the general human population, found no significance or a very weak significance in the correlation between NLR and IR.

Conclusion

As shown in Figure 6, it was revealed that there is no significant association between IR and NLR. Contrary to our hypothesis, insulin resistance did not explain chronic inflammation, represented by NLR. While the increase in each NLR and insulin resistance can cause an increase in mortality, disease, and several types of cancer, they seem to be risk factors independent of each other. Therefore, further studies on other factors that increase chronic inflammation and NLR values in the general population would be needed to develop a strategy to prevent chronic inflammation related to several morbidity and mortality.

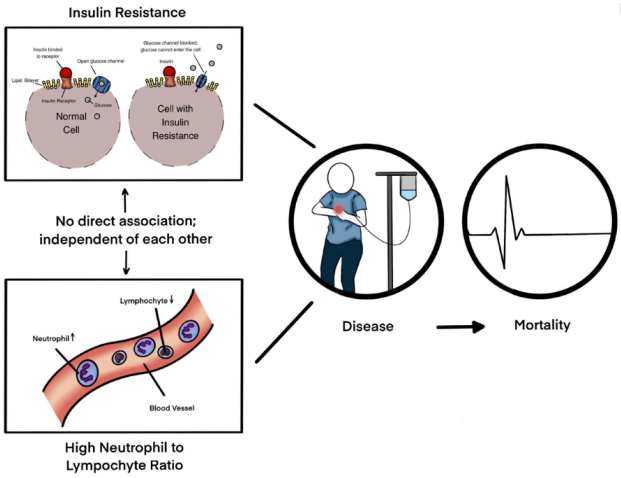

Figure 6: Summary of this study.

Acknowledgements

TPHS Medical Illustration Club (Claire Shin)

References

1. Song, M., B. I. Graubard, C. S. Rabkin, and E. A. Engels. 2021. "Neutrophil-to-lymphocyte ratio and mortality in the United States general population." *Sci Rep* 11 (1):464. DOI: 10.1038/s41598-020-79431-7.
2. Mayadas, Tanya N., Xavier Cullere, and Clifford A. Lowell. 2014. "The Multifaceted Functions of Neutrophils." *Annual Review of Pathology: Mechanisms of Disease* 9 (1):181-218. doi: 10.1146/annurev-pathol-020712-164023.
3. Lou, M., P. Luo, R. Tang, Y. Peng, S. Yu, W. Huang, and L. He. 2015. "Relationship between neutrophil-lymphocyte ratio and insulin resistance in newly diagnosed type 2 diabetes mellitus patients." *BMC Endocr Disord* 15:9. DOI: 10.1186/s12902-015-0002-9.
4. Liu, Yong-Lin, Jie-Kai Lu, Han-Peng Yin, Pei-Shan Xia, Dong-Hai Qiu, Man-Qiu Liang, Jian-Feng Qu, and Yang-Kun Chen. 2020. "High Neutrophil-to-Lymphocyte Ratio Predicts Hemorrhagic Transformation in Acute Ischemic Stroke Patients Treated with Intravenous Thrombolysis." *International Journal of Hypertension* 2020:5980261. Doi: 10.1155/2020/5980261.
5. Guo, X., S. Zhang, Q. Zhang, L. Liu, H. Wu, H. Du, H. Shi, C. Wang, Y. Xia, X. Liu, C. Li, S. Sun, X. Wang, M. Zhou, G. Huang, Q. Jia, H. Zhao, K. Song, and K. Niu. 2015. "Neutrophil: lymphocyte ratio is positively related to type 2 diabetes in a large-scale adult population: a Tianjin Chronic Low-Grade Systemic Inflammation and Health cohort study." *Eur J Endocrinol* 173 (2):217-25. doi: 10.1530/eje-15-0176.
6. Lattanzi, Simona, Francesco Brigo, Eugen Trinka, Claudia Cagnetti, Mario Di Napoli, and Mauro Silvestrini. 2019. "Neutrophil-to-Lymphocyte Ratio in Acute Cerebral Hemorrhage: A System Review." *Translational Stroke Research* 10 (2):137-145. DOI: 10.1007/s12975-018-0649-4.
7. Park, Jin-Sun, Kyoung-Woo Seo, Byoung-Joo Choi, So-Yeon Choi, Myeong-Ho Yoon, Gyo-Seung Hwang, Seung-Jea Tahk, and Joon-Han Shin. 2018. "Importance of prognostic value of neutrophil to lymphocyte ratio in patients with ST-elevation myocardial infarction." *Medicine 97* (48):e13471. DOI: 10.1097/md.0000000000013471.
8. de Jager, Cornelis P. C., Paul T. L. van Wijk, Rejiv B. Mathoera, Jacqueline de Jongh-Leuvenink, Tom van der Poll, and Peter C. Wever. 2010. "Lymphocytopenia and neutrophil-lymphocyte count ratio predict bacteremia better than conventional infection markers in an emergency care unit." *Critical Care* 14 (5): R192. Doi: 10.1186/cc9309.
9. Freeman, A. M., and N. Pennings. 2021. "Insulin Resistance." In *StatPearls.* Treasure Island (FL): StatPearls Publishing
10. McDade, Thomas W. 2012. "Early environments and the ecology of inflammation." *Proceedings of the National Academy of Sciences* 109 (Supplement 2):17281-17288. doi: 10.1073/pnas.1202244109.
11. Shoelson, S. E., J. Lee, and A. B. Goldfine. 2006. "Inflammation and insulin resistance." *J Clin Invest* 116 (7):1793-801. doi: 10.1172/jci29069.
12. Surendar, J., K. Indulekha, V. Mohan, and R. Pradeepa. 2016. "Association of neutrophil-lymphocyte ratio with metabolic syndrome and its components in Asian Indians (CURES-143)." *J Diabetes Complications* 30 (8):1525-1529. doi: 10.1016/j.jdiacomp.2016.08.006.
13. Wallace, T. M., J. C. Levy, and D. R. Matthews. 2004. "Use and abuse of HOMA modeling." *Diabetes Care* 27 (6):1487-95. doi: 10.2337/diacare.27.6.1487.
14. Center for Disease Control and Prevention. "National Health and Nutrition Examination Survey." accessed Nov 25. https://www.cdc.gov/nchs/nhanes/index.htm.
15. Rao SS, Disraeli P, McGregor T. 2004. "Impaired glucose tolerance and impaired fasting glucose." Am Fam Physician. 69 (8):1961-8.
16. SHOBHA S. RAO, M.D., PHILLIP DISRAELI, M.D., and TAMARA MCGREGOR, M.D., University of Texas Southwestern Medical Center at Dallas, Dallas, Texas.
17. Aminzadeh, Z., and E. Parsa. 2011. "Relationship between Age and Peripheral White Blood Cell Count in Patients with Sepsis." *Int J Prev Med* 2 (4):238-42.
18. Rajwani, A., R. M. Cubbon, and S. B. Wheatcroft. 2012. "Cell-specific insulin resistance: implications for atherosclerosis." *Diabetes Metab Res Rev* 28 (8):627-34. doi: 10.1002/dmrr.2336.
19. Martinez, Keilah E., Larry A. Tucker, Bruce W. Bailey, and James D. LeCheminant. 2017. "Expanded Normal Weight Obesity and Insulin Resistance in US Adults of the National Health and Nutrition Examination Survey." *Journal of Diabetes Research* 2017:9502643. Doi: 10.1155/2017/9502643.
20. Shimobayashi, M., V. Albert, B. Woelnerhanssen, I. C. Frei, D. Weissenberger, A. C. Meyer-Gerspach, N. Clement, S. Moes, M. Colombi, J. A. Meier, M. M. Swierczynska, P. Jenö, C. Beglinger, R. Peterli, and M. N. Hall. 2018. "Insulin resistance causes inflammation in adipose tissue." *J Clin Invest* 128 (4):1538-1550. doi: 10.1172/jci96139.
21. Uysal, K. T., S. M. Wiesbrock, M. W. Marino, and G. S. Hotamisligil. 1997. "Protection from obesity-induced insulin resistance in mice lacking TNF-alpha function." *Nature* 389 (6651):610-4. DOI: 10.1038/39335.
22. Talukdar, S., D. Y. Oh, G. Bandyopadhyay, D. Li, J. Xu, J. McNelis, M. Lu, P. Li, Q. Yan, Y. Zhu, J. Ofrecio, M. Lin, M. B. Brenner, and J. M. Olefsky. 2012. "Neutrophils mediate insulin resistance in mice fed a high-fat diet through secreted elastase." *Nat Med* 18 (9):1407-12. DOI: 10.1038/nm.2885.
23. Fu, W., and M. N. Hall. 2020. "Regulation of mTORC2 Signaling." *Genes (Basel)* 11 (9). DOI: 10.3390/genes11091045.

Author

Alicia Shin is a junior at Torrey Pines High School who has been eager to be part of the medical field since childhood. She hopes to expand her interest in biology and medicine by majoring in biology in college and possibly studying in medical school.

DOI: 10.36838/v5i1.1

IJHSR
ijhighschoolresearch.org
REVIEW ARTICLE

Naturalistic Neuroimaging: From Film to Learning Disorders

Asha Dukkipati

Alcuin School, 6144 Churchill Way, Dallas, Texas, 75230, USA; ashadukkipati@gmail.com

ABSTRACT: Cognitive neuroscience explores neural functioning and aberrant brain activity during cognitive and perceptual tasks. Neurocinematics is a subfield of cognitive neuroscience that observes neural responses of individuals watching a film to see similarities and differences between individuals. This method is typically used for commercial use, allowing directors and filmmakers to produce better visuals and increase their results at the box office. However, neurocinematics is increasingly becoming a standard tool for neuroscientists interested in studying similar brain activity patterns across viewers outside the film industry. In this review, I argue that neurocinematics provides a straightforward, naturalistic approach to researching and diagnosing learning disorders. While the neural underpinnings of developmental learning disorders are traditionally assessed with well-established methods like EEG and fMRI that target particular cognitive domains, such as simple visual and attention tasks, there is initial evidence and theoretical background supporting neurocinematics as a biomarker for learning differences. By using ADHD, dyslexia, and autism as case studies, this literature review discusses the potential advantages of neurocinematics as a new tool for learning disorders research.

KEYWORDS: Behavioral and Social Sciences; Neuroscience; Neurocinematics; Biomarkers; Neurobehavioral disorders.

Introduction

According to the Centers for Disease Control, 17% of children ages 3-17 in the US have a developmental disability or learning disorder.[1] Children with a learning disorder are at higher risk of adversity, including familial neglect and poorer health outcomes in adulthood. Moreover, children with learning disorders experience disproportionate levels of family adversity compared to typically developing children. The three most commonly diagnosed learning disorders are attention-deficit hyperactivity disorder (ADHD), dyslexia, and autism spectrum disorder (hereafter referred to as autism). Individuals with ADHD show signs of being inattentive and/or hyperactive-impulsive, while students with dyslexia demonstrate difficulty in talking, reading, writing, and spelling.[18] In contrast, children with autism exhibit impairment in communication, relationships, verbal skills, and restricted/repetitive behaviors.[2] These disorders are necessary to diagnose because they can help parents be proactive in finding the tools needed for their child's education and health and reduce the risk of adversity in their academic journey or social situations. Understanding a child's learning deficiencies will help parents and school faculty take the necessary interventions and provide the correct accommodations for growth.

Because learning disorders and neurological disparity can impact the adolescent brain and later behaviors, it is essential to identify learning disorders in children early in life.[3] One valuable method of diagnosing these disorders is by examining biomarkers. Biomarkers are a measurable characteristic of biological processes such as those relating to psychological activity.[4] Clinicians use behaviors and psychological indicators to diagnose learning disorders. Still, biomarkers add benefit by providing more objective criteria for diagnosis. Crucial biomarkers for learning disorders grounded in neurobiology have previously been identified through electroencephalography (EEG) and functional magnetic resonance imaging (fMRI). EEG is a form of brain imaging that acquires brain signals called event-related potentials (ERPs) through electrodes attached to the scalp.[5]Signals from EEG can determine neurological engagement and functional interactions across neural networks, making the signals valuable biomarkers for the types of psychological processes implicated in learning disorders.[6] This method is also beneficial for diagnoses because it has a higher tolerance for motion artifacts, which can better accommodate testing with infants and children who tend to move more during the testing process.[7] Indeed, combining behavioral measures and ERPs from EEG during a go/no-go impulsivity task enabled 84-97% accuracy at discriminating ADHD diagnostic status in two different cohorts of participants.[8] Yet, high heterogeneity in learning disorders and the tendency to rely on a single or handful of EEG measures limits the use of EEG as a diagnostic tool for ADHD and other learning disorders.[6] In comparison, fMRI indirectly measures brain activity by capturing changes in the hemodynamic response across the entire brain, which is the measurement of blood oxygenation. While fMRI is less portable than EEG, it gives a spatial resolution that may be important for distinguishing between brain activity in regions with high proximity but distinct functions.[9] For example, the go/no-go task has also been used to compare children with and without ADHD. It was shown that the pre-supplementary motor area, but not other frontal regions, was hypoactive compared to typically developing children.[10] Despite some promising success, similar issues limit the application of traditional fMRI and EEG as biomarkers of ADHD and other learning disorders. In particular, the use of highly controlled experiments with simple stimuli in neuroimaging

DOI: 10.36838/v5i1.2

limits the ability to capture dynamic responses that better resemble brain activity during real-world situations.[11]

Neurocinematics is a new and promising method to diagnose learning disorders, sometimes referred to as *naturalistic neuroimaging*. Historically, neurocinematics has been used to assess the effects of film and other forms of visual entertainment on a viewer's brain activity to inform cinematic techniques for filmmakers. However, this field has recently been used to explore cognitive processing during dynamic situations reminiscent of real life.[11,12] One popular analysis method is intersubject correlation, which measures the similarities between participants' perceptual, emotional, and cognitive states during the same event.[13,14] In a landmark study by Hasson and colleagues conducted in 2004, five participants watched the first thirty-minute sequence of *The Good the Bad and the Ugly* directed by Sergio Leone while their brain activity was measured using fMRI. Regions of the brain that are shown to be associated with faces and objects were synchronized across participants, particularly during moments when faces and objects were in focus.[15] This study provided evidence that neurocinematics can be a powerful technique for uncovering properties of cognitive processing that are similar across individuals.

This review will evaluate neurocinematics as a new strategy for identifying neurological biomarkers to diagnose three common neurodevelopmental disorders: ADHD, dyslexia, and autism. This review discusses each neurobehavioral disorder in-depth and also seeks to showcase the various physiological biomarkers present for each, but more comprehensive reviews include.[7,16,17] Overall, the paper highlights a few key studies that use neuroimaging measures to examine these disorders and then discusses neurocinematics as a new and promising method for diagnosis.

Section 1: Children with ADHD:

ADHD is a neurodevelopmental condition that affects 3-5% of children worldwide who typically exhibit symptoms as early as seven years old. However, the number of children with ADHD may be higher because the ability to diagnose and optimally manage the disorder is currently low in developing countries.[18] There is no cure for ADHD. Still, it can be managed through a multidisciplinary approach, including behavioral therapy, psychotherapy, and drug treatment. For instance, Neurotherapy or biofeedback has been seen to improve symptoms. Symptoms exhibited by individuals with ADHD include inattention, hyperactivity, and/or impulsivity. There are also symptoms associated with executive dysfunction leading to issues with initiation, time management, working memory, planning, and organizing. This disorder can be categorized into two subtypes: inattentive presentation and predominantly hyperactive-impulsive. Children who fall under the inattentive type demonstrate signs of distractibility, forgetfulness, difficulty in organizing and completing tasks, trouble listening when spoken to, and failing to remember to turn in asynchronous assignments. Individuals categorized as hyperactive-impulsive subtypes display squirming, talkativeness, and fidgeting, and they find it challenging to sit still. Along with this, they can also be impatient, demonstrate a lack of emotional restraint, and blurt random and, at times, inappropriate comments.[18] Clinical psychologists and psychiatrists diagnose ADHD primarily on psychological conditions based on a profile of symptoms associated with a reduction in the quality of social, academic, or occupational functioning.[18]

The causes of ADHD are unknown; however, hypothesized factors include genetics, diet, and social and environmental factors. Some onset symptoms can also occur from a close head injury (CHI). According to past research, 75% of cases of children with ADHD stem from their genetic background, specifically genes that affect dopamine transporters such as dopamine receptors D2 /D3 and dopamine beta-hydroxylase monoamine oxidase A. Dopamine can contribute based on its effects on learning and cognitive functioning.[19] However, no single gene has been shown to contribute to ADHD.[18] Another study demonstrates that 10% to 85% of cases of ADHD in childhood are potentially associated with comorbid psychopathology: mood and anxiety disorders.[20] The World Health Organization states that ADHD can also stem from social dysfunction that a child is exposed to, whether in their familial life or in the education system, which affects the child's self-regulatory abilities.[21]

Multiple biomarkers have been identified for ADHD to help with clinical diagnosis and treatment. EEG biomarkers use a combination of temporal, spectral, and spatial features for diagnosis.[22] Major EEG biomarkers include theta-beta waves ratio and Event-Related Potentials (ERP). However, previous studies have found difficulty in diagnosing ADHD with theta waves; a study conducted with 101 people by Ogrim and his team reported sensitivity of 63% and specificity of only 58% in differentiating between children with and without ADHD, in contrast with an accuracy of 85% based on classification by children's behavioral omission errors alone (as cited in 6). Nonetheless, theta waves relate to hyperarousal, one of the earliest symptoms associated with this neurobehavioral disorder.[6] ERPs are beneficial based on their ability to capture the temporal evolution of neural activity following a prescribed event (e.g., responses following selective attention or other executive function tasks), allowing for a more specific diagnosis. Although, they can be susceptible to high variance when relatively few trials are averaged, limiting the efficacy of ERP in predicting ADHD diagnosis in previous experimental studies.[6] Overall, EEG is not an effective tool for diagnosis. Still, it remains useful in a clinical setting via multivariate analyses and refined studies of EEG signal generators to capture additional sources of heterogeneity in ADHD.[6,22] Another common biomarker is genetics because the dopamine transporter gene (DAT1 gene) has been linked to the development of ADHD, showing deficits in inhibitory behavior and hyperactivity.[7] Dopamine is a modulator of learning and cognitive functioning.[3] A European Child & Adolescent Psychiatry study recruited 273 high-risk Chinese individuals diagnosed with ADHD and their family members. The results demonstrate that the haplotype rs27048 is strongly associated with the inattentive type, concluding that the DAT1 gene may primarily affect individuals with ADHD.[23]

DOI: 10.36838/v5i1.2

The use of neurocinematics to identify new biomarkers for ADHD was recently tested in an experiment with 51 adults with ADHD (no subtypes were specified) and 29 individuals without ADHD.[24] Patients and controls watched a curated film showing a conversation with auditory distractors in the background. ADHD-related aberrant brain responses to this naturalistic stimulus were identified using ISC on subjects' fMRI data. The ADHD group demonstrated abnormal functioning in the dorsal and ventral attention networks, salience network, and sensory areas — namely, patients displayed less synchronous activity in these regions when distractors were present compared to control subjects.[24] By creating a novel experimental design using movies, the authors discovered abnormal neural processing during a demanding yet highly realistic situation. This anomalous ISC signature also correlated with behavioral measures of ADHD symptoms specific to inattention. This method has been used to detect abnormal functioning and signatures of ADHD, which provides further evidence of the potential efficacy of this method for diagnosing learning disorders.

Despite the promising results of this study, it is not clear how effective neurocinematics is versus past methods in diagnosing ADHD in children, as no direct comparison has been made.[24] Thus, more neurocinematics studies are needed to determine if this method can account for other symptoms associated with ADHD, such as skills in sustaining or dividing attention and the ability to regulate the level of attention on demand. To date, most neuroimaging biomarkers of ADHD focus on impulsivity, but there is no promising current biomarker that distinguishes between the two ADHD subtypes. Distinguishing between different symptom profiles and ADHD subtypes is essential for prescribing treatments for patients.

In addition to traditional EEG and fMRI approaches, neurocinematics may be a good way of distinguishing ADHD subtypes based on which parts of the brain respond synchronously to a given set of stimuli. For instance, children with hyperactive and non-hyperactive subtypes may react differently when viewing films. For example, children with the hyperactive subtype may require short, attention-grabbing films (i.e., a cartoon episode versus a nature documentary) to stimulate brain activity. This is because hyperactive children may struggle to focus on a film long enough to acquire necessary stimulus data, such as readouts from EEG. Alternatively, it may be that neurocinematics, in combination with identifying other biomarkers, such as genetics, may yield the best detection of ADHD. However, the perfect diagnostic tool remains unknown until ADHD is examined more with neurocinematics.

Section 2: Children with Dyslexia:

Dyslexia is a learning disability characterized by difficulty in reading, word recognition, and spelling.[25] In one study, it was found that 80% of individuals diagnosed with learning disabilities have dyslexia.[16] Dyslexia is the most common neurobehavioral disorder affecting children.[26] While it is considered more prominent in girls, recent data has demonstrated that it occurs equally between both genders.[25] Students with dyslexia who have decreased capabilities in reading, causing a hindrance in academic performance, which leads to self-esteem issues and emotional and behavioral problems.[25,27] One study reported that children with reading difficulty at the ages of eight and twelve were unhappier, more anxious, and less competent scholastically, and their parents stated that their self-esteem issues were low.[28] There are two main strategies when prescribing treatment for dyslexia: assistance with the impaired learning areas (reading and spelling) and psychotherapy for any coexisting psychological disturbance that may be present.

The causes of this disorder are unknown; however, some research indicates that it is predominantly influenced by neurobiological and cognitive factors, as well as heritability. This is consistent with the statistic that 23% to 65% of all children with dyslexia have a parent with the same disorder.[16] Most theories on dyslexia primarily point to problems in temporal processing and stem from research on the visual and language systems. Some investigators believe the central difficulty displayed in dyslexia patients is rooted in the phonetic system, which is engaged in processing sounds and speech.[16]

There have been several biomarkers to diagnose and prescribe treatment for dyslexia. Pernet and his team (2009) argue that the right cerebellum may be a biomarker for dyslexia.[29] In this study, they compared cognitive abilities and the size of different brain regions in subjects with dyslexia and controls without this neurobehavioral disorder. The subjects with dyslexia had low cerebellar declive volume and performed worse than those with a high cerebellar decline in the phonological and lexical tasks assigned. This evidence suggests that various subtypes of dyslexia may be characterized by different neurological phenotypes that correlate to varying deficiencies in language processing.[29] The best performances on the language tests were observed in control subjects, who showed a different profile of brain size in basal ganglia and right cerebellar declive. Overall, the study indicated that the basal ganglia, particularly the right cerebellar declive, are effective biomarkers for classifying individuals with dyslexia.

In another study, two children with dyslexia and two without engaged in a lexical task while undergoing fMRI.[30] The results indicated that the children with dyslexia displayed greater activation during reading tasks in the frontal and occipital cortex than typical readers. Other differences in activation between children with and without dyslexia were recorded in five brain regions: the right inferior parietal lobe, the right middle frontal gyrus, the left frontal precentral gyrus, the left insula, and the left fusiform gyrus. However, this study is hindered based on the small number of subjects examined, making the results less dependable. Yet other studies with larger samples have also shown differences in brain activity in similar regions. A study that recruited 18 individuals with dyslexia scanned them using an fMRI machine before and after they received instructional treatment.[31] The study examined the inferior frontal gyrus, middle frontal gyrus, the occipital region, and cerebellum. The results concluded that children with dyslexia had greater functional connectivity from the left inferior frontal gyrus to the right inferior frontal gyrus than the children without dyslexia, showing another difference in these regions as in the study above, increasing the validity of the results.[31]

The current research on neural biomarkers of dyslexia is inconclusive, and neurocinematics may provide a new perspective helpful for diagnosing this disorder. In particular, it may be that more realistic scenarios in which children are reading in the context of achieving a goal, like understanding a homework assignment, may be important for understanding the aberrant neural processes involved in this disorder. For example, patients with dyslexia and typical readers could watch a film with a variety of texts, such as an old silent film, or even a Khan Academy-style (2021) video teaching on a topic appropriate to their age, such as history or language arts. While most neurocinematics studies use fMRI, temporal disruption is problematic for dyslexic subjects, meaning EEG might be a better technique to use in conjunction with neurocinematics than fMRI.

Section 3: Children with Autism:

Autism is a spectrum disorder meaning that a child with this neurobehavioral disorder can experience a wide range of symptoms varying from mild to severe. Children with autism can have difficulty with communication and social interaction. They also tend to exhibit repetitive behavior and have issues with adjustment or disturbances to their daily routine. Children with autism can also be sensitive to touch, specific smells, loud noises, extreme temperatures, and certain colors. Signs of autism can be seen as early as 12 months.

However, the criteria for diagnosis have changed several times over the last couple of decades, including the age of diagnosis. The mean age in 1990 was ten years and reduced to 5 years by 2002.[33] Also, the diagnostic criteria became broader over the years based on the wide range of symptoms one can have with autism since it is a spectrum disorder. For instance, one study examined 405 individuals between the ages of 10 and 53 diagnosed with an autism spectrum disorder.[33] Although 100% of the patients were diagnosed with autism before their adolescence, based on current criteria for diagnosis, only 54.8% would be classified as autistic.[33] For individuals to be diagnosed with this neurobehavioral disorder today, they must display impairments in social interaction and communication; restricted repetitive and stereotyped patterns of behaviors, interests, and activities; and delayed or abnormal functioning before age three years in social interaction, language, or symbolic or imaginative play.[33]

The severity of autism also varies between individuals. The manifestation of symptoms is based on the domain. For instance, adolescents improved more based on the reciprocal social interaction domain.[33] There is no cure for autism, but there are interventions that can be implemented to help reduce or relieve symptoms. For instance, a treatment known as applied behavioral analysis (ABA) is an educational behavioral intervention identified as an effective treatment to address learning deficiencies.[34]

Multiple factors can contribute to someone developing autism. There has been a current increase in autism cases in the United States, Europe, and Japan, a spike reported to stem at least partly from increased recognition directly, changed diagnostic criteria, and changed public attitudes.[35] Most researchers believe that the cause of autism is rooted in genetics and family factors. There is a concordance of autism in monozygotic twins, which is reported to be as high as 70%.[35] Currently, genetic factors are thought to account for 7-8% of autism cases, and this number is more reliable since this statistic is from a study in 2021.[35] Despite the evidence tying genetic background to autism, there is no direct genetic information that thoroughly explains certain clinical and epidemiological aspects of autism, which raises questions on other potential influences of this spectrum disorder. There is also reason to believe that autism can be caused by environmental factors such as exposure to toxic chemicals, including lead and methylmercury, and other prenatally environmental components during embryonic and fetal life.[35] However, in a case in Sweden of prenatal exposure to thalidomide, the percentage of exposed children later diagnosed with autism was only 4%. Another potential contributor is toxins or reactions to vaccines containing mercury.

Individuals with autism have a high rate of comorbidity with intellectual disability, about 45%, and many (between 29 and 47%) experience regression related to social behavior.[36] The rise in cases and severity of autism leads to the clinical need for the availability of objective biomarkers for use in the prognosis and diagnosis of these patients.[36] Methods used to identify more efficient biomarkers have included neuroimaging, gene testing, transcriptomics, proteomics, and metabolomics. Specifically, fMRI can be used to diagnose children at 6-12 months of age when autism behavior is first emerging and has a positive predictive value of 81%.[36] However, based on previous studies, autistic symptoms shown during infancy can begin to dissipate over time. Another method used is EEG, demonstrating that the most significant differences appear at ages 9 to 12 months. Infants were classified with over 80% accuracy into control and high risk of autism (HRA) groups at age 9. This study indicates that EEG may increase efficacy in diagnosis early on.[37] The identification of biomarkers for autism spectrum disorder has improved over the years. However, due to the heterogeneity of the disease, the utility of these biomarkers still faces difficulties and challenges.

Identifying new biomarkers is essential to developing proper therapeutic treatments and interventions for autism, and neurocinematics may be a potential method. Because films have Spatio-temporal complexity, neurocinematics can allow for a deeper understanding of the different brain regions and symptoms of autism compared to previous studies examining subjects with learning differences doing lexical tasks. Additionally, films often show complex social relationships amongst characters that require the audience to think through social interactions and language. Recently, a group of researchers created child-friendly cartoon "films" designed to tap into the theory of mind (i.e., the ability to think about another person's thoughts) during neuroimaging.[38] Curated media is an effective biomarker of autism given its emphasis on cognitive processes that go awry in this neurodevelopmental disorder.

■ Discussion & Conclusion

This review explained three different neurobehavioral disorders (ADHD, dyslexia, and autism spectrum disorder) and how traditional biomarkers are used for diagnosis. This argumentative review helps illustrate how neurocinematics—a

DOI: 10.36838/v5i1.2

rising field to help with cognitive neuroscience—can be utilized to identify better biomarkers for learning disorders based on the film's spatiotemporal complexity and ability to tap into more naturalistic cognitive contexts. This allows for examining brain functions that may not be present during typical tasks utilized in current diagnostic methods like fMRI and EEG. A common trend noticed throughout this paper is that although these traditional biomarkers have been somewhat effective with diagnosis, they contain limitations preventing a complete data analysis of one's neurological functioning, hindering our understanding of the causation of ADHD, dyslexia, and autism, and prescribing proper diagnosis and treatment. However, neurocinematics also presents limitations. There is a lack of clarity in using film to diagnose developmental disorders for early detection. For instance, 18 months or less early intervention is deemed critical for ensuring the best outcomes in autism. However, this age range may not be the appropriate target for neurocinematics that taps into more complex processes. Another limitation is that the studies examined in the paper discuss small sample sizes, which hinders the ability to identify biomarkers and understand the vast heterogeneity of these disorders. Although neurocinematics on its own may be limited, this field can be more effective in combination with other approaches. With the increasing interest in neurocinematics, it is now time to apply this method to answer some of the most critical questions about how children with neurodevelopmental disorders learn, with the aim of diagnosis and treatment.

Acknowledgements

Special thanks to my mentor Tristan Yates, a Ph.D. student in Psychology at Yale University. She helped me navigate the process of writing my first research paper and was a tremendous support to me in my goal of understanding learning differences through the lens of neurocinematics. I would like to also thank Diana Wang and Tyler Moulton, recent graduates from Harvard, who guided me in the editing process. Lastly, I want to thank both my parents for their continuous support and dedicate this honor in memory of my Dad who was a guiding example of a life invested in research.

References

1. CDC. Increase in developmental disabilities among children in the United States https://www.cdc.gov/ncbddd/developmentaldisabilities/features/increase-in-developmental-disabilities.html (accessed Oct 5, 2021).
2. Shattuck, P. T.; Seltzer, M. M.; Greenberg, J. S.; Orsmond, G. I.; Bolt, D.; Kring, S.; Lounds, J.; Lord, C. Change in Autism Symptoms and Maladaptive Behaviors in Adolescents and Adults with an Autism Spectrum Disorder. *J Autism Dev Disord* 2007, 37 (9), 1735–1747. https://doi.org/10.1007/s10803-006-0307-7.
3. Berke, J. D. What Does Dopamine Mean? *Nat. Neurosci*. 2018, 21 (6), 787–793.
4. Califf, R. M. Biomarker Definitions and Their Applications. *Exp. Biol. Med.* (Maywood) 2018, 243 (3), 213–221.
5. Hajat, Z.; Ahmad, N.; Andrzejowski, J. The Role and Limitations of EEG-Based Depth of Anaesthesia Monitoring in Theatres and Intensive Care. Anesthesia 2017, 72 *Suppl* 1, 38–47.
6. Lenartowicz, A.; Loo, S. K. Use of EEG to Diagnose ADHD. Curr. *Psychiatry Rep*. 2014, 16 (11), 498.
7. Mehta, T.; Mannem, N.; Yarasi, N. K.; Bollu, P. C. Biomarkers for ADHD: The Present and Future Directions. *Curr. Dev. Disord. Rep.* 2020, 7 (3), 85–92.
8. Häger, L. A.; Åsberg Johnels, J.; Kropotov, J. D.; Weidle, B.; Hollup, S.; Zehentbauer, P. G.; Gillberg, C.; Billstedt, E.; Ogrim, G. Biomarker Support for ADHD Diagnosis Based on Event Related Potentials and Scores from an Attention Test. *Psychiatry Res.* 2021, 300 (113879), 113879.
9. O'Shaughnessy, E. S.; Berl, M. M.; Moore, E. N.; Gaillard, W. D. Pediatric Functional Magnetic Resonance Imaging (FMRI): Issues and Applications. *J. Child Neurol.* 2008, 23 (7), 791–801.
10. Suskauer, S. J.; Simmonds, D. J.; Fotedar, S.; Blankner, J. G.; Pekar, J. J.; Denckla, M. B.; Mostofsky, S. H. Functional Magnetic Resonance Imaging Evidence for Abnormalities in Response Selection in Attention Deficit Hyperactivity Disorder: Differences in Activation Associated with Response Inhibition but Not Habitual Motor Response. *J. Cogn. Neurosci*. 2008, 20 (3), 478–493.
11. Hasson, U.; Landesman, O.; Knappmeyer, B.; Vallines, I.; Rubin, N.; Heeger, D. J. Neurocinematics: The Neuroscience of Film. *Projections* 2008, 2 (1), 1–26.
12. Sonkusare, S.; Breakspear, M.; Guo, C. Naturalistic Stimuli in Neuroscience: Critically Acclaimed. *Trends Cogn.* Sci. 2019, 23 (8), 699–714.
13. Nastase, S. A.; Gazzola, V.; Hasson, U.; Keysers, C. Measuring Shared Responses across Subjects Using Intersubject Correlation. *Soc. Cogn. Affect. Neurosci.* 2019, 14 (6), 667–685.
14. Finn, E. S.; Glerean, E.; Khojandi, A. Y.; Nielson, D.; Molfese, P. J.; Handwerker, D. A.; Bandettini, P. A. Idiosynchrony: From Shared Responses to Individual Differences during Naturalistic Neuroimaging. *Neuroimage* 2020, 215 (116828), 116828.
15. Hasson, U.; Nir, Y.; Levy, I.; Fuhrmann, G.; Malach, R. Intersubject Synchronization of Cortical Activity during Natural Vision. *Science* 2004, 303 (5664), 1634–1640.
16. Shaywitz, S. E. Dyslexia. *N. Engl. J. Med.* 1998, 338 (5), 307–312.
17. Anderson, G. M. Autism Biomarkers: Challenges, Pitfalls and Possibilities. *J. Autism Dev. Disord*. 2015, 45 (4), 1103–1113.
18. Frank-Briggs, A. Attention Deficit Hyperactivity Disorder (ADHD). *J. Pediatr. Neurol*. 2015, 09 (03), 291–298.
19. Cheon, K.-A.; Ryu, Y.-H.; Kim, J.-W.; Cho, D.-Y. The Homozygosity for 10-Repeat Allele at Dopamine Transporter Gene and Dopamine Transporter Density in Korean Children with Attention Deficit Hyperactivity Disorder: Relating to Treatment Response to Methylphenidate. *Eur. Neuropsychopharmacol.* 2005, 15 (1), 95–101.
20. Millstein, R. B.; Wilens, T. E.; Biederman, J.; Spencer, T. J. Presenting ADHD Symptoms and Subtypes in Clinically Referred Adults with ADHD. J. *Atten. Disord.* 1997, 2 (3), 159–166.
21. Fayyad, J.; Sampson, N. A.; Hwang, I.; Adamowski, T.; Aguilar-Gaxiola, S.; Al-Hamzawi, A.; Andrade, L. H. S. G.; Borges, G.; de Girolamo, G.; Florescu, S.; Gureje, O.; Haro, J. M.; Hu, C.; Karam, E. G.; Lee, S.; Navarro-Mateu, F.; O'Neill, S.; Pennell, B.-E.; Piazza, M.; Posada-Villa, J. The Descriptive Epidemiology of DSM -IV Adult ADHD in the World Health Organization World Mental Health Surveys. A*DHD Attention Deficit and Hyperactivity Disorders* 2016, 9 (1), 47–65. https://doi.org/10.1007/s12402-016-0208-3..
22. Müller, A.; Vetsch, S.; Pershin, I.; Candrian, G.; Baschera, G.-M.; Kropotov, J. D.; Kasper, J.; Rehim, H. A.; Eich, D. EEG/ERP-Based Biomarker/Neuroalgorithms in Adults with ADHD: Development, Reliability, and Application in Clinical Practice. *World J. Biol. Psychiatry* 2020, 21 (3), 172–182.
23. Shang, C.-Y.; Gau, S. S.-F.; Liu, C.-M.; Hwu, H.-G. Association between the Dopamine Transporter Gene and the Inattentive Subtype of Attention Deficit Hyperactivity Disorder in Taiwan. *Prog-*

ress in Neuro-Psychopharmacology and Biological Psychiatry 2011, 35 (2), 421–428. https://doi.org/10.1016/j.pnpbp.2010.08.016.
24. Salmi, J.; Metwaly, M.; Tohka, J.; Alho, K.; Leppämäki, S.; Tani, P.; Koski, A.; Vanderwal, T.; Laine, M. ADHD Desynchronizes Brain Activity during Watching a Distracted Multi-Talker Conversation. *Neuroimage* 2020, 216 (116352), 116352.
25. Novita, S. Secondary Symptoms of Dyslexia: A Comparison of Self-Esteem and Anxiety Profiles of Children with and without Dyslexia. *Eur. J. Spec. Needs Educ.* 2016, 31 (2), 279–288.
26. Schulte-Körne, G. The Prevention, Diagnosis, and Treatment of Dyslexia. *Dtsch Arztebl Int.* 2010, 107 (41), 718-27. https://doi.org/10.3238/arztebl.2010.0718.
27. McNulty, M. A. Dyslexia and the Life Course. *J. Learn. Disabil.* 2003, 36 (4), 363–381.
28. Casey, R.; Levy, S. E.; Brown, K.; Brooks-Gunn, J. Impaired Emotional Health in Children with Mild Reading Disability. *J Dev Behav Pediatr* 1992, 13 (4), 256–260.
29. Pernet, C. R.; Poline, J. B.; Demonet, J. F.; Rousselet, G. A. Brain Classification Reveals the Right Cerebellum as the Best Biomarker of Dyslexia. *BMC Neurosci.* 2009, 10 (1), 67.
30. Berman, S.; Cicchino, N.; Hajinazarian, A.; Mescher, M.; Holland, S. K.; Horowitz-Kraus, T. An FMRI Study of a Dyslexia Biomarker. *Journal of Young Investigators* 2014, 26 (1).
31. Richards, T. L.; Berninger, V. W. Abnormal FMRI Connectivity in Children with Dyslexia during a Phoneme Task: Before but Not after Treatment. *J. Neurolinguistics* 2008, 21 (4), 294–304.
32. Dietz, P. M.; Rose, C. E.; McArthur, D.; Maenner, M. National and State Estimates of Adults with Autism Spectrum Disorder. *J. Autism Dev. Disord.* 2020, 50 (12), 4258–4266.
33. Seltzer, M. M.; Krauss, M. W.; Shattuck, P. T.; Orsmond, G.; Swe, A.; Lord, C. The Symptoms of Autism Spectrum Disorders in Adolescence and Adulthood. *J. Autism Dev. Disord.* 2003, 33 (6), 565–581.
34. Vismara, L. A.; Rogers, S. J. Behavioral Treatments in Autism Spectrum Disorder: What Do We Know? *Annu. Rev. Clin. Psychol.* 2010, 6 (1), 447–468.
35. Landrigan, P. J. What Causes Autism? Exploring the Environmental *Contribution. Current Opinion in Pediatrics* 2010, 22 (2), 219–225. https://doi.org/10.1097/MOP.0b013e328336eb9a.
36. Shen, L.; Zhao, Y.; Zhang, H.; Feng, C.; Gao, Y.; Zhao, D.; Xia, S.; Hong, Q.; Iqbal, J.; Liu, X. K.; Yao, F. Advances in Biomarker Studies in Autism Spectrum Disorders. *Adv. Exp. Med. Biol.* 2019, 1118, 207–233.
37. Bosl, W.; Tierney, A.; Tager-Flusberg, H.; Nelson, C. EEG Complexity as a Biomarker for Autism Spectrum Disorder Risk. *BMC Med.* 2011, 9 (1). https://doi.org/10.1186/1741-7015-9-18.
38. Borbás, R.; Fehlbaum, L. V.; Rudin, U.; Stadler, C.; Raschle, N. M. Neural Correlates of Theory of Mind in Children and Adults Using CAToon: Introducing an Open-Source Child-Friendly Neuroimaging Task. *Developmental Cognitive Neuroscience* 2021, 49, 100959.

Author

Asha Dukkipati — I struggled with ADD and dyslexia during my adolescence while my brother battled Asperger's. So experimenting with alternative treatments such as neurofeedback became a way of life. My love of neuroscience and film grew from seeking solutions and documenting the therapies for spreading awareness. This evolved into discovering the interdisciplinary field of neurocinematics and wanting to research further into this developing science to treat neurodiverse individuals with learning differences.

DOI: 10.36838/v5i1.2

IJHSR
ijhighschoolresearch.org
■ RESEARCH ARTICLE

A Quantitative Analysis of the Active Ingredients of Broad-leaved Bamboo and Study on Its Skin Condition Improvement Effect

Christine Yuna Jang

Saint Johnsbury Academy Jeju, 1159, Gueok-ri, Daejeong-eup, Seogwipo-si, Jeju-do. 63644, S. Korea; yuna4ulove@gmail.com

ABSTRACT: Je-ju-jo-rit-dae is a medicinal plant widely used in oriental medicine. However, its high reproductive rate has become a problem for the environmental ecosystem in Jeju. The extracts of the je- ju-jo-rit-dae are known for their antioxidant and anti-cancer effects. Still, no research has been conducted on significant impact and efficacy as an external skin agent, which has yet to be used commercially. This study performed a highly anti-oxidizing analysis by extracting the handle with methanol as a non-skin material at Je-ju-jo-rit-dae and identified its anti-inflammatory function and collagen synthesis ability. The HPLC analysis of these functional divisions shows Asiatic acid and Asiaticoside among the high levels of flavonoids and triterpenoid. The efficiency of Je-ju-jo-rit-dae found in the study is likely a good material for high-functioning skin external agents.

KEYWORDS: Nutrition and Natural Products; Immunology; Anti-inflammation; Collagen-neogenesis; *Sasa-Borealis*.

■ Introduction

Sasa borealis, a bamboo genus plant belonging to the Gramineae, is also called *Phyllostachys nigra* var. hennis Stapf, *Phyllostachys bambusoides S. et Z*, or *Sasa borealis* in oriental medicine. Among these, *Sasa borealis* is classified into the species of *Sasa borealis Hackel Makino*, *Sasa kurilensis Makino et Shibata*, and *Sasa quelpaertensis Nakai*. The leaves used as medicine are narrow needle-shaped, 7-15 cm long, 1-2 cm wide, sharp at one end, and a leafstalk attached to the other. Overall, it is green, and the back is light green and observed from the base.[1] *Sasa borealis* in the plant ecosystem on Jeju Island is not welcomed. In the plains with low altitudes, it is not a significant threat because the growth rate of the *Sasa borealis* can be relatively controlled. On the other hand, at the high altitude of Hallasan Mountain, where there are many natural protected species and rare plants, the strong vitality of *Sasa borealis* gradually dominates the growing area of the native species growing in the region is a problem because their numbers are increasing. However, the range of use of the naturally existing *Sasa borealis* has not been expanded to a particular industrial area, and thus the number of populations has not been controlled.[2,3]

Human skin is a multi-layered tissue composed of stratum corneum, epidermal, dermal, and basal layers, and the fat and muscle layers below it. It is a vital organ that protects the human body from external stimuli and mediates sensations such as touch and pain.[4] Skin naturally loses its function and structure due to aging as well as stress and toxic environmental stimulation, and in this process, inflammation occurs, and collagen loss occurs.[5] It has been shown that *Sasa borealis* contains polyphenols, including flavonoids, isoorientine, tricin, luteolin, etc. Whether *Sasa borealis* can induce skin inflammation relief and collagen resynthesis has not been studied.[1,6] This study aimed to increase the need for ecological control of Je-ju-jo-rit-dae by applying external skin preparations for Je-ju- jo-rit-dae and to discover new active ingredients that exist in Je-ju-jo-rit-dae by sorting the methanol extract of Je-ju-jo-rit-dae and confirming the stimulating activity of anti-inflammatory and collagen synthesis.

■ Methods

1. Reagents and research substances:

1,1-diphenyl-2-picrylhydrazyl (DPPH), 2,2'-azino-bis (3-ethylbenzothiazoline-6-sulfonic acid) diammonium salt (ABTS), gallic acid, Folin & Ciocalteu's phenol reagent, sodium carbonate (Na_2CO_3), aluminum chloride ($AlCl_3 \cdot 6H_2O$), quercetin, quercetin-3-O-rutinoside, myrcetin, luteolin, kaempferol, madecassic acid, madecassoside, Asiatic acid, Asiaticoside used in this experiment were purchased and used from Sigma-Aldrich (St. Louis, MO, USA).

2. Method and preparation for extracting Sasa borealis:

Sasa borealis used in this experiment was collected from September to October 2019 in the area of Hallasan in Jeju Island, was washed with purified water, dried at room temperature, cut into 1~2 cm in size, and dried at 40°C for two days. The completely dried *Sasa borealis* was weighed in units of 500g with a precision balance, mixed with 3 liters of methanol, and extracted at room temperature. After extraction and filtering with Whatman Filter paper, the filtrate was concentrated until completely evaporated with a rotary vacuum evaporator (N-1200, EYELA, Tokyo, Japan) at 40°C. The remaining solid extract was dissolved in distilled water and methanol. The same amount of n-hexane, chloroform, ethyl acetate, and n-butanol were sequentially solvent fractionated to obtain a fraction (Figure 1).

3. The fixed amount of flavonoids:

The content of total phenolic compounds was measured using the Folin-Denis method.[7] After each extract was prepared at a concentration of 1 mg/ml, 72 μl of distilled water was added to 24 μl of the sample solution, and 24 μl of Folin-ci-

DOI: 10.36838/v5i1.3

calteu reagent was added and mixed, followed by incubation for 5 minutes. After adding 24 μl of Na_2CO_3 and 56 μl of distilled water, the mixture was left in the dark for 1 hour and 30 minutes, and the absorbance was measured at 725 nm (Perkin Elmer, Victor2 1420 Multilabel counter). Then, the amount was converted from a standard curve using Gallic acid.

The total flavonoid content was measured using the Zhishen method.[8] After adding 50 μl of distilled water and 7.5 μl of a 5% $NaNo_2$ solution to 75 μl of the sample solution, the mixture was allowed to stand for 5 minutes. Then 15 μl of a 10% $AlCl_3 \cdot 6H_2O$ aqueous solution was added and reacted for 6 minutes. After 6 minutes, 50 μ l of 1N- NaOH aqueous solution was added and reacted at room temperature for 10 minutes, and the absorbance was measured at 450 nm. Then, the Quercetin was compared with the standard solution, and the content was calculated.

Confirmation of antioxidant activity: DPPH and ABTS assay :

The method of Wayner nine was modified to measure the antioxidant efficacy. In the case of the hydrogen donating activities for DPPH, 100 μl of the sample solution and 100 μl of the DPPH solution were mixed in a 96-well plate, left to stand at room temperature for 30 minutes, and then measured with a spectrophotometer (Perkin Elmer, Victor2 1420 Multilabel counter) at 540 nm. After comparison with the control group to which the sample was not added, the free radical scavenging effect was calculated as follows and expressed as a percentage (%).

$$Inhibition(\%) = (1 - \frac{absorbance of sample solution - absorbance of blank test solution}{absorbance of no additives}) \times 100$$

In the case of ABTS radical scavenging effect, 2.6 mM $K_2S_2O_8$ was mixed with 7.4 mM ABTS solution and reacted in the dark for about 12 hours, and then an ABTS solution was adjusted to have an absorbance value of 1.0 ± 0.1 at 734 nm was used. 285 μl of ABTS solution was mixed with 15 μl of samples for each concentration and reacted in the dark for 30 minutes to measure absorbance at 734 nm. The resulting value was expressed as a percentage (%) of the radical scavenging effect after comparing the extract-added and non-added groups.

5. Confirmation of in vitro anti-inflammatory effects:

To determine the anti-inflammatory effect of the extract, the extracts were distributed and used in RAW264.7 cells (ATCC, American Type Culture Collection, USA). For culture, an RPMI medium containing 10% FBS (fetal bovine serum, Gibco, USA) and 1% antibiotics was used. Then, it was cultured under conditions of 37°C and 5% CO_2.In the case of LPS (Lipopolysaccharide derived from *E. coli*, Sigma-Aldrich), it was diluted to 200 ng/ml in the medium on the second day of cell stabilization and treated. For 6 hours after treatment, the activation of cells was observed and calculated based on the degree of adhesion of the cells and the formation of dendritic structures.

6. Immunofluorescence measurement of collagen formation:

To confirm the collagen formation effect of the extract, human fibroblasts were received from ATCC and used. Twenty-four hours after the sample treatment, each cell was fixed with 4% formalin for 5 minutes at room temperature, washed several times with PBS (Phosphate buffered saline), and then treated with 0.05% Triton-X100 to permeabilize for 5 minutes at room temperature. The treated cells were blocked in 1% albumin solution for 1 hour, and the primary antibody was treated with 1:200 (Collagen I/IV antibody, 9007-34-5, Sigma-Aldrich) at 4° C for 12 hours. After treatment, it was washed several times with PBS, and Alexafluro-488 conjugated rabbit antibody (cellsignaling, USA) as a secondary antibody was treated at room temperature at 1:250 for 3 hours. Then the nuclei were stained with DAPI (1mg/ml) at room temperature for 5 minutes. The treated sample was observed with confocal laser microscopy (LSM800, Zeiss, Germany), and quantitative analysis was performed with ZEN blue software.

7. HPLC analysis:

For analysis, the extracts were centrifuged, and the supernatant was filtered through a 0.45 μm filter and used as a sample solution. Then, 15 μl was injected into the HPLC for analysis. Agilent 1200 series (Agilent Technologies, Santa Clara, CA, USA) was used as the HPLC analyzer, and the column was Phenomenex Gemini NX C18 (4.6×150 mm, three μm), and the temperature was 30°C. Agilent DAD was used as the detector, and the wavelength was set to 254 nm. The flow rate was 0.6 ml/min, and 15 μl was set as an injection volume. The moving bed was 0.5% aqueous formic acid solution (A) and acetonitrile (B), 5% B-3 min, 10% B-8 min, 10% B-12 min, 15% B 15 min, 15% B-20 min, 40% B-27 min, 40% B-32 min, 65% B-39 min, 65% B-43 min, 30% B-48 min, 10%-B 50 min were analyzed under gradient conditions. As external standards, quercein-3-O-rutinoside, kaempferol-3-O-glucoside, myricetin, luteolin, kaempferol, Madecassoside, Madecassic acid, Asiatic acid, and Asiaticoside were used. The qualitative and quantification of each standard were compared with the original standard's retention time. The result of the content of each fraction and the fraction using silica column chromatography was obtained from the calibration curve.

8. Statistical analysis:

All experiments were repeated at least three times and expressed as mean and standard deviation (S.D). Statistical analysis was done using ANOVA (one-way analysis of variance) and Student's t-test, which was determined to be significant when $p<0.05$.

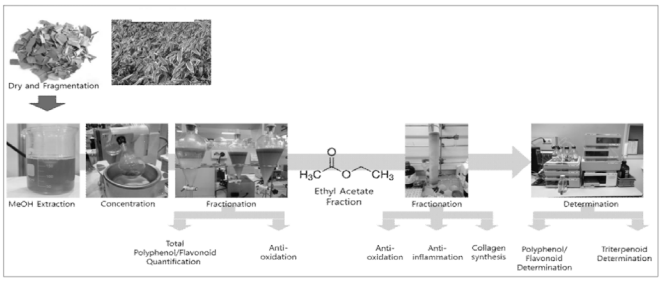

Figure 1: Design and progress of the experiment.

DOI: 10.36838/v5i1.3

Results

1. Extraction and extraction yield of Broad-leaved Bamboo:

500 g of dried leaves of *Sasa borealis* were pulverized, immersed in 3 liters (L) of methanol solvent for 24 hours at room temperature, filtered, and reduced pressure to obtain an extracted solid in an average yield of 21.30% (S.D = 7.24, N = 5). After stirring and dissolving the extract in a mixture of distilled water and methanol (9:1 v/v), the fractions are kept for 3 hours in 4 solvents with different polarities: n-hexane (Hx), CHCl3 (Cf), Ethyl acetate (EA) and n-BuOH (Bu), and then extracted, filtered, and reduced pressure to obtain a solid as shown in Table 1. Among the fractions, the yields of EA and Bu fractions were the highest.

Table 1: Total extract and TPC, TFC result.

Sample	Yield (%)	Total Polyphenolic compounds (mg Gallic acid equivalent/g)	Total Flavonoid compounds (mg Quercetin equivalent/g)
Methanol	21.30	78.54±5.0	248.39±3.5
n-hexane	0.54	15.50±0.4	247.23±3.9
Chloroform	0.02	28.01±1.0	219.64±0.2
Ethyl acetate	2.95	374.30±7.1	213.20±2.4
n-butnol	4.37	128.58±2.1	294.34±7.8

2 Measurement of flavonoid content in total extract of Sasa borealis:

According to a study by Nam *et al.*, it was found that phenolic compounds were present in the extract of *Sasa borealis*, but an accurate analysis of the content was not performed.[10] Therefore, the amount of total phenolic compounds (TPC) and the number of total flavonoids (TFC) were compared and analyzed in the extracts and extracted fractions used in this study. In the case of TFC, it was generally about 220 mg/g (SD = 45.35) as a result of quantification by the Folin-Ciocalteu method using Quercetin as a reference substance. In contrast, in the case of TPC, it showed the highest impact, 374.30 mg/g (SD = 7.1) in the EA fraction (SD = 7.1).

3 Measurement of Antioxidant Activity of Total Extract of Sasa borealis:

DPPH and ABTS assays were performed to evaluate antioxidant activity. DPPH turns purple depending on the presence of antioxidant activity and is chemically stabilized, water-soluble, and is mainly used to detect antioxidants and aromatic amine substances. ABTS radical scavenging effect method developed based on the fact that antioxidants inhibit the absorbance of ABTS cationic radicals in plasma can be compared with Trolox, a positive control. It can be expressed by measuring the level at which the turquoise color gradually disappears since it has the opposite color development tendency as DPPH.

In the case of the antioxidant activity of the extract of *Sasa borealis*, as a result of comparing vitamin C (Ascorbic acid; AA) as positive control by the DPPH method, it was confirmed that the total extract (MeOH), EA, and Bu fractions had relatively high antioxidant activity (Figure 2A). Similarly, compared with the positive control Trolox in the ABTS method, overall higher antioxidant activity was detected compared to the DPPH method, and relatively high antioxidant activity was also confirmed in EA and Bu fractions (Figure 2B).

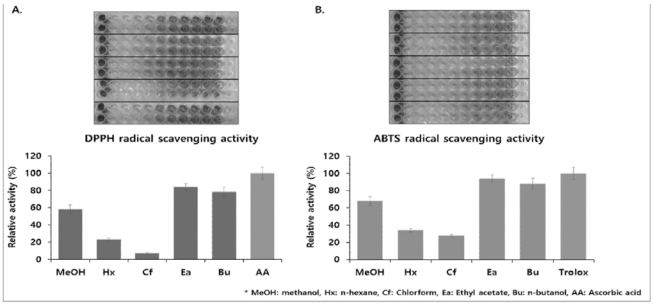

Figure 2: Antioxidant Activity of total extracts and fractions (A) DPPH assay result (B) ABTS assay result

4. Fraction of EA fraction and measurement of antioxidant Activity of Fraction:

Five fractions were obtained using Silica gel column chromatography (CHCl3: Methanol = 100:0 to 0:100 gradient) for further separation of the EA fraction, showing consistent antioxidant activity among the fractions of the extract of *Sasa borealis* (Figure 3A).

The antioxidant activity of each fraction was high in F3 and F4 in the DPPH method (Figure 3B) and F3, F4, and F5 in the ABTS method (Figure 3C).

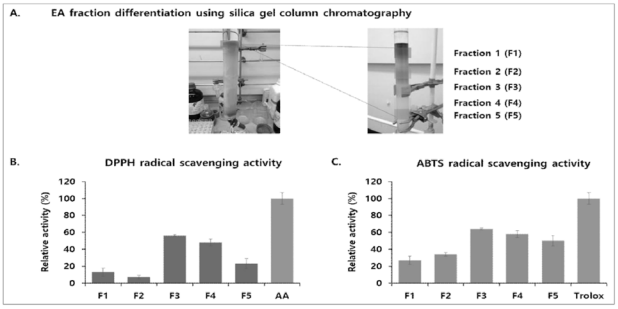

Figure 3: Ethyl acetate Fraction (A) Result of Silica gel chromatography (B) DPPH assay result for each fraction (C) ABTS assay result for each fraction

5. Confirmation of the differentiation inhibitory ability of fractional extract against LPS-stimulated macrophages:

Activating macrophage cell line RAW264.7 cells by treatment with Lipopolysaccharide (LPS), a cell membrane component of the infectious agent, is a frequently used method for measuring anti-inflammatory activity.[12] To identify the active ingredient in the EA fraction, it was determined whether the activation of macrophages occurred in cells treated with or without LPS after treating the RAW264.7 cell line with LPS. As shown in Figure 4A, in the group treated with the same amount of DMSO as the vehicle without any fraction treatment, the cells reacted to LPS and dendritic differentiation. Still, in the group treated with the fraction at a low concentration (5% v/v), the number of activated cells drops sharply. In particular, when fractions were treated at a high concentration (20% v/v), macrophage activity decreased to a level similar to that of the negative control (Figure 4B).

6 Confirmation of the collagen new synthesis promoting effect of the fractional extract on fibroblasts:

Polyphenols and flavonoids may cause the anti-inflammatory effect of the fraction. Still, it is well known that Triterpenoid, a representative, effective polysaccharide present in plants, also has excellent anti-inflammatory effects and the effect of

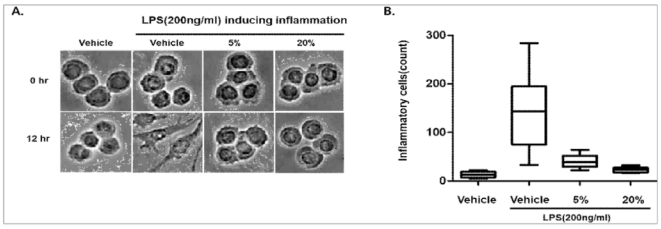

Figure 4: Determination of the anti-inflammatory activity of ethyl acetate activity (A) Optical microscope showing the degree of macrophage activation (B) Quantitative analysis result of activation energy

promoting collagen synthesis.[13,14] To confirm this, the fractions were treated by concentration in human fibroblast cells and then quantified by immunofluorescence compared to the positive control vitamin C (AA) (Figure 5A). As a result, it was confirmed that in cells treated with AA around the cell's nucleus labeled (blue fluorescence), high levels of collagen were expressed (green fluorescence) in the entire cytoplasm and even in cells treated with a low concentration (5% v/v) fraction, a slightly increased level of collagen was observed compared to the negative control group. Surprisingly, it was found that higher levels of collagen were synthesized in cells treated with the fraction at a high concentration (20% v/v) than in the positive control group, indicating that the fraction had a higher content of components that induce collagen synthesis (Figure 5B).

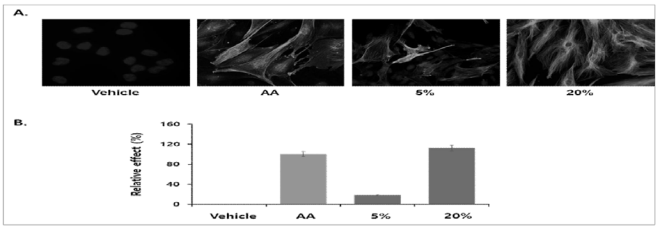

Figure 5: Measurement of ethyl acetate fraction's ability to induce collagen synthesis (A) Immunofluorescence Image of collagen1, Blue: Nucleus, Green: Collagen (B) Quantitative analysis result for expression level

7. Isolation of active ingredients from fractional extract: Triterpenoids and Flavonoids:

To separate the previously identified polyphenols, flavonoids, and components having anti-inflammatory and collagen synthesis promoting effects, the corresponding fractions were analyzed using HPLC. The chromatogram of the standard components detected in the standard solution and sample extracts of each sample is shown in Figure 6. The calibration level of each element in the standard solution was checked to establish the analysis method of each standard component. During the precision (%), the yield for QC, RE, and CV of LLOQ were less than 20%, and LQC, MQC, and HQC were less than 10%.

As a result of the analysis, the contents of Kaempfetol-3-glucoside and quercetin-3-rutinoside as flavonoids were high, 44 ug/ml and 27 ug/ml, respectively (Figure 6A), and as a Triterpenoid, the contents of Asiatic acid and Asiaticoside among the reference substances were high, 637 ng/ml and 213 ng/ml respectively (Figure 6B).

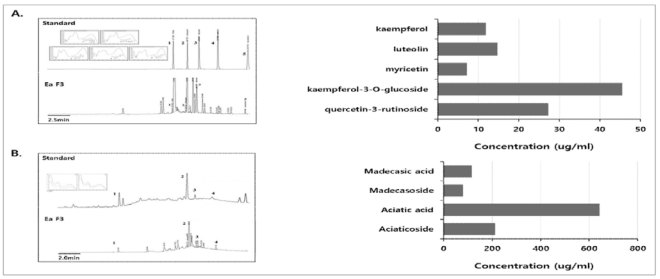

Figure 6: HPLC analysis of Polyphenol, Flavonoid, and Triterpenoid in Ethyl Acetate Fraction (A) HPLC analysis results for flavonoids and polyphenols (B) HPLC analysis results for representative triterpenoids

Discussion

Broad-leaved Bamboo has been recognized for its efficacy in the past. It has been used as a medicinal material in oriental medicine but has not received attention for its pharmacological use due to its wide growing area and high fertility.[15] In particular, the extract of *Sasa borealis* has been studied not only for metabolic diseases such as diabetes and high blood pressure but also for its anticancer effect.[1,10,16]

This study aimed to expand the scope of industrial use of Broad-leaved Bamboo, confirm whether Broad-leaved Bamboo is effective in human skin health, and isolate and identify active ingredients that cause the efficacy.

First, this study focused on non-aqueous active ingredients by extracting them with methanol. Previous studies have found that antioxidants of polyphenols can be identified by hot water extraction. In particular, to be used in skin health products that mainly use the emulsion properties of water, oils, and fats, it is also essential to confirm a non-aqueous active ingredient. As a result of the experiment, TPC and TFC, like hot water extraction, were also found in fractions of different solvents for the total methanol extract. It was found that extraction of phenolic compounds higher than hot water extraction was possible in the entire content portion.[1]

Ethyl acetate is a solvent mainly used to remove caffeine from tea and coffee, and the content of the active ingredient in the extract of *Sasa borealis* was the highest.[17] The fraction by Silica gel chromatography showed high antioxidant activity and anti-inflammatory and collagen synthesis promoting effects, confirming the possibility as an active ingredient for external skin preparations.

Polyphenols and flavonoid compounds, known mainly as active ingredients of *Sasa borealis*, have high antioxidant activity but relatively low anti-inflammatory effects. In particular, little is known about the impact of promoting collagen synthesis on fibroblasts.[18] This study confirmed high levels of anti-inflammatory and collagen synthesis in certain fractions of Ethyl acetate from *Sasa borealis*. It established the hypothesis that these effects were not simply due to the high polyphenol content. Triterpenoid is a compound commonly known to promote collagen synthesis among many plant-derived active ingredients. In particular, Madecassic acid, Madecassoside, Asiatic acid, and Asiaticoside have excellent efficacy enough to be used in pharmaceuticals.[19] Therefore, it has the possibility that the high collagen synthesis induction ability of *Sasa borealis* may be caused by these Triterpenoids. As a result of

DOI: 10.36838/v5i3.3

HPLC analysis of the EA fraction, it was confirmed that the content of Madecassic acid or Madecassoside is low in the extract of *Sasa borealis*. Still, the content of Asiaticoside or Asiatic acid is high.

This study expanded the industrial applicability of Broad-leaved Bamboo by studying the content of previously unknown active ingredients and new functions of anti-inflammatory and collagen synthesis-inducing ability through fractional extraction from the native Broad-leaved Bamboo of Hallasan Mountain. However, in this study, since only *Sasa borealis* harvested from Hallasan Mountain around September 2019 were used, additional studies are needed to determine whether Sasa borealis harvested in different regions of Jeju or at other times have the same content or distribution of active ingredients.

In summary, this study aimed to expand the scope of industrial use of *Sasa borealis* through the development of natural vegetable raw materials that have anti-inflammatory and collagen synthesis induction ability necessary for skin inflammation or wrinkle improvement, confirmed the antioxidant efficacy of *Sasa borealis* through methanol extraction and fraction extraction, the anti-inflammatory efficacy and collagen synthesis induction ability in the Ethyl acetate fraction with high antioxidant activity to identify new functions of *Sasa borealis*, and not only investigated the new function of Sasa borealis but also reported the previously unknown contents of Asiatic acid and Asiaticoside as well as the high content of formerly known phenols in the fraction. As a result, the methanol extract of *Sasa borealis* appears to have high antioxidant, anti-inflammatory, and collagen synthesis ability due to its active ingredients. Thus it is highly likely to be used as an essential material for functional skin external preparations.

Acknowledgments

I want to acknowledge and express my sincere appreciation to Professor Woojin Kim (Department of Molecular Genetics at Seoul National University), who made this project possible. His delicate guidance carried me through all phases of this research. I would also like to thank my family, especially my father, for his ongoing assistance and understanding when during all stages of this work.

References

1. Park, H. S., Lim, J. H., Kim, H. J., Choi, H. J., & Lee, I. S. (2007). Antioxidant flavone glycosides from the leaves of *Sasa borealis*. Archives of pharmacal research, 30(2), 161-166.
2. Kim, H. C. (2009). Ecological characteristics and management methods of Sasa quelpaertensis Nakai (Doctoral dissertation, Jeju National University).
3. Lee, J., Lee, J. Y., Jang, B. J., Jeong, G., & Choi, S. W. (2019). Effects of elevation and canopy openness on a dwarf bamboo (Sasa quelpaertensis Nakai) vegetation and their consumer communities. Korean Journal of Environmental Biology, 37(3), 249-259.
4. Norlen, L. (2003). Skin barrier structure, function and formation–learning from cryo-electron microscopy of vitreous, fully hydrated native human epidermis. International journal of cosmetic science, 25(5), 209-226.
5. de Faria, J. C., Costa, M. P., Quagliano, A. P., & Ferreira, M. C. (1995). Skin aging and collagen. Revista do Hospital das Clinicas, 50, 39-43.
6. Jeong, Y. H., Chung, S. Y., Han, A. R., Sung, M. K., Jang, D. S., Lee, J., ... & Seo, E. K. (2007). P-Glycoprotein Inhibitory Activity of Two Phenolic Compounds,(–)-Syringaresinol and Tricin from *Sasa borealis*. Chemistry & biodiversity, 4(1), 12-16.
7. Attanzio, A., D'Anneo, A., Pappalardo, F., Bonina, F. P., Livrea, M. A., Allegra, M., & Tesoriere, L. (2019). Phenolic composition of hydrophilic extract of manna from sicilian fraxinus angustifolia vahl and its reducing, antioxidant and anti-inflammatory activity *in vitro*. Antioxidants, 8(10), 494.
8. Hamdy, A. A., Ismail, H. M., Ael-M, A. A., & Gomaa, N. F. (2009). Determination of flavonoid and phenolic Acid contents of clover, cotton and citrus floral honeys. The Journal of the Egyptian Public Health Association, 84(3-4), 245-259.
9. Wayner, D. D. M., Burton, G. W., Ingold, K. U., & Locke, S. (1985). Quantitative measurement of the total, peroxyl radical-trapping antioxidant capability of human blood plasma by controlled peroxidation: The important contribution made by plasma proteins. FEBS letters, 187(1), 33-37.
10. Nam, J. S., Chung, H. J., Jang, M. K., Jung, I. A., Park, S. H., Cho, S. I., & Jung, M. H. (2013). Sasa borealis extract exerts an antidiabetic effect via activation of the AMP-activated protein kinase. Nutrition research and practice, 7(1), 15-21.
11. Ullah, F., Iqbal, N., Ayaz, M., Sadiq, A., Ullah, I., Ahmad, S., & Imran, M. (2017). DPPH, ABTS free radical scavenging, antibacterial and phytochemical evaluation of crude methanolic extract and subsequent fractions of Chenopodium botrys aerial parts. Pak. J. Pharm. Sci, 30(3), 761-766.
12. Min, K. J., Cho, K. H., & Kwon, T. K. (2012). The effect of oxidized low density lipoprotein (oxLDL)-induced heme oxygenase-1 on LPS-induced inflammation in RAW 264.7 macrophage cells. Cellular signalling, 24(6), 1215-1221.
13. Vasconcelos, J. F., Teixeira, M. M., Barbosa-Filho, J. M., Lúcio,A. S. S. C., Almeida, J. R. G. D. S., De Queiroz, L. P., ... & Soares, M. B. P. (2008). The triterpenoid lupeol attenuates allergic airway inflammation in a murine model. International immunopharmacology, 8(9), 1216-1221.
14. Aminzadeh, M. A., Reisman, S. A., Vaziri, N. D., Khazaeli, M., Yuan, J., & Meyer, C. J. (2014). The synthetic triterpenoid RTA dh-404 (CDDO-dhTFEA) restores Nrf2 activity and attenuates oxidative stress, inflammation, and fibrosis in rats with chronic kidney disease. Xenobiotica, 44(6), 570-578.
15. Choi, Y. J., Lim, H. S., Choi, J. S., Shin, S. Y., Bae, J. Y., Kang, S. W., ... & Kang, Y. H. (2008). Blockade of chronic high glucose–induced endothelial apoptosis by Sasa borealis bamboo extract. Experimental Biology and Medicine, 233(5), 580-591.
16. Patil, M. P., Jin, X., Simeon, N. C., Palma, J., Kim, D., Ngabire, D., ... & Kim, G. D. (2018). Anticancer activity of Sasa borealis leaf extract-mediated gold nanoparticles. Artificial cells, nanomedicine, and biotechnology, 46(1), 82-88.
17. Wang, Y., Zhu, C., Zou, X., Huang, L., & Yan, D. (2013). Solvent demulsification-dispersive liquid-liquid microextraction based on solidification of floating organic drop coupled with gas chromatography-mass spectrometry for simultaneous determination of organochlorine pesticides in aqueous samples. Se pu= Chinese Journal of Chromatography, 31(11), 1076-1080.
18. Jean-Gilles, D., Li, L., Vaidyanathan, V. G., King, R., Cho, B., Worthen, D. R., ... & Seeram, N. P. (2013). Inhibitory effects of polyphenol punicalagin on type-II collagen degradation *in vitro* and inflammation in vivo. Chemico-biological interactions, 205(2), 90-99.
19. Bonte, F., Dumas, M., Chaudagne, C., & Meybeck, A. (1994). Influence of asiatic acid, madecassic acid, and asiaticoside on human collagen I synthesis. Planta medica, 60(02), 133-135.

Author

Christine Yuna Jang is a high school student with an extraordinary passion for biology. She attends Saint Johnsbury Academy Jeju in

South Korea. Currently, She pursues to major in Biomedical Engineering in college as a pathway to achieve her goal of becoming a biology researcher.

DOI: 10.36838/v5i3.3

IJHSR
ijhighschoolresearch.org
■ RESEARCH ARTICLE

Aberrant Human Gut Microbiome Composition in COVID-19 Patients: A Meta-Analysis

Cindy H. Lu

Arcadia High School, 180 Campus Dr, Arcadia, CA, 91006, U.SA.; cindyhlu711@gmail.com

ABSTRACT: The COVID-19 pandemic has created a global emergency that calls for a better understanding of our immune defenses against SARS-CoV-2. The gut microbiome plays a vital role in regulating host immunity. Emerging evidence has suggested a possible association of the irregular gut microbiome with COVID-19. However, the heterogeneity among the results of these studies requires thorough statistical analysis. This study examines the relationship between gut microbiome composition and COVID-19 through a systematic review of published research and statistical analysis. Three databases, including PubMed, Web of Science, and Embase, were searched for articles that reported measures of gut bacterial composition in COVID-19 patients. Eleven publications containing appropriate information were selected and analyzed for alpha diversity, beta diversity, and relative abundance indexes. The results of this study suggest that COVID-19 patients are associated with abnormal microbiome composition, as reflected by a statistically significant decrease in microbial diversity compared to healthy individuals. In addition, COVID-19 patients exhibited notably decreased health-promoting bacteria. The result of this study indicates that the gut microbiome can be used as a biomarker in monitoring COVID-19 disease progress and recovery. These findings suggest restoring the immunomodulatory bacteria may serve as a promising novel adjuvant therapy for COVID-19.

KEYWORDS: Microbiology; Applied Microbiology; COVID-19; Gut Microbiome; Bacterial Diversity.

■ Introduction

COVID-19, caused by SARS-CoV-2, has rapidly spread worldwide, resulting in over 500 million infections and 6 million deaths globally since December 2019.[1] It is a respiratory illness with a spectrum of clinical implications, and the symptoms can range from mild fever and cough to severe pneumonia and multiple organ failures. Infection by SARS-CoV-2 induces an immune response to eradicate the virus. Still, plenty of evidence has suggested that an aberrant immune response is responsible for severe illness and damage to the lung and other organs. It is also common that long-term implications on the body remain after the patients have recovered from the acute phase of the disease.[2,3] The severity of this disease has elicited the development of multiple COVID-19 therapies, most of which are focused on virus clearance, such as neutralizing monoclonal antibodies and small molecule drugs targeting the viral protease or RNA polymerase. However, due to the long-lasting effects of SARS-CoV-2 infection on the human body even after viral removal, it is necessary to develop novel therapy that allows patients to recover from the severe damages caused by COVID-19 entirely. The gut microbiome is the collection of many microorganisms living in symbiosis with hosts that contribute to human health. The gut microbiome is involved in the host nutrient metabolism, drug metabolism, protection from pathogens, and maintenance of structural integrity of the intestinal mucosal barrier. Studies in recent years have shown that the gut microbiome also plays an essential role in regulating the host immune system. Maintaining a healthy gut microbiome and the imbalance of the microbiome are implicated in metabolic diseases, autoimmune and inflammatory diseases, neurodegenerative disorders, and cardiovascular illness.[4,5] The goal of this study was to systematically review the emerging evidence on the association between gut microbiome alterations and COVID-19, highlighting the potential of using gut microbiome composition as a biomarker for monitoring disease progression and treatment effectiveness and its promise as a potential new adjuvant therapy for COVID-19.

■ Methods

A systematic review of the original clinical articles was conducted to evaluate the human gut microbiome in COVID-19. The "preferred reporting items for systematic review and meta-analysis" (PRISMA) reporting guidelines were followed.[6] PubMed, Embase, and Web of Science were searched to identify articles with original data published before February 1, 2022. Search terms or keywords include: "COVID-19," "COVID-19," SARS-CoV-2 Infection," "Gastrointestinal Microbiome," and "Gut Microbiome."

Selection Criteria:

The PRISMA guidance stipulates that the literature retrieval of systematic review and meta-analysis shall comply with PICOS:

P(Population): Patients with COVID-19
I(Intervention): SARS-CoV-2 infection
C(Comparison): Healthy controls without COVID-19
O(Outcomes): Aberrant gut microbiota composition
S(Study): Observational study

Data Extraction:

Publications details, including several patients and methodological information, were extracted. The community-level measures of gut microbiota composition (using alpha and beta diversity indexes) and taxonomic findings at the phylum and

DOI: 10.36838/v5i1.4

species levels (using relative abundance indexes) were then determined. Alpha diversity provides an overview of microbial communities in individual samples. It can be compared across groups to assess the samples' richness (number of species) and uniformity (representation of each species). Beta diversity is a measure of diversity among individuals (between samples). It evaluates the similarity between the community and control samples analyzed.[7,8] For the relative abundance of microbial groups, qualitative synthesis was conducted.

Results

1235 original studies in PubMed, Embase and Web of Science databases were obtained. 11 original studies were included according to the inclusion criteria. The literature screening flowchart is shown in Figure 1.

Characteristics of Included Studies:

Of the 11 studies included, seven were from China, and the remaining four were from the United States, Italy, India, and the United Arab Emirates. A total of 436 patients with COVID-19 infection and 336 healthy people were included in the analysis. The detailed characteristics of the included studies are shown in Table 1.

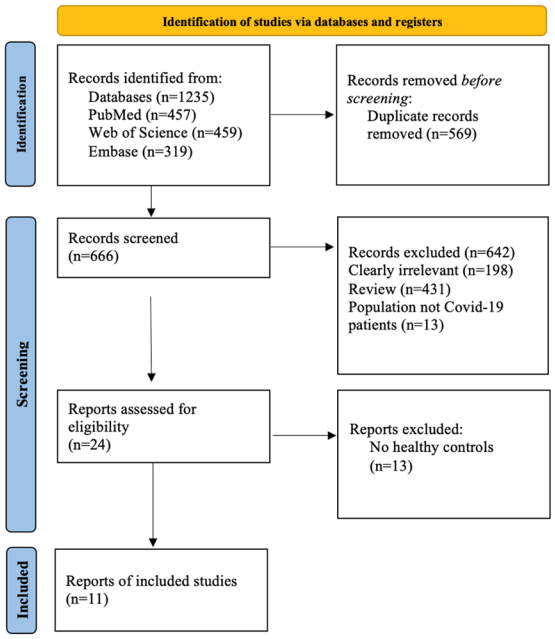

Figure 1: Screening flowchart.

Alpha Diversity:

Six of the eight studies that reported the Shannon index provided available data and were included in the analysis (230 patients and 182 controls). Although there is heterogeneity between the studies(I2=89%), the pooled estimate demonstrated a significant difference between groups (Standard Mean Difference (SMD) = −0.81; 95% *CI*, −1.56 to -0.06; p=0.03) (Figure 2). Compared with healthy people, COVID-19 patients had significantly lowered intestinal flora diversity.

Beta Diversity:

10 of the 11 studies performed the difference test based on principal component analysis. The results of the beta diversity analysis are summarized in Table 2. These studies showed that the composition of intestinal flora after infection with COVID-19 was significantly different from that of healthy people.

Relative Abundance:

All studies assessed the relative abundance of gut microbes, and 10 of 11 studies identified significant differences between patients and controls at phylum or genus levels. The differences between COVID-19 patients and healthy controls in microbial taxa spanned 14 phyla and 37 genera.

Table 1: Summary of included studies.

Study ID	Authors	Year	Country	# COVID	# Control	Alpha Diversity	Beta Diversity	Relative Abundance
1	Silan Gu et al.[9]	2020	China	30	30	Shannon Index; Chao Index	PCoA of Bray-Curtis	phylum, class, family, and genus
2	Mohammad Al Bataineh et al.[10]	2021	UAE	86	57	Shannon Index	PCoA of weighted UniFrac	genus
3	Jiabao Cao et al.[11]	2021	China	13	5	Shannon Index	PCoA of Bray-Curtis	species
4	Paolo Gaibani et al.[12]	2021	Italy	69	69	Simpson Index	PCoA of Bray-Curtis	family, genus and species
5	Sabine Hazan et al.[13]	2021	USA	50	20	Shannon Index; Simpson Index	weighted UniFrac	family, and genus
6	Mahejibin Khan et al.[14]	2021	India	30	10	Simpson Index; ACE Index; Fisher index	-	phylum, family, genus, and species
7	Sijia Li et al.[15]	2021	China	47	19	-	PCoA of Bray-Curtis	phylum, family, genus, and species
8	Zhigang Ren et al.[16]	2021	China	24	48	Shannon Index	-	phylum, and genus
9	Yun Kit Yeoh et al.[17]	2021	China	87	78	Shannon Index	-	phylum, and species
10	Tuoyu Zhou et al.[18]	2021	China	13	13	Shannon Index; Chao Index	-	phylum, family, genus and species
11	Zhonghan Sun et al.[19]	2022	China	63	8	Shannon Index	PCoA of unweighted Unifrac	phylum, and species

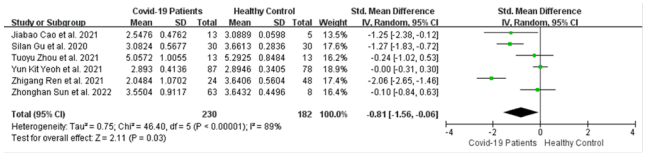

Figure 2: Compared with healthy controls, forest plots of Alpha Diversity richness estimators in the gut microbiota of patients with COVID-19.

Because the microbial taxa in the human intestine are very complex, and the microbial taxa studied in the 11 included articles are quite different, I chose to compare the typical flora in the top 7 phylum and top 7 genera. The phylum *Bacteroidetes, Firmicutes, Fusobacteria, Proteobacteria, Actinobacteria, Tenericutes*, and *Verrucomicrobia* account for more than 95% of the healthy human gut microbes,[20] and the genera Bacteroides, *bifidobacterium*, *eubacterium, clostridium, peptococcus, peptostreptococcus*, and *ruminococcus* are predominant in human gut microbes,[21-23] so the differences between the two groups in those categories were summarized.

Table 2: Methodology and findings of the included studies assessing beta diversity for comparing the COVID-19 and healthy control groups.

Study	Metric	Analysis	Result
Silan Gu 2020	PCoA of Bray-Curtis	ANOSIM	Significant different
Mohammad Al Bataineh 2021	PCoA of weighted UniFrac		Significant different
Jiabao Cao 2021	PCoA of Bray-Curtis	PERMANOVA	Significant different
Paolo Gaibani 2021	PCoA of Bray-Curtis	Permutation test with pseudo-F ratio	Significant different
Sabine Hazan 2021	PCoA of weighted UniFrac		Significant different
Sijia Li 2021	PCoA of Bray-Curtis		Significant different
Zhigang Ren 2021	PCoA based on OTU distribution		Significant different
Yun Kit Yeoh 2021	PCoA	PERMANOVA	Significant different
Tuoyu Zhou 2021	PCoA of Bray-Curtis		Significant different
Zhonghan Sun 2022	PCoA of unweighted Unifrac	PERMANOVA	Significant different

The differences between healthy control and COVID-19 groups are shown in Figure 3.

DOI: 10.36838/v5i1.4

At the Phylum level, Firmicutes showed a trend of reduced relative abundance in the intestines of COVID-19 patients compared to healthy individuals. At the genus level, the relative abundance of *bifidobacterium*, *ruminococcus*, and *peptostreptococcus* is significantly reduced in COVID-19 patients in most of the included studies.

Discussion

Because of the strong infectious characteristics of SARS-CoV2, there is no large-scale population study on the intestinal flora of COVID-19 patients. The limited number of cases in each study and the choice of reference population may be an essential source of heterogeneity between studies. I performed alpha diversity analysis on 230 patients and 182 healthy controls through a systematic and comprehensive search of published research. The result (Shannon Index SMD: -0.81(-1.56, -0.06)) showed that the alpha diversity of intestinal flora decreased significantly in COVID-19 patients (Figure 2). The decrease of intestinal flora diversity may be an essential process of a series of pathological conditions caused by SARS-CoV-2 virus invasion.

The beta diversity analysis has shown that the components of the patient's gut flora have changed significantly compared to healthy controls (Table 2).

The relative abundance of specific phyla and genera in COVID-19 patients compared to healthy controls was also summarized (Figure 3). Due to the limited number of cases and the fact that not all phylum and genus were studied in each publication, the relevant abundance for the majority of the phylum and genus is not yet apparent, and more studies with an increased number of cases will be needed to obtain a solidified conclusion. However, the results show that the relevant abundance of the *ruminococcus* genus, *peptostreptococcus* genus, and the *bifidobacterium* genus was significantly reduced in COVID-19 patients. Bifidobacterium is an abundant type of health-promoting bacteria in the gut of healthy individuals that helps with digestion and has immunomodulatory functions.

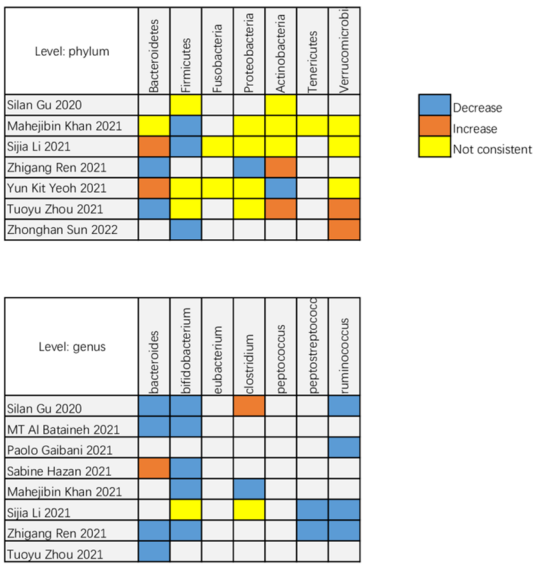

Figure 3: Compared to the healthy group, changes in the relative abundance of gut microbial taxa in the COVID-19 group.

To my knowledge, this is the first research to assess gut microbiota perturbations in COVID-19 patients through a systematic and comprehensive search and statistical analysis. As the gut microbiome is severely perturbed in COVID-19 patients, it can be used as a biomarker in monitoring patients' disease progress and recovery. Additionally, restoring the gut microbiome can be used as an adjuvant therapy to treat COVID-19 patients. COVID-19 can involve sequelae and a broad range of medical complications that last months after the initial recovery. Coincidently, the perturbation of the gut microbiome in COVID-19 patients can also last months after recovery. Since the gut microbiome plays a vital role in many host functions, including metabolism, strengthening gut integrity, and regulating host immunity, restoring the gut microbiome by supplementing patients with beneficial microorganisms may serve as a promising novel adjuvant therapy during the disease phase and post-acute phase to counteract long-lasting complications of COVID-19.

Conclusion

I performed a systematic and comprehensive search of published studies in this study and analyzed 11 selected studies for gut microbiome alpha diversity, beta diversity, and relative abundance indexes. The results suggest that COVID-19 patients are associated with aberrant microbiome composition, as reflected by a statistically significant decrease in microbial diversity compared to healthy individuals. In addition, COVID-19 patients exhibited decreased health-promoting bacteria, especially *Bifidobacterium*, which is abundant in healthy individuals. This study indicates that the gut microbiome can serve as a biomarker to monitor the disease progression and treatment effectiveness; that is, full recovery of a healthy microbiome is a valid indicator for the recovery of the patients. These findings also suggest that restoring the health-promoting bacteria may serve as a promising novel adjuvant therapy for COVID-19.

Acknowledgments

I want to thank Dr. Kaihong Su from Kaiser Permanente Medical School for her helpful discussions on the topics of COVID-19 and immunology.

References

1. https://www.who.int/emergencies/diseases/novel-coronavirus-2019.
2. Proal A.D. and B. Vanelzakker. Long COVID or post-acute sequelae of COVID-19 (PASC): an overview of biological factors that may contribute to persistent symptoms. Frontiers in Microbiology, 2021, 12: 698169.
3. Desai A. D., M. Lavelle, B. C. Boursiquot, and E. Y. Wan. Long-term complications of COVID-19. Am J Physiol Cell Physiol 2022, 322: C1-C11.
4. Hamming, I.; Timens, W.; Bulthuis, M. L.; Lely, A. T.; Navis, G.; van Goor, H., Tissue distribution of ACE2 protein, the functional receptor for SARS coronavirus. A first step in understanding SARS pathogenesis. J Pathol 2004, 203 (2), 631-7.
5. Hashimoto, T.; Perlot, T.; Rehman, A.; Trichereau, J.; Ishiguro, H.; Paolino, M.; Sigl, V.; Hanada, T.; Hanada, R.; Lipinski, S.; Wild, B.; Camargo, S. M.; Singer, D.; Richter, A.; Kuba, K.; Fukamizu, A.; Schreiber, S.; Clevers, H.; Verrey, F.; Rosenstiel, P.; Penninger, J. M., ACE2 links amino acid malnutrition to microbial ecology and intestinal inflammation. Nature 2012, 487 (7408), 477-81.

6. Hutton, B.; Salanti, G.; Caldwell, D. M.; Chaimani, A.; Schmid, C. H.; Cameron, C.; Ioannidis, J. P.; Straus, S.; Thorlund, K.; Jansen, J. P.; Mulrow, C.; Catalá-López, F.; Gøtzsche, P. C.; Dickersin, K.; Boutron, I.; Altman, D. G.; Moher, D., The PRISMA extension statement for reporting of systematic reviews incorporating network meta-analyses of health care interventions: checklist and explanations. Ann Intern Med 2015, 162 (11), 777-84.
7. Ait Chait, Y.; Mottawea, W.; Tompkins, T. A.; Hammami, R., Unravelling the antimicrobial action of antidepressants on gut commensal microbes. Sci Rep 2020, 10 (1), 17878.
8. Simpson, C. A.; Diaz-Arteche, C.; Eliby, D.; Schwartz, O. S.; Simmons, J. G.; Cowan, C. S. M., The gut microbiota in anxiety and depression - A systematic review. Clin Psychol Rev 2021, 83, 101943.
9. Gu, S.; Chen, Y.; Wu, Z.; Chen, Y.; Gao, H.; Lv, L.; Guo, F.; Zhang, X.; Luo, R.; Huang, C.; Lu, H.; Zheng, B.; Zhang, J.; Yan, R.; Zhang, H.; Jiang, H.; Xu, Q.; Guo, J.; Gong, Y.; Tang, L.; Li, L., Alterations of the gut microbiota in patients with coronavirus disease 2019 or H1N1 influenza. Clinical Infectious Diseases 2020, 71 (10), 2669-2678.
10. Al Bataineh, M. T.; Henschel, A.; Mousa, M.; Daou, M.; Waasia, F.; Kannout, H.; Khalili, M.; Kayasseh, M. A.; Alkhajeh, A.; Uddin, M.; Alkaabi, N.; Tay, G. K.; Feng, S. F.; Yousef, A. F.; Alsafar, H. S., Gut Microbiota Interplay With COVID-19 Reveals Links to Host Lipid Metabolism Among Middle Eastern Populations. Frontiers in Microbiology 2021, 12.
11. Cao, J. B.; Wang, C.; Zhang, Y. Q.; Lei, G. L.; Xu, K.; Zhao, N.; Lu, J. J.; Meng, F. P.; Yu, L. X.; Yan, J.; Bai, C. Q.; Zhang, S. G.; Zhang, N.; Gong, Y. H.; Bi, Y. H.; Shi, Y.; Chen, Z.; Dai, L. P.; Wang, J.; Yang, P. H., Integrated gut virome and bacteriome dynamics in COVID-19 patients. Gut Microbes 2021, 13 (1), 1-21.
12. Gaibani, P.; D'Amico, F.; Bartoletti, M.; Lombardo, D.; Rampelli, S.; Fornaro, G.; Coladonato, S.; Siniscalchi, A.; Re, M. C.; Viale, P.; Brigidi, P.; Turroni, S.; Giannella, M., The Gut Microbiota of Critically Ill Patients With COVID-19. Frontiers in Cellular and Infection Microbiology 2021, 11.
13. Hazan, S.; Stollman, N.; Bozkurt, H.; Dave, S.; Papoutsis, A. J.; Daniels, J.; Dolai, S.; Barrows, B. D.; Quigley, E. M. M.; Borody, T. J., The lost microbes of COVID-19: Bifidobacteria depletion and decreased microbiome diversity are a predictability marker of severe COVID 19, a cross sectional study. 2021.
14. Khan, M.; Mathew, B. J.; Gupta, P.; Garg, G.; Khadanga, S.; Vyas, A. K.; Singh, A. K., Gut Dysbiosis and IL-21 Response in Patients with Severe COVID-19. Microorganisms 2021, 9 (6), 16.
15. Li, S.; Yang, S.; Zhou, Y.; Disoma, C.; Dong, Z.; Du, A.; Zhang, Y.; Chen, Y.; Huang, W.; Chen, J.; Song, D.; Chen, Z.; Liu, P.; Li, S.; Zheng, R.; Liu, S.; Razzaq, A.; Chen, X.; Tao, S.; Yu, C.; Feng, T.; Liao, W.; Peng, Y.; Jiang, T.; Huang, J.; Wu, W.; Hu, L.; Wang, L.; Li, S.; Xia, Z., Microbiome Profiling Using Shotgun Metagenomic Sequencing Identified Unique Microorganisms in COVID-19 Patients With Altered Gut Microbiota. Frontiers in Microbiology 2021, 12.
16. Ren, Z.; Wang, H.; Cui, G.; Lu, H.; Wang, L.; Luo, H.; Chen, X.; Ren, H.; Sun, R.; Liu, W.; Liu, X.; Liu, C.; Li, A.; Wang, X.; Rao, B.; Yuan, C.; Zhang, H.; Sun, J.; Chen, X.; Li, B.; Hu, C.; Wu, Z.; Yu, Z.; Yu, Z.; Kan, Q.; Li, L., Alterations in the human oral and gut microbiomes and lipidomics in COVID-19. Gut 2021, 70 (7), 1253-1265..
17. Yeoh, Y. K.; Zuo, T.; Lui, G. C. Y.; Zhang, F.; Liu, Q.; Li, A. Y. L.; Chung, A. C. K.; Cheung, C. P.; Tso, E. Y. K.; Fung, K. S.C.; Chan, V.; Ling, L.; Joynt, G.; Hui, D. S. C.; Chow, K. M.; Ng, S. S. S.; Li, T. C. M.; Ng, R. W. Y.; Yip, T. C. F.; Wong, G. L. H.; Chan, F. K. L.; Wong, C. K.; Chan, P. K. S.; Ng, S.
18. Zhou, T.; Zeng, Y.; Wu, J.; Li, J.; Yan, J.; Meng, W.; Han, H.; Feng, F.; He, J.; Zhao, S.; Zhou, P.; Wu, Y.; Yang, Y.; Han, R.; Jin, W.; Li, X.; Yang, Y.; Li, X., SARS-CoV-2 triggered excessive inflammation and abnormal energy metabolism in gut microbiota. 2021.
19. Sun, Z.; Song, Z. G.; Liu, C.; Tan, S.; Lin, S.; Zhu, J.; Dai, F. H.; Gao, J.; She, J. L.; Mei, Z.; Lou, T.; Zheng, J. J.; Liu, Y.; He, J.; Zheng, Y.; Ding, C.; Qian, F.; Zheng, Y.; Chen, Y. M., Gut microbiome alterations and gut barrier dysfunction are associated with host immune homeostasis in COVID-19 patients. BMC Medicine 2022, 20 (1).
20. Eckburg, P. B.; Bik, E. M.; Bernstein, C. N.; Purdom, E.; Dethlefsen, L.; Sargent, M.; Gill, S. R.; Nelson, K. E.; Relman, D. A., Diversity of the human intestinal microbial flora. Science 2005, 308 (5728), 1635-8.
21. Bengmark, S., Ecological control of the gastrointestinal tract. The role of probiotic flora. Gut 1998, 42 (1), 2-7.
22. Guarner, F.; Malagelada, J. R., Gut flora in health and disease. Lancet 2003, 361 (9356), 512-9.
23. Simon, G. L.; Gorbach, S. L., Intestinal flora in health and disease. Gastroenterology 1984, 86 (1), 174-93.

Author

Cindy Lu is a senior at Arcadia High School who enjoys biomedical research and community outreach. Her work was awarded at the California State Science Fair and by the Yale Science and Engineering Association. She is an International Medicine Gold Medalist, British Biology Olympiad Silver Medalist, and USABO Semifinalist.

DOI: 10.36838/v5i1.4

IJHSR
ijhighschoolresearch.org
■ RESEARCH ARTICLE

Effect of Temperature on the Purity and Yield of Aspirin

Dhiman Roy

Saint Joseph's Institution International, Singapore 298191; dhiman.d.roy@gmail.com

ABSTRACT: Acetylsalicylic acid (aspirin) is a popular over-the-counter medication possessing anti-inflammatory and antipyretic properties. Given the large amount of aspirin manufactured annually worldwide, any modification of the manufacturing process that could increase its yield or purity would have industrial implications. In this study, we prepared aspirin through the esterification of salicylic acid with acetyl anhydride in the presence of phosphoric acid over a duration of 20 min while varying the temperature from 50 to 80 °C at 10 °C intervals. We observed increases in the percentage purity and yield of 1.25- and 1.28-fold, respectively, upon increasing the temperature from 50 to 80 °C at intervals. Linear relationships existed in the yield and purity of the synthetic aspirin, with both increasing upon increasing reaction temperature.

KEYWORDS: Acetylsalicylic acid; esterification; yield; spectrophotometry; thin layer chromatography.

■ Introduction

Salicylic acid has been used since ancient times, with the Sumerians and Egyptians describing the application of willow leaves containing it, for joint pain. In 1828, Johann Buchner at the University of Munich purified salicin from willow leaves. Still, it was not until Felix Hoffman from Bayer synthesized acetylsalicylic acid (aspirin) for the first time that it became a staple in medicine cupboards in every home.[1]

Salicylic acid is a weak acid isolated initially from the bark of the willow tree. Its structure features a hydroxyl (OH) group in an ortho position with respect to a carboxylic acid functional group on a benzene ring (Figure 1).[2]

Approximately 40,000 metric tons of aspirin are produced annually worldwide; as such, determining the optimal reaction temperature—to give the highest yield and purity—would dramatically affect industrial efficiency. The e-factor for the equilibrium reaction would also be significantly lower. Yield is the ratio of the actual number of moles of the product to the theoretical number of moles expected; purity is characterized by the mass of the desired chemical relative to the total mass of the product.

In this study, we explored the efficiency of the method used by pharmaceutical firms to synthesize aspirin: the acetylation of salicylic acid with acetic anhydride under reflux. Using an acid catalyst for this acetylation provides the reaction with a lower activation energy.[3] A concentrated acid is preferred because the water present in a dilute acid would also react with acetic anhydride to form acetic acid. This study aimed to evaluate the effect of the temperature of the reaction mixture (50, 60, 70, or 80 °C) on the yield and purity of the aspirin produced.

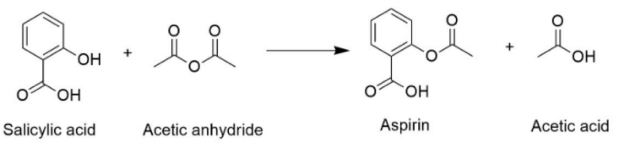

Figure 1: Synthesis of acetylsalicylic acid.

Reaction 1 is the primary reaction employed in this study for the synthesis of aspirin.

$$\textit{Reaction 1: } C_7H_6O_3 + C_4H_6O_3 \rightarrow C_9H_8O_4 + CH_3COOH$$
$$\textit{Salicylic acid} + \textit{acetic anhydride} \rightarrow \textit{aspirin}\ (\textit{acetylsalicylic acia}) + \textit{acetic acid}$$

Salicylic acid undergoes acetylation in the presence of acetic anhydride and a strong acid catalyst. Salicylic acid can, however, also react with acetic acid to form aspirin in an equilibrium reaction. As displayed above, acetic acid is a product of Reaction 1 and can, therefore, react with any unreacted salicylic acid to form aspirin, as shown in Reaction 2.

$$\textit{Reaction 2: } C_7H_6O_3 + CH_3COOH \rightleftharpoons C_9H_8O_4 + H_2O$$
$$\textit{Salicylic acid} + \textit{acetic acid} \rightleftharpoons \textit{aspirin}\ (\text{acetylsalicylic } \textit{acid}) + \textit{water}$$

■ Methods

In this experiment, the controlled variables included the time under reflux during the synthesis, the quantity of salicylic acid used, and the concentration of the acid catalyst (phosphoric acid). The independent variable was the temperature of the reaction mixture (50, 60, 70, or 80 °C), modified by changing the temperature of the water bath. The water bath was controlled such that if the water temperature fell below the set temperature, then the heating system would switch on to keep the actual temperature of the water close to the set value. The temperature was measured using a digital thermometer with an error of 0.5°C. The dependent variables were the purity and yield of the aspirin product. The purity of each aspirin sample was measured using a UV–V is spectrophotometer (Ultraviolet-Visible Imaging Spectroscope) and a calibration curve.[4,5] The percentage purity by mass was calculated from the mass of salicylic acid present (i.e., the major impurity) and the total mass of the product.[6] Thin layer chromatography (TLC) was used to check the purity of the aspirin. Since different compounds have different polarities, TLC can be used to identify the compounds present in a mixture because each component would have different affinities toward the stationary (silica gel) and mobile (solvent) phases.[7] For this

DOI: 10.36838/v5i1.5

carboxylic acid and phenol/ester functional groups render salicylic acid and aspirin as relatively polar.

Procedure

Synthesis of aspirin :

Salicylic acid (2.000 g) was placed in a round-bottom flask equipped with a condenser (Figure 2). Cool tap water was passed through the condenser to prevent fumes of acetic anhydride and acetic acid from escaping and being inhaled during the reaction. A water bath was prepared at 50 °C. The round-bottom flask was heated in the water bath to a temperature of 50 °C over a period of 10 min. Using a graduated pipette, concentrated phosphoric acid (1 mL) and acetic anhydride (5 mL) were added to the flask. The amounts of acetic anhydride and phosphoric acid were measured in a fume hood. The mixture was left to react for 20 min.[2,3] Distilled water (2 mL) was added to the mixture to stop the reaction through hydrolysis of the acetic anhydride. The flask was removed from the water bath. Distilled water (10 mL) was added slowly at the 21-min mark to decrease the solubility of the aspirin in the solvent mixture, inducing it to crystallize. The mixture was submerged in an ice bath for 5 min, allowing the aspirin to crystallize further (its solubility decreases at lower temperatures). Although the addition of water would have caused some of the aspirin to hydrolyze, the extent of hydrolysis was minimized by the low temperature of the ice bath.

During the cooling period, a Büchner filter funnel was set up using filter paper and some distilled water; prior to filtration, the filter paper was weighed to the third decimal place. The reaction mixture was then passed through the funnel with vacuum suction and the solids were left to dry for 20 min under constant vacuum pressure. The dryness of the sample was confirmed by treating a small amount of the mixture with cobalt(II) chloride, which would have turned pink in the presence of water. The aspirin sample was weighed, with the weight of the filter paper subtracted from the total weight. This whole process was repeated by applying the other water bath temperatures (60, 70, and 80 °C). Each run was replicated three times to improve the precision of the data collected.

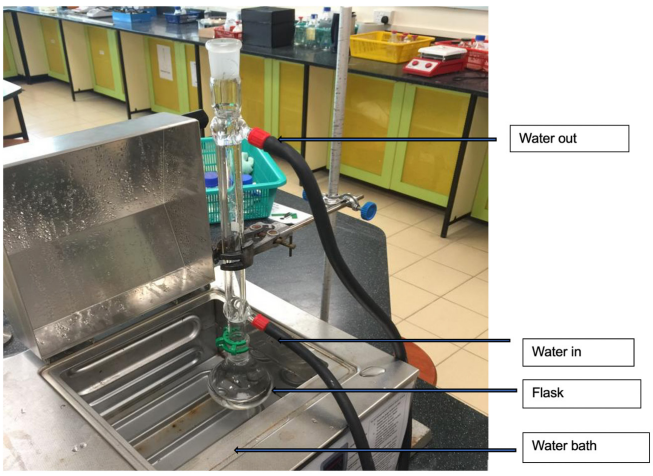

Figure 2: Experimental setup for the synthesis of aspirin.

Spectrophotometry:

A solution of 1% ferric chloride was prepared. Iron(III) chloride hexahydrate (5.000 g) was added to a 500-mL volumetric flask. 1 M Hydrochloric acid (20 mL) was added to the flask, followed by distilled water up to the 500 mL mark. This 1% ferric solution was used for the spectrophotometric analysis.

A calibration curve was established relating the concentration of the tetraaquosalicylatroiron(III) complex to its absorbance. Salicylic acid (0.200 g) was measured, with its mass recorded to the third decimal place. Ethanol (10 mL) was added to the powder, and then the solution was transferred to a 250-mL volumetric flask. Distilled water was added up to the 250 mL mark. A portion (20 mL) of the solution was transferred to a 100-mL volumetric flask. The 1% ferric chloride solution was added to the flask up to the 100 mL mark. Four different solutions were prepared to construct the calibration curve, using 2, 4, 6, and 8 mL of the complex solution and 8, 6, 4, and 2 mL of water. A spectrophotometer was used to determine the absorbance of the various solutions; the calibration curve was plotted, with absorbance on the y-axis and concentration on the x-axis.

To determine the concentration of salicylic acid in a sample of crude aspirin, the sample (0.200 g) was weighed and dissolved in ethanol (10 mL). The solution was transferred to a 250-mL volumetric flask, and distilled water was added up to the mark. The solution (20 mL) was transferred to a 100-mL volumetric flask, and then the 1% ferric chloride solution was added up to the mark. A cuvette was filled with the sample, and the absorbance was measured at 530 nm.

Measurements of the concentration of salicylic acid were used to calculate the aspirin concentration. Because the combined number of moles of unreacted and reacted salicylic acid was equal to the initial number of moles present, the number of moles of acetylsalicylic acid could be measured by subtracting the number of moles of unreacted salicylic acid from its initial number of moles.

Thin layer chromatography:

All of the following steps were performed in a fume hood. Three test tubes, A, B, and C, were set up on a rack. Pure salicylic acid, pure aspirin, and lab-synthesized aspirin (approximately one-third of a spatula) were added to test tubes A, B, and C, respectively. The aspirin sample was prepared by crushing a single tablet of store-bought aspirin (Cardiprin 100). A mixture of dichloromethane (DCM) and ethanol was prepared at a ratio of 1:1, using a 10-mL pipette. A portion of the mixture (5 mL) was measured in a measuring cylinder and added to each test tube. A TLC plate was marked with a horizontal starting line, drawn using a pencil (pen ink would have interfered with the results), featuring three equally distanced starting points labeled A (aspirin), PS (pure salicylic acid), and SA (synthesized aspirin). Using capillary tubes, the solutions from test tubes A, B, and C were drawn up and placed on the respective labeled marks on the TLC plate. The spots were left to dry. The last two steps were repeated five times to ensure that sufficient quantities of the solutes were present on the TLC plate. Ethanol was poured into the chro

DOI: 10.36838/v5i1.5

matography chamber to a height of at least 1 cm below the starting line of the TLC plate.

A lid was placed over the chamber to saturate the chamber with ethanol vapor, thereby preventing the rate of ethanol evaporation from significantly exceeding the rate of ethanol condensation on the TLC plate. If the evaporation rate were significantly higher than the condensation rate, the values of R_f obtained would be lower than those expected. The TLC plate allowed the mobile phase to move the analytes without hindrance. The TLC plate was developed for 1 hr.; the solvent level was marked with a pencil line, and then the TLC plate was left to dry for another 1 hr. The plate was placed under a short-wavelength UV lamp, and the locations of the spots of pure salicylic acid, aspirin, and lab-synthesized aspirin were identified. The distance between the starting and final points was recorded for each spot, as was the distance between the starting line and the final solvent level.

Results

Figure 2 displays the experimental setup. Figure 3 reveals that the gradient of the calibration curve was 1140±90. The plotted data and its line of best fit had a correlation coefficient of 0.973, suggesting a strong positive linear fit. The spectrophotometer was calibrated to measure an absorbance of 0 μM for a solution of iron(II) chloride with no salicylic acid present. The line of best fit must pass through the origin because the absorbance is directly proportional to the concentration (Tables 1 and 2; Figures 2, 3,4).

Table 1: Absorbance data was recorded to construct the calibration curve for aspirin solutions.

Calibration curve	
Concentration of salicylic acid ($mol\ dm^{-3}$)	Absorbance at 530 nm
9.27×10^{-4}	1.135
6.95×10^{-4}	0.802
4.63×10^{-4}	0.436
2.32×10^{-4}	0.080
0.00	0.000

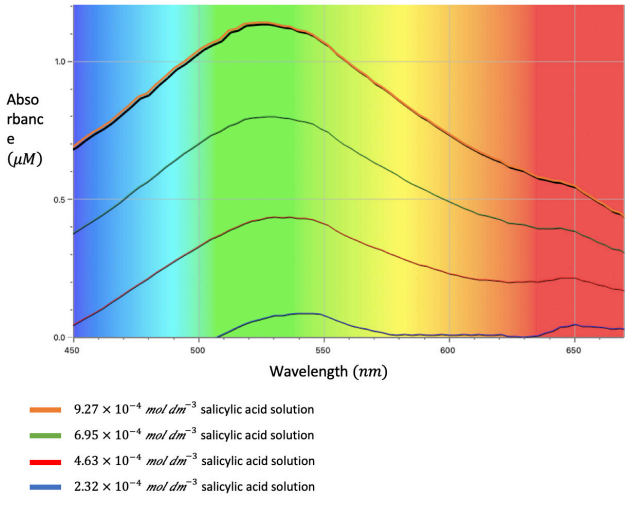

Figure 3: UV–Vis spectra were recorded to construct the calibration curve for salicylic acid solutions.

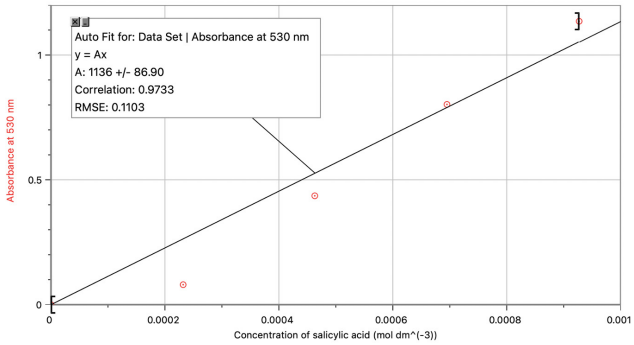

Figure 4: Calibration curve plotting the average absorbance of three runs with respect to the concentration of salicylic acid.

Table 2: Spectrophotometric data for the samples of synthetic aspirin.

Spectrophotometric data						
No.	Temperature/ ℃ ± 0.5 (replicate number)	Mass of crude aspirin produced/g ± 0.001	Average mass of crude aspirin produced (excluding anomalies)/g	Absorbance	Average absorbance (excluding anomalies)	Anomaly (any data point ±10% of the mean)
1	50 (1)	2.464	2.449	0.3895	0.3894	
2	50 (2)	2.438		0.3953		
3	50 (3)	2.445		0.3833		
4	60 (1)	1.739	2.473	0.3466	0.3126	✓
5	60 (2)	2.480		0.3120		
6	60 (3)	2.466		0.3132		
7	70 (1)	2.492	2.481	0.2349	0.2330	
8	70 (2)	2.471		0.2317		
9	70 (3)	2.385		0.2751		✓
10	80 (1)	2.487	2.505	0.1583	0.1594	
11	80 (2)	2.524		0.1607		
12	80 (3)	2.503		0.1592		

Table 2 lists the spectrophotometric data obtained for all of the samples of synthetic aspirin. Table 3 lists the corresponding TLC data. Table 4 provides the calculated yields and purities of the aspirin samples synthesized in this study.

Table 3: TLC data for the products of aspirin syntheses performed at various temperatures.

TLC data						
No.	Temperature/ ℃ ± 0.5	Distance moved (cm) ±0.2				
		Spot A	Spot B	Solvent front	Aspirin	Pure salicylic acid
1	50 (3)	14.8	14.3	17.3	14.8	14.3
2	60 (3)	14.8	14.3	17.3	14.8	14.3
3	70 (3)	14.8	14.3	17.3	14.8	14.3
4	80 (3)	14.7	14.2	17.2	14.7	14.3

Table 4: Procedures used to calculate the yields and purities of the synthetic aspirin samples.

Calculating the yield and purity of synthetic aspirin	
Step	Explanation and example
1	The concentration was calculated by dividing the absorbance of the sample by the gradient of the calibration curve, which was equal to 1140 (Appendix II). Therefore, the concentration of salicylic acid in the solution was: $\frac{absorbance}{1140} = concentration$ Example (50 °C): $\frac{0.389}{1140} = 3.43 \times 10^{-4}\ mol\ dm^{-3}$
2	The solution contained 0.200 g of the lab-synthesized aspirin dissolved in 175 cm^3 of solvent. Using the concentration of salicylic acid, determine the number of moles present in the initial 0.200 g sample, as follows: $\left(\frac{concentration}{1000} \times 100\right) \div 20 \times 250 = moles\ (salicylic\ acid\ in\ 0.2\ g\ sample)$ Example (50 °C): $\left(\frac{3.43 \times 10^{-4}}{1000} \times 100\right) \div 20.0 \times 250 = 4.29 \times 10^{-4}\ mol$
3	To obtain the total number of moles of salicylic acid in the total sample, divide the number of moles of salicylic acid by 0.2 and multiply by the total mass of the sample: $\frac{moles}{0.2} \times total\ mass\ of\ aspirin = total\ moles\ of\ salicylic\ acid\ in\ the\ sample$ Example (50 °C): $\frac{4.29 \times 10^{-4}}{0.200} \times 2.45 = 5.25 \times 10^{-3}\ mol$
4	To calculate the mass of salicylic acid, multiply the number of moles of salicylic acid in the sample by the relative molecular mass (138.122 $g\ mol^{-1}$) (Gruyter, 2017) $total\ moles\ of\ salicylic\ acid \times 138.122 = mass\ of\ salicylic\ acid$ Example (50 °C): $5.25 \times 10^{-3} \times 138 = 7.25 \times 10^{-1}\ g$
5	To get the mass of aspirin, subtract the mass of salicylic acid from the total mass: $Total\ mass - mass\ of\ salicylic\ acid = mass\ of\ aspirin$ Example (50 °C): $2.45 - 7.25 \times 10^{-1} = 1.73\ g$
6	To calculate the percentage purity, divide the mass of aspirin by the total mass and multiply the number by 100. $\frac{mass\ of\ aspirin}{total\ mass} \times 100 = percent\ purity$ Example (50 °C): $\frac{1.73}{2.45} \times 100 = 70.4\%$
7	To calculate the number of moles of aspirin produced, divide the mass by its relative molecular mass (180.157 $g\ mol^{-1}$) (Chemistry LibreTexts, 2019): $\frac{mass\ of\ aspirin}{180.157} = moles\ of\ aspirin\ synthesised$ Example (50 °C): $\frac{1.72}{180} = 9.56 \times 10^{-3}\ mol$
8	In the balanced equation for the reaction, the coefficients for aspirin and salicylic acid are equal; thus, the theoretical yield of aspirin is equal to the initial number of moles of salicylic acid used (limiting agent). Therefore, calculate how may moles there are in 2.000 g of salicylic acid: $moles = \frac{mass}{Mr} = \frac{2.00}{138} = 1.45 \times 10^{-2}\ mol$
9	The percentage yield is calculated by dividing the actual number of moles of aspirin obtained by the theoretical yield, and multiplying by 100: $\frac{actual}{1.45 \times 10^{-2}} \times 100 = percentage\ yeild$ Example (50 °C): $\frac{9.57 \times 10^{-3}}{1.45 \times 10^{-2}} \times 100 = 66.1\%$

Table 5: Purities and yields of aspirin samples synthesized at various temperatures.

Processed data				
Temperature /°C	50.0	60.0	70.0	80.0
Percentage purity /%	70.4	76.2	82.3	87.9
Percentage yield /%	66.1	72.2	78.3	84.4

Discussion

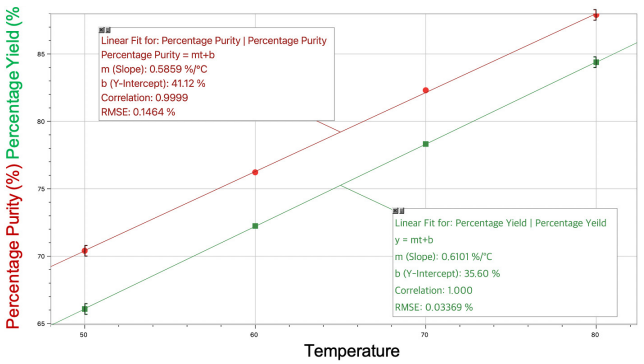

Figure 5: Percentage purity and yield of the aspirin produced, plotted with respect to the reaction temperature.

Figure 5 reveals that the temperature of the reaction mixture had a strong, positive, and linear correlation with respect to both purity and yield. The yield and purity of the aspirin depended on the rate of the reaction. The three factors affecting the rate of reaction in this exploration were the temperature, the concentration of the reactants, and the concentration of the catalyst. To understand these processed data, it was necessary to examine the roles of all three factors.

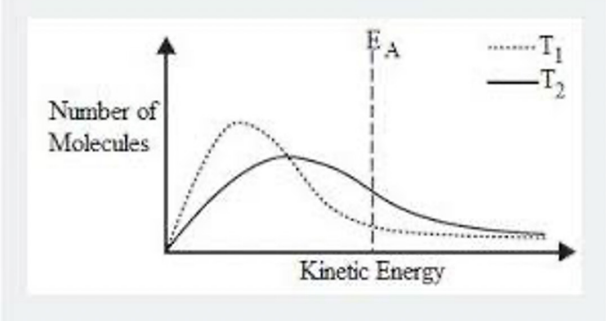

Figure 6: Maxwell–Boltzmann curve (temperature).[8]

The relationship between the temperature and both the yield and purity can be explained by considering the Maxwell–Boltzmann curve and collision theory, as displayed in Figure 6. The two curves represent the distributions of the speeds of molecules in a sample at two different temperatures, T_1 and T_2, where E_A signifies the activation energy (the minimum energy required to have successful collisions). The curve T_2 has a greater number of molecules with sufficient energy to undergo successful collisions per unit time, as indicated by the larger area under the curve. In other words, reactants in a solution of higher temperature will undergo collisions at a greater frequency.

By considering the enthalpies of formation, we can determine whether a reaction is endothermic or exothermic.[9]

DOI: 10.36838/v5i1.5

Table 6: Enthalpies of formation for the components of the reaction used to prepare aspirin.

Enthalpies of formation	
Chemical	Enthalpy of formation (kJ mol^{-1})
Salicylic acid (Verkade, 1932)	−585.3
Aspirin (Kirklin, 2000)	−758.2
Acetic anhydride (Guthrie, 1974)	−625.0
Water (Chase, 1998)	−285.8
Acetic acid (Lebedeva, 1964)	−484.5

Using the values above, the reaction enthalpies for *reaction* 1 and *reaction* 2 are -32.4 kJ mol^{-1} and 25.8 kJ mol^{-1}. *Reaction 1* is exothermic, and the forward reaction of reaction 2 is endothermic. *Reaction 1* is exothermic; therefore, more energy is released in the form of heat as *Reaction 1* continues. This release will heat the mixture to a greater degree. The forward reaction for the equilibrium reaction is endothermic. Using Le Chatelier's principle, an increase in temperature should shift the equilibrium in *Reaction 2* to the right, producing more aspirin.[10,11]

As *Reaction 1* occurs, the concentrations of acetic anhydride and salicylic acid decrease, while the concentration of acetic acid increases. Upon increasing the concentration of the reactant acetic anhydride, in the equilibrium reaction, the rate of the forward reaction would increase because of the frequency of collisions. Because the amount of product from the equilibrium reaction (water) was extremely low (in addition to using 95% phosphoric acid as the catalyst), the backward reaction was extremely slow.

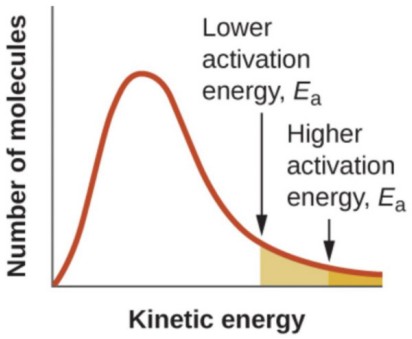

Figure 7: Maxwell–Boltzmann curve (catalyst).

Catalysis is the final factor to consider as affecting the reaction rate. Both reactions were catalyzed by H^+ ions. Because H^+ ions take part in the rate-determining step, the reaction was on the first order with respect to the acid catalyst.[12] Therefore, as more acetic anhydride was consumed to produce acetic acid and aspirin, the rates of both reactions increased because the concentration of H^+ ions had increased. A catalyst allows a reaction to follow an alternative pathway with a lower activation energy, as shown in Figure 7. Therefore, a greater number of successful collisions would occur because more particles would have energy greater than the new, lower activation energy. As a result, considering all of these concepts, increasing the temperature would cause the reaction to reach closer to completion with less salicylic acid left unreacted, leading to a higher percentage yield and purity, respectively.

Limitations:

When using the water bath to control the temperature of the reaction, the temperature might not have remained constant throughout the whole 20 min of the experiment. Minor fluctuations in temperature might have been a source of error. The aspirin samples could not be left out for long periods of time because they would hydrolyze naturally in response to moisture in the air. Similarly, the acetic acid could react with moisture in the air, potentially making it less pure as the study progressed.

Because of time constraints, only three replicates were performed. A greater number of replicates would have increased the reliability of the data produced. Furthermore, acetic anhydride is very reactive, and its concentration might have decreased during this study due to contact with moisture in the air. When drying the aspirin samples, a Büchner filter was used instead of an oven because the heat would have increased the rate of hydrolysis. Nevertheless, because of Singapore's hot and humid climate, some of the aspirin would have been hydrolyzed in the Büchner filter, leading to some systematic errors.

TLC helped increase the reliability of the data and the method of calculating the yield and purity because it revealed that there were no UV-active impurities present, other than salicylic acid, in the aspirin samples. Nevertheless, it is possible that some UV-inactive impurities were present, but they were not fluorescent under short-wavelength UV light and, therefore, were not detectable.

Extension:

Heterogeneous solid acid catalysts can be sustainable alternatives to liquid acid catalysts in industrial processes. Solid catalysts are easier to remove, resulting in less wasted resources. Nevertheless, diffusion is limited for a liquid solvent reaction when a porous acid solvent is used. Additional studies could be performed using solid acid catalysts to determine whether more efficient catalysts might be available for the acetylation of salicylic acid.

■ Conclusion

A higher temperature resulted in aspirin being obtained in greater yield and purity. A linear relationship existed between both the yield and purity of the aspirin synthesized when varying the reaction temperature between 50 °C and 80 °C.

■ Acknowledgments

Dhiman Roy was the sole conductor of this experiment, and also performed the literature search. He is grateful for the feedback his chemistry teachers, Mr. MacFarlane and Dr. Olson, gave.

■ References

1. Montinari, M. R.; Minelli, S.; De Caterina, R. The First 3500 years of Aspirin History from Its Roots: A Concise Summary. *Vascular Pharmacology* **2019**, 113, 1–8. https://doi.org/10.1016/j.vph.2018.10.008.
2. Barry, E.; Borer, L. L. Experiments with Aspirin. *J. Chem. Educ.* **2000**, 77 (3), 354. https://doi.org/10.1021/ed077p354.
3. Fersht, A. R.; Kirby, A. J. Hydrolysis of Aspirin. Intramolecular General Base Catalysis of Ester Hydrolysis. *J. Am. Chem. Soc.* **1967**, 89 (19), 4857.
4. Arecchi, A.; Messadi, T.; Koshel, R. J. Transmittance, Reflectance, and Absorptance. *Field Guide to Illumination* **2007**, FG11. https://doi.org/10.1117/3.764682.p27.
5. Beer Lambert Law | Transmittance & Absorbance | Edinburgh Instruments https://www.edinst.com/blog/the-beer-lambert-law/
6. Experiment_613_Spectrophotometric Determination of Aspirin_1_2_2 https://chem.libretexts.org/Courses/Los_Medanos_

College/Chemistry_6_and_Chemistry_7_Combined_Laboratory_Manual/Experiment_613_Spectrophotometric_Determination_of_Aspirin_1_2_2 (accessed 2022 -04 -10).
7. Lewis, D.; Osborne, C. Aspirin: A Curriculum Resource for Post-16 Chemistry Courses; Education Division, Royal Society of Chemistry: London, 2003.
8. Chemistry: For use with the IB diploma programme. Higher level / Lanna Derry [and six others]. - Trove https://trove.nla.gov.au/work/26569525/version/211022211 (accessed 2021 -03 -23).
9. Ruscic, B.; Pinzon, R. E.; Morton, M. L.; von Laszevski, G.; Bittner, S. J.; Nijsure, S. G.; Amin, K. A.; Minkoff, M.; Wagner, A. F. Intoduction to Active Thermochemical Tables: Several "key" enthalpies of formation revisited. *J. Phys. Chem. A* **2004**, 108 (45), 9979
10. 11.2: Le Chatelier's Principle https://chem.libretexts.org/Bookshelves/General_Chemistry/Book%3A_Chem1_ (Lower)/11%3A_Chemical_Equilibrium/11.02%3A_Le_Chatelier's_Principle (accessed 2022 -04 -09).
11. 6.1.6: The Collision Theory https://chem.libretexts.org/Bookshelves/Physical_and_Theoretical_Chemistry_Textbook_Maps/Supplemental_Modules_(Physical_and_Theoretical_Chemistry)/Kinetics/06%3A_Modeling_Reaction_Kinetics/6.01%3A_Collision_Theory/6.1.06%3A_The_Collision_Theory (accessed 2022 -04-9).
12. Olmsted, J. A. Synthesis of Aspirin: A General Chemistry Experiment. *J. Chem. Educ.* **1998**, 75 (10), 1261. https://doi.org/10.1021/ed075p1261.

Author

Dhiman Roy has just completed his International Baccalaureate from Saint Joseph's Institution International, Singapore. He has a passion for chemistry and environmental issues.

DOI: 10.36838/v5i1.5

IJHSR
ijhighschoolresearch.org
RESEARCH ARTICLE

An Examination of Habitability in Exoplanet Systems

Divya Kumari

Hillsborough High School, 466 Raider Boulevard, Hillsborough, NJ, 08844, USA; divya.k2517@gmail.com

ABSTRACT: By reviewing what is known and describing future research directions, this paper explores the qualities that make a planet habitable and the environment it may create. We consider two planetary systems — TRAPPIST-1 and Kepler-62 — and develop a metric to rank the likelihood of habitability on their respective planets. Our guideline for habitability includes the capability of sustaining liquid water, reasonable environmental conditions, and the presence of molecules known to sustain life. Previous research has determined specific values and rankings within each system for planet density, obliquity, effective temperature (T_{eff}) of the planet, equilibrium temperature (T_{eq}) of the planet, and semimajor axes (among others) that increase the likelihood of habitability. After compiling these system properties from the literature, we rank the planets in each system based on their expected probability of habitability. The two systems are compared to demonstrate how different environments might affect habitability. The rankings, system comparisons, and other information lead us to conclude that Kepler-62 f and TRAPPIST-1 e are likely the most habitable planet in each system. We compare these planets to each other and individually to Earth. We conclude by placing these findings into the broader context of exoplanet discovery and discussing future constraints on planetary habitability.

KEYWORDS: Physics and Astronomy, Astronomy, Planetary Systems, Exoplanets, Habitability, Kepler-62, TRAPPIST-1.

Introduction

Currently, there are over 5,000 known exoplanets, and more continue to be discovered.[1] In a grander sense, little is known about them; however, this does not mean the absence of information entirely. While we cannot physically go to these planets, we can collect critical data through various methods and compile them to form conclusions about individual systems and/or planets. These planets can be broadly categorized as falling into one of four categories: high-mass gas giants, sub-Neptunes, super-Earths, and terrestrial planets.[2] They are all located in a relatively small region of the Milky Way that surrounds Earth.[1] Being hundreds or thousands of light years away, there are two main ways of finding exoplanets: transit and radial velocity.[3] The transit method uses the light a planet blocks as it goes in front of its star to detect an exoplanet. The radial velocity method observes a slight change in the color of a star when it wobbles slightly due to an exoplanet hinting toward an orbiting planet. Collectively, the transit and radial velocity methods (along with other complementary measurements) are used to deduce the key properties of planetary systems.

This paper explores how various properties of a planet and its system come together to produce a unique environment. Through the data available, we study individual parameters and their implications for habitability, focusing on one parameter at a time for simplicity before considering each planet's properties as a whole. Our primary comparison point is the Earth, the only planet on which life has been confirmed to date. In other words, we use the life we know of as a baseline to identify the possibility of life elsewhere.

Habitability is not clearly defined by one decisive set of qualities, as we base it solely on life as we know it on Earth and do not know of the other forms in which it might manifest. This paper considers a planet most likely to be habitable if it has a solid surface, is capable of hosting liquid water, has no sign of abnormal climate conditions, and has a protective atmosphere.[3] Evidence related to these requirements can be collected through measurements of a variety of qualities such as planet density, semimajor axis, formation history, obliquity, etc., that have a cumulative impact on the planet. We acknowledge that some shortcomings are inherent to this definition of habitability, discussed later in this work, along with possible pathways to more robustly evaluate our candidates' likelihood of habitability.

This work demonstrates that Kepler-62 f and TRAPPIST-1 e are the most likely habitable planets in their respective systems. We first discuss the reasoning behind choosing the Kepler-62 and TRAPPIST-1 systems to focus on. We then define each of the parameters used to rank the planets. After providing a ranking, we analyze the results and determine each system's most likely habitable planet. Then, we compare (1) the properties of the two systems, (2) the most likely habitable planets to each other, and (3) each potentially habitable planet with Earth.

Lastly, we outline our conclusions' broader implications for habitability and discuss future research.

Materials and Methods

How systems were selected:

As a general guideline, certain qualities were considered when looking for systems to study. We favored systems with at least 4-5 rocky planets, at least 1-2 planets in the habitable zone (area in the system in which liquid water can exist), and relatively well-characterized properties from existing data/research. We differentiate between the optimistic and

DOI: 10.36838/v5i1.6

conservative habitable zone when possible and use these characterizations to aid in considering habitability.[9] Most quantitative data on planet properties were taken from the NASA Exoplanet Archive. We ultimately selected two promising systems, outlined below.

Overview of TRAPPIST-1:

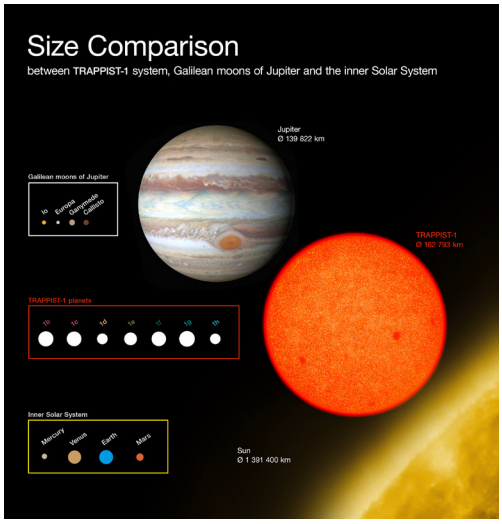

Figure 1: Visualization of the size of TRAPPIST-1's planets and host star alongside our Sun, the inner solar system, Jupiter, and its moons. European Southern Observatory. (2017). Comparison of the sizes of the Trappist-1 planets with Solar System bodies. European Southern Observatory. Retrieved July 1, 2022, from https://www.eso.org/public/images/eso1706d/.

TRAPPIST-1 was selected due to its extensive set of promising terrestrial planets, which have cooler than our Sun, at 0.1192 R⊙ and 2566K.[5] Figure 1 contains a scaled depiction of TRAPPIST-1 and our Sun; evidently, our sun is much larger, and TRAPPIST-1 is more comparable in size to Jupiter. While this difference from the Sun might make TRAPPIST-1 initially seem, unlike the solar system, all seven planets orbit much closer to TRAPPIST-1, at a distance of 0.0619 au at most.[5] This places a total of 2 planets in the optimistic, conservative, and/or tidal habitable zones (TRAPPIST-1 d & e) and another in the optimistic and tidal habitable zones. The system is predicted to be slightly younger (TRAPPIST-1 f).[6] The inner six planets are also believed to be rocky based on planet density.[7] Figure 1 demonstrates that the TRAPPIST-1 planets are all near the size of the planets in our inner solar system. In a more general sense, the system's parameters (other than star size and temperature) are similar to or near Earth's. These include planet density—that is, the system consists of a large number of small, rocky planets— and the expected temperature of the planets. The combination of promising qualities (parameters that are promising for studying habitability) and a system relatively similar to our own solar system distinguished TRAPPIST-1 from other planetary systems. As mentioned before, the TRAPPIST-1 system has extensive research on it in the form of data, analysis, and predictions. As a well-studied system with desired qualities, TRAPPIST-1 was ideal for the ranking and analysis conducted within this paper.

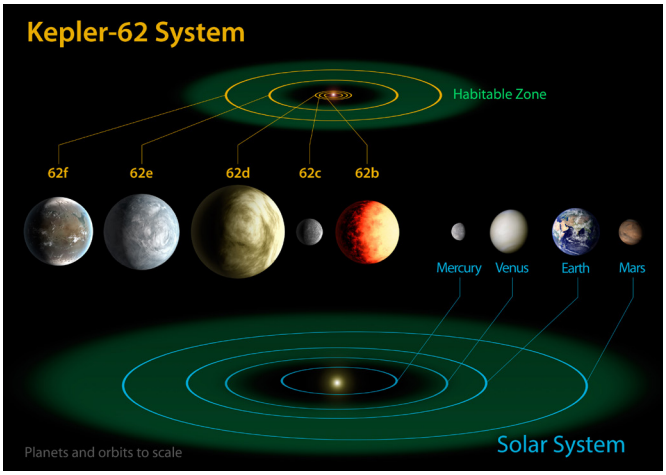

Figure 2: Size comparison of individual Kepler-62 planets to our solar system's planets. NASA Ames/JPL-Caltech. (2013). Kepler-62 and the Solar System. NASA. NASA. Retrieved July 1, 2022, from https://www.nasa.gov/content/kepler-62-and-the-solar-system.

Overview of Kepler-62:

Similarly, Kepler-62 possesses qualities that make it optimal to study for potential habitability. Kepler-62 is smaller and cooler than our sun at 0.73 R⊙ and 4842K.[8] The system has five planets, each orbiting at 0.05-0.718 au.[8] Figure 2 shows a scaled comparison of all five planets to the planets in our own inner solar system. One of the planets is in the optimistic habitable zone (Kepler-62 e), while a second is in the conservative habitable zone (Kepler-62 f).[9] While the other planets within this system have high temperatures, Kepler-62 e & f are more temperate. These two planets provide a chance for more in-depth study and have potential in terms of habitability. Overall, the Kepler-62 system is well-studied, with rare constraints on planetary obliquities and potential atmospheric properties. Overall, the qualities of the Kepler-62 system make it optimal for this paper.

Parameters used in rankings:

It is vital to understand the reason behind each category used to rank and evaluate these planets, along with the impact they can have on habitability. The categories used are equilibrium temperature (T_{eq}) of the planet, orbital semimajor axis (which we use as a proxy for the distance from the host star), planet density, and obliquity. Unless otherwise stated, rankings for each category were made in direct comparison with Earth, and a higher ranking denoted greater similarity with Earth's properties. The motivation behind our inclusion of each of these properties is as follows:

- T_{eq}: As per the definition of habitability used in this paper, T_{eq} is essential to knowing whether liquid water can exist on the planet. If the planet cannot sustain liquid water, it will likely be unable to maintain or create an environment full of life. Water, a versatile and key molecule for different cellular reactions, is needed to enable cell growth and the existence of life on Earth more broadly.
- Semimajor axis: The distance of a planet from its star is directly related to its temperature. Previously determined habitable zones for each system were compared with the semimajor axis of each planet, measured in astronomical units

DOI: 10.36838/v5i1.6

(au; distance from the Sun to the Earth). If a planet was not in the conservative or optimistic habitable zone, it was determined that it could not support liquid water.

- Planet density: Planet density, derived from planetary radius (R_p) and mass (M_p), determines the planet's gravitational pull. A planet's density is directly related to its expected ability to retain an atmosphere, and it is crucial to characterize whether a planet is rocky or gaseous. Because it is assumed that a rocky planet is best for habitability, density and its implications were considered during the analysis, as stated in referenced papers.
- Obliquity: Data on obliquity (degree of tilt to a planet) was used as another way to predict environmental conditions. The obliquity of the Earth is known to partially drive the long-term climate variations of the planet, producing different seasons in the northern and southern hemispheres. An obliquity close to 0° or one that is unusually high can cause adverse wind patterns and highly varying temperatures throughout a planet of interest.

Results and Discussion

The results of our rankings are provided in Table 1 (Kepler-62) and Table 2 (TRAPPIST-1), together with all properties used in this study for reference. Rankings are provided from top to bottom (top: most similar to Earth; bottom: least similar to Earth).

Table 1: Overview of Kepler- 62 properties, in order of most favorable for each parameter. T_{eq} and semimajor axis, planet radius, and mass (radius and mass values were used to calculate planet density) were obtained from https://exoplanetarchive.ipac.caltech.edu/overview/Kepler- 62. Obliquity rankings were obtained from https://doi.org/10.1017/s1743921415007832.

Kepler-62			
T_{eq}(K) [Earth: 255 K]	Semimajor axis Conservative: 0.48-0.85 au Optimistic: 0.36-0.92 au [Habitable zones specific to this system]	Planet density (g/cm^3) [Earth: 5.51 g/cm^3]	Obliquity (°) [Earth: ≈23.4°]
e: 270±15	f: 0.718±0.007	f: 5.5±2.02	f
f: 208±11	e: 0.427±0.004	b: 5.2±3.83	e
d: 510±28	d: 0.120±0.001	e: 6.0±0.78	b, c, & d
c: 578±31	c: 0.09±0.009	d: 4.1±0.60	
b: 750±41	b: 0.05±0.0005	c: unconstrained	

Table 2: Overview of TRAPPIST-1 properties, in order of most favorable for each parameter. We exclude obliquity from our parameter list in this table because this parameter has not been measured for the TRAPPIST-1 planets. T_{eq}, semimajor axis, and planet density were obtained from https://exoplanetarchive.ipac.caltech.edu/overview/TRAPPIST-1. Semimajor axis rankings were decided with predictions made in https://doi·org/10.1093/mnras/stx2980.

TRAPPIST-1		
T_{eq}(K) [Earth: 255 K]	Semimajor axis [Earth: 1.000 au]	Planet density (g/cm^3) [Earth: 5.51 g/cm^3]
e: 251.3±4.9	e: 0.02925±0.00250	c: $5.464^{+0.221}_{-0.237}$
f: 219±4.2	f: 0.03849±0.00033	b: $5.442^{+0.265}_{-0.276}$
d: 288±5.6	d: 0.02227±0.00019	g: $5.06^{+0.14}_{-0.14}$
g: 198.6±3.8	c: 0.01580±0.00013	f: $5.02^{+0.14}_{-0.14}$
h: 173±4	g: 0.04683±0.00040	e: $4.90^{+0.17}_{-0.18}$
c: 341.9±6.6	b: 0.01154±0.00010	d: $4.37^{+0.15}_{-0.17}$
b: 400.1±7.7	h: 0.06189±0.00053	h: $4.16^{+0.33}_{-0.30}$

Discussion of rankings:

Kepler-62:

Rankings listed in Table 1 suggest that Kepler-62 f and Kepler-62 e are most likely habitable since they are the two highest ranked for all individual parameters. In all parameters, Kepler-62 f is ranked above Kepler-62 e, aside from the Teq(K). Kepler-62 f has a Teq of 208 K, which is lower than the 255 K of Earth and 270 K of Kepler-62 e.[8] Kepler-62 e & f are predicted to have less evolving obliquity (degree of tilt) through time relative to the other planets in the Kepler-62 system.[10]

However, Kepler-62 e is predicted to have reached pseudo-synchronization, where the frequency of the planet's spin and orbital velocity at its closest approach ("periastron") are very close or the same.[11] This would mean that the planet only shows one face to its host star for the majority of the time. This would cut off an entire half of the planet from sunlight and create a hostile environment for the side facing away. The side facing the sun would be extremely warm, while the side facing away would be extremely cold.

Kepler-62 e is also predicted to have a slower rotation period in comparison to Kepler-62 f.[12] This may have contributed to an unusual and varying environment across the planet, with no longitudinal circulation. Kepler-62 f has an obliquity close to Earth's, along with a more rapid rotation period (20-40 hours) based on model predictions.[12] This may produce similar wind patterns to those on Earth due to a similar heating pattern for Kepler-62 f. By these criteria, we conclude that Kepler-62 f is the most likely habitable planet in the Kepler-62 system.

TRAPPIST-1:

Rankings for the TRAPPIST system in Table 2 show that TRAPPIST-1 e and TRAPPIST-1 f are the most similar to Earth in terms of T_{eq} and semimajor axis rankings based on model predictions.[13] We also know that the outer planets (beyond TRAPPIST-1 d) have lower ion escape rates ($<10^{27}s^{-1}$) that would have helped them to retain their atmospheres if the planets formed further out and migrated closer to the TRAPPIST-1 star as the system evolved.[14] So, TRAPPIST-1 e, f, g, & h are most likely to have retained their atmospheres. TRAPPIST-1 b and c are likely completely dry due to X-ray and UV irradiation. At the same time, TRAPPIST-1 d is predicted to be hot and dry, with minimal water in limited regions.[15] On the other end of the scale, TRAPPIST-1 g and h are too cold (T_{eq} is too low) to be likely habitable. The estimated masses of the planets indicate that the six inner planets are probably rocky.[7]

Furthermore, we use tidal parameters to examine a planet's properties further. The tidal parameter describes how resilient a planet is to distortion by tidal interactions. For instance, the Earth experiences a change in rotation rate due to our moon's tidal tug.[13] Any gravitational force exerted on a planet often plays some role in determining its climate and rotation, an effect that the tidal parameter measures. Simulations show that when Q', the tidal parameter, is equal to 100, TRAPPIST-1 e & f are in the conservative habitable zone. However, when Q'=103, TRAPPIST-1 e was the only planet in the conservative habitable zone.[13]

Considering the tidal parameter, T_{eq}, predicted atmospheres, and likely formation history, we determine that TRAPPIST-1 e is the most likely habitable planet in the system.

Comparison between systems:

To further examine the most likely habitable planets from each system, we will compare the systems as a whole and their host stars. The findings from these comparisons will be considered when comparing the most likely habitable planets themselves. This comparison broadens our understanding of each system and, most likely habitable planet.

Host star comparison:

The two host stars must also be compared to understand their influence on their companion planets. TRAPPIST-1 has an effective temperature of 2566 K, a stellar mass of 0.0898 $M_\odot$, and a stellar radius of 0.1192 $R_\odot$.[5] Kepler-62, at 4842 K, has a stellar mass of 0.79 $M_\odot$, and a stellar radius of 0.73 $R_\odot$.[8] For reference, our sun has an effective temperature of 5778 K. These parameters classify Kepler-62 as a K-type main sequence star and TRAPPIST-1 as an M-type main sequence star. While the two host stars and our sun are different, both of their most likely habitable planets lie within their respective liquid-water habitable zones. Furthermore, our analysis focuses on the incident thermal radiation that reaches the planet rather than just the planet's distance from the host star. Therefore, the size and temperature differences in host stars do not strongly affect our analysis beyond what has already been included in this study.

Non-thermal radiation from the host star:

The TRAPPIST-1 planets do, however, receive intense X-ray and extreme ultraviolet (EUV) radiation from the star. An analysis of this radiation demonstrates that the inner three planets would receive tens to thousands of times more radiation than present-day Earth.[15] As a result, TRAPPIST-1 b and c are predicted to be completely dry from radiation, while TRAPPIST-1 d, e, and f each have a chance of retaining some of their initial water.[15] Kepler-62 does not emit analogous high-energy radiation in problematic amounts.

Atmospheric properties:

TRAPPIST-1 has an age of ~3-8 Gyr, while Kepler-62 has an age of 7 Gyr.[7,9] This has implications for each system's formation history and atmosphere (discussed in the next section). The Kepler-62 planets are expected to have varying obliquities, yet none are considerably higher than Earth's. This allows us to predict that the planet's wind patterns and temperatures are not extreme. The obliquities of the TRAPPIST-1 planets are not yet well-constrained. TRAPPIST-1 b and c have been observed to have clouds and/or hazes; however, it is unknown what they are composed of.[16]

Expected formation mechanism:

The formation history of TRAPPIST-1 has been particularly well-studied. The TRAPPIST-1 planets likely formed further from the star, then migrated inwards to their current orbits.[13] More specifically, simulations revealed that the inner two planets must have migrated separately from the others to allow the present-day system to exist.[13] The formation history of Kepler-62 has not yet been well-constrained.

Comparison of the most likely habitable planet from each system:

We concluded from the data we have that the planets predicted to be most similar to Earth in each system are Kepler-62 f and TRAPPIST-1 e.

Similarities between planets:

Kepler-62 f and TRAPPIST-1 e have some similarities, despite being from different solar systems. Both are in their systems' conservative habitable zones and are the only planets in their respective systems within this zone. They are predicted to most likely have atmospheres capable of maintaining agreeable temperatures and weather. Lastly, the planets have similar eccentricities. Kepler-62 f is consistent with an e=0, circular orbit for 267 days.[17] TRAPPIST-1 e has an eccentricity of <0.085.[7] Since these eccentricities are close to zero and close to each other, both planets likely experience minimal net heating variations over their orbits.

Differences between planets:

Kepler-62 f and TRAPPIST-1 e do, however, differ in their temperatures and sizes. Kepler-62 f is 208 K, while TRAPPIST-1 e is 251.3 K. TRAPPIST-1 e is also slightly smaller than Kepler-62 f at 0.92 $R_\oplus$, while Kepler-62 f is 1.41 $R_\oplus$.[17]

Kepler-62 f comparison with earth:

In comparison with Earth, Kepler-62 f has a cooler temperature at 208 K, while Earth has an equilibrium temperature of 255 K. The planet also has an obliquity close to Earth's, meaning it will experience seasonal effects.[12] Its predicted rapid rotation period (20-40 hrs.) means stronger wind patterns.[12] This is a positive sign for its habitability, confirming that the planet may have Earth-like weather.

TRAPPIST-1 e comparison with earth:

TRAPPIST-1 e is very close to Earth in temperature, at 251K compared to Earth's 255K. It has a planet density of 0.80±0.76 ρ_{Earth}[7]. While not an exact match, these parameters are all similar to Earth's. Models predict that TRAPPIST-1 e has been able to retain an atmosphere throughout time.[14] This is due to the low ion escape rate that prevents a loss of atmosphere. While TRAPPIST-1 e and Earth are similar in that they have atmospheres, the details of TRAPPIST-1 e's atmosphere are unknown and may not be comparable to Earth's.

Conclusions

Broader implications for habitability:

The Kepler-62 and TRAPPIST-1 planets are among the most promising for habitability compared to the 5,000+ confirmed exoplanets discovered. However, the scope is much larger than this. These confirmed exoplanets are relatively close to Earth and large enough to be detected by our technology. Even with various methods being used to find exoplanets, some limitations render us incapable of finding smaller, more distant planets. To summarize, the planets studied in this paper are the ones that are the most realistic ones known today to do further study on and are most likely habitable in comparison to other exoplanets that have been found.

DOI: 10.36838/v5i1.6

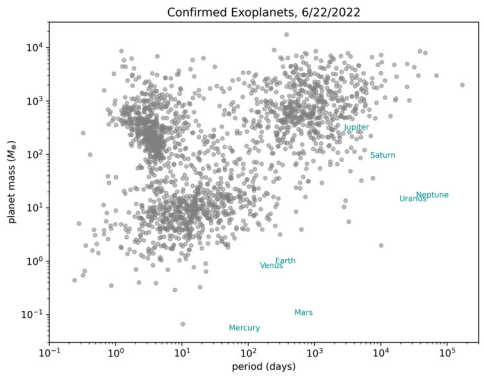

Figure 3: Distribution of all confirmed exoplanets and planets in our solar system, plotted with an x-axis of the period (days) and a y-axis of planet mass ($M_\oplus$). Rice, M. (2022, June 22). Confirmed Exoplanets, Retrieved June 22, 2022, from https://exoplanetarchive.ipac.caltech.edu/docs/acknowledge.html.

It is essential to keep in mind that, thus far, very few exoplanets have resembled any of the planets in our solar system, as Figure 3 displays. Figure 3 shows that the currently confirmed exoplanets are not similar to the inner solar system in terms of orbital period and planet mass. In fact, Figure 3 shows that not one exoplanet is plotted near Mercury, Venus, Earth, Mars, Uranus, or Neptune, and very few are plotted near Saturn and Jupiter. Despite having discovered more than 5,000 exoplanets, we can infer that we are not yet capable of discovering planets precisely like our inner solar system's and that there is more work to do in the field of exoplanet discovery.[1] It is essential to keep this in mind as a disclaimer when considering the findings and conclusions discussed in this paper.

Moreover, it is not feasible to consider a direct mission to any of these planets, as they are all light-years away. The TRAPPIST-1 system, which is about 40 light years from Earth[18], can be characterized in much greater detail with JWST and other upcoming space missions. However, the Kepler-62 system is relatively dim and is located about 1,200 light-years from Earth, making it substantially more challenging to characterize in comparison with the TRAPPIST-1 system.[19]

Specific molecules and biosignatures would help in verifying the habitability of a planet.

PH3, or phosphine, is produced only by anaerobic organisms on Earth (ex., bacteria, and microbes) and is thought to be difficult to form in the absence of life.[20] CH4, or methane, is produced by anaerobic organisms as a waste product.[20] CH3Cl, or methyl chloride, is a gas whose primary sources are oceanic algae, tropical/subtropical plants, certain aquatic and terrestrial planets, and the decay of organic matter.[20] The presence of these biosignatures, along with others, would provide convincing evidence pointing to some form of life or organism living on the planet. On the other hand, properties (beyond those mentioned in this paper) that make a planet highly inhabitable would also be useful to rule out the potential for habitability.

Final Takeaways:

This paper analyzes the available data to conclude that TRAPPIST-1 e and Kepler-62 f are the most likely habitable planets within their respective systems. Our findings are reached through an individual study of the planets of each system, comparisons with Earth, and an analysis of the environment within which each planet resides. We discuss how our findings fit into the demographics of exoplanets found thus far; the limitations of currently confirmed exoplanets; plans of characterization and observation for the TRAPPIST-1 system; and possible biosignatures that would be of use in future research.

Acknowledgments

I would like to thank Dr. Malena Rice for her guidance and assistance throughout the analysis and writing of this paper. This research has used the NASA Exoplanet Archive, operated by the California Institute of Technology, under contract with the National Aeronautics and Space Administration under the Exoplanet Exploration Program.

References

1. NASA. (2015, December 17). Exoplanet exploration: Planets beyond our solar system. NASA. Retrieved June 19, 2022, from https://exoplanets.nasa.gov/
2. NASA. (2022, April 13). Overview. NASA. Retrieved June 19, 2022 , from https://exoplanets.nasa.gov/what-is-an-exoplanet/planet-types/overview/
3. NASA. (2019, June 20). *5 ways to find a planet*. NASA. Retrieved June 19, 2022, from https://exoplanets.nasa.gov/alien-worlds/ways-to-find-a-planet/
4. NASA. (2022, April 13). *The big questions*. NASA. Retrieved June 19, 2022, from https://exoplanets.nasa.gov/search-for-life/big-questions/
5. California Institute of Technology. (n.d.). *TRAPPIST-1 Overview - California Institute of Technology*. NASA Exoplanet Archive. Retrieved June 18, 2022, from https://exoplanetarchive.ipac. caltech.edu/overview/TRAPPIST-1
6. Papaloizou, J. C., Szuszkiewicz, E., & Terquem, C. (2017). The TRAPPIST-1 system: Orbital Evolution, tidal dissipation, formation and habitability. *Monthly Notices of the Royal Astronomical Society*, 476(4), 5032–5056. https://doi.org/10.1093/mnras/stx2980
7. Gillon, M., Triaud, A. H., Demory, B.-O., Jehin, E., Agol, E., Deck, K. M., Lederer, S. M., de Wit, J., Burdanov, A., Ingalls, J. G., Bolmont, E., Leconte, J., Raymond, S. N., Selsis, F., Turbet, M., Barkaoui, K., Burgasser, A., Burleigh, M. R., Carey, S. J., … Queloz, D. (2017). Seven temperate terrestrial planets around the nearby ultracool dwarf star TRAPPIST-1. Nature, 542(7642), 456–460 https://doi.org/10.1038/nature21460
8. California Institute of Technology. (n.d.). *Kepler-62 Overview - Nasa Exoplanet Archive*. NASA Exoplanet Archive. Retrieved June 18, 2022, from https://exoplanetarchive.ipac.caltech.edu/overview/Kepler-62
9. Kane, S. R., Hill, M. L., Kasting, J. F., Kopparapu, R. K., Quintana, E. V., Barclay, T., Batalha, N. M., Borucki, W. J., Ciardi, D. R., Haghighipour, N., Hinkel, N. R., Kaltenegger, L., Selsis, F., &Torres, G. (2016). A catalog of Kepler habitable zone exoplanet candidates. *The Astrophysical Journal*, 830(1), 1. https://doi.org/10.3847/0004-637x/830/1/1
10. Deitrick, R., Barnes, R., Quinn, T. R., Armstrong, J., Charnay, B., & Wilhelm, C. (2018). Exo-Milankovitch cycles. I. Orbits and rotation states. *The Astronomical Journal*, 155(2), 60. https://doi.org/10.3847/1538-3881/aaa301
11. Bolmont, E., Raymond, S. N., Leconte, J., Correia, A., & Quintana, E. (2015). Tidal evolution in multiple planet systems: Application to kepler-62 and kepler-186. *Proceedings of the International Astronomical Union*, 9(S310), 58–61. https://doi.org/10.1017/s17439

21415007832
12. Bolmont, E., Raymond, S. N., Leconte, J., Hersant, F., & Correia, A. C. (2015). mercury-t: A new code to study tidally evolving multi-planet systems. applications to kepler-62. *Astronomy & Astrophysics*, 583. https://doi.org/10.1051/0004-6361/201525909
13. Papaloizou, J. C., Szuszkiewicz, E., & Terquem, C. (2017). The TRAPPIST-1 system: Orbital Evolution, tidal dissipation, formation and habitability. *Monthly Notices of the Royal Astronomical Society*, 476(4), 5032–5056. https://doi.org/10.1093/mnras/stx2980
14. Dong, C., Jin, M., Lingam, M., Airapetian, V. S., Ma, Y., & van der Holst, B. (2017). Atmospheric escape from the TRAPPIST-1 planets and implications for habitability. *Proceedings of the National Academy of Sciences*, 115(2), 260–265. https://doi.org/10.1073/pnas.1708010115
15. Wheatley, P. J., Louden, T., Bourrier, V., Ehrenreich, D., & Gillon, M. (2016). Strong XUV irradiation of the Earth-sized exoplanets orbiting the ultracool dwarf TRAPPIST-1. *Monthly Notices of the Royal Astronomical Society: Letters*, 465(1). https://doi.org/10.1093/mnrasl/slw192
16. de Wit, J., Wakeford, H. R., Gillon, M., Lewis, N. K., Valenti, J. A., Demory, B.-O., Burgasser, A. J., Burdanov, A., Delrez, L., Jehin, E., Lederer, S. M., Queloz, D., Triaud, A. H., & Van Grootel, V. (2016). A combined transmission spectrum of the Earth-sized exoplanets TRAPPIST-1 b and C. *Nature*, 537(7618), 69–72. https://doi.org/10.1038/nature18641
17. Borucki, W. J., Agol, E., Fressin, F., Kaltenegger, L., Rowe, J., Isaacson, H., Fischer, D., Batalha, N., Lissauer, J. J., Marcy, G. W., Fabrycky, D., Désert, J.-M., Bryson, S. T., Barclay, T., Bastien, F., Boss, A., Brugamyer, E., Buchhave, L. A., Burke, C., … Winn, J. N. (2014). Kepler-62: A five-planet system with planets of 1.4 and 1.6 earth radii in the habitable zone. Science, 340(6142), 587–590. https://doi.org/10.1126/science.1234702
18. NASA. (2022, February 15). Exoplanet discovery: *Seven Earth-sized planets around a single star.* NASA. Retrieved August 28, 2022, from https://exoplanets.nasa.gov/trappist1/
19. NASA. (2022, February 15). *Kepler-62 and the solar system - exoplanet exploration: Planets beyond our solar system*. NASA. Retrieved August 28, 2022, from https://exoplanets.nasa.gov/resources/124/kepler-62-and-the-solar-system/
20. Schwieterman, E. W., Kiang, N. Y., Parenteau, M. N., Harman, C. E., DasSarma, S., Fisher, T. M., Arney, G. N., Hartnett, H. E., Reinhard, C. T., Olson, S. L., Meadows, V. S., Cockell, C. S., Walker, S. I., Grenfell, J. L., Hegde, S., Rugheimer, S., Hu, R., & Lyons, T. W. (2018). Exoplanet biosignatures: A review of remotely detectable signs of life. *Astrobiology,* 18(6), 663–708. https://doi. org/10.1089/ast.2017.1729

Author

Divya Kumari is currently a junior at Hillsborough High School. She is interested in astronomy, astrophysics, and astrobiology and looks forward to pursuing a future career in the field.

DOI: 10.36838/v5i1.6

IJHSR
ijhighschoolresearch.org
■ RESEARCH ARTICLE

Discovery of Novel Genetic Alteration Using Meta-analysis of Colorectal Cancer

Haryeong Eo

Shanghai American School Puxi, 258 Jinfeng Road, Minhang District, Shanghai, China 201107; hre1308@gmail.com

ABSTRACT: More than 5.25 million people worldwide are diagnosed with colorectal cancer (CRC), representing 10% of the global cancer incidence and 9.4% of all cancer-caused deaths. It is common to find genetic and epigenetic alterations in CRC, which are the driving force of tumorigenesis. Therefore, discovering a novel genetic alteration in colorectal cancer can support early diagnosis and finding novel targets for cancer treatment. However, genetic alterations found in colorectal cancer are not fully elucidated. A meta-analysis of colorectal cancer genomics data sets was performed using 12 different studies provided by cBioPortal to identify the novel genetic alteration in colorectal cancer patients. Through cBioPortal analysis, it was hypothesized that chromosome 17q21 amplification is associated with tumor progression. Patient survival analysis was performed through cBioPortal analysis. Also, nine genes located in 17q21 were further analyzed with GeneMania, a web-based program that predicts the function of gene sets. Using cBioPortal analysis, it was discovered that chromosome 17q21 amplification was enriched in deceased patients. Furthermore, through patient survival analysis, amplification of each of the nine genes located in chromosome 17q21 was significantly associated with decreased patient survival rate. Hence, using GeneMania analysis, it was discovered that the gene network of the nine genes was significantly associated with DNA integrity checkpoint function. Through this study, chromosome 17q21 amplification, which may alter the part of DNA integrity in cancer cells, can be used as a biomarker that predicts poor patient survival.

KEYWORDS: Human genetics; Colorectal cancer; Patient survival rate; Chromosome 17; DNA integrity checkpoint.

■ Introduction

Colorectal cancer (CRC) mostly begins as a polyp, a non-cancerous growth that develops in the colon's inner lining.[1] Polyps are classified as either adenomatous or serrated.[2] Similar to adenomas, serrated polyps, traditional serrated adenomas, and large hyperplastic polyps are associated with an increased risk for CRC.[3] Because sessile serrated polyps (SSPs) are difficult to detect during colonoscopy as they are usually flat, these features make them the precursors for a large proportion of cancers.[4]

Gene mutation found in colorectal cancer affects overall patient survival.[5] For example, approximately half of all colorectal cancers show *TP53*, otherwise known as P53, gene mutations, with higher frequencies observed in the distal colon and rectal tumors.[6] The role of the *TP53* gene is to regulate the cell cycle and apoptosis. Specifically, the P53 protein induces G1 cell-cycle arrest and controls the repairing of the DNA before the cell goes into DNA replication.[7] If the DNA repair is unsuccessful, P53 causes cell death. *TP53* mutation occurs at the time of transition from adenoma to cancer. Several studies attempted to explain the significance of *TP53* mutation in colorectal cancer, with conflicting results. A study concluded that the survival rate for P53 positive patients was far greater than that for P53 negative patients. However, overexpression of P53 in stage three CRC carried a better overall survival in CRC patients.[8]

Gene deletion in colorectal cancer also affects colorectal patients' survival. In chromosome 18, loss of heterozygosity (LOH) in the region of 18q21 is often seen in advanced colorectal cancer. LOH is defined as the loss of one allele at a specific locus.[10] Often, the remaining allele is affected by a deletion mutation or a loss of chromosome from a chromosome pair. Some studies found an inverse relationship between CRC patient survival and 18q LOH. A previous study evaluated the effect of 18q LOH on 532 non-MSI-high, stage I-IV CRC tumors; in patients with non-MSI-high CRC, 18q LOH were not significantly associated with a difference in survival.[11]

The cBio Cancer Genomics Portal (cBioPortal) contains numerous multidimensional cancer genomics data sets.[12] The cBioPortal minimizes the tasks needed to collect data by summarizing complex genomic data from large-scale cancer genomics projects.[13] Through cBioPortal, it is possible to better understand biology and clinical applications.

GeneMania provides hypotheses about gene function by showing a list of genes and categorizing genes based on their functions.[14] After receiving comprehensive gene lists, GeneMania groups the genes based on their function, followed by genomics and proteomics data. GeneMania determines whether the functional genomic dataset follows its predictive value during this process. GeneMania also predicts gene function. Using a single gene, GeneMania searches for several genes with the same function based on its interactions with other genes.[14] Overall, GeneMania allows researchers to analyze genes more efficiently and intuitively.

DOI: 10.36838/v5i1.7

After analyzing colorectal cancer genomics data sets consisting of 12 different studies via cBioPortal, novel genetic alterations were found in colorectal cancer patients. Using the given data, it was hypothesized that 17q21 amplification is highly associated with tumor progression, affecting the patient survival rate. In addition, using GeneMania, nine genes located in 17q21 that play a role in the function of gene sets were further identified.

Methods

Analyzing genomic alteration on colorectal patients' genomic data using cBioPortal:

Through cBioPortal, 4341 colorectal patients (4488 samples) were analyzed to find a novel genetic alteration associated with patients' survival. After the patient samples were divided into two groups: living group (n= 1275) and deceased group (n= 273), amplified genes enriched in the deceased group were found. The gene location, percentage of alteration in each group, log-ratio between living and deceased group, p-value, and q-value was analyzed using cBioPortal. The log-rank statistical test was used to calculate the p-value.

Gene network analysis using the GeneMania program:

Gene network analysis was performed with eleven genes found in the cBioPortal (*GJD3, CCR7, TOP2A, CDC6, IGFBP4, WIPF2, KRT222, SMARCE1, RARA*). GeneMania predicts the function of listed genes and their genetic network, including co-expression, physical interaction, shared domains, and biological pathways. GeneMania analyzes the gene lists and prioritizes the genes for functional assays. It finds functionally similar genes within the genomics and proteomics data that have been previously published. Since hundreds of millions of interactions had been collected by the database from GEO, BioGRID, IRefIndex, and I2D, the interaction databases were used to predict the gene function.

Patient survival analysis using cBioPortal:

cBioPortal for cancer genomics provides visualization analysis of overall patient survival status. The overall survival of patient groups between the gene amplified group (*TOP2A and CDC6*) and the non-amplified group was analyzed. Kaplan-Mier analysis and log-rank test were performed to calculate the p-value. The median survival month in each group was also investigated.

Results and Discussion

Table 1: The amplified genes located on 17q21.2 enriched in the deceased colorectal cancer patient's group.

Gene	Cytoband	LIVING (n = 1275)	DECEASED (n = 273)	Log Ratio	p-Value	q-Value	Enriched in
GJD3	17q21.2	19 (1.49%)	15 (5.49%)	-1.88	2.57E-04	5.97E-03	DECEASED
CCR7	17q21.2	17 (1.33%)	12 (4.82%)	-1.85	1.06E-03	0.0149	DECEASED
TOP2A	17q21.2	19 (1.49%)	13 (4.76%)	-1.68	1.72E-03	0.0209	DECEASED
CDC6	17q21.2	19 (1.49%)	12 (4.82%)	-1.69	2.13E-03	0.0239	DECEASED
IGFBP4	17q21.2	19 (1.49%)	12 (4.82%)	-1.69	2.13E-03	0.0239	DECEASED
WIPF2	17q21.2	19 (1.49%)	12 (4.82%)	-1.69	2.13E-03	0.0239	DECEASED
KRT222	17q21.2	14 (1.10%)	10 (4.02%)	-1.87	2.65E-03	0.0289	DECEASED
SMARCE1	17q21.2	15 (1.18%)	10 (4.02%)	-1.77	3.79E-03	0.0358	DECEASED
RARA	17q21.2	28 (1.27%)	26 (2.73%)	-1.1	3.84E-03	0.0359	DECEASED

Gene amplification is when there is an increase in the copy number of DNA present in a specific region of the chromosome or an increase in the RNA and protein made from that gene. Cancer cells often produce multiple copies of genes, and some of the amplified genes can cause cancer cells to grow faster or become resistant to anticancer drugs. 4341 colorectal patients (4488 samples) were analyzed to find a novel genetic alteration associated with patients' survival through the cBioPortal database. First, the patient samples were divided into two groups: living group (n = 1275) and deceased group (n = 273). It was found that chromosome position 17q21.2 amplification is enriched in the decreased patient group (Table 1). In total, nine amplified genes are located in 17q21.2: *GJD3, CCR7, TOP2A, CDC6, IGFBP4, WIPF2, KRT222, SMARCE1*, and *RARA*. Overall, it was found that the novel amplification of nine genes in colorectal cancer patient samples enriched in decreased patient groups.

Previous studies showed that 17q21 amplification was detected in gastric cancer and breast cancers.[15,16] The comparative analysis of DNA copy number and microarray in gastric cancer shows that the 17q12-q21 region is amplified and many genes in this region are overexpressed. A breast cancer study indicated that HER2/NEU amplification (both positioned on 17q21) is responsible for the development of Trastuzumab, one of the first immunotherapeutic drugs for the successful treatment of breast cancers.[17] In conclusion, the amplification in region 17q21 not only caused colorectal cancer but also gastric cancer and breast cancer. This shows how 17q21 plays a critical role in cancer progression.

Table 2: The result of functional prediction of nine amplified genes with extended genes that are functionally similar using GeneMANIA.

Function	P-value	Coverage
DNA integrity checkpoint	3.33e-1	4/147
Negative regulation of epithelial cell proliferation	3.33e-1	3/54
Hormone receptor binding	3.33e-1	4/148
Mitotic cell cycle checkpoint	3.33e-1	4/136
DNA replication checkpoint	3.68e-1	2/10
Insulin-like growth factor binding	5.30e-1	2/13
Cell cycle checkpoint	5.75e-1	4/201
Regulation of chromosome organization	6.13e-1	4/239
Positive regulation of DNA-templated transcription, initiation	6.13e-1	2/23
DNA recombination	6.13e-1	4/229

GeneMANIA analysis was performed to find a novel function of nine amplified genes on colorectal cancer progression. It was found that DNA integrity checkpoint, negative regulation of epithelial cell proliferation, hormone receptor binding, and mitotic cell cycle checkpoint were determined to be the most significant functions of the nine amplified genes (p-value= 3.33e-1) (Table 2). Since the maintenance of genomic integrity is important in normal cell growth and development, gene alteration on DNA integrity checkpoints is found in many cancer cells. In addition, DNA integrity checkpoints provide cells with time to repair damaged DNA, but cancer-initiating cells have lost DNA repair or cell-cycle checkpoints. In conclusion, four genes among nine amplified genes were significantly associated with the function of the DNA integrity checkpoint meaning alteration in this func-

DOI: 10.36838/v5i1.7

function may be linked to the poor survival rate of colorectal patients.

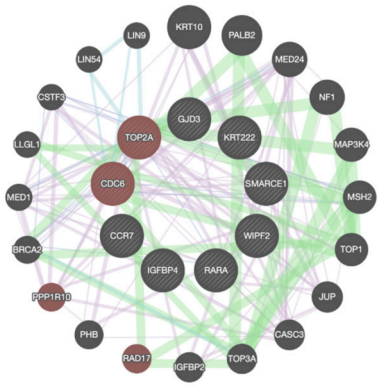

Figure 1: Gene network analysis of ten DEGs, located in the center as slash patterned. The gene sets associated with ten DEGs are located around the ten DEGs. The four red genes are associated with the DNA integrity checkpoint. The green line indicates the physical interaction between the genes. The purple line indicates the co-expressed genes. The blue line indicates the co-localized genes.

Cancer-associated necrosis produces more abnormal DNA fragments than apoptosis in human cells. Therefore, this study focused on the DNA integrity checkpoints because DNA integrity, which relates to the uneven copy number of DNA fragments, is highly related to cancer. According to the model, *TOP2A* and CDC6 are among the nine amplified genes, and *PPP1R10* and *RAD17* are functionally related to the nine amplified genes. In conclusion, amplification of *TOP2A* and *CDC6* and the alteration of relative genes (*PPP1R10* and *RAD17*) may affect DNA integrity checkpoints, which shortens the survival rate of colorectal cancer patients (Figure 1).

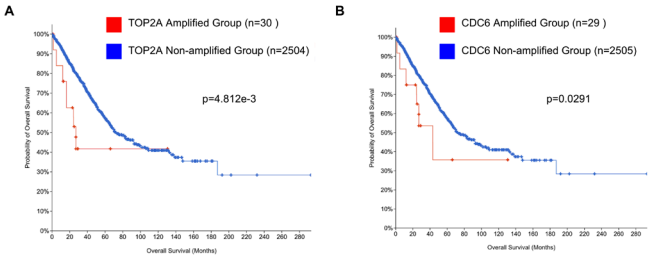

Figure 2: The analysis of overall survival of *TOP2A* and CDC6 amplified patient group compared to *TOP2A* and CDC6 non-amplified patient group. (A) *TOP2A* amplified group (n=30) showed a lower survival rate compared to *TOP2A* non-amplified group (n=2504) (p= 4.812e-3). (B) CDC6 amplified group (n=29) showed lower survival rate compared to CDC6 non-amplified group (n=2505). (p= 0.0291) Log-rank test was used to calculate the p-value.

To validate the effect of *TOP2A* and *CDC6* amplification on colorectal cancer patients' survival, the overall patient survival rate was further analyzed with the cBioPortal database. The patients were divided into two groups: the groups with amplified genes and the groups without amplified genes. A graph in Figure 2 shows the probability of overall survival (Y-axis) and overall survival months (X-axis). It was found that the median survival months of *TOP2A* amplified patients (27 months) was significantly lower than those of *TOP2A* non-amplified patients (71.93 months). Similarly, the median survival months of *CDC6* amplified patients (43.17 months) was significantly lower than the median survival months of *CDC6* non-amplified patients (72.47 months). In conclusion, it was speculated that since *TOP2A* and *CDC6* are associated with the function of DNA integrity checkpoint, the lower survival rate in amplified groups may have abnormal DNA structure with severe DNA damage.

Conclusions

To reiterate the findings shown in Figure 2, two genetic alterations *TOP2* and *CDC6* both significantly decreased the patient survival rate. Using the given information, when analyzing genomics for colorectal cancer patients in the future, it is possible to more accurately diagnose and predict the survival rate of the patients. Furthermore, it was found that 17q21 amplification affected DNA integrity checkpoints the most. With a better understanding of the impact of amplified genes, ways to recover the affected DNA integrity checkpoint can be found, possibly supporting the development of a novel treatment for colorectal cancer. Lastly, a considerably large sample size of 4448 patients was analyzed. Therefore, the results from this study provide a more accurate interpretation of the impact of 17q21 amplification, further reducing the margin of error when treating colorectal patients in general.

However, the study is limited in the methods used, as only data analysis was performed. The media used to perform meta-analysis has the potential for publication bias, skewed data, and difficulties in combining studies that may have differences in population, interventions, etc. Furthermore, the study is limited in scope, as only gene copy alterations, disregarding other genetic alterations, such as mutation and fusion genes, were focused on. Therefore, cancer cell experiments to not only validate the real implications of 17q21 amplification on cancer cell development can be performed but it is also possible to find potential treatments for colorectal cancer. In addition, cBioPortal can be used to further analyze other genetic variations which could have played a significant role in tumor progression.

Acknowledgments

I would like to acknowledge and thank my research mentor Dr. Lee, who provided constructive feedback and support. His guidance helped me overcome some of the difficulties I faced while researching. I would also like to give special thanks to my parents for encouraging me to take this opportunity to research more about cancer. Throughout this project, they warmly listened to every progress I made and asked questions that helped me to make a better research paper.

References

1. Bond, J. H. Colon Polyps and Cancer. Endoscopy 2003, 35 (1), 27–35.
2. Alecu, M.; Simion, L.; Straja, N.; Brătucu, E. Multiple Polyps and Colorectal Cancer. *Chirurgia (Bucur)* **2014**, 109 (3), 342–346.
3. Demetriades, H.; Kanellos, I.; Blouhos, K.; Tsachalis, T.; Vasiliadis, K.; Pramateftakis, M. G.; Betsis, D. Synchronous Polyps in Patients with Colorectal Cancer. *Tech. Coloproctol.* **2004**, 8 Suppl 1, s72-5.
4. Farris, A. B.; Misdraji, J.; Srivastava, A.; Muzikansky, A.; Deshpande, V.; Lauwers, G. Y.; Mino-Kenudson, M. Sessile Serrated Adenoma: Challenging Discrimination from Other Serrated Colonic Polyps. *Am. J. Surg. Pathol.* **2008**, 32 (1), 30–35.
5. Cavagnari, M. A. V.; Silva, T. D.; Pereira, M. A. H.; Sauer, L. J.; Shigueoka, D.; Saad, S. S.; Barão, K.; Ribeiro, C. C. D.; Forones, N.

M. Impact of Genetic Mutations and Nutritional Status on the Survival of Patients with Colorectal Cancer. *BMC Cancer* **2019**, 19 (1), 644.
6. Iacopetta, B. TP53 Mutation in Colorectal Cancer. *Hum. Mutat.* **2003**, 21 (3), 271–276.
7. Guimaraes, D. P.; Hainaut, P. TP53: A Key Gene in Human Cancer. *Biochimie* **2002**, 84 (1), 83–93.
8. Williams, D. S.; Mouradov, D.; Browne, C.; Palmieri, M.; Elliott, M. J.; Nightingale, R.; Fang, C. G.; Li, R.; Mariadason, J. M.; Faragher, I.; et al. Overexpression of TP53 Protein Is Associated with the Lack of Adjuvant Chemotherapy Benefit in Patients with Stage III Colorectal Cancer. *Mod. Pathol.* **2020**, 33 (3), 483–495.
9. Armaghany, T.; Wilson, J. D.; Chu, Q.; Mills, G. Genetic Alterations in Colorectal Cancer. *Gastrointest. Cancer Res.* **2012**, 5 (1), 19–27.
10. Chang, S.-C.; Lin, J.-K.; Lin, T.-C.; Liang, W.-Y. Loss of Heterozygosity: An Independent Prognostic Factor of Colorectal Cancer. World J. *Gastroenterol.* 2005, 11 (6), 778–784..
11. Ogino, S.; Nosho, K.; Irahara, N.; Shima, K.; Baba, Y.; Kirkner, G. J.; Meyerhardt, J. A.; Fuchs, C. S. Prognostic Significance and Molecular Associations of 18q Loss of Heterozygosity: A Cohort Study of Microsatellite Stable Colorectal Cancers. *J. Clin. Oncol.* **2009**, 27 (27), 4591–4598.
12. Cerami, E.; Gao, J.; Dogrusoz, U.; Gross, B. E.; Sumer, S. O.; Aksoy, B. A.; Jacobsen, A.; Byrne, C. J.; Heuer, M. L.; Larsson, E.; *et al*. The CBio Cancer Genomics Portal: An Open Platform for Exploring Multidimensional Cancer Genomics Data. *Cancer Discov.* **2012**, 2 (5), 401–404.
13. Gao, J.; Aksoy, B. A.; Dogrusoz, U.; Dresdner, G.; Gross, B.; Sumer, S. O.; Sun, Y.; Jacobsen, A.; Sinha, R.; Larsson, E.; *et al*. Integrative Analysis of Complex Cancer Genomics and Clinical Profiles Using the CBioPortal. *Sci. Signal*. **2013**, 6 (269), pl1.
14. Warde-Farley, D.; Donaldson, S. L.; Comes, O.; Zuberi, K.; Badrawi, R.; Chao, P.; Franz, M.; Grouios, C.; Kazi, F.; Lopes, C. T.; *et al*. The GeneMANIA Prediction Server: Biological Network Integration for Gene Prioritization and Predicting Gene Function. *Nucleic Acids Res*. **2010**, 38 (Web Server issue), W214-20.
15. Tanner, M.; Hollmén, M.; Junttila, T. T.; Kapanen, A. I.; Tommola, S.; Soini, Y.; Helin, H.; Salo, J.; Joensuu, H.; Sihvo, E.; et al. Amplification of HER-2 in Gastric Carcinoma: Association with Topoisomerase IIalpha Gene Amplification, Intestinal Type, Poor Prognosis and Sensitivity to Trastuzumab. *Ann. Oncol*. **2005**, 16 (2), 273–278.
16. McDonald, S. L.; Stevenson, D. A. J.; Moir, S. E.; Hutcheon, A. W. ; Haites, N. E.; Heys, S. D.; Schofield, A. C. Genomic Changes Identified by Comparative Genomic Hybridisation in Docetaxel-Resistant Breast Cancer Cell Lines. *Eur. J. Cancer* **2005**, 41 (7), 10 86–1094.
17. Negri, T.; Tarantino, E.; Orsenigo, M.; Reid, J. F.; Gariboldi, M.; Zambetti, M.; Pierotti, M. A.; Pilotti, S. Chromosome Band 17q21 in Breast Cancer: Significant Association between Beclin 1 Loss and HER2/NEU Amplification. *Genes Chromosomes Cancer* **2010**, 49 (10), 901–909.

Author

Haryeong Eo is a junior at Shanghai American School Puxi. She is interested in studying biochemical engineering and genetics. She hopes this research paper will open a wider door in preparing herself to study more sophisticated biology topics in the future.

DOI: 10.36838/v5i1.7

IJHSR
ijhighschoolresearch.org
REVIEW ARTICLE

Unveiling the Role of MicroRNA-132 on Alzheimer's Disease Brain Cells

Hannah Kim, Youngwook David Kim

Seoul International School, Seongnam, Korea; gosyber1@gmail.com

ABSTRACT: Alzheimer's Disease (AD) is a neurological disease that degenerates memories and cognitive abilities. A key factor of the disease that is still being studied is microRNA (miRNA), a non-coding strand of RNA that regulates gene expression. Particularly, miRNA-132 is known to play a significant role in AD. Past research has shown that miRNA-132 functions as a negative regulator and slows down the progression of the disease in the later stages. Through this study, four genes were identified to be associated with the regulating G1/S transition: *RB1, EP300, PTEN*, and *CDKN1A*. These four genes were known to inhibit the G1/S transition. However, the result was contrary to our expectations because if the microRNA-132 activates G1/S transition in neurons by silencing these four genes, the neurofibrillary tangles and amyloid plaques may be formed, inducing apoptosis in neurons. We transfected miRNA-132 on A172 (human brain cell) to confirm this result. The miRNA-132 transfection cells showed decreased cell proliferation and increased cell death. This result indicates that microRNA-132 may advance the progression of AD in the early stages.

KEYWORDS: Alzheimer, Brain, Gene Network Analysis, G1/S transition, micro-RNA.

Introduction

Alzheimer's disease is one of the most common neurodegenerative diseases worldwide.[1] It is a neurodegenerative disease that worsens the functions of neurons and destroys the connections between its networks. The disease most commonly harms the neurons that are part of the brain associated with memory, such as the hippocampus and entorhinal cortex.[2] This disease causes symptoms including memory loss, abrupt changes in personality and emotions, and cognitive impairments.[3] Although drugs were created to reduce their symptoms; an effective cure has not been developed yet due to a lack of funding.[4]

miRNA is a single strand of non-coding RNAs that regulates gene expression.[5] These strands, mainly composed of 22 nucleotides, silence the mRNAs by binding to mRNAs and controlling the types and number of proteins.[6] A miRNA is first transcribed from the DNA sequence into primary miRNA, which then undergoes modifications (such as RNA splicing) to become mature miRNA. In the cytoplasm, the miRNA binds to RISC molecules (RNA Interference Silencing Complex) before binding to a specific mRNA.[7] The binding between the miRNA and the mRNA in the 3' untranslated region leads to suppression in translation and even degradation. A miRNA-bound mRNA that was not destroyed is preserved for translation.[7]

miRNA-132 is a non-coding RNA that has several roles within the brain. It is crucial for axon growth, the development of brain cells, and plasticity.[8] This RNA is vital for maturation, a process of neurons developing molecular functions to be complete brain cells. In addition, studies have shown that miRNA-132 could correlate with Alzheimer's Disease. Against the Amyloid Beta, which is a polypeptide of amino acids that can cause AD, miRNA-132 has shown to have the strongest neuroprotective activity.[9]

Target Scan is a website that predicts biological targets of microRNAs. It does so by searching for 8mer, 7mer, or 6mer sites that match the seeding region of a miRNA. It also finds mismatches within the seed regions and uses conserved 3' pairing and centered sites to fix them.[10] The seed region is vital because miRNA can repress mRNA by binding the miRNA's seed region and the mRNA's 3' UTR. And this is also how miRNA targets are recognized as well. However, many of the sites are ineffective, and the mRNAs are targeted through non-canonical interactions.[11]

EnrichR is a system application that can identify the specific genes or proteins from the gene sets of interest.[12] For this research, this program was used to find the genes that could be linked to the protective role of miRNA-132 during a case of Alzheimer's disease. Gene enrichment analysis was performed in this research to identify the correlated genes between miRNA-132 and Alzheimer's Disease. This program provides a wide variety of studies, including transcription analysis, biological pathway analysis, ontology analysis, disease, and drugs analysis, etc.[12]

GeneMania is a system application that finds and visually illustrates the correlation between the inputted genes. This application provides multiple ways the correlation of genes can be viewed, along with the networks, such as the physical interaction or co-expression of each gene.[13] For this research, the genes that EnrichR identified were inserted into GeneMANIA, revealing the genes that are associated with the G1/S transition of the cell cycle. It also identified the specific genes linked to several neurodegenerative diseases, including Alzheimer's.

DOI: 10.36838/v5i1.8

The cell cycle is a process that cells undergo to replicate themselves. There is a difference in the cell cycle between somatic cells and gametes. Still, for somatic cells (non-reproductive cells), the cycle mainly consists of stages called G1, S, G2, and M.[14] During the G1 phase, the cell prepares for division by growing larger and making more organelles. In the S phase, the DNA is replicated. The synthesis of organelles, proteins, and cell growth continues during the G2 phase. These three stages are known as Interphase. After the G2 phase ends, mitosis begins. The M phase also occurs in several steps: Prophase, Prometaphase, Metaphase, Anaphase, Telophase.[15]

Cell cycle regulation is the ability of cells to control the progression into the cycle. A dysregulation would lead to an uncontrollable division of cells; a typical result of dysregulation is cancer.[16] This dysregulation can also be seen in patients with Alzheimer's disease. Instead of progressing into the cell cycle and dividing, most neurons stay in the stage of G1 or G2. Alzheimer's disease can cause the G1 and S control mechanisms to fail and cause the neurons to divide. As a result, neurofibrillary tangles and amyloid plaques are formed, and then the neurons undergo apoptosis.

MicroRNA-132 has been extensively studied in Alzheimer's disease for its protective role. However, it is still unclear how MicroRNA-132 interacts with the target genes and how these target gene networks protect the neuronal cells in the brain. To find how MicroRNA-132 has a protective role in Alzheimer's disease, we screened all potential target genes of MicroRNA-132 by Target Scan. Then, these target genes were further analyzed by the web-based programs Enrich R and Gene Mania. Enrich R identified the significant biological pathways of the target genes of MicroRNA-132. GeneMania provided the protein physical interacting gene network among the target genes of MicroRNA-132.

Methods

Target Scan:

Target Scan is a web-based program that predicts the target genes of the specific miRNA in human cells. To find all possible target genes of miR-132. On the microRNA name, "miR-132-3p" was inserted in the search tab. Then, the program provides the list of all the predicted target genes. The list of all predicted genes was saved as an excel file.

EnrichR analysis:

EnrichR is a web-based program that profiles the genes and proteins in mammalian cells. To find the novel role of the miR-132-3p target genes, all 474 genes were inserted into the input data. This program provides interactive visualizations of the results in many ways. The biological pathway section showed a significant result of gene enrichment analysis.

GeneMania:

GeneMania analyzes the gene list and prioritizes the genes for functional assays. The 14 genes analyzed from the Enrich R were used to analyze the relative gene functions and biological pathways.

Cell culture and Maintenance:

A172 cells were purchased from Korea Cell Line Bank. A172 cells were cultured with RPMI 1640 cell culture media (Gibco). The cells were maintained in the CO2 incubator.

Cell transfection and viability assay:

RNAimax transfection (Invitrogen) reagent was used to transfect miR-132 on A172 cells. First, A172 cells were plated 24 hrs. before the experiment into 24-well plates at 50,000 cells/well. Subsequently, each well was provided with the appropriate amount of complex solution in 500 µL Opti-MEM, corresponding to 10 pmol of siRNA per well. After four hrs. incubation, the transfection medium was replaced by fresh culture medium. After 48 hrs. transfection, the cells were imaged, and cell viability was measured by Prestoblue assay (Invitrogen). PrestoBlue® reagent was added directly to the wells (1:10) and incubated at 37° C for 60 min. To measure the samples' absorbance (570 nm) was measured using a spectrophotometer (Biotek).

Statistical analysis:

An enrichment p-value is calculated by comparing the observed frequency of an annotation term with the frequency expected by random chance. The individual terms beyond a cut-off (p-value ≤ 0.05) were used for enrichment. One-way ANOVA with Tukey's post hoc test was performed for cell proliferation to calculate the p-value. A p-value less than 0.05 was considered to be statistically significant.

Results and Discussion

The purpose of this analysis was to find out the number of human genes that the miRNA-132-3p targets. Using Target Scan, 474 genes were identified. They were sorted by cumulative weighted context, which means they are listed in order of the possibility of being targeted by the miRNA-132-3p. The next step was to identify the biological pathways and connections these identified genes have. The program EnrichR was used for this pathway enrichment analysis to find which genes are involved in AD progression.

Table 1: Result of EnrichR biological pathway analysis.

EnrichR_Wikipathway 2019 human	Overlap	P-value
Signaling Pathways in Glioblastoma WP2261	14/82	7.35×10^{-09}
Focal Adhesion-PI3K-Akt-mTOR-signaling pathway WP3932	26/303	1.77E-08
Pathways Affected in Adenoid Cystic Carcinoma WP3651	12/65	3.53E-08
Signaling of Hepatocyte Growth Factor Receptor WP313	9/34	6.77E-08
VEGFA-VEGFR2 Signaling Pathway WP3888	21/236	2.30E-07

Pathway enrichment analysis helps researchers gain mechanistic insight into gene lists generated from genome-scale data. This method identifies biological pathways enriched in a gene list more than would be expected by chance. Gene set pathway enrichment analysis allows one to identify classes of genes or proteins over-represented in a large set of genes or proteins and may be associated with disease phenotypes. The method uses statistical approaches to identify significantly enriched or depleted groups of genes.

Table 1 shows the result of the EnrichR biological pathway enrichment analysis based on the 474 genes that Targetscan previously identified. The P-value indicates the probability of the biological pathway occurring by random chance. Therefore, the p-value was used to rank the biological pathway. Table 2 results show that the lowest p-value was identified as signaling pathways in glioblastoma.

DOI: 10.36838/v5i1.8

The lowest p-value pathway indicates that out of 82 genes associated with glioblastoma, 14 overlapped with 474 genes identified in Enrich R. Glioblastoma as a type of cancer that occurs in the brain or spinal cord starts from astrocyte cells. Interestingly, glioblastoma is also known to be associated with Alzheimer's disease. To find more information about these 14 genes, we further analyzed the protein-protein interaction of these genes using GeneMania (Figure 1).

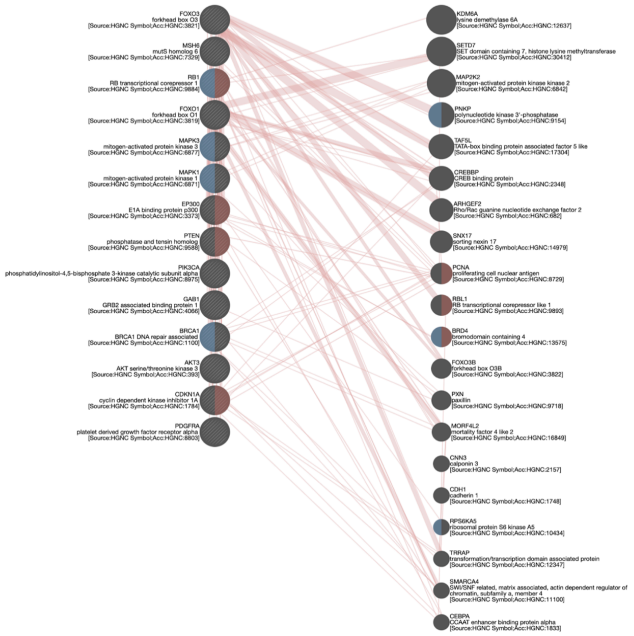

Figure 1: The result of protein-protein physical interaction analysis by GeneMania. The left column represents the 14 gene sets identified from signaling pathways in glioblastoma.

The right column represents the gene sets, known as protein-protein physical interaction with 14 gene sets (Figure 1). The red line represents the protein-protein interaction between genes. The Red in the circle represents the genes associated with the G1/S transition of the mitotic cell cycle. The blue in the circle indicates the genes associated with regulating chromosome organization.

As shown in Figure 1, the genes responsible for regulating G1/S transition, colored red, were *RB1, EP300, PTEN*, and *CDKN1A*. The genes that regulated chromosome organization, colored blue, were *RB1, MAPK3, MAPK1*, and *BRCA1*. In this case, RB1 is responsible for regulating both G1/S transition and chromosome organization, thus indicated with blue and red together.

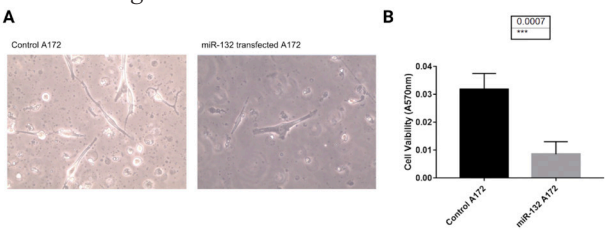

Figure 2: miR-132 decreased cell viability of human brain neurons. (A) The cell image of the A172 human brain cells compared to the control condition and miR-132 transfected A172. (B) The bar graph of cell viability comparing control A172 and miR-132 transfected A172 cells. The mean and standard deviation of 570 nm absorbance is shown in the graph. One-way ANOVA with Tukey's post hoc test was performed to calculate the p-value. ($p = 0.0007$)

To confirm the miR-132 function in human brain neurons, cell viability was analyzed in A172 cells. Figure 2 results show that neurons that were transfected with miRNA-132 died at a quicker rate. Figure 2A shows the two cell conditions: control A172 cells and miR132 transfected A172 cells in the brightfield image. Less viable cells were observed in miR132 transfected A172 cells. A prestoblue assay was performed in Figure 2B to quantify the cell viability. This result is consistent in Figure 2A that cell viability decreased after the miRNA-132 transfection.

Among 474 target genes, four genes are associated with the G1/S transition of the mitotic cell cycle. Interestingly, all four

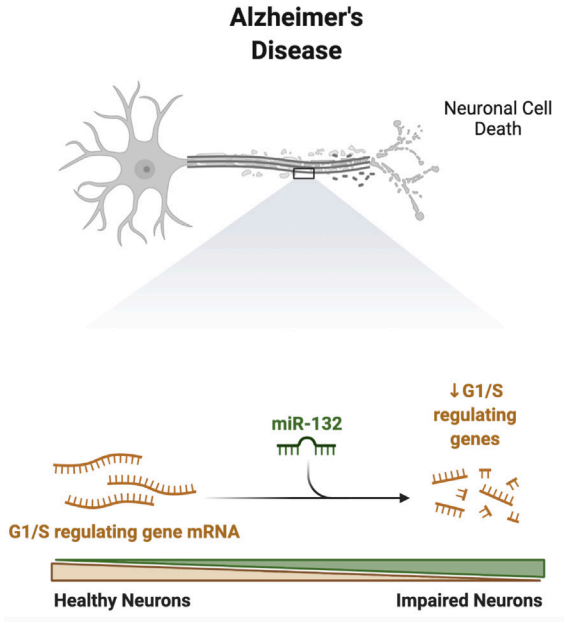

Figure 3: Our proposed model of miR-132 impairing neurons in Alzheimer's disease.

genes encode proteins that inhibit the G1/S transition. For example, *RB1* is a tumor-suppressor gene that codes for proteins called *RB*.[17] These proteins are essential because, without them, the cells would continuously divide without control. Thus, the *RB1* gene acts as an inhibitor of G1/S transition. Through the creation of *RB*, the transition into the G1 or S phase is regulated.[17]

EP300, also known as p300, is a gene that codes for p300 transcriptional co-activator protein. Cells lacking the p300 proteins progress through the G1 phase without fully developing, suggesting that the protein acts as a negative regulator of the G1/S transition. p300 inhibits cdk6-mediated RB phosphorylation from occurring early in the G1 phase to prevent premature entry into the S phase.

PTEN is a well-known tumor-suppressor phosphatase that plays a key role in cell growth, embryonic development, and apoptosis.[18] As a PI3-phosphatase (phosphatidylinositol-3 phosphatase) negatively regulates the PI3 kinase pathway; thus, *PTEN* blocks the G1/S phase. In addition, by controlling the expression of cyclin D1 and p27Kip1, *PTEN* inhibits the transition to the G1/S phase.[18]

CDKN1A is a gene that encodes for a protein called p21. The protein acts as an inhibitor of the cyclin E/Cdk2 complex.[19] For p53-dependent G1 inhibition to happen, p21 is needed. Its presence is also required for G2 inhibition when there is DNA damage.[19]

Overall, the gene network analysis found that miR-132 targets four genes (*RB1, EP300, PTEN, CDKN1A*) that inhibit G1/S transition. This result indicates that miR-132 may enhance the cell cycle in brain neuronal cells (Figure 3). However, many previous studies show that dysregulation of G1/S transition leads to an uncontrollable division of cells, a typical characteristic of cancer, and has been discovered in the brain neuronal cells of Alzheimer's patients. Therefore, our gene network data suggest that miR-132 may be involved in Alzheimer's progression by targeting G1/S inhibiting genes.

Interestingly, one study suggested an initial increase in miR-132 levels during early AD Braak stages I and II in the human prefrontal cortex, which contrasts with the decrease seen at more advanced stages of the disease. The Braak stages I and II are determined by the tau pathology, which is found within the entorhinal and transentorhinal cortex (stage 1) and hippocampus (stage 2). In conclusion, this study discovered that miR-132 might play an essential role in developing the early stage of Alzheimer's by targeting genes that inhibit G/S transition.

■ Conclusion

Overall, the gene network analysis found that miR-132 targets four genes (*RB1, EP300, PTEN, CDKN1A*) that inhibit G1/S transition. This result indicates that miR-132 may enhance the cell cycle in brain neuronal cells. However, many previous studies show that dysregulation of G1/S transition leads to an uncontrollable division of cells, a typical characteristic of cancer, and has been discovered in the brain neuronal cells of Alzheimer's patients. To verify the effect of miR-132 on AD, miR-132 transfection was conducted in A172 neuron cells (Figure 3). miR-132 decreased the cell viability of neuron cells. However, our study has several limitations. We only investigated miR-132 target genes. Therefore, another type of miRNA should be examined in the future. Also, we only used one type of A172 brain cell. Therefore, more types of brain cells should be tested in the future. Overall, we concluded that miR-132 is a positive regulator of Alzheimer's Disease by impairing neuronal cells in the human brain.

■ Acknowledgments

We want to give special thanks to Prof. Woo Rin Lee from the University of Suwon, South Korea, for his support.

■ References

1. Weller, J.; Budson, A. Current Understanding of Alzheimer's Disease Diagnosis and Treatment. [Version 1; Peer Review: 2 Approved] . *F1000Res*. **2018**, 7.
2. What Happens to the Brain in Alzheimer's Disease? | National Institute on Aging https://www.nia.nih.gov/health/what-happens-brain-alzheimers-disease#:~:text=In%20Alzheimer's%20 disease%2C%20as%20neurons,significant%20loss%20of%20 brain%20volume.brain%20volume. (accessed Jul 12, 2021).
3. What Are the Signs of Alzheimer's Disease? | National Institute on Aging https://www.nia.nih.gov/health/what-are-signs-alzheimers-disease (accessed Jul 12, 2021).
4. Why don't we have a cure for Alzheimer's disease? https://theconversation.com/why-dont-we-have-a-cure-for-alzheimers-disease-156473 (accessed Jul 12, 2021).
5. O'Brien, J.; Hayder, H.; Zayed, Y.; Peng, C. Overview of microRNA Biogenesis, Mechanisms of Actions, and Circulation. *Front Endocrinol (Lausanne)* **2018**, 9, 402.
6. Micro RNA and the importance of basic biology https://www.jax.org/news-and-insights/2017/may/narry-kim-hugo# (accessed Jul 12, 2021).
7. microRNA - What it is and How it Works | OSUCCC - James https://cancer.osu.edu/microrna (accessed Jul 12, 2021).
8. Qian, Y.; Song, J.; Ouyang, Y.; Han, Q.; Chen, W.; Zhao, X.; Xie, Y.; Chen, Y.; Yuan, W.; Fan, C. Advances in Roles of MiR-132 in the Nervous System. *Front. Pharmacol*. **2017**, 8, 770.
9. El Fatimy, R.; Li, S.; Chen, Z.; Mushannen, T.; Gongala, S.; Wei, Z.; Balu, D. T.; Rabinovsky, R.; Cantlon, A.; Elkhal, A.; et al. MicroRNA-132 Provides Neuroprotection for Tauopathies via Multiple Signaling Pathways. *Acta Neuropathol*. **2018**, 136 (4), 537–555.
10. Agarwal, V.; Bell, G. W.; Nam, J.-W.; Bartel, D. P. Predicting Effective MicroRNA Target Sites in Mammalian mRNAs. *eLife* **2015**, 4.
11. Mullany, L. E.; Herrick, J. S.; Wolff, R. K.; Slattery, M. L. Microrna Seed Region Length Impact on Target Messenger RNA Expression and Survival in Colorectal Cancer. *PLoS ONE* **2016**, 11 (4), e0154177.
12. Chen, E. Y.; Tan, C. M.; Kou, Y.; Duan, Q.; Wang, Z.; Meirelles, G. V.; Clark, N. R.; Ma'ayan, A. Enrichr: Interactive and Collaborative HTML5 Gene List Enrichment Analysis Tool. *BMC Bioinformatics* **2013**, 14, 128.
13. Warde-Farley, D.; Donaldson, S. L.; Comes, O.; Zuberi, K.; Badrawi, R.; Chao, P.; Franz, M.; Grouios, C.; Kazi, F.; Lopes, C. T.; et al. The GeneMANIA Prediction Server: Biological Network Integration for Gene Prioritization and Predicting Gene Function. *Nucleic Acids Res*. **2010**, 38 (Web Server issue), W214-20.
14. Phases of the cell cycle (article) | Khan Academy https://www.khanacademy.org/science/ap-biology/cell-communication-and-cell-cycle/cell-cycle/a/cell-cycle-phases (accessed Jul 12, 2021).
15. Hunt, T.; Nasmyth, K.; Novák, B. The Cell Cycle. Philos. Trans. R. Soc. Lond. *B Biol. Sci.* **2011**, 366 (1584), 3494–3497.
16. Nagy, Z. The Dysregulation of the Cell Cycle and the Diagnosis of Alzheimer's Disease. Biochim. *Biophys. Acta* **2007**, 1772 (4), 402–408.
17. Jeanblanc, M.; Mousli, M.; Hopfner, R.; Bathami, K.; Martinet, N.; Abbady, A.-Q.; Siffert, J.-C.; Mathieu, E.; Muller, C. D.; Bronner, C. The Retinoblastoma Gene and Its Product Are Targeted by ICBP90: A Key Mechanism in the G1/S Transition during the Cell Cycle. *Oncogene* **2005**, 24 (49), 7337–7345.
18. Iyer, N. G.; Xian, J.; Chin, S. F.; Bannister, A. J.; Daigo, Y.; Aparicio, S.; Kouzarides, T.; Caldas, C. P300 Is Required for Orderly G1/S Transition in Human Cancer Cells. *Oncogene* **2007**, 26 (1), 21–29.
19. Radhakrishnan, S. K.; Feliciano, C. S.; Najmabadi, F.; Haegebarth, A.; Kandel, E. S.; Tyner, A. L.; Gartel, A. L. Constitutive Expression of E2F-1 Leads to P21-Dependent Cell Cycle Arrest in S Phase of the Cell Cycle. *Oncogene* **2004**, 23 (23), 4173–4176.

■ Author

Hannah Kim is a junior in high school who is highly interested in researching oral and neurological diseases such as Alzheimer's and is the president of a student-led science journal oculussj.com.

DOI: 10.36838/v5i1.8

David Kim is a sophomore at Seoul International School who currently takes AP biology and is interested in researching neurological diseases such as Alzheimer's. He is a member of the Medical Society club at his school and the student-led science journal club on oculussj.com.

IJHSR
ijhighschoolresearch.org
■ RESEARCH ARTICLE

Design and Development of an Economic and Effective Hybrid Space Suit

Hridyanshu, Madhav Sharma

SAmity International School, Saket, Road 44, M Block, New Delhi, Delhi, 110017, India; hridyanshu.2410@gmail.com

ABSTRACT: This research paper aims to create a hybrid spacesuit design by a unique amalgamation of the two most popular spacesuit design techniques - Gas pressure and mechanical counterpressure in such a configuration that the overall suit can essentially capitalize on both advantages. In contact with the skin, the mechanical pressure layer has been modified with bands of Magnetic Shape Memory Alloys (MSMA's) to reduce donning/doffing time and solve the key limitation of a static fiber by allowing it to fit securely over curves of the body. Numerous other enhancements and safety mechanisms have been made possible due to this unique configuration, all in a cost-effective package. Furthermore, experiments were conducted to construct a breathing bladder to map its pressure regions uniformity and map airflow vectors. Apart from this computational experiment, a physical glove was prepared to check the differential pressure and hand movements. Lastly, a trait study was conducted to observe the difference between our suit and the other commercial ready-to-use spacesuits.

KEYWORDS: Engineering Mechanics; Mechanical Engineering; Shape Memory Effect; Computational Pressure Mapping.

■ Introduction

With Project Artemis, Mars Missions, Space Tourism, etc. planned for the near future, new spacesuit designs must be brought into production to enhance efficiency and reduce the cost of these missions. Gas Pressure layers are very stiff and uncomfortable. The current models need to sacrifice sensitive fingertip control and fine motor skills. Poor-fitting results in a significant discrepancy between the wearer's and suit's movements. It is estimated that the wearer moves about 30% more than the suit, which is exhausting and inefficient.

Due to stiffness and rigidity, a solution has been adopted to adjust the internal pressure in a spacesuit at 0.3 atm. But this can cause decompression sickness, a medical condition caused by dissolved gases emerging from solution as bubbles inside the body tissues during decompression.[1] Current spacesuits are "anthropomorphic balloons," Despite over 50 years of development, the pre-breathe time and protocols make them high maintenance. The 100% pure oxygen pre-breathe protocol for Extra-Vehicular Activity (EVA) is a 12 hours-long process. Such emergencies will consume much valuable time for long missions on the Martian or Lunar surface.

Dust on other planets or moons is different from that experienced on Earth.[2] The soil is usually very coarse and jagged and tends to be very sticky. Thus, it is required that new spacesuit designs minimize gaps like zippers. Current suits are responsible for musculoskeletal injuries in the hands, shoulders, and other joints.

Our suit aims to tackle these challenges with a reimagined design, combining gas and mechanical pressure layers with the strategic use of new-age materials like Magnetic Shape Memory Alloys and thinner Breathing Bladders.

A new spacesuit design is not a luxury; it is essential to enhance the efficiency of future manned missions to the Moon, Mars, and beyond. With the increased focus on EVA, current systems, which use Gas Pressure, cannot sustain the demands of astronauts much longer.

■ Methodology

Firstly, a trait study was conducted (refer to Table 1) among the current commercial spacesuits and a thorough analysis of their shortcomings to decide on the garments to be used in the two pressure layers. The following six criteria were utilized. A scoring rubric was decided with a score range of 0-5, where 0 represented non-existence/critical failure, and 5 represented absolute success. This study paved the way to integrate the best features in our suit and introduce new features, as seen in the Results and Discussion sections.

Table 1: Trait study criteria for the physical and economic aspects.

Criteria	Meaning
Mobility	Describes how easy it is to perform movements
Feasibility	Addresses the difficulty of creating a full suit with cost considerations on its development
Decompression Sickness	Capability of the spacesuit architecture to prevent DCS and/or have quick contingency
Mass	Calculating the total spacesuit configuration weight
Complexity	Amount of parts needed to complete a certain configuration, which drives the capability to effectively operate over time
Robustness	Ability to withstand or overcome adverse/contingency conditions

Secondly, using NASA's Man Systems Integration Standards, Volume 1, Section 14 as a reference for the human body and device standards, a human body was modeled in Autodesk Maya and exported to Fusion 360 and ExactFlat for 2D cutouts (to get precise measurement) with our desired coverage area of breathing bladder on the torso (refer to Figure 1 for the pipeline). Torso covers two regions of significant importance. Firstly, the chest (C) and the abdomen (A). These are further

DOI: 10.36838/v5i1.9

divided into four regions for simulations, which are, Chest 1 (C1), Chest 2 (C2), Abdomen 1 (A1), and Abdomen (A2). C1, C2, A1, and A2 are the pillars of all calculations that are required to be carried out for the simulations.

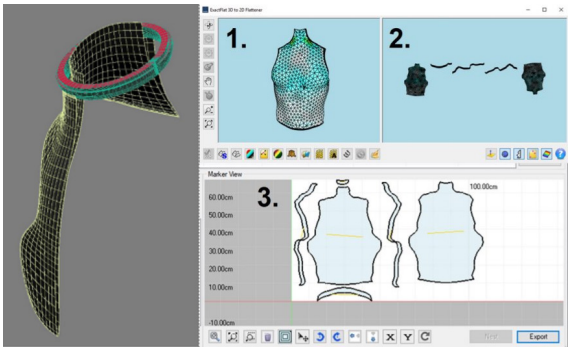

Figure 1: The pipeline of bladder creation. Autodesk Maya 3D model (left) and 2D cutouts in ExactFlat (right).

Accordingly, MIT's research document determined the volume changes for breathing bladder in two cases of EVA were decided, that are, 4 liters for adult males during maximal forced inspiratory and expiratory maneuver (MFIEM) and 0.5 liters for quiet breathing.[3] Using Fusion 360 static pressure simulation, the torso was divided symmetrically into four parts (refer to 2) to achieve uniform pressure on the whole bladder. Sample pressure applying needles were developed similar to those used by doctors to map put points on the Chest-Abdomen 1 (CA1) and Chest-Abdomen 2 (CA2) pressure applied to keep the breathing bladder in order with the body (as shown in Figure 2).

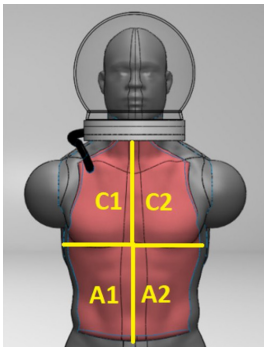

Figure 2: Symmetrical division of the breathing bladder on the torso.

Thirdly, a flow duct was designed between the gas pressure-filled helmet to identify the airflow vectors, which in turn helps us decode the breathing process for future astronauts and space tourists.[4] Here, low and high-pressure vectors were designed in the helmet. Through the CA1 and CA2 pressure data, the upper and lower limit of the airflow speed was set. Further, from NASA's xEMU (Extravehicular Mobility Unit) and mEMU spacesuit data, data was collected about the EVA missions to understand the physiological changes in astronauts.[5]

Fourthly, an Arduino-based glove prototype was made with five flex sensors, five servo motors, multiple resistors,[1] Arduino Mega Board, and batteries.[6] Each flex sensor was placed on one finger, and the same was followed with servo motors (refer to Figure 3). Additionally, glove materials were prepared using NASA's xEMU and mEMU paper, and we came up with our custom volume and thickness of the glove.[7] Figure 4 shows you the variables and a code snippet.

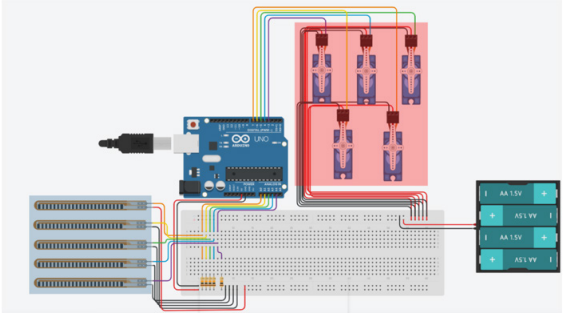

Figure 3: Circuit diagram showing the components.

```
#include <Servo.h>
//define servo motors
Servo pinkie, ring, middle, index, thumb;

//define flex sensors on glove (F1 = flex sensor 1)
const int pinkieFlex = A0; //bent - 710, flat - 900 (values vary depending on your own flex sensors))
const int ringFlex = A1; //bent - 920, flat - 965
const int middleFlex = A2; //bent - 966, flat - 993
const int indexFlex = A3; //bent - 808, flat - 870
const int thumbFlex = A4; //bent - 490, flat - 525


void setup(){
  //attach servo motors to digital pins
  pinkie.attach(13);
  ring.attach(12);
  middle.attach(11);
  index.attach(9);
  thumb.attach(10);
```

Figure 4: Code snippet highlighting the variables.

Results and Discussion

Spacesuit Configuration and Advantages:

In Table 2, a detailed comparison has been conducted between the commercial spacesuits and ours - CosmoVest and accordingly explained the scores below.

Table 2: Trait study scores for commercial spacesuits.

Factors/ Suit names	ILC Dover Extra Mobility Unit (EMU) (1983)	David Clark Company Incorporated Red Bull Stratos Pressure Suit (2012)	SpaceX Starman Suit (2018)	NASA xEMU (2020)	CosmoVest (To be done as per estimates by 2023)
Purpose	EVA	Test Suit+IVA	IVA	EVA	EVA+IVA
Mobility	3	2	3	3	5
Feasibility	2	2	1	4	4
DCS	2	1	2	3	5
Mass	1	3	4	3	3
Complexity	1	1	3	2	4
Robustness	2	1	1	3	5
Total	11	10	14	18	26

Mobility Factor: Elevated gas pressurization will increase system cost because it decreases mobility. Mechanical Counter Pressure (MCP) garments will do the same, but with less loss of mobility and increased pressurization. Our hybrid spacesuit will thus reign at first position here because other companies still use the 1960s and 70s-based gas pressure systems.

Feasibility Factor: Other configurations will have a smaller system cost than ours because they have been widely manu-

factured and successfully flown. Ours is equal to xEMU due to the objectives they both fulfill.

Decompression Sickness (DCS): Since our suit is driven by two pressure layers, it will reduce the chance of decompression sickness compared to the older suits, especially International Latex Corporation Dover's, which have only one pressure garment and no backup. Lower total pressure will increase system cost because it increases the risk for DCS, as seen in the David Clark Company Incorporated test suit.

Mass Factor: Our suit took inspiration from NASA's xEMU suit and used its garment for the gas pressure layer (external) but modified it according to the internal layer in our suit. This reduced the volume, thickness, and quantity of each material and its sublayers. This makes our suit light and production costs less. Compare this to xEMU with 20 times more mass than ours, International Latex Corporation Dover's commercial suits having 40 times the mass of ours.

Complexity: Designs incorporating both layers will increase internal components and make it easier and more accessible for astronauts during EVA. A significant factor is the storability of CosmoVest compared to International Latex Corporation Dover's clunky suits that took more space on the external layer for mechanical components than EVA tools.

Robustness: Designs incorporating only one layer will increase system costs because using both technologies decreases the risk if one technology fails.

Accordingly, the pressure layers were decided. Firstly, the mechanical counterpressure layer is a skin-tight thin layer working on the Magnetic Shape Memory Alloys (MSMAs).[8] SMAs mesh generates voltage-controlled mechanical counterpressure. Secondly, the traditional Gas Pressure Layer is the outermost layer that keeps the mechanical pressure layer tight by applying uniform pressure. This eliminates the need for a complex locking mechanism which has held back some other mechanical pressure designs.

The reason for combining these layers is to capitalize on both advantages. Since the gas pressure layer is not relied upon alone, only a 2-2.5 PSI layer will be required compared to a traditional 4-4.5 PSI, significantly reducing bulk and enhancing mobility.[9] Besides this, the skin-tight nature of the innermost mechanical layer allows for fine motor control. MSMAs are further used to ensure the mechanical pressure layer can be contracted upon curves and cavities, which has traditionally been a problem for mechanical pressure suits. The use of MSMAs also reduces the donning/doffing time as the MSMAs can be expanded/contracted to ease the process. Figure 5 shows the flexible working of the MSMAs.

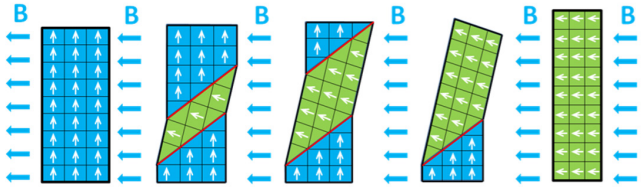

Figure 5: The shape memory effect of MSMAs.

Pressure Layers and Garments:

Table 1 shows that our space suit needs to be less bulky and less complex regarding its composition and mass load. Due to the two layers complementing each other and the internal layer (mechanical counterpressure layer) being so thin, it was easy to reduce the outer gas layer by 60%, decreasing each garment's volume and overall cost, as shown in Figure 6.

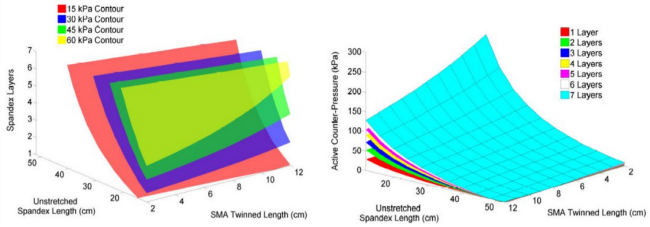

Figure 6: Each layer's pressure contour and thickness of the eight layers.

As explained in the previous section, it will work on the Magnetic Shape Memory Alloys (MSMAs). Pressure is distributed by a viscous thermal regulating gel layer (for regulating temperature shifts in alloys). MSMA has four primary layers (from outside to inside); the abrasion-resistant layer, SMAs mesh, distribution gels, evaporative cooling, perspiration, thermal control, and radiation protection layer (ECPTCRPL). The last layer further contains Shape memory alloys for fabric tensioning, nylon-spandex layers, boron nitride nanotubes (BNNT), aerogel radiation, and a thermal protective layer.10 Refer to Figure 7 for its layer.

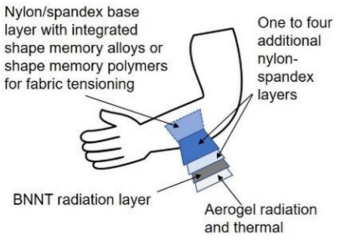

Figure 7: Mechanical counterpressure layer's garments.

The gas pressure layer (external layer) has an Ortho-Fabric inspired from xEMU suits that contain layers of multi-layer aluminized layer, neoprene coated ripstop for liner, and dacron resistant layer.[11] The LCVG is worn underneath the pressure enclosure and is designed to circulate cold water and oxygen to cool the user and ventilate the system. It uses a stretch, nylon knit fabric integrated with ethyl vinyl acetate cooling tubes and a nylon tricot comfort liner. This entire system together provides the functionality of the soft elements of the spacesuit and protects the user from the external environment (as shown in Figure 8).[13]

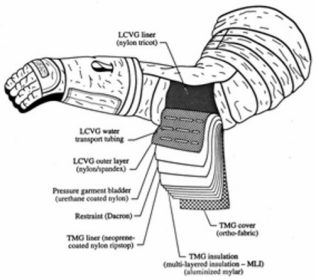

DOI: 10.36838/v5i1.9

Breathing Bladder Construction and Airflow Vector Simulation:

The breathing bladder of CosmoVest is made of semi-elastic and puncture-resistant thermoplastic polyurethane (TPU). The interior layer is composed of a latex rubber seal, and it is surrounded by an external layer to be attached on top of it, forming a complete seal. Gortex Fabric, a fabric semi-permeable to water vapor while remaining airtight, shall address the issue of sweat salt in the suit.[14] Two criteria were focused upon for the creation of the bladder, i.e., pressure and volume consistency throughout the suit, which is demonstrated in our computational experiment as well. The force to radius ratio was calculated through the relation,

$$F=Pbr$$

where F is force exerted, P is pressure applied, b is bandwidth, and r is the radius of curvature. Table 2 represents the Pressure to radius ratio calculated. Here each bandwidth was taken as 5cm as a standard reference in Table 3.

Table 3: The observation regarding the pressure to radius ratio.

Pressure (psi)	Radius (cm)	Ratio
5.6	1.92	3:1
4.2	1.72	2:1
3.5	1.43	2:1
2.9	1.15	3:1

Accordingly, the selected ratio was the smallest of 2:1, where the radius was the least. Hence 1.43 cm with a 3.5 psi was the ideal choice. The pressure and volume were balanced according to the standard guidelines. As our helmet would be filled with gas for pressure, the air must be regulated between the helmet and the breathing bladder. Two pressure conditions were identified to achieve a successful breathing and pressure flow. The first condition is low pressure, and the second is high pressure generated during EVA. Using MATLAB for the inputs and algorithm and SigmaPlot for the graphing with Adobe Photoshop, the airflow vectors were mapped with the pressure contours, as shown in Figure 9.

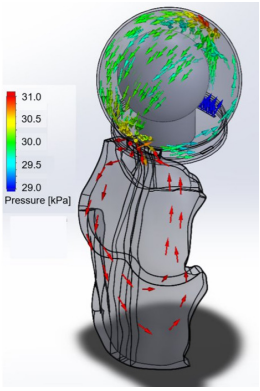

Figure 9: Internal airflow vectors at varying pressure contours.

Glove Prototype:

Firstly, the individual reading of the sensors was taken into account for a linear pressure increase in Figure 10. Secondly, the user's personal experience with stiffness was recorded too. Figure 11 shows the final prepared glove. A striking feature is that this design has reduced our glove's thickness to the maximum extent. Our glove is based on the principle of getting Earth-like uniform pressure for smoother movements. Hence the glove had external servo motors. Accordingly, it was found that Graph 2 is the best possible option based on the user's experience and experimental data.

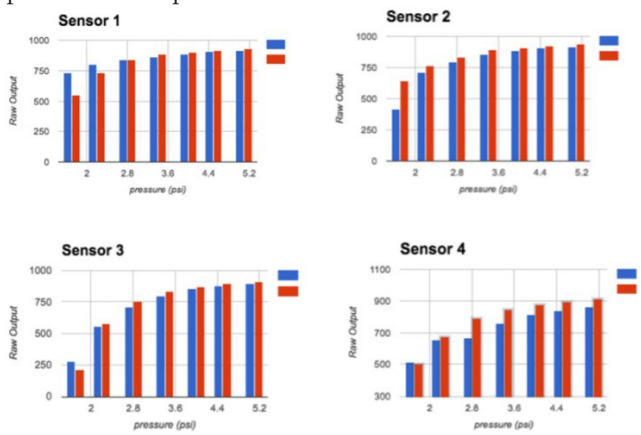

Figure 10: Graphs for each sensor placement.

Figure 11: Physical glove prototype.

Other External Components and Utilities

Utility Belt :

A simple yet functional utility belt (as shown in Figure 12) has been imagined that can be attached to the waist of the suit using hooks. This allows for convenient storage of tools/instruments required for ExtraVehicular Activity (EVA). This belt can also be used to store other modern accessories that are currently being researched by other members of the scientific community, including a surface impingement nozzle that stores the "magical" puncture healing resin - thiolene-trialkyl borane.[15]

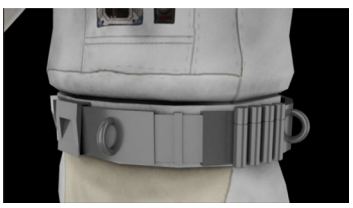

Figure 12: Utility Belt.

Portable Life Support System (PLSS):

A backpack-like module will host the life support systems in our design (as shown in Figures 13 and 14). This allows maximum freedom during EVA as the life support system exists separate from the suit's internal systems. The suit uses a Primary Life Support System (PLSS) configuration similar to those used in the Apollo Missions, with minor changes in the module's volume and total mass load.[16] No significant modification has been proposed to other generic components, such as the helmet, boots, etc.

Figure 13: The portable life support system.

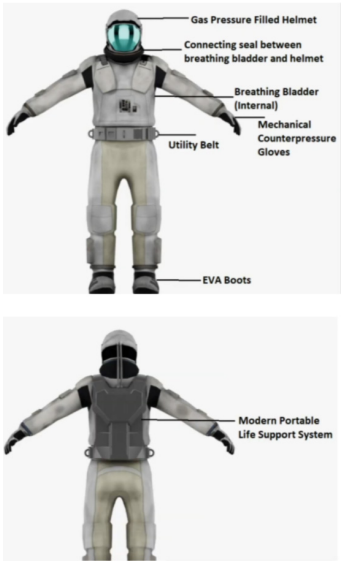

Figure 14: Front view of the suit with its major components (top) and back view of the suit with the portable life support system (down).

Conclusion

In this research, a realistic attempt has been made to categorically solve the issues in conceptualizing and manufacturing a hybrid spacesuit combining gas and mechanical counterpressure techniques. Our design combines contemporary gas and mechanical pressure layers, which provides enhanced motor control, reduced suit mass, lower cost, and other advantages which will be essential for future space missions. Using a Shape Memory Alloy further eliminates some of the significant drawbacks of a skin-tight space suit.

Compared to the expensive experiments for gloves, the team tried to simulate the same using Arduino. Computational results for the experiments show a positive sign that the suit's development is achievable and shall be a significant milestone in streamlining the future EVA missions for astronauts and space tourists.

Acknowledgments

Expressing gratitude to thank our school and the Atal Tinkering Labs, an initiative by the Government of India, for funding our work and giving us a place during the pandemic to prepare our prototype and also acknowledging their management, who helped to conduct the experiments safely in an organized manner and carried out this incubation process. The professors and engineers there revised the research paper and guided us whenever any help was required with developing the prototype and the research.

Extending gratitude to the CONRAD Foundation for motivating and supporting us to develop this project over the past year.

Lastly, sincere thanks to our parents who supported us from the beginning and all other associated members who gave us tips to develop this project and not lose hope.

References

1. Kluis, L., Diaz-Artiles, A. Revisiting decompression sickness risk and mobility in the context of the SmartSuit, a hybrid planetary spacesuit. *npj Microgravity* 7, 46 (2021).
2. O'Brien, Brian & Gaier, James. (2009). Indicative Basic Issues About Lunar Dust in the Lunar Environment. LPI Contributions.
3. Stroming, Jeremy & Newman, Dava. (2020). Design of an External Compensatory Breathing Bladder for the BioSuit.1-9. 10.1109/AERO47225.2020.9172486.
4. Duda Kevin R., Vasquez Rebecca A., Middleton Akil J., Hansberry Mitchell L., Newman Dava J., Jacobs Shane E., West John J., The Variable Vector Countermeasure Suit (V2Suit) for space habitation and exploration, Frontiers in Systems Neuroscience, Volume 9 (2015).
5. Olthoff, Claas. (2019). Comprehensive System Simulation of Extravehicular Activities in Support of Exploration System Development.
6. Waldie, James & Tanaka, Kunihiko & Tourbier, Dietmar & Webb, Paul & Jarvis, Christine & Hargens, Alan. (2002). Compression under a mechanical counter pressure space suit glove. Journal of gravitational physiology: a journal of the International Society for Gravitational Physiology. 9. 93-7.
7. Nixon, M.A. & Michaels, Joseph. (2021). The Future of NASA. 10.3139/9783446470118.007.
8. Buljak, Vladimir & Ranzi, Gianluca. (2021). Shape memory alloys.
9. Luo, Jianping & Liu, Wei & Ye, Sullivan. (2020). Human-Centered Design for the Spacesuit Development: A Case Study of the "Feitian" EVA Spacesuit.
10. Chen, Ying & Zhang, Hongzhou. (2006). Boron Nitride Nanotubes.
11. Nixon, M.A. & Michaels, Joseph. (2021). The Future of NASA.
12. Kesterson, Matthew & Sverdrup, Jacobs & Bue, Grant & Trevino, Luis. (2006). Wissler Simulations of a Liquid Cooled and Ventilation Garment (LCVG) for Extravehicular Activity (EVA). SAE Technical Papers. .
13. Tanaka, Kunihiko & Nakamura, Koji & Katafuchi, Tetsuro. (2014). Self-perspiration garment for extravehicular activity improves skin cooling effects without raising humidity. Acta Astronautica.
14. Yin, Jianjun & Ma, Wensuo & Gao, Zuobin & Lei, Xianqing & Chenhui, Jia. (2022). A Review of Electromagnetic Shielding Fabric, Wave-Absorbing Fabric and Wave-Transparent Fabric. Polymers.
15. Zavada, Scott & McHardy, Nicholas & Gordon, Keith & Scott, Timothy. (2015). Rapid, Puncture-Initiated Healing via Oxygen-Mediated Polymerization. ACS Macro Letters.
16. Jiang, Jin-Gang & Chen, Yihao & Ma, Xuefeng & Zhang, Yongde

DOI: 10.36838/v5i1.9

& Huang, Zhiyuan & Liang, Dexian. (2019). Portable Life Support System: Current Status and Future Perspectives. Recent Patents on Engineering.

Authors

Hridyanshu is a physics and engineering researcher interested in deducing situations to their simplest by utilizing 3D design tools and computational methods. He is currently interning under the Rowing Federation of India and is interested in pursuing aerospace engineering in the future.

Madhav Sharma is a high school student interested in aerospace and computer engineering. He has won numerous aerospace competitions in association with NASA, Conrad, and Aerospace Education Competitions (AEC), to name a few.

IJHSR
ijhighschoolresearch.org
■ RESEARCH ARTICLE

Livestock Manure Recycling for Vegetable Farms in Hong Kong

Lauren Hsu

Choate Rosemary Hall, 333 Christian Street, Wallingford, CT, 06492, U.S.A; laurenkanru@gmail.com

ABSTRACT: Urbanization and zoonotic disease in Hong Kong have resulted in a shrinking agricultural industry. Locally grown vegetables account for only 1.6% of total vegetable consumption, while imported meats make up a greater percentage of meat consumption each year. Imported meat made up 40% of all meat consumption in 1982 but rose to 78% in 2002. At the same time, years of unregulated livestock manure disposal into waterways have created pollution problems in several rivers. For example, the River Ganges, located in an area with a high concentration of farms, has phosphorus levels of 0.72 mg/L. This far exceeds the recommended limit of 0.05 mg/L established by the United States Environmental Protection Agency in 1986 to control eutrophication. Livestock manure recycling for vegetable farms is explored as an option for supporting the sustainability and growth of the agriculture industry. Using data from literature, the paper estimated the amounts of N, P, and K produced and demanded from clusters of farms in Hong Kong, as well as possible savings in fertilizer if manure is utilized. *Allium fistulosum* was grown with fertilizer and livestock manure to evaluate the differences in treatment. The control, *Allium fistulosum*, grew better than manure and fertilizer-treated plants. The untreated *Allium fistulosum* reached a height of 13 cm, while manure-treated pots reached 7 cm and fertilizer treated reached 3 cm. However, manure and fertilizer improved soil nutrients. This study concluded that the government-backed field experiments must be conducted to confirm the viability of manure application, followed by technical support, financial incentives, and stricter regulations to encourage manure recycling.

KEYWORDS: Hong Kong; Agriculture; Manure production; Manure recycling; Soil quality; Nutrient demand; Nutrient balance.

■ Introduction

The Hong Kong agricultural industry is facing many challenges, including insufficient workforce and policy support, expensive land, and mountainous terrain.[1] In 2006, agriculture and fisheries workers made up only 0.3% of the working population; by 2016 it diminished to 0.1%.[2] Overall, agriculture, fishing, mining, and quarrying combined only made up 0.06% of the 2019 GDP of Hong Kong.[2] The decline in the agricultural workforce and economic footprint is reflected in local food consumption trends. Between 1982 and 2002, overall beef consumption increased. However, domestically-produced beef consumption decreased from 30.5 thousand tonnes to 12.1 thousand tonnes in 2002 and local production of pigs dropped from 23,200 tonnes in 2007 to 8,443 tonnes in 2016[3] as the city has grown more reliant on chilled and frozen beef.[4] Increases in chilled and frozen meat consumption and decreases in fresh meat consumption were also present in per capita consumption (Figures 1 and 2). The same trend occurred in poultry consumption as avian flu shook the local poultry industry.[5]

Although local vegetable production decreased from 42,500 tonnes in 2000 to 14,200 tonnes in 2016,[3] fertilizer application rates have grown tenfold from 390.8 kg/ha in 2004 to 3,573.9 kg/ha of arable land in 2018.[6] In comparison, the United States applied an average of 128.7 kg/ha of fertilizer in 2018.[6] The decrease in vegetable production and increase in fertilizer consumption suggests that fertilizer is being applied in excess. Over-applying fertilizer for an extended period can damage soil quality by decreasing organic matter, microbial activity, altering acidity, and more.[7] It also pollutes surrounding bodies of water and potentially leads to surface water eutrophication. Depleted soil threatens important ecological services.

One way to support crop production, soil health, and sustainability of the farming industry is by applying livestock manure to the soil.[8] In 2017, 160 tons of livestock waste were produced per day in Hong Kong, of which 43% were disposed of at landfills. The remaining waste was treated through on-site composting, aerobic treatment, or dry muck-out.[9]

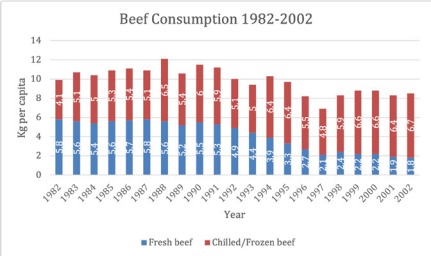

Figure 1: Hong Kong beef consumption per capita,1982-2002.

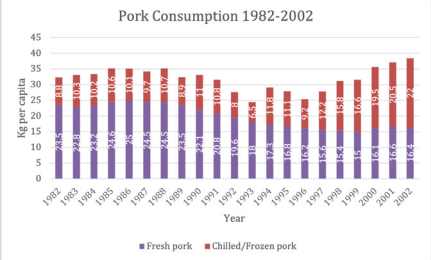

Figure 2: Hong Kong pork consumption per capita,1982-2002.

DOI: 10.36838/v5i1.10

However, livestock waste from farms is a major source of pollution in waterways (see Figure 3). *E. Coli*, phosphorus, and ammonia nitrogen levels[10] can increase with the presence of livestock waste in the water. Other potential issues include soil contamination[11] and overfertilizing the soil.[12] Therefore, manure management is needed to harness livestock manure as a valuable resource while protecting the environment.

This paper serves to analyze the current situation of manure management in Hong Kong and explore potential policies and infrastructure that will support livestock manure application. First, the paper will estimate nutrient balances, crop nutrient demands, recycled nutrients, and fertilizer savings. The paper will then suggest infrastructure schematics to assist farmers in recycling manure and policies to manage manure application. The aim is to develop management methods that cover the multiple steps of manure application in the context of Hong Kong's urban setting while filling the gaps in knowledge of livestock manure management in urban areas.

Government Policy and Programs:

The Agriculture, Fisheries, and Conservation Department (AFCD) is the branch of the Hong Kong government responsible for facilitating food production, conserving natural habitats, and monitoring disease in animals. It is divided into five branches: Agriculture, Fisheries, Country and Marine Parks, Inspection and Quarantine, and Conservation. In 2004, 2005, and 2008, the AFCD launched a Voluntary Surrender Scheme for poultry farms which paid them to surrender their Livestock Keeping License and cease operations.[13] Figure 4 shows the timeline of government policies and programs. These measures were taken to combat avian influenza outbreaks. As local poultry farms decreased in number, consumption of frozen and chilled chicken went from 58% in 2003 to 85% in 2008.[13] In 2006, the government proposed a Voluntary Surrender Scheme for pig farmers. There were 265 pig farms at the time which produced 520 tonnes of manure per day,[14] along with over 130 poultry farms.[15]

The illegal discharge of livestock manure was one of the main causes of polluted rivers and streams.[10] E *Coli* counts and quantities of ammonia nitrogen, nitrate-nitrogen, and phosphorus were highest in Northwestern New Territories (see Figure 3), where most livestock farms are located. Additionally, farmers indiscriminately dumped dead pigs and illegally slaughtered pigs, and there was public concern over disease transmission through pigs. There are two abattoirs for livestock and seven locations where slaughtered animals can be disposed of and destructed.[16] It appears these resources were insufficient and located too far away for farmers. As a result, farmers would rather illegally slaughter and dispose of pigs than transporting them to the proper sites.[16] Pollution, illegal slaughtering and dumping, and outbreaks of Japanese encephalitis were the leading deciding factors behind the Voluntary Surrender Scheme for pig farming. Heightened public concern over zoonotic disease from livestock before 2006 led the Health, Welfare, and Food Bureau (HWFB) and the Environmental Protection Department (EPD) to conclude that sustainably developing pig farming was not a realistic long-term policy option. In addition to voluntary surrender tection of African swine fever in recent years has resulted in the government culling animals. The Hong Kong government culled 6000 pigs in 2019[17] and 3000 pigs in 2021.[18]

In 2014, the HWFB and (AFCD) released the New Agricultural Policy on Sustainable Agricultural Development in Hong Kong. It stated that the agricultural sector was diminishing as the city became more urban. Additionally, public opinion on the agriculture sector had shifted to a more positive stance, and the government reviewed its position on agricultural policy and developed new policies to support the sector's growth. The initiatives outlined included the Sustainable Agricultural Development Fund (SADF) to support the research and adoption of modern farming practices. The proposal added that the government was looking to boost fruit and vegetable farming, not the livestock sector, though the SADF could help upgrade their operations.[19]

By 2021, there were 43 pig farms and 29 poultry farms.[20] Of these, the Hong Kong Environmental Protection Department provided free livestock waste collection to 68 farms.[21] In Hong Kong, the government classifies the collection of livestock waste into three areas:

1. Livestock waste prohibition areas: urban areas where livestock keeping is banned.

2. Livestock waste control areas: farmers must apply for a license from the ACFD and comply with the Waste Disposal Ordinance.

3. Livestock waste restriction areas: livestock keeping is banned unless the land has been used for livestock keeping twelve months before 1994, the keeper holds a license, and follows the Waste Disposal Ordinance.

The Waste Disposal Ordinance provides regulations on livestock waste disposal. Farmers must store livestock waste for collection in secure containers intended for livestock waste only. Solid livestock waste used as fertilizer must be stored securely and composted on the farmer's land and the farmer must take all precautions to prevent spillage. Liquid manure must be disposed of through channels, into a collection vehicle, or a soakaway pit greater than 30 meters away from a drinking water source. Treated liquid manure should be disposed of through channels into a soakaway pit, sewer, saline water, or watercourse. Farmers must also construct a permanent barrier to prevent livestock waste from escaping the grounds.[22]

Targeting Breast CSCs' Markers:

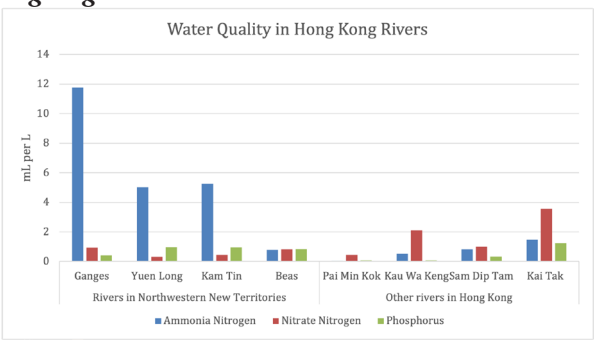

Figure 3: Hong Kong river water quality, 2019.

Failure to follow the Waste Disposal Ordinance or discharging livestock waste into public spaces and drinking water elicits a fine. Prosecutions can only happen when the offender is caught red-handed, thus making it difficult to determine those responsible for pollution.[23]

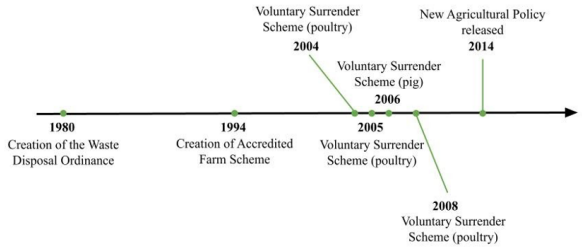

Figure 4: Timeline of government policies and programs. See Appendix A.

Methods

Through government data, we identified the 286 local vegetable farms involved in the Accredited Farm Scheme 1 in addition to 43 pig farms and 29 poultry farms located in the city. In total, these farms have a total rearing capacity of 50,000[24] and 130 million[25] respectively for pigs and poultry. The farms were divided into four zones, or clusters, based on location (Figure 5). Each zone consists of farms close in proximity, allowing for easier transportation of livestock manure to vegetable farms. The area of accredited vegetable farms was 14.80 ha, 25.32 ha, 45.04 ha, and 1.40 ha for zone 1, 2, 3, and 4 respectively, which amounts to 86.56 ha of land.

Next, the NPK input and output flow were identified through the literature. Nutrient balance was estimated by calculating the difference between inputs and outputs. Inputs were both environmental and farm managed, while outputs included the harvested crop and losses to the environment. Manure production per zone was determined with the following equation:[26]

Manure N, P, and K production per zone [kg] = Number of farms per zone * average LSU per farm* average manure NPK per LSU [kg]

Data for the number of farms, average manure NPK per livestock unit, or LSU , and average LSU were found in the literature. The daily manure production per livestock unit was determined based on data in the literature. This helped identify the annual N, P, and K production from animal manure. Manure recovery fractions (RF) were found through literature. RF is the percent of N, P, and K excreted in manure that is recycled. A low percentage indicates poor nutrient management. The RF for N was 22%, and 50% for P and K.[27] The low RF values suggest that there were nutrient losses, possibly during the storing stages through ammonia emissions or because the manure was discharged into a landfill or body of water. Finally, the crop nutrient demand (kg ha-1 year-1) was estimated for each zone. Based on its relevance in terms of production, three major crops in Hong Kong were selected for this analysis: Chinese white cabbage, flowering Chinese cabbage, and Chinese Kale.[28] Fertilizer savings were estimated using fertilizer composition data from Sinofert, China's largest fertilizer supplier. Data for the cost per ton of fertilizer was taken from late 2020 to 2021.

Figure 5: Distribution of livestock (pig farms in pink, poultry farms in yellow)[29] and accredited vegetable farms in Hong Kong,[30] divided into four zones.

Additionally, an experiment was performed to determine the effects of manure on plant growth and soil health (see Appendix B). *Allium fistulusom* was planted in three pots of plain soil, three pots of fertilizer-treated soil, and three pots of cow-manure-treated soil. The plants were watered daily and parameters such as soil type, soil nutrients, and plant growth were recorded. Plants grown without any treatment grew the most, while little growth was seen in manure and fertilizer-treated pots. However, applying fertilizer or manure improved the nutrient content in the soil. The results showed some potential for manure application to crops, though further research is needed to implement the change without impacting crop production.

Results and Discussion

In 2018, the flow of nutrients N, P, and K were found to be 220 kg/ha/year.[31] Data from 2004 was used to calculate the nutrient balance.[32] The results in Tables 1 and 2 indicated a positive N and P balance, but a negative K balance. The surplus of N and P can be attributed to inputs of fertilizer and manure.

Table 1: Nutrient N, P, and K balance.

Nutrient	Input [kg]	Output [kg]	Balance [kg]
N	458,696.55	231,036.80	226,659.75
P	83,198.55	35,517.25	47,681.30
K	189,464.15	204,952.00	-15,487.85

Table 2: Nutrient N, P, and K balance by zone.

Zone	Nutrient Balance N [kg]	Nutrient Balance P [kg]	Nutrient Balance K [kg]
1	39,465.46	8,302.16	-2,696.71
2	67,512.61	14,202.3	-4,613.19
3	120,103	25,265.5	-8,206.74
4	3,733.22	785.34	-255.10

Then, we estimated the following annual manure N, P, and K production per zone as shown in Table 3.[33] The mean N:P: K ratio was 1.2: 1.0: 0.7. Thus, phosphorus levels were high and potash contents were low.

DOI: 10.36838/v5i1.10

[1] The Accredited Farm Scheme is a program that has run since 1994. It aims to improve farm management and production by promoting sustainable agricultural practices, production process standards, and pre-sales testing.
[2] A livestock unit, or LSU, is defined as one adult dairy cow producing 3,000 kg of milk per year (Glossary, n.d.)

Table 3: Nutrient N, P, and K manure production by zone.

Zone	N [kg/year]	P [kg/year]	K2O [kg/year]	Total manure [kg/year]
1	176,797.76	146,103.73	100,582.1	20,116,417.8
2	1,063,591.71	836,105.31	555,663.17	111,132,633
3	176,797.76	146,103.73	100,582.09	20,116,417.8
4	16,495.84	14,827.61	10,591.15	2,118,230.05

We found the total NPK nutrient crop demands as shown in Table 4. They were determined by crop type, crop nutrient needs, and the area of each zone. As Zone 4 had the smallest area of farmland, the nutrient demands were the lowest.

Table 4: Nutrient N, P, and K crop demands by zone.

Zone	N [kg/year]	P [kg/year]	K [kg/year]
1	203,520.35	57,531.3	378,950.3
2	347,222.22	98,153.06	646,519.94
3	619,361.93	175,081.74	1,153,237.95
4	192,51.93	5,442.5	35,846.65

The total fertilizer application rate in 2018 in Hong Kong was 3,573.9 kg/ha.[6] Assuming an application rate of 90-296 kg/ha N, 75-180 kg/ha P, and 90-270 kg/ha K based on farmer's traditional practice and application rates determined from yield response, soil testing, and agronomic efficiency,[34] the following amounts of fertilizer N, P, and K are applied per zone (Tables 5 and 6).

Table 5: Minimum fertilizer application rate by zone and nutrient.

Zone	Fertilizer N applied [kg/year]	Fertilizer P applied [kg/year]	Fertilizer K applied [kg/year]
1	1,332	1,110	1,332
2	2,278.62	1,898.85	2,278.62
3	4,053.6	3,378	4,053.6
4	126	105	126

Table 6: Maximum fertilizer application rate by zone and nutrient.

Zone	Fertilizer N applied [kg/year]	Fertilizer P applied [kg/year]	Fertilizer K applied [kg/year]
1	4,380.8	2,664	3,996
2	7,494.13	4,557.24	6,835.86
3	13,331.84	8,107.2	12,160.8
4	414.4	252	378

As is shown in Tables 1 through 6, even with low recovery fractions, livestock manure could potentially account for 100% of fertilizer N, P, and K applied. By replacing fertilizer with manure, between 1,075.05 - 12,193.39 USD could be saved in urea fertilizer[35], 7,328 - 21,984 USD could be saved in diammonium phosphate[36] and 4,950.11 - 18,409.46 USD in potash fertilizer.[37] The overall fertilizer savings over twenty years are shown in Figure 6.

Discussion

Even with low recovery fractions of 22% for nitrogen and 50% for phosphorus and potassium, there is sufficient manure produced to replace the number of nutrients currently supplied by fertilizer. However, differences in nutrient demand and balances mean that manure application alone may not be adequate. The nutrient balance showed a major deficit in potassium and surpluses in nitrogen and phosphorus. Potassium has the greatest nutrient demand and deficit, yet more nitrogen is applied in fertilizer than potassium. With a manure replacement, more phosphorus and nitrogen would be produced than potassium. To avoid a deficiency in nutrients would require overapplying nitrogen and phosphorus to fulfill potassium needs. Therefore, manure should be applied until phosphorus requirements are met since those are the lowest. The remaining nitrogen and potassium needs can be supplemented with organic nitrogen and potassium fertilizer. A different approach would be to fertilize areas of high nitrogen and potassium demand with nitrogen and potassium-rich pig and cattle manure. Phosphorus and some nitrogen fertilization needs would be met with phosphorus and nitrogen-rich manure fractions. If manure replaces all phosphorus fertilizer, that would reduce 11% of all fertilizer imports.

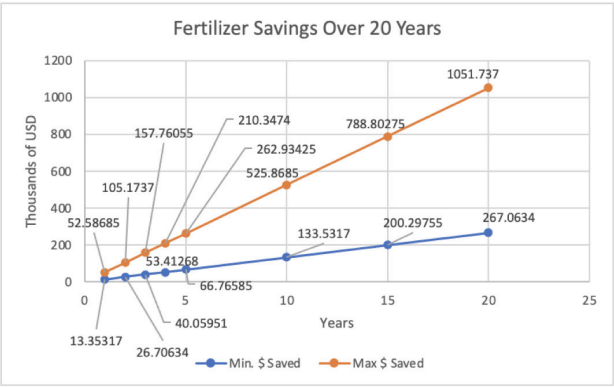

Figure 6: Maximum and minimum fertilizer savings in Hong Kong over twenty years.

There are multiple benefits to increased manure recycling in Hong Kong. Soil pH, electrical conductivity, and nutrients can all increase with higher manure application rates.[8] Livestock manure application increased the nutrient content in *B. Chinensis* and *Z. Mays L.* Pollution from importing and manufacturing chemical fertilizers as well as water pollution could be decreased. Multiple considerations need to be taken to account before applying livestock manure.[38] Emissions and nutrient loss need to be minimized during storage and transportation. Contaminants can be present in livestock manure, making the application of manure to crops hazardous for the environment

and human health. For example, Hong Kong experienced zoonotic diseases such as avian influenza and Japanese encephalitis which can be spread through manure. Transporting manure between farms increases the risks of disease exposure, however, it is necessary given that farms have become more specialized, as they either have crops or livestock. The creation of zones in Hong Kong can minimize the spread of pathogens by keeping the livestock manure within a closer range.

Experiment on Allium Fistulosum:

The results of the experiment both supported and disagreed with other findings in the literature. A study in Hong Kong found that manure application increased pH, potassium, and dry weight of *B. Chinensis* and *Z. mays L.*[8] However, growth in manure-treated pots was not better than in control pots as manure-treated plants withered and turned white after three weeks. It is possible that the soil was already rich in nutrients, or that manure application increased salt content to a detrimental level. Another study saw increases in nutrients P and K and taller chili peppers with manure application.[39] Levels of nutrient P and K did increase in this paper's experiment, but the tallest manure-treated onion remained 0.5 cm shorter than the smallest control and 5.5 cm shorter than the tallest control.

We believe one significant reason for the lack of growth in manure and fertilizer-treated pots is the lack of technical support in irrigation. The pots were watered twice a day for a total of 115 mL of water. Along with several days of heavy rain on the pots and a humid climate, the pots appeared to be overwatered and lacked a strong drainage system, resulting in algae growth on the soil in manure and fertilizer-treated pots. In addition, there was not enough soil in the pots to buffer the fertilizer and manure. This demonstrates the importance of involving farmers in field experiments with technical support before implementing major policy changes. The 286 farms involved in the Accredited Farm Scheme should receive guidance from the Accredited Farm Scheme program and support from the Sustainable Agriculture Development Fund in manure storage and application. While plant growth was negatively affected by manure application, applying manure did increase the nutrients in the soil, though there was some imbalance as there was a surplus of potassium and phosphorus but not enough nitrogen. To meet all three NPK nutrient requirements with just livestock manure would result in excess potassium and phosphorus. One option to solve this would be applying enough manure to fulfill potassium and phosphorus nutrient demands and supplement the nitrogen requirement with organic nitrogen fertilizer.

Limitations of the paper:

There was not much data available on the farming industry in Hong Kong. As a result, much of the data used to make estimations came from studies run nearby in China. Additionally, this paper does not fully represent every farm and source of animal manure in Hong Kong. There were over 1,200 racing horses in 201940, creating up to 8,443.618 kg of manure per year.[41] However, manure from racehorses should be tested first, as steroids can be present in the manure. The vegetable farms represented in this paper are the ones that are a part of the Accredited Farm Scheme. There are 347 ha, 128 ha, 7 ha, and 273 ha of land used for vegetables, flowers, field crops, and orchards respectively.[42] They may not receive the same support needed to make farm-wide changes or explore new farming practices like those in the Accredited Farm Scheme. However, there is enough manure to replace the fertilizer needed for all vegetable crops. This would save up to 411,365.32 USD in fertilizers per year. In five years, 2,056,826.61 USD could be saved in fertilizer costs.

Conclusion

Nutrient imbalances on farms and in manure production mean that nitrogen and phosphorus fertilizer is still needed, but most nutrient requirements can be fulfilled through manure application. Soil testing can help determine the exact amount of manure and fertilizer that needs to be applied, to avoid nutrient leaching and the environmental impact that comes from it. The experiment with *Allium fistulosum* did not yield results that support the case for manure application. However, this may be a matter of a poor irrigation system and low technical support, which shows that additional field experiments and guidance for farmers in the future are crucial. The benefits of livestock manure application to crops are multifaceted but come with environmental and health risks. Nevertheless, these risks can be mitigated through strong manure management. There remain more options in livestock manure recycling that can be further explored.

To move closer to a livestock manure recycling system in Hong Kong, there first needs to be more field experiments with soil testing done to test different manure application strategies and confirm their viability. These include effects on food production, the more accurate amount of manure needed across a variety of crops, differences between technology used to spread the manure, etc. Second, technical support should be given to farmers to help them adjust practices. To promote manure recycling, fines for the illegal discharge of manure should increase. Monetary incentives for recycling should be created as manure is a valuable resource. Hong Kong currently has regulations for livestock manure handling, these could be revised to further reduce nutrient loss and emissions. Additionally, the government should implement stronger policing in areas where rates of illegal livestock manure discharge into water are known to be higher. They could also market livestock manure to vegetable farmers as a sustainable, more economical option compared to chemical fertilizer. Finally, using the data from field experiments, the government can create a nutrient recommendation system that covers different crops, soils, farm types, etc.[43]

Acknowledgments

Thank you for the guidance of Mauricio Hernandez from Duke University in the development of this research paper. I am also gratefull to Professor Oene Oenema from Wageningen University for this thoughtfull feedback.

References

1. Yee, L. Y. Challenges in Hong Kong's Farming Development. 1.
2. Main Tables | 2016 Population By-census https://www.bycensus2016.gov.hk/en/bc-mt.html (accessed 2021 -07 -15).
3. Agriculture Sector in Hong Kong. 2.
4. Hong Kong Monthly Digest of Statistics. November 2003.

DOI: 10.36838/v5i1.10

5. About the Poultry Industry in Hong Kong. 5.
6. Fertilizer consumption (kilograms per hectare of arable land) - Hong Kong SAR, China, United States | Data https://data.worldbank.org/indicator/AG.CON.FERT.ZS?locations=HK-US (accessed 2021 -07 -18).
7. Pahlavi, H. N.; Rafiya, L.; Rashid, S.; Nisar, B.; Kamili, A. N. Chemical Fertilizers and Their Impact on Soil Health. In Microbiota and Biofertilizers, Vol 2: *Ecofriendly Tools for Reclamation of Degraded Soil Environs*; Dar, G. H., Bhat, R. A., Mehmood, M. A., Hakeem, K. R., Eds.; Springer International Publishing: Cham, 2021; pp 1–20. https://doi.org/10.1007/978-3-030-61010-4_1.
8. Wong, J. W. C.; Ma, K. K.; Fang, K. M.; Cheung, C. Utilization of a Manure Compost for Organic Farming in Hong Kong. *Bioresour. Technol.* **1999**, 67 (1), 43–46. https://doi.org/10.1016/S0960-8524(99)00066-8.
9. Monitoring of Solid Waste in Hong Kong. 2019.
10. River Water Quality in Hong Kong 2019. 2019.
11. Muhammad, J.; Khan, S.; Lei, M.; Khan, M. A.; Nawab, J.; Rashid, A.; Ullah, S.; Khisro, S. B. Application of Poultry Manure in Agriculture Fields Leads to Food Plant Contamination with Potentially Toxic Elements and Causes Health Risk. *Environ. Technol. Innov.* **2020**, 19, 100909. https://doi.org/10.1016/j.eti.2020.100909.
12. Dietz, F.; Hoogervorst, N. Towards a Sustainable and Efficient Use of Manure in Agriculture: The Dutch Case. *Environ. Resour. Econ.* **1991**, 1 (3), 313–332. https://doi.org/10.1007/ BF00367923.
13. POULTRY SUPPLY IN HONG KONG. October 22, 2008.
14. Voluntary Surrender of Pig Farming Licences. April 11, 2006.
15. Poultry sellers and farmers urge more licenses to cut prices https://www.scmp.com/news/hong-kong/health-environment/article/2084758/hong-kong-poultry-sellers-and-farmers-urge-more (accessed 2022 -03 -11).
16. Enforcement https://www.epd.gov.hk/epd/misc/ehk99/home/english/ch4/p101.htm (accessed 2021 -08 -29).
17. AFP. Hong Kong to cull 6,000 pigs as first swine fever case found https://hongkongfp.com/2019/05/11/hong-kong-cull-6000-pigs-first-swine-fever-case-found/ (accessed 2021 -08 -29).
18. 3,000 pigs to be culled after African swine fever found at Hong Kong farm https://www.scmp.com/news/hong-kong/health-environment/article/3121210/3000-pigs-hong-kong-farm-be-culled-after-african (accessed 2021 -08 -29).
19. THE NEW AGRICULTURAL POLICY: SUSTAINABLE AGRICULTURAL DEVELOPMENT IN HONG KONG. 2014.
20. Pik Chun Wong. Gathering Information, 2021.
21. SS Wong. Gathering Information, 2021.
22. LCQ17: Control on the operation of livestock farms https://www.info.gov.hk/gia/general/201711/29/P2017112900624.htm (accessed 2021 -08 -04).
23. Waste Disposal (Livestock Waste) Regulations. 2021.
24. Pig farmers threaten to release hogs if slaughterhouse not reopened https://www.scmp.com/news/hong-kong/health-environment/article/3010219/hong-kong-pig-farmers-threaten-release-their-hogs (accessed 2021 -08 -08).
25. Study on the Way Forward of Live Poultry Trade in Hong Kong. **2017**, No. 5, 60.
26. Tadesse Solomon Tulu; Oenema Oene; van Beek Christy; Ocho Fikre Lemessa. Manure Recycling from Urban Livestock Farms for Closing the Urban-Rural Nutrient Loops. *Nutr. Cycl. Agroecosystems* **2021**, 119 (1), 51–67. https://doi.org/10.1007/s10705-020-10103-8.
27. Bai, Z.; Ma, L.; Jin, S.; Ma, W.; Velthof, G. L.; Oenema, O.; Liu, L.; Chadwick, D.; Zhang, F. Nitrogen, Phosphorus, and Potassium Flows through the Manure Management Chain in China. *Environ. Sci. Technol.* **2016**, 50 (24), 13409–13418. https://doi.org/10.1021/acs.est.6b03348.
28. Agriculture and Fisheries. May 2020.
29. Livestock farms map | Environmental Protection Department https://www.epd.gov.hk/epd/english/laws_regulations/enforcement/lw_map.html (accessed 2021 -08 -14).
30. Distribution of Local Accredited Farms. April 2021.
31. Bellarby, J.; Surridge, B. W. J.; Haygarth, P. M.; Liu, K.; Siciliano, G.; Smith, L.; Rahn, C.; Meng, F. The Stocks and Flows of Nitrogen, Phosphorus and Potassium across a 30-Year Time Series for Agriculture in Huantai County, China. *Sci. Total Environ.* **2018**, 619–620,606–620.https://doi.org/10.1016/j.scitotenv.2017.10.335.
32. Improving plant nutrient management for better farmer livelihoods,food security, and environmental sustainability http://www.fao.org/3/ag120e/AG120E21.htm (accessed 2021 -08 -08).
33. NPK Nutritional Values of Animal Manures & Compost Etc. Allotment & Gardens.
34. A Sustainable Way of Fertilizer Recommendation Based on Yield Response and Agronomic Efficiency for Chinese Cabbage. August 12, 2019.
35. Chinese regulators move to rein in surging urea prices after probe - Global Times https://www.globaltimes.cn/page/202106/1227241.shtml (accessed 2021 -08 -22).
36. Diammonium phosphate (DAP) price in China expected to rise during winter-China market news http://www.cnchemicals.com/Press/91369-Diammonium%20phosphate%20(DAP)%20price%20in%20China%20expected%20to%20rise%20during%20winter.html (accessed 2021 -08 -24).
37. Fertilizer companies suspected of price gouging put on file for investigation - Global Times https://www.globaltimes.cn/page/202108/1230614.shtml (accessed 2021 -08 -24).
38. Petersen, S. O.; Sommer, S. G.; Béline, F.; Burton, C.; Dach, J.; Dourmad, J. Y.; Leip, A.; Misselbrook, T.; Nicholson, F.; Poulsen, H. D.; Provolo, G.; Sørensen, P.; Vinnerås, B.; Weiske, A.; Bernal, M.-P.; Böhm, R.; Juhász, C.; Mihelic, R. Recycling of Livestock Manure in a Whole-Farm Perspective. *Recycle. Livest. Manure Whole-Farm Perspect.* **2007**, 112 (3), 180–191. https://doi.org/10.1016/j.livsci.2007.09.001.
39. Khaitov, B.; Yun, H. J.; Lee, Y.; Ruziev, F.; Le, T. H.; Umurzokov, M.; Bo Bo, A.; Cho, K. M.; Park, K. W. Impact of Organic Manure on Growth, Nutrient Content and Yield of Chilli Pepper under Various Temperature Environments. *Int. J. Environ. Res. Public. Health* **2019**, 16 (17), 3031. https://doi.org/10.3390/ijerph16173031.
40. Hong Kong needs more trainers, horses to stop betting decline: Engelbrecht-Bresges https://www.scmp.com/sport/racing/article/3018486/hong-kong-needs-more-trainers-horses-stop-betting-decline-winfried (accessed 2021 -08 -08).
41. Horse Stable Manure Management https://extension.psu.edu/horse-stable-manure-management (accessed 2021 -08 -08).
42. Agriculture in HK https://www.afcd.gov.hk/english/agriculture/agr_hk/agr_hk.html (accessed 2021 -08 -28).
43. Strategies to Reduce Nutrient Pollution from Manure Management in China. Front. Agric. Sci. Eng. 2020, 7 (1), 45–55. https://doi org/10.15302/J-FASE-2019293. 44.Soil Texture Triangle.

Author

Lauren Hsu is a student at Choate Rosemary Hall but is originally from Hong Kong. She is interested in the environmental sciences and hopes to further her knowledge in agriculture.

Appendix A

Date	Name of government program	Description of government program
1980	Waste Disposal Ordinance	"To provide for the control and regulation of the production, storage, collection and disposal including the treatment, reprocessing and recycling of waste of any class or description, the licensing and registration of places and persons connected with any such activity, the protection and safety of the public about any such activity and to provide for matters incidental thereto."
1994	Accredited Farm Scheme	The Accredited Farm Scheme's objective is to promote "good horticultural practice and environmentally-friendly production" as well as "providing a stable supply of high quality and safe vegetables."
2004, 2005, 2006, 2008	Voluntary Surrender Scheme	The Voluntary Surrender Schemes were an effort to reduce pig and poultry farming in Hong Kong. They were a result of outbreaks of zoonotic diseases such as avian flu and African swine fever.
2014	New Agricultural Policy	The New Agricultural Policy was a review of Hong Kong's agricultural policy. The goal was to modernize the industry and maximize societal benefits from farming in Hong Kong.

Appendix B

Allium fistulosum, commonly known as bunching onions, was grown in pots with a diameter of 5.5 inches and 5.5 inches in depth. The pots were filled with 200g of soil and treated as follows:

1. 10g of Fertiplus COW 2-2-2 (cow manure pellets)
2. 10g Manutec 9:2:4 vegetable fertilizer
3. Control

There were three replicas of each treatment, making for nine pots total. The different treatments were mixed into the soil before planting the seeds. Five seeds were planted in each pot. Each pot was watered twice a day using the Claber Oasis Automatic Drip Watering System, for a total of 115 mL of water per day. The soil texture was identified as clay loam using a sedimentation test. The percentage of clay, sand, and loam was determined using the soil textural triangle.[44] See Table 7 for soil characteristics. Soil pH, moisture, and sunlight were measured using a soil detector. An outdoor temperature sensor was used to measure ambient temperature and relative humidity. Plant height was recorded daily. Additionally, the first cotyledon and the percentage of seeds that germinated for each pot were noted. Nitrogen, phosphorus, potassium, and pH were measured using a Luster Leaf 1601 Rapitest soil test kit. The test kit graded nutrient levels on a scale of 0 to 4, with 0 being depleted, 1 being deficient, 2 being adequate, 3 is sufficient, and 4 being a surplus.

Table 7: Soil characteristics. pH, N, P, and K levels were tested with the Luster Leaf 1601 Rapitest soil test kit.

Parameter	Value
pH	7.5
Texture	Silty clay loam
Nitrogen	Deficient
Phosphorous	Deficient
Potassium	Sufficient
Sand	40%
Clay	0%
Silt	60%

Growth of Allium fistulosum and soil quality:

The control pots had an overall germination percentage of 80%, while the fertilizer-treated pots were at 13% and manure at 40%. In all three control pots, the first cotyledon occurred six days after planting. The first cotyledon happened six days after planting for two of the manure-treated pots, and eight days for the third. For fertilizer-treated pots, the first cotyledon occurred six days after planting for one pot and seven days for the second one. The third pot never germinated. Additionally, the onions in one of the manure pots and one of the fertilizer pots withered and turned white after three weeks. Figures 7, 8, and 9 show the growth of the plants over three weeks after planting. The nutrients in fertilizer and manure-treated pots increased (Table 8). According to the results reported by the soil analyzer, manure-treated pots were nitrogen deficient but had enough potassium and phosphorus. Fertilizer-treated pots had a surplus of nitrogen, and enough phosphorus and potassium.

Table 8: Soil nutrient content (C controls, F is fertilizer, M is manure). N, P, and K graded on a 0-4 scale with 0 being depleted and 4 being a surplus.

	C #1	C #2	C #3	F #1	F #2	F #3	M #1	M #2	M #3
N	1	1	1	4	4	4	1	0	1
P	1	3	3	4	2	3	4	3	4
K	2	3	3	3	3	3	4	4	3
pH	6.00	6.00	6.00	5.00	6.5	6.00	6.5	6.5	6.0

Figure 7: Control pot 26 days after planting.

Figure 8: Fertilizer pot 26 days after planting.

Figure 9: Manure-treated pot 26 days after planting.

DOI: 10.36838/v5i1.10

IJHSR
ijhighschoolresearch.org
REVIEW ARTICLE

Multi-functional, Bioresorbable Stent Technology for Real-time Diagnosis

Jason Kim, Sunny Kim

Saint Paul Preparatory, 06593, Seoul, Korea; gosyber1@gmail.com

ABSTRACT: Heart failure is one of the most significant public health concerns, with a mortality rate greater than most cancers. Due to this, cardiovascular disease has attracted intensive attention in the fields of medicine and engineering. Atherosclerosis is the underlying pathology responsible for these deaths. As people get older, it becomes a more common disease. High blood pressure and genetic factors are mainly related to this, which could be exacerbated by obesity and diabetes from an unhealthy lifestyle. For clinical improvement in the future, we could respond immediately to medical issues to prevent the recurrence of the disease. In this review, we investigate the current bioresorbable stent technology and the future of micro-fluidic sensing/wireless devices to overcome issues in current diagnosis. With advances in nanofabrication, new bioresorbable sensing/wireless components could be integrated into the stent without failure under expansion. The future shape of a bioresorbable electronic stent in the context of the emerging "Internet of Things" and how this will significantly influence future diagnosis technology for future generations are also discussed.

KEYWORDS: Multi-functional; Bioresorbable; Electronic Stent; Cardiovascular disease diagnosis; Wireless.

Introduction

The blood flow in an artery can be reduced or even reversed by a buildup of plaque inside the coronary arteries, which prevents heart muscles from receiving sufficient blood supply. If the blood supply to the arms and legs is cut off, severe agony and tissue death may result. A damaged cardiac muscle may be unable to pump effectively, resulting in heart failure. A stent is a device that helps to widen a section of an artery to enhance blood flow; they are crucial pieces of technology used to improve blood flow and revitalize the heart. Among many cardiac diseases, the most common cardiovascular disease is coronary artery disease. It commonly occurs with atherosclerosis. Atherosclerosis is a type of thickening or hardening of the arteries caused by the accumulation of plaque inside the wall of the coronary arteries. Cholesterol, fatty compounds, waste materials, calcium, and the clot-inducing substance fibrin make up plaques. Over time, plaques continue to collect and form in your arteries, causing them to narrow and harden. This makes vessels lose elasticity and limits blood flow to the heart muscle. Most hospitals use implantable medical devices (IMD) called stents to treat atherosclerosis.

Stents are tubular, implantable vascular scaffold devices that have a circular cross-section (Figure 1). They retain their shape when deployed in a vessel but are also designed to be elastic. Stents are used to reopen blocked vessels in various deployment locations from the biliary duct to the coronary arteries. The doctor uses the percutaneous coronary intervention to insert the stent into the target artery. PCI is a process that involves the usage of a stent to treat cardiovascular disease.[1] This technique involves a four-step process, which uses balloon angioplasty to open up clogged arteries. First, a series of catheters and guiding wires are inserted through the patient's skin. To be precise, they are most commonly inserted from the wrist's brachial artery. Next, the catheter is carried up the arterial vasculature to the location of occlusive disease inside the heart's coronary arteries. Then, a balloon inside the stent is inflated; subsequently, the stent expands with the balloon and is deployed through the catheters. The plaque material, which consists of fat deposits and cellular components like smooth muscle cells or inflammatory cells, is pushed back by the expansion of the balloon. Finally, the balloon is deflated, but the stent keeps its expanded shape to prevent plaque from recoiling. As a result, the proper flow of lumen in the location is restored.

Patients treated with PCI have shown improved coronary heart disease symptoms and enjoyed the procedure's benefits: reduced costs, less invasive than coronary artery bypass graft (CABG) surgery, and faster in-hospital recovery. However, one obstacle to this procedure was in-stent restenosis (ISR), a process where the overgrowth of scar tissue cells occurs nearby or inside the stents, obstructing the flow of blood again. 17%-41% of first-generation stents developed ISR. Second-generation stents were coated with drugs that prevent cell proliferation from addressing this issue. A drug-eluting stent (DES) slowly releases a drug from the stent to block cell proliferation.[2]

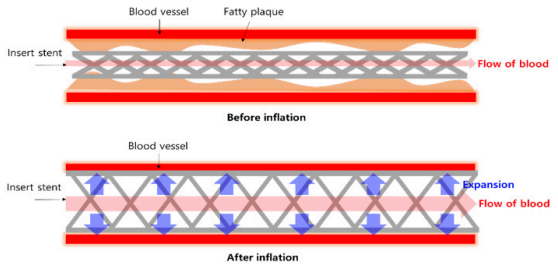

Figure 1: Schematic showing stent in an artery.

DOI: 10.36838/v5i1.11

Discussion

Why is a multi-functional bioresorbable stent required?:

With the advancement of micro and nanofabrication techniques and wireless technology, bio-implantable technology for medical diagnosis has been improved.[3] Specifically, developing miniaturized microelectronics devices to continuously monitor the internal phenomena in real-time *in vivo*, such as blood flow velocity and pressure for cardiovascular implants,[4] and real-time measurement of pressure for intraocular and brain implants enhance the quality of diagnosis. Stents, which are typically tubular, with a circular cross-section, implantable vascular devices also have been developed with this multi-functional system to improve its functionality. When it is deployed in the vessel, restenosis occurs when an artery that was opened with a stent or angioplasty becomes narrowed vessel again. Currently, early diagnosis of restenosis is almost impossible to detect, and it is shown with significant chest pain or a second cardiac event in the worst case. Luckily, patients who find their restenosis still rely on lifelong medication. We should make medical treatments to predict possible issues in advance to prevent the worst cases. Remote detection of medical problems would significantly impact patient welfare and costs and decrease the risk of adverse events occurring outside the hospital environment unexpectedly. A promising solution is a stent with integrated sensors/wireless systems that can detect the growth or accumulation of cells (endothelial cells) and measure changes in flow and pressure across the local site of the blood vessel. A vital technology to achieve this integrated system within a limited space is micro/nanofabrication technology. As such, stents integrated with sensors/wireless systems will offer an advanced solution to unexpected restenosis detection (Figure 2).[5]

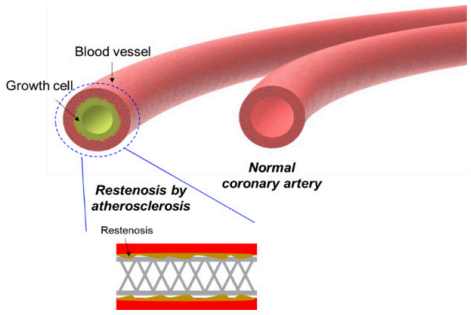

Figure 2: Schematic illustration of Restenosis.

Transient materials for stent application:

Using bioresorbable materials for stents in interventional cardiology is a novel approach to treating coronary artery disease.[6] The transient technology was introduced to the stent to overcome the limitations of current metallic stents, including late in-stent restenosis and permanent location in the vessel. The purpose of a bioresorbable stent is to provide mechanical support to the vessel for a long time before degradation and absorption in the body, enabling vessel healing and restoration of vasomotion. To develop practical bioresorbable stents, there have been many issues regarding the stability of materials in the fluidic environment of the body. In this section of the review, we investigate the current technologies of a bioresorbable stent, including the chemical and mechanical aspects of available materials and many approaches to improve it.

Transient metallic materials for stent application:

Many researchers have developed bioresorbable metallic materials to tune the mechanical, electrical, and degradation properties for bioelectronic applications. Mg (Magnesium), Mg-alloy, Mo, Zn (Zinc), and their oxide form have been considered promising metallic materials for bioresorbable electronics due to their biocompatibility.[7] Among them, the Mg-alloy metallic materials have been used commonly for bioresorbable stent applications.

Due to its mechanical properties and low degradation rate, pure magnesium is not suitable as a structural material for stents. For example, pure magnesium has a high modulus (41-45 GPa) and a low elasticity, so using it to make stents would cause it to be prone to damage under stress. As a result, magnesium alloys are appealing due to their excellent mechanical properties in terms of radial stiffness, biocompatibility, low cost, and low density. As the elastic modulus is proportional to radial stiffness, stents manufactured of magnesium-based materials have 50–240% thinner struts than cobalt-chromium and polymer stents, respectively, to maintain the required level of performance. Pure Mg, aluminum-containing alloys (AZ91, AZ31, LAE422, AM60, etc.), rare-earth elements containing alloys (AE21, WE43, etc.), and aluminum-free alloys (WE43, MgCa, MgZn) are the four main classes of Mg-based bioresorbable materials. These alloying elements optimize grain size, enhance corrosion resistance, and provide intermetallic states. The addition of rare-earth metals enhances castability and pressure resistance but exhibits low strength at room temperature.[8]

For effective functionality, stent materials need appropriate mechanical features in expandability, plasticity, rigidity, and resistance to the elastic recoil of blood arteries, depending on the type of stent (balloon-expandable or self-expandable). In addition, the stent should also remain mechanically stable after at least 4-6 months after implantation. The mechanical properties of magnesium alloys are refined through their processing history of hot rolling, hot extrusion, and equal-channel angular pressing. This increases the strength of magnesium alloys while sometimes decreasing their ductility in some cases. Additionally, alloying has the potential to enhance the mechanical properties of Mg-based bioresorbable, including ductility and strength.

The degradation of metallic bioresorbable stents occurs through the corrosion of metals; an electrochemical reaction caused that produces oxides, hydroxides, hydrogen gas, and possibly other compounds (chemical equation 1).

$Mg + 2H2O \rightarrow Mg(OH)2 + H2$ (chemical eq. 1)

High-purity magnesium exhibits the lowest corrosion when exposed to air at room temperature. Pure magnesium has limitations as it corrodes quickly in a physiological environment (pH 7.4-7.6), generating hydrogen gas at rates unmanageable by the host tissue. In addition, corrosion speed is high in chloride-containing liquids or acid solutions. NaCl and minor amounts of other inorganic molecules, including $Ca2+$ and HCO_3- are present in the human body. The

DOI: 10.36838/v5i1.11

presence of chloride ions accelerates corrosion, whereas phosphates and carbonates may foster the formation of corrosion product layers that protect or partially protect Mg from corrosion. Currently, the two most popular methods for enhancing Mg alloy biodegradation resistance are alloying and surface treatment or coatings.[9]

Synthetic polymeric materials for stent application:

The degradation of synthetic biodegradable polymeric materials in our body occurs mainly through two mechanisms: hydrolysis and oxidation. Polymers, including polyesters, polycaprolactone (PCL) polycarbonates, polyvinyl alcohol (PVA), and polylactic acid (PLA), degrade mainly via hydrolysis.[10] In hydrolysis-based degradation, water causes the cleavage of ester bonds in the polymer chain, separating polymers into a few oligomers or monomers that can be clearly absorbed in the bodily fluid. For example, the products from the degradation of PLA and PCL are small molecules, including lactic acid and 6-hydroxyhexanoic acid. These small molecules could be eventually eliminated from the body to the outside, like carbon dioxide and water. Unlike natural biodegradable polymers, synthetic polymers with a specific degradation rate can be produced, allowing us to control the degradation time in the artery. The degradation rate of biodegradable polymers can be tuned by many strategies, including change of composition, molecular weight, the crystallinity of polymers, blending, copolymerization, and surface modification (Figure 3).[11] Typically, blending and copolymerization are used to increase the degradation rate of a slowly degrading polymer. To reduce the degradation rate, increasing the crystallinity and molecular weight of the polymer can be the solution. The polymeric stent's mechanical softness and low modulus are considered critical advantages. Generally, polymeric materials consist of cross-linked polymeric chains which have freedom of movement in the matrix, enabling the relaxation of external stress. So a stent fabricated by polymeric material is mechanically robust under radial stress induced by expansion in an artery. In the future, we need to fulfill the requirements in biomedical engineering, including biodegradation rate, mechanical robustness, and biocompatibility.

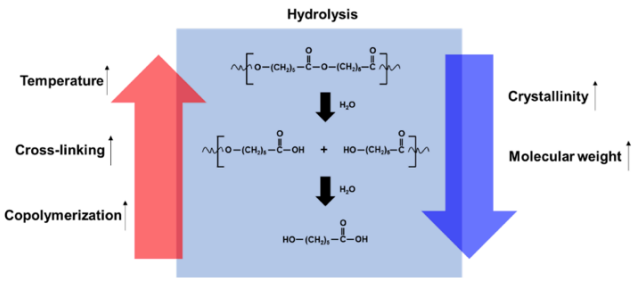

Figure 3: Strategies for tuning biodegradable polymers.

What kinds of components could be integrated with the transient property?:

Implantable electronic devices allow physicians to extract meaningful data in real-time and activate corresponding tissue functions by electrical stimuli to interface with the human body. Unlike most conventional bio-implantable electronic devices that remain functional and intact in the body for an infinite time frame, biodegradable electronic devices feature a stable operation in a defined time before complete degradation within the body. The concept of the transient device has strong advantages for immediately controlling diagnostic or therapeutic functions, enabling the monitoring of short-term biological responses, such as for wound healing and infections, while avoiding adverse effects associated with long-term implantation of bio-implantable devices. Moreover, secondary surgical procedures are needed for device removal without this property. We need an advanced version of bio-implantable sensor/wireless electronic components to make such a system. There have been many signs of progress in bioresorbable electronic devices, which could be integrated with a stent for biomedical applications, including implantable pH and a pressure sensor for detecting a rheological property of blood flow in a vessel, impedance sensor to detect the cell growth near endothelium, wireless antenna for data and power transmission,[12] and memory to memorize data. Of those parts, the doctor might miss.[13] As we could find in previous reports, bioresorbable electronic components should be fabricated in a flexible thin film to be integrated into the stent. For example, researchers report materials, device architectures, integration strategies, and *in vivo* demonstrations in rats of implantable, multifunctional silicon sensors for the brain.

All of the constituent materials naturally resorb via hydrolysis and/or metabolic action eliminating the need for extraction.[14] All sensors are fabricated in the shape of thin film and can detect flow rate, temperature, and pH of the internal body, which are also vital components in bioresorbable electronics stents. Another research group showed the multi-functional stent integrated with an antenna for power/data transmission, flow/temperature sensors, memory storage devices, anti-inflammatory nanoparticles, and drug-loaded core/shell nanospheres activated by an external optical stimulus. The entire operation mode of the stent is as follows: the flow sensor measures blood flow, which is stored in the embedded memory module for pattern analysis and diagnosis. Catalytic reactive oxygen species scavenging and hyperthermia-based drug release can be used as advanced therapies.

Real-time monitoring stent:

As previously mentioned, the smart stent has been developed to minimize the surgical process. In conventional stent technology without multi-functions, detecting other diseases was challenging because the doctor must check the status of inserted stents via medical instruments, including Computed Tomography (CT), Magnetic Resonance Angiography (MRI), which could provide discontinuous data by capturing the image. For this reason, it is impossible to respond immediately in an emergency. For example, despite using stents to improve blood flow, the physiological process can produce restenosis, a phenomenon that causes tissue growth, again closing the vessels. In-stent restenosis obstructs blood flow inside the artery and will result in variations in local blood pressure, hemodynamics, and blood flow characteristics. The early signs of the in-stent restenosis can be detected with pressure/flow sensors and wireless platforms by properly monitoring these parameters (Figure 4).

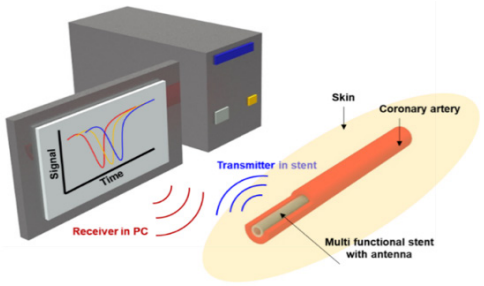

Figure 4: Real-time, wireless monitoring stent.

Conclusion

In this review, we consider the promising technologies for the stent. First, we introduce the necessity of a multi-functional bioresorbable stent fabricated from a biocompatible and bioresorbable material. To investigate the candidates, we divided the bioresorbable materials into two categories: i) metallic and ii) polymeric materials. Metal is an essential component in a stent for supporting the shape of the stent and providing electrical functions. Most of the sensors integrated on bioresorbable stents have been fabricated with bioresorbable metals such as Mg, Zn, and Mo. Bioresorbable polymer is also the main component for the stent to provide mechanical flexibility to all components on the stent.

Moreover, in contrast with metal, it could be used as an encapsulation layer for preventing current leakage from the wireless/sensor components, resulting in malfunction. The lifetime of a bioresorbable stent dominantly depends on the bioresorbable polymeric materials. We review the available kinds of sensor/wireless devices which could be integrated into the stent and their valuable functions. Such devices have great potential for real-time and continuous monitoring of parameters such as the stress of endothelium and blood flow. In addition, the monitoring done with smart stents may help prevent some clinical complications of conventional stents, which include stent thrombosis (a life-threatening event where the artery is completely blocked due to the formation of a blood clot in the stent) and in-stent restenosis (a slow re-narrowing of the segment with the stent).

Acknowledgments

I want to thank Sunny Kim for his guidance and encouragement during the process of this review and J.W. Lee for edits of writing throughout the writing.

References

1. H. Daniel, B. Anubhav, N. Steven, M. Nosrat, and M. John (2019) The Future of Cardiovascular Stents: Bioresorbable and Integrated Biosensor Technology, Advanced Science, 6, 1900856
2. A. Fernando, B. A. Robert, R. Fernando, K. Adnan (2014) Current Treatment of In-Stent Restenosis, Journal of the American College of Cardiology, 63, 2659
3. V. Jithin, M. Geetha (2020) Perspectives on smart stents with sensors: From conventional permanent to novel bioabsorbable smart stent technologies, Medical devices and Sensors, 3, e10116.
4. J.H. Koo, J.-K. Song, D.-H. Kim, D. Son (2021) Soft Implantable Bioelectronics, ACS Materials Letters, 3, 1528–1540.
5. C. Eric Y., L. C. Arthur, C. Sudipto, C. William J, I. Pedro P. (2010) Fully Wireless Implantable Cardiovascular Pressure Monitor Integrated with a Medical Stent, IEEE Transactions on Biomedical Engineering, 57, 6
6. W. B. Han, J. H. Lee, J.-W. Shin, and S.-W. Hwang (2020) Advanced Materials and Systems for Biodegradable, Transient Electronics, Advanced Materials, 32, 2002211..
7. G. D. Cha, D. Kang, J. Lee, D.-H. Kim (2019) Bioresorbable Electronic Implants: History, Materials, Fabrication, Devices, and Clinical Applications, Advanced Healthcare Materials, 8, 1801660
8. X. Li, X. Liu, S. Wu, K.W.K. Yeung, Y. Zheng, R. K. Chu (2016) Design of magnesium alloys with controllable degradation for biomedical implants: From bulk to surface, Acta Biomaterialia, 45, 2-30
9. L. Aljihmani, L. Alic, Y. Boudjemline, Z. M. Hijazi, B. Mansoor, E. Serpedin, K. Qaraqe (2019) Magnesium-Based Bioresorbable Stent Materials: Review of Reviews, Journal of Bio- and Tribo-Corrosion, 5, 26
10. C. Li, C. Guo, V. Fitzpatrick, A. Ibrahim, M. J. Zwierstra, P. Hanna, A. Lechtig, A. Nazarian, S. J. Lin, D. L. Kaplan (2020) Design of biodegradable, implantable devices towards clinical translation, Nature Reviews Materials, 5, 61–81
11. P. Xiao, K. Dong, Z. Wu, J. Wang, Z. L. Wang (2021) A review on emerging biodegradable polymers for environmentally benign transient electronic skins, Journal of Materials Science, 56, 16765–16789
12. V. Jithin, G. Manivasagam (2020) Perspectives on smart stents with sensors: From conventional permanent to novel bioabsorbable smart stent technologies, Medical Devices & Sensors, 3, e10116
13. D. Son, J. Lee, D. J. Lee, R. Ghaffari, S. Yun, S. J. Kim, J.E. Lee, H. R. Cho, S. Yoon, S. Yang, S. Lee, S. Qiao, D. Ling, S. Shin, J.- K. Song, J. Kim, T. Kim, H. Lee, J. Kim, M. Soh, N. Lee, C. S. Hwang, S. Nam, N. Lu, T. Hyeon, S.H. Choi, and D.-H. Kim (2015) Bioresorbable Electronic Stent Integrated with Therapeutic Nanoparticles for Endovascular Diseases, ACS Nano, 9, 5937-5946
14. S.-K. Kang, R. K. J. Murphy, S.-W. Hwang, S. M. Lee, D. V. Harburg, N. A. Krueger, J. Shin, P. Gamble, H. Cheng, S. Yu, Z. Liu, J. G. McCall, M. Stephen, H. Ying, J. Kim, G. Park, R. C. Webb, C. H. Lee, S. Chung, D. S. Wie, A. D. Gujar, B. Vemulapalli, A. H. Kim, K.-M. Lee, J. Cheng, Y.Huang, S. H. Lee, P. V. Braun, W. Z. Ray, and J. A. Rogers (2016) Bioresorbable silicon electronic sensors for the brain, Nature, 530, 71–76

Author

Jason Kim is a twelfth-grader attending Saint Paul Preparatory. He is interested in Biomedical engineering, especially in non-invasive diagnosis for patients. Now he also has patents related to non-invasive medical treatment and pursues practical, higher studies in biomedical engineering.

DOI: 10.36838/v5i1.11

IJHSR
ijhighschoolresearch.org
■ RESEARCH ARTICLE

Modeling Socioeconomic, Demographic, and Chronic Medical Conditions Correlated with COVID-19 Incidence

Jenna Chuan

Memorial High School 935 Echo Lane, Houston, Texas 77024, U.S.A.; jenna.ctx4@gmail.com

ABSTRACT: Since its initial discovery in November 2019, COVID-19 has caused a worldwide pandemic with substantial medical, economic, and social repercussions, with over 4.22 million deaths.[1] Although pandemics are inevitable, consequences from them can be minimized. Non-pharmaceutical interventions have been helpful in decreasing COVID-19 transmission, but they are broad and have severe educational and economic consequences. Understanding the factors that affect disease transmission is pivotal for non-pharmaceutical interventions to maximize their effectiveness while minimizing their repercussions. This study examined COVID-19 cases in each U.S. county to create a multiple linear regression model predicting incidence based on socioeconomic, demographic, and chronic disease factors. The model accuracy had a coefficient of determination of 71%, and the most impactful factors were population density, rural/urban status, social vulnerability, and multi-unit housing. Results from this study are necessary to help stakeholders decide how to allocate resources and target interventions to minimize the spread of the virus.

KEYWORDS: Translational Medical Sciences; Disease Prevention; virology; Computational Epidemiology; COVID-19.

■ Introduction

COVID-19, the coronavirus disease caused by the SARS-CoV-2 virus, has caused a widespread pandemic resulting in severe economic, social, and chronic medical consequences. After first being detected in Wuhan, China, in November 2019, it has spread to over 197 million people worldwide.[1] Within the United States, COVID-19 cases first began in January 2020, and by June 2021, there were over 33 million cases and nearly 600 thousand deaths.[2] Nearly 1 in every 10 Americans has received a positive COVID-19 test[3] and the number of Americans that have had COVID-19 is likely 2-3 times that number.[4]

Within the US, there have been striking differences in incidences across geographic areas. According to data collected by the New York Times (NYT) on June 29, 2021, of over 3,000 U.S. state counties, there have been 18 counties in which over 20% of the population has had COVID-19 and ten counties in which less than 2% of the population has had COVID-19.[2] This is a tenfold difference in COVID-19 incidence between these two different groups of counties. A reasonable follow-up question to this interesting find would be, what factors lead to differences in COVID-19 incidences across different areas within the US?

The COVID-19 pandemic has caused significant disruption to daily lives. Consequently, non-pharmaceutical interventions have been a primary means of reducing the spread of the virus. Many sectors have moved to remote workplaces to decrease workspace transmission rates,[5] and consumers have changed their shopping habits from in-person to online platforms.[6] Many schools moved to remote learning or hybrid (combination of both virtual and in-person) plans to minimize classroom crowding.[7] The pandemic has even caused trends of migration away from metropolitan areas. A recent study showed a 3.92% increase in the movement of people across the United States, most moving away from large cities such as New York, Chicago, San Francisco, and Los Angeles.[8] Many of these behavioral changes are based on assumptions and extrapolation from previous knowledge of virus transmission. However, these have adverse effects, such as learning loss for children not in school,[9] and economic consequences for closed businesses.[10] More research is needed so that the impact of these non-pharmaceutical interventions (on reducing the spread of the virus) can be effectively maximized while minimizing the pandemic's economic, educational, and social costs.

Although previous papers have been published regarding demographic, socioeconomic, and spatial factors that correlate with COVID-19 incidence, the great majority of these papers used data from the first six months of the pandemic and thus under-represent the current situation. This paper updates these studies by analyzing 16 months of data to determine which demographic, socioeconomic, and medical factors continue to correlate with COVID-19 incidence strongly. The aspects of focus include demographic characteristics (age, ethnicity), socioeconomic factors (the Social Vulnerability Index, poverty, multi-unit or single-unit homes, rural versus urban populations, population density, average household size), percent of the population staying at home (from pre-pandemic compared to the pandemic time period), and chronic health conditions (obesity and diabetes).

Furthermore, this study combines the factors that have shown a correlation in previous papers into a model that explains the varying incidence of cumulative COVID-19 incidence within U.S. counties. Understanding this model and the components that lead to increased COVID-19 incidence are critical for di-

DOI: 10.36838/v5i1.12

recting policies and decisions for the future of this pandemic. It can also help institutions decide how to allocate resources and target interventions. Post-pandemic, these results are still crucial in planning for future pandemics.

Literature Review:

Previous research has been done on demographic factors that significantly impact COVID-19 incidences, such as age, sex, and ethnicity. Multiple studies have found that underrepresented racial and ethnic groups were two to three times more likely to contract this virus.[11,12] In August 2020, Moore *et al.* examined U.S. counties with sufficient data on COVID-19 infection and race, finding that Hispanic, Black, American Indian, Asian, and Pacific Islander races were two to four times more disproportionately affected by COVID disease.[11] Mahajan and Larkins-Pettigrew also found a positive correlation between counties with increased percentages of African Americans and Asian Americans and increased COVID-19 incidence and mortality rates in May 2020.[12]

Many studies combined demographic and socioeconomic factors in their COVID-19 risk factor analysis. Rozenfeld *et al.* studied over 34,000 patients who took COVID-19 tests in the Providence Health System in April 2020 and found that the COVID-19 positive patients were more likely to be male, of older age, of Asian or Black race, Latino ethnicity, non-English language, or residing in a neighborhood with financial insecurity, low air quality, housing insecurity, transportation insecurity, or in a senior living community.[11] Gunness and Milheiser compared communities in Queens, NY, in April 2020 and found overcrowded communities with lower education levels, less healthcare access, and more chronic disease rates were more severely affected by the COVID-19 outbreak.[13]

Poverty, income disparity, and social vulnerability, therefore, seem to play a vital role in COVID-19 incidence in communities. The Centers for Disease Control and Prevention (CDC) Social Vulnerability Index (SVI) measures a community's ability to prevent human suffering and financial loss in disasters. This index is subdivided into socioeconomic status, household composition and disability, minority status and language, and housing type and transportation in communities and ranges from 0-1 (1 representing an extremely vulnerable community).[14] In May 2020, Karaye and Horney used the SVI in U.S. counties and found that a percentile increase in SVI resulted in a 16% increase in COVID-19 case counts.[15] In July 2020, Karmakar *et al.* also studied SVI and found a 0.1 point increase (or 10% increase on the 0-1 scale) in SVI resulted in a 14.3% increase in the COVID-19 incidence rate.[16] Long-standing inequality in healthcare access for vulnerable communities contributes to increased incidence.

Several studies demonstrated increased COVID-19 transmission in urban settings. Karim and Chen divided all U.S. counties into metropolitan, micropolitan, and rural. They collected data up to June 2020, showing that most COVID-19 cases and deaths were in urban areas.[17] Hamidi *et al.* also noted in May 2020 that metropolitan areas correlated with increased COVID-19 incidence, but population density did not correlate with increased COVID-19 incidence after controlling for urban populations.[18] Similarly, in June 2020, Cromer *et al.* noted that patients who tested positive for COVID-19 were more likely to live in census tracts with higher rates of household crowding, a higher percentage of multifamily homes, and lower rates of high school completion.[19]

Only a few studies focused on movement and COVID-19 incidence. Badr *et al.* examined anonymous mobile phone data before April 2020 and determined that decreased movement resulted in decreased COVID-19 transmission 9-12 days later.[20] Gatalo *et al.* continued this analysis with data into July 2020. Although early data showed a correlation between mobility data and transmission, later time frames showed weaker correlations, which suggested other non-pharmaceutical measures had a more important role as time passed.[21]

As noted, many of these studies were conducted with data from the first six months of the pandemic; however, dynamics may have changed since then because the pandemic has persisted for about 16 months at the time of this study. Academic literature has identified many factors that may correlate with increased COVID-19 incidences across counties. All of these studied factors are combined and analyzed with 16 months of data to build a machine learning model (multiple linear regression) for predicting COVID-19 incidence.

Methods

Data Collection:

Data for each of the following factors was collected from publicly available sources.

COVID-19 Incidence per U.S. County:

COVID-19 cumulative U.S. county incidence data was gathered from the NYT GitHub website, a publicly available repository of U.S. COVID-19 data.[2] Each county was identified by unique Federal Information Processing Standards (FIPS) codes. Data related to the U.S. territories or data not associated with a FIPS code (for example, cases associated with a state but unknown county) comprised 3.28% of the data set and were eliminated. Cumulative COVID-19 cases from January 21, 2020, to June 29, 2021, were used in the study.

Percentage of Multi-unit and Single-unit Housing:

Data was collected from the 2019 American Community Survey (ACS) on the United States Census Bureau website.[22] To determine percentages from the data, single-family homes (detached and attached) per county were summed and divided by the total housing units in that county. Likewise, to determine the percentage of multifamily dwellings, structures with greater than 20 units were also added per county and divided by the total housing units in that county. FIPS codes were used to identify each county.

Population Density, Average Household Size, and Poverty:

U.S. Census Bureau published data on April 7, 2020, that provided average household size per county and population density based on people per square kilometer.[23] The percentage of residents in poverty was available through the 2019 US Census Small Area Income and Poverty Estimates (SAIPE) data.[24] The SAIPE data is based on income tax returns, U.S. census estimates, and Supplemental Nutrition Assistance Program (SNAP) benefits.[25]

DOI: 10.36838/v5i1.12

Rural-Urban Continuum Codes:

The Rural-Urban Continuum Codes (RUCC) were collected from the U.S. Department of Agriculture Economic Research Service (ERS) website.[26] The ERS divided counties into nine classifications, with lower numbers signifying a more urban area and higher numbers corresponding to a more rural area. The first three RUCC codes were divided by population size into metropolitan areas, and the last six codes were non-metropolitan areas classified by proximity to a metro area and population.

Population Mobility:

The U.S. Department of Transportation Bureau of Transportation Statistics.[27] provides mobility statistics for each U.S. county. The data is produced from a survey of an anonymous national panel of mobile devices.[28] The data also defines trips as movements that include a stay of longer than ten minutes at an anonymized location away from home. Every day, the county population is divided into two parts: the percentage staying at home and the percentage not staying at home.

The data can be averaged over a period of time. This study collected data from April 7, 2020, to January 10, 2021. The data start date was chosen because most mandatory stay-at-home orders were initiated between mid-March and April 7, 2020,[29] while the end date is representative of the peak of the pandemic (i.e., the date with the most daily cases).[1] Daily cases declined after the peak of January 10, 2021, so it was inferred that before this date would be when the importance of social distancing would be most crucial. The percentage of the population that stayed at home over the pandemic time period in each county was calculated as the average number of people that stayed at home each day from April 7, 2020, to January 10, 2021, divided by the total population monitored in that county.

In addition, the pandemic time period (April 7, 2020, to January 10, 2021) was compared to the same time period one year prior (April 7, 2019, to January 10, 2020) to establish a baseline of comparison for the movement of individuals on a county level. The change in movement was calculated as the number of people that stayed home during the pandemic period, subtracted by the number of people that stayed home during the baseline period divided by the baseline period again.

Obesity and Diabetes Rates:

The original data used to estimate obesity and diabetes rates in each county was derived from the Behavioral Risk Factor Surveillance System (BRFSS) through the CDC.[30] The most recent BRFSS survey data was from 2019 and reported the percentage of the population diagnosed with diabetes and the percentage of the population with obesity (defined as a body mass index greater than 30).

Social Vulnerability Index (SVI), Percentage of Population Greater than 65 years of age, and Percentage of Minority Population:

The Social Vulnerability Index (SVI), as mentioned previously, is a measure of a community's susceptibility to loss in a disaster or anthropogenic event. Each county is given a score between 0 and 1, with higher scores indicating higher levels of vulnerability. SVI is calculated from four key factors: socioeconomic status, household composition and disability, minority status and language, and housing type and transportation. The data is available from 2018 on the CDC website.[31] This SVI database also included estimations for the number of people in each county over 65 years old, minorities, and the total population.

Data Preprocessing:

All analyses in this study were done with Python 3.7.11.[32] A Jupyter notebook[33] using Google Colab workspaces[34] was utilized as well. Data preprocessing, descriptive statistics, data visualizations, data transformations, linear models, and multiple linear regression were all performed for the data set used in this study.

Before fitting the linear regression model, data were preprocessed in two steps: removing outliers and feature scaling (standardizing normally distributed variables and normalizing variables with non-normal distributions). Initially, outliers were considered as data points greater than three standard deviations away from the mean. Still, parameters were modified to 2.5 standard deviations to account for the large number of outliers. The removed points consisted of 1.24% of the data. After adjusting for outliers, the dataset used in this study had 2,662 data points and 12 features.

For feature scaling, the data was divided into normally distributed variables and non-normally distributed variables. The normally distributed predictor variables were standardized using StandardScaler from the sci-kit-learn library in Python 3.7.11. This shifted the mean to zero and scaled the variables to unit variance. The non-normally distributed predictor variables were normalized using MinMaxScaler from the sci-kit-learn library in Python 3.7.11. This adjusts all values in the non-normal features to a 0-1 range. Both of these two feature scaling techniques were necessary to have a standard range for all the variables, as their values encompassed a wide range (for instance, percentages range from 0 - 100, SVI ranges from 0 - 1, rural/urban status ranges from 1 – 9, etc.).

Linear Regression:

To create the multiple linear regression model, the data was divided into 80% for training and 20% for testing, also known as the 80-20 split. These ratios were based upon the Pareto Principle, which states that 20% of causes form 80% of effects.[35] The linear model was then fit to the training data and analyzed using sklearn's ordinary least squares linear regression summary. Statistically insignificant features ($p<0.05$) were removed iteratively until a parsimonious linear model was fit. The outcome (COVID cases per county) was noted to have a non-normal distribution, so it was transformed into a normal distribution.

For the results of a regression model to be accurate, the following five assumptions must be met: linearity, normal distribution of error terms, no multicollinearity among predictors, homoscedasticity, and no relationship between residuals and variables. Linearity is the ability to draw a linear relationship between the predictor and outcome variables. Next, error terms must be normally distributed, which can be checked using an Anderson-Darling test or quantile-quantile plot. Multicol

linearity among predictor variables cannot be present; if there is, it is challenging to make interpretations from the model. Homoscedasticity is associated with no relationship or patterns between residuals and variables. Violation of this implies the lack of a linear relationship. After trying out different transformation techniques, including log transforming the outcome variable (elaborated in the results section), the Box-Cox method was the most optimal for this study.

Results

In the preliminary analysis, the model with COVID-19 cases as the outcome variable yielded higher accuracy than that with COVID-19 deaths as the outcome. For this reason, data was focused on COVID-19 cases. Three metrics were utilized to evaluate the performance of the model: the coefficient of determination measured how much of the variance in outcome was explained by the predictors, the mean squared error measured the average magnitude of errors, and the root mean squared error also measured magnitude, but was more tolerant of outliers. The metrics after each model iteration is summarized in Table 1. After data preprocessing, the first model fit did not have high accuracy because the data had not yet been narrowed down or transformed. It concluded in a coefficient of determination of 52%, mean absolute error of 4916.28, and mean squared error of 9536.76. After fitting the ordinary least squares regression model, features with a p-value <0.05 were considered statistically insignificant to the model. As a result, two components (average household size and percentage of single-family homes) were removed from the model one at a time to achieve a parsimonious model. This new model had a coefficient of determination of 58%, a mean absolute error of 5398.93, and a mean squared error of 10344.53. However, the linear model assumptions were violated because the outcome variable (COVID-19 cases) was not normally distributed.

Table 1: Coefficient of determination, mean absolute error and mean squared error of the experimental models.

	Coefficient of determination	Mean absolute error	Mean squared error
First model after data preprocessing	52%	4916.28	9536.76
Model after fitting OLS regression	58%	5398.93	10344.53
Model after log transformation	58%	5391.53	10382.79
Final model after Box Cox method	71%	0.46	0.60

To rectify this, data transformation was executed on the outcome by log transforming it. After fitting the model to the dataset with the log-transformed outcome, the coefficient of determination was 58%, the mean absolute error was 5391.53, and the mean squared error was 10382.79. Although the model's accuracy improved, it still needed modification because it did not pass all of the assumptions of a linear model. The model violated linearity and homoscedasticity (Figures 1 and 2). Because there are numerous ways to transform an outcome from a non-normal variable to a normal variable (log transformation, square root transformation, inverse transformation, etc.), there were no guarantees as to which exact transformation would work for the outcome. Consequently, a Box-Cox method was chosen to transform the outcome variable. The Box-Cox method does this by finding the best lambda value to transform the outcome variable to follow a normal distribution optimally. This function returns a lambda value (For instance, lambda = 2 for a square root transformation; lambda = -1 for an inverse transformation; etc.).

Following the Box-Cox method, the optimal lambda value for COVID-19 cases was -0.02187. Figure 3 shows the distribution of the outcome variable before and after the box cox transformation. Fitting the model with this newly transformed outcome, all five linear model assumptions were met. Figure 4 displays a plot of predicted and actual values, following the assumption of linearity. Figure 5 is a quantile-quantile (QQ) plot, which tests for the normality of residuals. Figure 6 is a residual graph with equal variance throughout, following homoscedasticity of error terms. In Table 2, there are no significant variance inflation values, proving no multicollinearity was present in my variables. Finally, the model also passed the Durbin-Watson test, which checked for independent errors assumption. The test resulted in 2.11, which is in the normal range of 1.5 - 2.5. Thus, there was no multicollinearity present in my variables.

After ensuring the validity of all five tests, the final model had a coefficient of determination of 71%, a mean absolute error of 0.46, and a mean squared error of 0.60. The details for the final model are available in Table 3. Now that all five assumptions have been met, results could be drawn from the model.

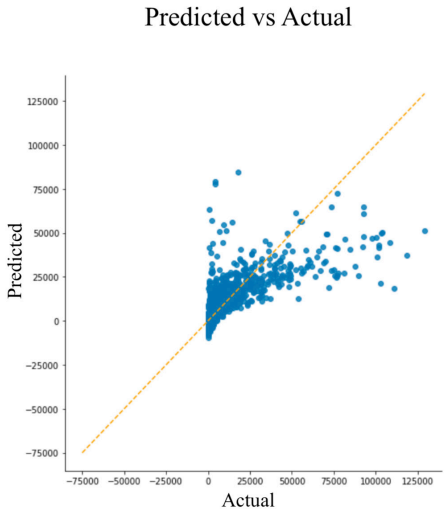

Figure 1: A residual graph of predicted values and actual values. The log-transformed model violates linearity, as the points are patterned and not clustered evenly along the orange line.

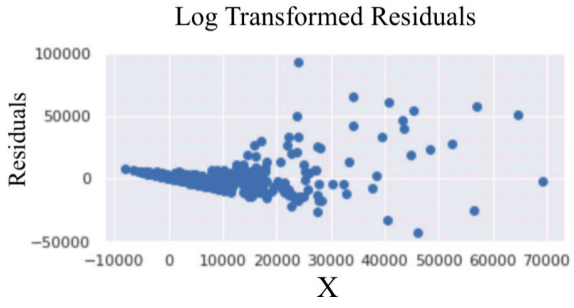

Figure 2: A graph of the log-transformed residuals, which violates homoscedasticity. As X increases, the variance of the residual increases, creating a patterned funnel shape that is inconsistent.

DOI: 10.36838/v5i1.12

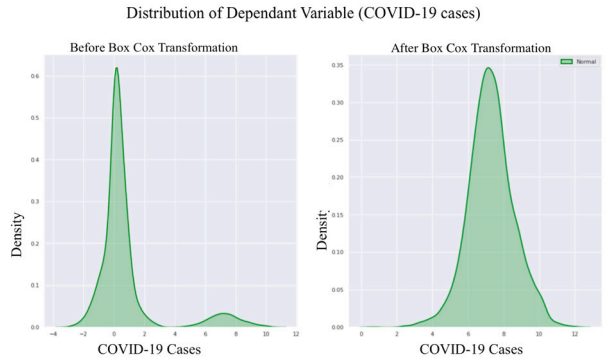

Figure 3: Distribution of dependent variable (COVID-19 cases) before and after box cox transformation. The image on the right shows the COVID-19 cases transformed into a normal distribution.

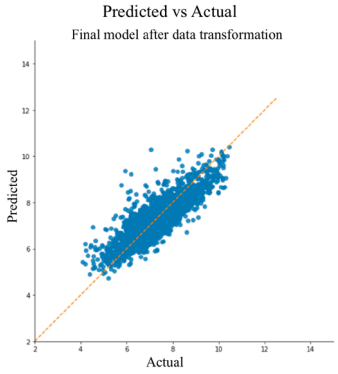

Figure 4: Residual graph (plot of predicted values vs. actual values). The figure shows that the linearity assumption is well satisfied with a strong linear relationship.

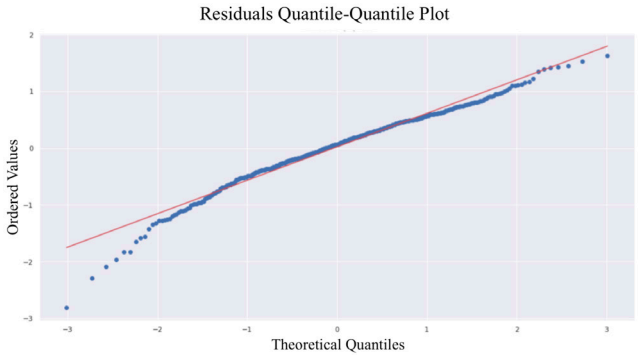

Figure 5: This quantile-quantile (QQ) plot indicates the normality of the residuals, as the points closely lie along the orange line.

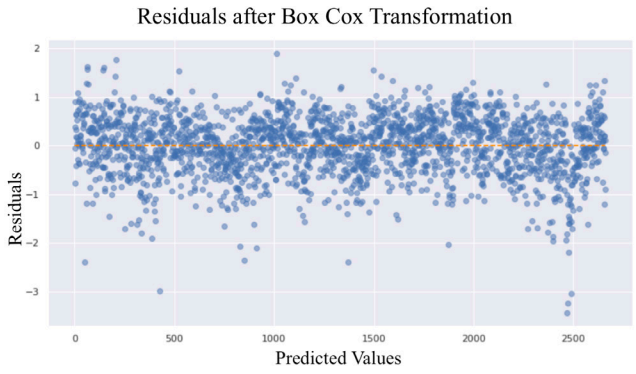

Figure 6: The model qualifies as Homoscedasticity of Error Terms. This model graphs variance in residuals, and there is no pattern.

Discussion

Variance Inflation Factors of Model Variables

	Model Variables	VIF
1	Population Density	1.89
2	% of Housing Units with > 20 Units	3.20
3	% Diabetes	2.76
4	% Obesity	2.01
5	% Poverty	2.12
6	% of Population Over 65	1.85
7	% Minority	5.08
8	Social Vulnerability Index	9.28
9	Rural Urban Classification Status	4.31
10	Change in % Population at Home	1.70

Table 3: The greater absolute value of the model coefficient determines the weight the factor is given in the model. This chart includes factors that had a significant p-value ($p<0.05$), the remaining two factors not included (percentage of single-family homes and average household size, with p-values of 0.356 and 0.232, respectively) were eliminated because their p-values were greater than 0.05.

Factors that affect number of COVID-19 cases	*Model Coefficient*	*Standard Error of Model Coefficient*	*P-Value <0.05 considered significant*
Percentage of population over 65 years of age	-0.1977	0.016	0.000
Change in percentage of population staying at home each day during pandemic time (4/7/20 to 1/10/21) compared to prepandemic time (4/7/19 to 1/10/20)	0.2261	0.015	0.000
Social Vulnerability Index	1.0200	0.082	0.000
Percentage of homes in multiunit buildings with greater than 20 units	2.0076	0.085	0.000
Rural versus urban code (urban codes lower)	-1.1441	0.051	0.000
Population Density	1.3430	0.174	0.000
Percentage of population with diabetes	0.0895	0.019	0.000
Percentage of population in poverty	-0.1167	0.021	0.000
Percentage of population with a BMI>30	0.0427	0.016	0.009
Percentage of population that is of minority ethnicity	-0.5654	0.073	0.000

The multi-linear regression model was able to predict COVID-19 cases successfully using the ten factors listed in Table 3. Two variables (average household size and percent of housing units that were single-family homes) were statistically insignificant ($p>0.05$) and subsequently removed from the

model. The model had a coefficient of determination of 0.71, indicating reasonable accuracy. The four factors that had the most influence on the model included the percentage of multi-unit housing, population density, rural-urban classification status, and Social Vulnerability Index (SVI).

Percentage of Multi-Unit Housing:

Multi-unit housing is the percentage of housing units in buildings with more than twenty units per building, correlated with increased COVID-19 incidence. These results concurred with Cromer *et al*., who found that high household crowding and occupancy contributed to higher COVID-19 incidence.[19]

Population Density:

The population density was calculated by dividing the total county population by the county's area in square kilometers. In the model coefficients, population density contributed positively, showing increased COVID-19 cases in denser counties. Results from some previous studies are consistent with this, while other studies did not find any significant contribution of population density to COVID-19 incidences.[18,36] For instance, Hamidi *et al*. showed that population density did not correlate positively with increased COVID-19 incidence after controlling for metropolitan populations.[18] In contrast, Wong *et al*. showed that population density did correlate positively.[36] These results concur with Wong and show that population density positively correlates with COVID-19 incidence.

Rural Urban Classification:

According to the model, urban areas had increased incidences of COVID-19. A 0.1 unit increase in rural status would correspond to a decrease of 18.69% in COVID-19 cases. Calculated from the model coefficients, this statistic supported the finding of Karim *et al*. that metropolitan areas continue to have higher rates of disease compared to micropolitan and rural areas, and the majority of COVID-19 cases and deaths in 2020 were in urban areas.[17] This data is also consistent with Hamidi *et al*., that metropolitan areas correlated with increased COVID-19 incidence.[18]

Social Vulnerability Index:

Social vulnerability plays a vital role in COVID-19 incidence in communities. According to the model coefficients, a percentile increase in SVI leads to 4.79% more COVID-19 cases. This is consistent with other studies of COVID-19 and SVI, although the magnitude of contribution varies in each study. Karaye and Horney found that a percentile increase in SVI resulted in 16% more COVID-19 cases.[15] Karmakar *et al*. found a 0.1 point increase in SVI increased the incidence of COVID-19 by 14.3%.[16] Long-standing inequities in healthcare access for vulnerable communities appear to contribute to increased incidence; however, variations in the effect of SVI changes on COVID-19 cases in these different studies could be due to the various time periods examined.

Obesity and Diabetes:

The remaining two factors, diabetes and obesity did not add much significance to the model. Nonetheless, the model showed a positive correlation between increased incidence of obesity and diabetes with increased incidence of COVID-19, which supported findings in other studies. A one-unit increase in the percentage of the population with obesity matched with a 4.16% increase in COVID-19 cases. This parallels with Jayawardena *et al*., who also found that increased rates of obesity correlated with increased incidence of COVID-19.[37] In addition, Chen *et al*. found that COVID-19 hospitalized patients with diabetes had two to three times higher mortality rates.[38]

Other Factors:

Some factors had minimal effects in the model that seemed to contradict previous studies. First, there was a positive correlation between an increase in the percentage of the population that stayed at home during the pandemic and COVID-19 incidence. However, this might reflect stricter stay-at-home orders in metropolitan areas with higher incidences of COVID-19. Next, the model indicated that higher poverty rates corresponded with lower rates of COVID-19. Again, this could be attributed to metropolitan areas having higher rates of COVID-19 and increased average income. Metropolitan poverty rates in 2019 were only 11.9% compared to 15.4% in non-metropolitan areas.[39]

An increase in the percentage of the population that were of minority ethnicity also unexpectedly had a negative correlation with COVID-19 cases. This contradicted previous studies that concluded that minority populations were positively correlated with COVID-19.[11] However, this played only a minor role in the model and could be because the data targeted the number of COVID-19 cases as opposed to the percentage of the population that had been diagnosed with COVID-19.

Finally, the model showed that counties with higher percentages of people over 65 had lower cumulative incidences of COVID-19. This seemed to challenge earlier reports that indicated elderly patients were more at risk of contracting COVID-19.[39] However, reviewing CDC weekly cases by age 40, early data from the first three months showed older age groups having a higher incidence of COVID-19. However, after June 2020, the group with the highest incidence of COVID-19 transitioned to ages 18-29. Perhaps elderly patients can socially distance themselves more due to their retired status, so as the pandemic progressed, the incidence of elderly patients declined.

Pearson's Correlation Coefficient:

In addition to the multiple linear regression model, the strength of correlation and direction between the predicting factors and COVID-19 incidence was tested. Correlation between the independent variables and the normally-distributed dependent variable (with all outliers removed) was measured. As shown in Table 4, the Pearson's correlation coefficient was calculated for each of the ten statistically significant variables from the initial model ($p<0.05$). The factors that correlated best with higher COVID-19 cases included greater population density, more multi-unit housing, more urban locations, and an increased percentage of the population that stayed at home. These results concur with the results seen both in this model and in other studies as well.[18,19,21,36]

DOI: 10.36838/v5i1.12

Table 4: Pearson correlation coefficient – correlation of various factors studied with cumulative COVID-19 incidence in U.S. countries.

Factor affecting COVID-19 incidence	*r* Pearsons correlation coefficient
Percentage of population over 65 years of age	-0.188
Change in percentage of population staying at home each day during pandemic time (4/7/20 to 1/10/21) compared to prepandemic time (4/7/19 to 1/10/20)	0.279
Population Density	0.524
Rural versus urban code (urban codes lower)	-0.287
Precentage of homes are in multiunit buildings with greater than 20 units	0.514
Percentage of population in poverty	-0.084
Percentage of population with diabetes	-0.148
Percentage of population is minority ethnicity	0.213
Social Vulnerability Index	0.035
Percentage of population obese (BMI>30)	-0.196

In conclusion, this study emphasizes that COVID-19 transmission is complicated, with numerous aspects to consider. Upon examining this model, the data suggests that the most effective non-pharmaceutical measures would include reducing shared spaces in multi-unit housing, enforcing social distancing, especially in urban areas with increased population density, and investing more resources into medically underserved communities to compensate for persistent healthcare inequities.

Limitations and Future Work:

There were several significant limitations to this study. First, COVID-19 incidence relies on COVID-19 testing being accessible. At the beginning of the pandemic, there were severe supply shortages for testing, and many people with suspected symptoms were never able to receive a confirmatory test. Therefore, the data may be skewed towards more severe cases of COVID-19, as milder cases are less likely to be tested. In addition, some areas had more severe test shortages than others, highlighting the effect of healthcare iniquities. Secondly, demographic information was gathered from surveys between 2018-2020, so some of these variables may have changed compared to 2020. Thirdly, this study focused on the number of COVID-19 cases in each county, in contrast to most studies that focused on the incidence of COVID-19 per 100,000 population. Consequently, the data was skewed towards larger, more populated counties. Attempts to minimize this bias were made with feature scaling and pre-processing, but the bias still may affect the data.

There are several directions in which this research can progress. Although this study was based on 16 months of pandemic data, the pandemic continues to evolve with time, and factors that affect incidence will continue to change. In addition, effective immunizations against COVID-19 will also change the transmission dynamics of COVID-19. Even more importantly, variants such as the new delta variant may increase transmission as initial studies have already found it to be 50% more contagious and can be transmitted through brief contact.[41]

Conclusion

This paper compares COVID-19 cases at a county level to multiple factors, including age, obesity, diabetes, poverty, minorities, urban populations, population density, multi-unit housing, SVI, and population mobility. Furthermore, a reliable model was created to accurately predict the incidence of COVID-19 and showed that multi-unit housing, population density, urban population, and SVI were the most significant factors. The model also provided a measure of how each factor changed COVID-19 incidence; for example, a 0.1 unit move towards more rural status led to 18.69% fewer COVID-19 cases. In addition, a 0.01 unit increase in SVI (meaning more social vulnerability) increased COVID-19 cases by 4.79%. This study highlights the importance of continuing demographic studies over time as the pandemic evolves. Analyzing the factors that lead to higher COVID-19 rates can determine which non-pharmaceutical interventions are most effective. This knowledge is critical to crafting policies that reduce the consequences of pandemics and to improving health worldwide.

Acknowledgements

I would like to thank the staff of the Summer Stem Institute for their guidance and the opportunity to further my interests in epidemiology research. I am especially grateful to my research mentor, Marian Obuseh, for her incredible dedication and guidance throughout the program.

References

1. "COVID Live Update: 198,031,336 Cases and 4,224,346 Deaths from the Coronavirus - Worldometer," July 2021.
2. "COVID-19 Map - Johns Hopkins Coronavirus Resource Center," July 2021.
3. "covid-19-data/us-counties.csvat1eea97d0652b04ceda2d9b88c3f21db5ef643b36 · nytimes/covid-19-data · GitHub," June.
4. "COVID Vaccine Updates: 1 in 10 people in US has tested positive

for virus - ABC7 New York," Apr. 2021.
5. "Estimated COVID-19 Burden | CDC," July 2021.
6. A. Bartik, Z. Cullen, E. Glaeser, M. Luca, and C. Stanton, "What Jobs are Being Done at Home During the Covid-19 Crisis? Evidence from Firm- Level Surveys by Alexander Bartik, Zoe Cullen, Edward L. Glaeser, Michael Luca, Christopher Stanton: SSRN," June 2021.
7. "We're all shopping more online as consumer behaviour shifts | World Economic Forum," July 2021.
8. "Map: Coronavirus and School Closures in 2019-2020," June 2021.
9. C. Bowman, "Coronavirus Moving Study Shows More Than 15.9 Million People Moved During COVID-19 | MYMOVE," June 2021.
10. "New Data from Curriculum Associates Quantifies Impact of COVID Learning Loss; Raises Questions about At-Home Testing | Curriculum Associates," Oct. 2020.
11. A. Klein and E. Smith, "Explaining the economic impact of COVID-19: Core industries and the Hispanic workforce."
12. "A model of disparities: risk factors associated with COVID-19 infection | International Journal for Equity in Health | Full Text."
13. U. Mahajan, "Racial demographics and COVID-19 confirmed cases and deaths: a correlational analysis of 2886 US counties," 2020.
14. G. Harlem and M. Lynn, "Descriptive analysis of social determinant factors in urban communities affected by COVID-19," June 2020.
15.] "At A Glance: CDC/ATSDR Social Vulnerability Index | Place and Health | ATSDR," Apr. 2020.
16. I. Karaye and J. Horney, "The Impact of Social Vulnerability on COVID-19 in the U.S.: An Analysis of Spatially Varying Relationships," Sept. 2020.
17. M. Karmaker, P. Lantz, and R. Tipirneni, "Association of Social and Demographic Factors With COVID-19 Incidence and Death Rates in the US | Health Disparities | JAMA Network Open | JAMA Network," Jan. 2021.
18. S. Karim and H.-F. Chen, "Deaths From COVID-19 in Rural, Micropolitan, and Metropolitan Areas: A County-Level Comparison - Karim - 2021 - The Journal of Rural Health - Wiley Online Library," Nov. 2020.
19. S. Hamidi, S. Sabouri, and R. Ewing, "Full article: Does Density Aggravate the COVID-19 Pandemic?," 2021.
20. S. Cromer, L.Chirag, D. Wexkler, and M. U. Patel, "Geospatial Analysis of Individual and Community-Level Socioeconomic Factors Impacting SARS- CoV-2 Prevalence and Outcomes | medRxiv," 2020.
21. H. Badr, H. Du, M. Marshall, and E. Dong, "Association between mobility patterns and COVID-19 transmission in the USA: a mathematical modelling study | Request PDF," July 2020.
22. H. Badr, M. Marshall, E. Dong, and M. Squire, "Association between mobility patterns and COVID-19 transmission in the USA: a mathematical modelling study - The Lancet Infectious Diseases, " July 2020.
23. "Census - Table Results," 2019.
24. "Census COVID-19 Data Hub: Average Household Size and Population Density - County: Average Household Size and Population Density - County," June 2020.
25. "Small Area Income and Poverty Estimates (SAIPE) Program," 2019.
26. "SAIPE," 2019.
27. "USDA ERS - Rural-Urban Continuum Codes," Dec. 2020.
28. "Bureau of Transportation Statistics," Jan. 2021.
29. "Trips by Distance | Open Data | Socrata," 2020.
30. "Timing of State and Territorial COVID-19 Stay-at-Home Orders and Changes in Population Movement — United States, March 1–May 31, 2020, | MMWR," Sept. 2020.
31. L. Berry, "Living Atlas: Diabetes, Obesity, and Inactivity by US County: Diabetes, Obesity, and Inactivity by US County," June 2021.
32. "CDC/ATSDR SVI Data and Documentation Download | Place and Health | ATSDR," 2018.
33. "Python Release Python 3.7.11 | Python.org," June 2021.
34. "Project Jupyter | Home."
35. "Welcome To Colaboratory - Colaboratory."
36. T. D. D., "The 80/20 Split Intuition and an Alternative Split Method | by The Data Detective | Towards Data Science," Jan. 2020.
37. D. Wong and Y. Li, "Spreading of COVID-19: Density matters," Dec. 2020.
38. R. Jayawardena, D. Jeyakumar, A. Misra, H. Andrew, and P. Ranasinghe, "Obesity: A potential risk factor for infection and mortality in the current COVID-19 epidemic."
39. X. Chen, D. Yang, B. Cheng, J. Chen, A. Peng, C. Yang, C. Liu, M. Xiong, A. Deng, Y. Zheng, and L. Zheng, "Clinical Characteristics and Outcomes of Patients With Diabetes and COVID-19 in Association With Glucose-Lowering Medication," July 2020.
40. "USDA ERS - Rural Poverty & Well-Being," June 2021.
41. "CDC COVID Data Tracker," July 2021.
42. K. Katella, "5 Things To Know About the Delta Variant > News > Yale Medicine," July 2021

Author

Jenna Chuan is a sophomore at Memorial High School in Houston, Texas. She is passionate about understanding physiology and disease and aspires to study medicine in the future. She pursues Tae Kwon Do, piano, and loves to read in her free time.

DOI: 10.36838/v5i1.12

IJHSR
ijhighschoolresearch.org
RESEARCH ARTICLE

High Glucose Transglutaminase 2 Promotes YAP/TAZ and Fibroblast Proliferation in Pulmonary Hypertension

Jennifer Wu

Winchester High School, 80 Skillings Road, Winchester, Massachusetts, 01890, U.S.A.; jwu1830@gmail.com

ABSTRACT: Pulmonary hypertension (PH) is a cardiopulmonary disease characterized by uncontrollable cell proliferation of adventitial fibroblasts in the pulmonary artery, leading to increased pulmonary arterial stiffness and eventual right ventricular dysfunction and heart failure. Previous studies have reported a significant role for glycolysis-induced transglutaminase 2 (TG2) in cell proliferation, fibrogenesis and PH. Furthermore, a direct relationship was established between TG2 and YAP/TAZ, molecules that activate extracellular matrix remodeling when triggered by vascular stiffness in cancer cells. Thus, this study sought to determine whether the same relationship between TG2 and YAP/TAZ existed in cell culture models of PH. Utilizing human pulmonary artery adventitial fibroblasts, we conducted a series of three experiments 1) analyzing the effect of high glucose concentrations on YAP and TAZ levels, 2) the effect of TG2 inhibition (ERW1041E) on high-glucose induced YAP and TAZ levels, and 3) the effect of YAP/TAZ inhibition (YAP/TAZ siRNA) on fibroblast proliferation. We found that high glucose significantly induced TG2-mediated YAP and TAZ mRNA expression. Furthermore, YAP and TAZ mediate high-glucose-induced fibroblast proliferation. This confirmed our hypothesis that glycolysis- mediated TG2 activation plays a significant role in YAP/ TAZ upregulation, promoting pulmonary arterial adventitial fibroblast proliferation in response to high glucose. These findings support a novel role for glycolysis-induced TG2 and YAP/TAZ in pulmonary arterial remodeling associated with experimental PH.

KEYWORDS: Biomedical and Health Sciences; Cell, Organ, and Systems Physiology; Cardiovascular; Pulmonary Hypertension; Transglutaminase 2; YAP/TAZ.

Introduction

Pulmonary hypertension (PH) is a proliferative cardiac disease affecting between 50 to 70 million individuals worldwide. The condition may be caused by uncontrollable cell proliferation of smooth muscle cells (SMCs) and fibroblasts in the pulmonary artery, composed of an inner layer of endothelial cells, a middle layer of SMCs, and an outer layer of adventitial fibroblasts. In PH, aberrant pulmonary arterial (PA) remodeling resulted in a rapid buildup of muscle in the arterial walls and increased pressure in the right ventricle of the heart. This adverse remodeling of the PA further causes remodeling of the right ventricles, eventually culminating in heart failure. Currently, there is no effective treatment for PH.

In previous years, a notable role for transglutaminase 2 (TG2) has been identified in PH.[1,2] As a cross-linking enzyme that alters protein function, TG2's post-translationally modified extracellular matrix (ECM) proteins were shown to promote cell growth and migration.[1] This may result in the increased ECM's stability, fibrogenesis, and tissue stiffness. TG2 has also been shown to cross-link between protein glutamine and lysine residues, enabling its contribution to the serotonylation of vascular proteins such as fibronectin.[2] In PH specifically, TG2 was shown to mediate heightened collagen deposition and tissue fibrosis in the PA, which may promote increased vascular resistance and, eventually, right ventricle (RV) pressure. Recently, experiments showed TG2 levels were stimulated by glycolysis, which could be induced through high-glucose concentrations.[1]

More and more researchers acknowledge vascular ECM modifications as an important molecular contributor to PH.[5] During both the early and late stages of PH, uncontrolled collagen and elastin assembly have been detected.[5] However, activities connecting PH vasculature to ECM mechanotransduction, a series of activities allowing cells to perceive and adjust to external stimulants, have only started to be identified.[4,5] In particular, Yes-associated protein 1 (YAP) and TAZ, two regulators of the Hippo signaling pathway, are triggered by ECM rigidity; its activity is directly controlled by cell shape and polarity, which is governed by the cell's cytoskeleton. They can pick up on how cells perceive both themselves and their environment within tissues, communicating with others.[4,5] Its ability to modify cells' actions to an organ's specific needs, combined with its regulation of cell division, allows it to aid tissue growth and repair. In early PH *in vivo* models, it was found that pulmonary vascular stiffness triggers YAP/TAZ, inducing further ECM remodeling and cell proliferation. Thus, when regular pathways fail, abnormal YAP/TAZ induction results in diseases such as fibrosis, cancer, and atherosclerosis.

TG2 is thought to serve as a direct target gene of YAP/TAZ in cancer cells.[6] In response to YAP/TAZ overexpression, TG2 levels significantly increased, and YAP/TAZ knockdown decreased TG2 expression in multiple cell lines. Data analysis showed that mRNA levels of TG2 positively correlated with numerous downstream target genes of YAP/TAZ, including the expression levels of YAP/TAZ. This suggests that TG2 is a direct target of YAP/TAZ, significantly contributing to the hostile transformation in cancer cells activated by YAP/TAZ.[6]

Analyzing these points, we connected TG2's role in PA tissue fibrosis to YAP/TAZ's role in ECM stiffness and the correla-

DOI: 10.36838/v5i1.13

tion between TG2 and YAP/TAZ in cancer cells. Therefore, in the present study, we chose to investigate if a similar relationship between YAP/TAZ and TG2 expression is implicated in PH pathogenesis and if these pathways could be explored as potential targets for novel therapies for PH. We hypothesized that high glucose induces glycolysis-mediated TG2 activation and YAP/TAZ upregulation, promoting pulmonary arterial adventitial fibroblast proliferation.

Methods

Materials:

This study utilized human pulmonary artery adventitial fibroblasts (HPAAFs) grown in 6-well cell culture plates. Cells were grown in a fibroblast medium supplemented with fetal bovine serum (FBS) and varying high glucose concentrations. Glucose-free media was used to starve fibroblasts overnight. To test TG2 effects, fibroblasts were pre-treated with varying concentrations of ERW1041E, a known inhibitor of TG2 activity, or vehicle control (dimethyl sulfoxide; DMSO). To test the effects of YAP/TAZ, fibroblasts were transfected with a 20nM concentration of YAP and TAZ siRNA or control scrambled siRNA. The quantitative PCR method was used at the experimental endpoints to determine the mRNA expression of TG2, YAP, and TAZ genes. For PCR analysis, Trizol, nuclease-free centrifuge tubes, DNase I, RNA primers (TG2, YAP, TAZ, and beta-actin), reverse transcriptase enzyme, DNA Polymerase, dNTPs, SYBR Green I dye, and a qPCR machine were used according to previously published methods (1). Cell counting was performed to quantify cell proliferation. This analysis required a hemocytometer chamber with a coverslip, trypan blue, tally counter, pasteur pipettes, and a microscope.

High Glucose Cell Culture:

Seeking to investigate the impact of TG2 activity on YAP/TAZ expression and fibroblast proliferation, this study used high glucose concentrations to stimulate TG2 activity. Three sets of experiments were conducted: one to determine if high glucose concentrations induced TG2 and YAP/TAZ mRNA expression, another to determine the effect of TG2 inhibition on high glucose-induced YAP/TAZ mRNA expression, and lastly to determine the relationship between YAP/TAZ inhibition and high glucose-induced fibroblast proliferation.

The first experimental set mentioned above attempted to discover the effect of high glucose concentrations on TG2 and YAP/TAZ expression. Thus, the study used glucose concentrations of 0, 5.5, 10, 25, and 50 mM as the independent variable and YAP/TAZ expression levels as the dependent variables. The experiment was conducted with HPAAFs, placed in 6-well plates with approximately 300,000 cells per well. After reaching about 70% confluency, fibroblasts were starved overnight with glucose-free media without FBS to ensure all cells began the experiment at the same conditions before glucose introduction. They were then exposed to varying glucose concentrations of 5.5, 10, 25, and 50 mM for 72 hours. Cells receiving no glucose were used as controls. Each of these concentrations was replicated in at least three cell culture wells. PCR analysis was then carried out at the experimental end points to determine TG2 and YAP/TAZ mRNA expression levels.

TG2 Inhibitor:

The second experimental set, as mentioned above, hoped to identify the effect of TG2 inhibition on high glucose-induced YAP/TAZ mRNA expression. Thus, the independent variables were the varying ERW1041E concentrations and high glucose, while the dependent variable was YAP/TAZ expression. The experiment was conducted with HPAAFs, placed in 6-well plates with approximately 300,000 cells per well. After reaching about 70% confluency, fibroblasts were starved overnight with glucose-free media without FBS to ensure all cells began the experiment at the same conditions before glucose introduction. Following pretreatment with vehicle-control (DMSO) or 50uM concentration of known TG2 inhibitor ERW1041E for 1 hour, fibroblasts were cultured with high glucose (25mM) for 72 hours. Each experimental condition was replicated in at least three cell culture wells. PCR analysis was then carried out at the experimental endpoints to determine YAP/TAZ mRNA expression levels.

siRNA Transfection:

The final experimental set mentioned above sought to determine the relationship between the YAP/TAZ pathway and high glucose-induced fibroblast cell proliferation. The present study used YAP/TAZ siRNA inhibition and high glucose as the independent variables and fibroblast proliferation as the dependent variable. It was conducted with HPAAFs, which were cultured in a fibroblast medium. The cell cultures were done in 6 well plates, with approximately 300,000 cells per well. After reaching about 70% confluency, fibroblasts were transfected with a 20nM concentration of control siRNA, YAP, and TAZ siRNA for 6 hours in growth medium without antibiotics. Fibroblasts were cultured in normal (5.5 mM) glucose medium overnight. Cells were then subjected to varying glucose concentrations for 72 hours. Each transfection was replicated in at least three cell culture wells. After 72 hours, cell counting was then carried out at the experimental endpoint to quantify fibroblast growth.

Polymerase Chain React (PCR) Analysis:

At the experimental endpoints of the first and second experiments, cell lysis and total RNA extraction was performed on each individual cell culture well using Trizol. This lysis process was conducted in stabilizing conditions required to maintain its contents. Specifically, it was done with nuclease-free plasticware (tubes, pipettes, etc.) in a neutral pH environment and stored at -20 degrees Celsius to avoid nucleic acid degradation.

With the cell lysate recovered, RNA estimation was first carried out through spectroscopic methods to normalize RNA amounts, taking measurements of RNA concentration and purity. Real-time PCR was then conducted. While the polymerase chain reaction (PCR) is a technique that amplifies DNA fragments after the reaction completes, real-time PCR allows the PCR reaction to be visualized as the reaction progresses. By adding Deoxyribonuclease I, or DNase I, the RNA solution underwent DNase treatment to cleave any genomic DNA strands, leaving RNA with a ribosom-

DOI: 10.36838/v5i1.13

ribosomal majority. With DNA removed, reverse transcription was conducted with the addition of targeted RNA primers, the reverse transcriptase enzyme, DNA polymerase to extend the DNA strands, and dNTPs to allow the reaction to occur. SYBR Green I dye was added to the solution to detect the final DNA product.

The qPCR machine was used to conduct real-time PCR, allowing the number of cycles and temperatures per cycle to be constantly set. To denature proteins, the qPCR machine began at 95 degrees Celsius, allowing the primer to begin binding to the DNA strands and beginning DNA replication. At this point, the temperature was lowered to around 72 degrees Celsius to optimize replication. This heating and cooling cycle was replicated in about 45 cycles. Cycle threshold (Ct) values were then used for qPCR analysis.

Cell Counting:

At the experimental endpoint of the third experiment, cell counting was conducted on each individual cell culture well. The cell suspensions were dropped into a hemocytometer chamber using a Pasteur pipette, and capillary action drew the suspension into the chamber. The opposite chamber was similarly filled. Next, the chamber was placed on a microscope, where the 10x objective was used to count the number of cells in a 1mm square area. Cells on the other side of the hemocytometer were similarly counted. To calculate the cells' concentration, we counted the average of all 1mm 2 areas and applied the formula c=n/v, where c was the cell concentration in cells per mL, n was the average number of cells per mm square area, and v was the volume counted.

Results and Discussion

Role of High Glucose in YAP and TAZ mRNA Expression:

When stimulated with higher glucose concentration levels, YAP mRNA expression increased in a glucose-concentration-dependent manner. A significant increase in expression was seen in glucose levels of 10 mM, 25 mM, and 50mM, indicating that high glucose levels serve as a stimulant for YAP expression (Figure 1). TAZ expression showed similar results when met with high-glucose levels, except for a significant change in the presence of 10 mM glucose levels (Figure 1). Nevertheless, high glucose concentrations also stimulate TAZ mRNA expression. However, in the normal glucose concentration level of 5.5mM, YAP and TAZ expression did not significantly differ compared to no glucose (Figure 1). With the confirmation that high glucose concentrations stimulate both YAP and TAZ expression, 25 mM glucose concentrations were used to induce YAP and TAZ expression in each subsequent experiment.

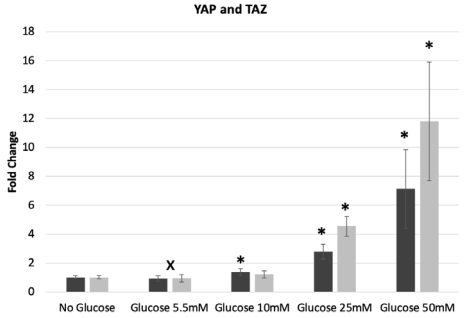

Figure 1: High glucose significantly induced YAP and TAZ mRNA expression in HPAAFs. Dark grey bars denote YAP expression, while light grey bars denote TAZ expression. The reference groups, normal glucose (5.5 mM), are devoted with (x). Significant differences compared to normal glucose (5.5mM) are denoted with (*), utilizing p-values. Error bars depicting standard deviation are represented throughout.

Role of TG2 Inhibition in High-Glucose Induced YAP and TAZ mRNA Expression:

YAP expression significantly increased in the presence of high glucose at a concentration of 25 mM (Figure 2) compared with normal glucose, in line with findings from (Figure 1). More importantly, high glucose-induced YAP expression significantly decreased when treated with a 50 uM concentration of ERW1041E, a known inhibitor of TG2 activity, compared to vehicle control (Figure 2). TAZ expression was affected similarly, with a significant increase in the presence of high glucose at a concentration of 25 mM compared to no glucose (Figure 2). High glucose-induced YAP expression also significantly decreased when treated with ERW1041E at a concentration of 50 uM compared to vehicle control (Figure 2). These results indicate that TG2 activity directly affects the glucose-induced expression of both YAP and TAZ mRNA.

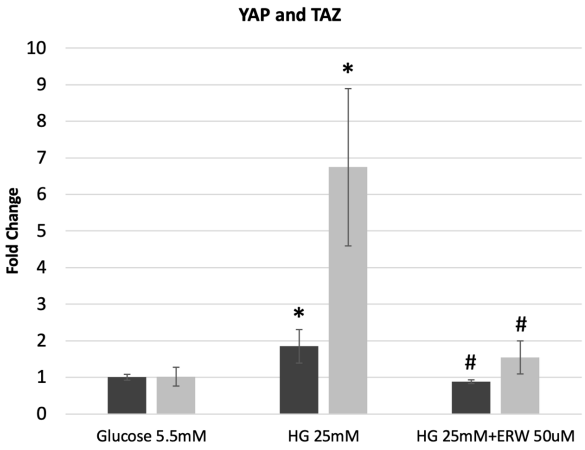

Figure 2: TG2 mediates high glucose-induced YAP and TAZ mRNA expression in HPAAFs. Dark grey denotes YAP expression, while light grey denotes TAZ expression. Significant differences compared to normal glucose (5.5mM) are marked with (*), and significant differences compared to high glucose (25 mM) are denoted with (#), utilizing p-values. Error bars depicting standard deviation are represented throughout.

Role of YAP and TAZ siRNA in High-Glucose Induced Cell Proliferation:

HPAAF Cell number significantly increased in the presence of high glucose compared to normal glucose (Figure 3), suggesting high glucose induces cell proliferation. As there was no significant change when high glucose-induced fibroblasts were transfected with control siRNA (Figure 3), it was further indicated that siRNA did not adversely impact the fibroblast's growth. Fibroblasts transfected with YAP siRNA and TAZ siRNA, which largely inhibited YAP and TAZ translation, showed a significant decrease in fibroblast cell numbers compared to high glucose control siRNA (Figure 3). Thus, this indicates that YAP and TAZ both play a substantial role in high-glucose-induced fibroblast proliferation.

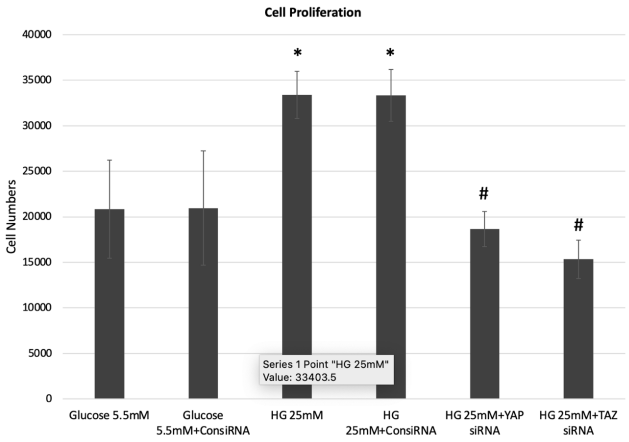

Figure 3: YAP and TAZ mediate high glucose-induced HPAAF cell proliferation. Significant differences compared to normal glucose (5.5 mM) with control siRNA are denoted with (*), and significant differences compared to high glucose (25 mM) with control siRNA are marked with (#), utilizing p-values. Error bars depicting standard deviation are represented throughout.

Discussion

We found that in HPAAFs, high glucose induces YAP and TAZ mRNA expression levels, TG2 activity significantly blocks glucose-induced YAP/ TAZ expression, and YAP/TAZ expression plays a significant role in fibroblast cell proliferation (Figure 4). Figure 4 shows the pathways our study verified, or the pathways between high glucose and YAP/TAZ, TG2 and YAP/TAZ, and YAP/TAZ and fibroblast proliferation. This proves our hypothesis that TG2 and YAP/TAZ are essential in promoting PA adventitial fibroblast growth, suggesting these molecular pathways may contribute to the adverse PA remodeling seen in PH patients.

In future studies, we hope to confirm real-time PCR mRNA analysis of the three experiments through Western Blot protein analysis. As for potential next steps, we suggest looking at YAP/TAZ inhibition's effect on collagen deposition through real-time PCR and Western Blot analysis. Finally, we recommend investigating the impact of TG2 inhibition on YAP/TAZ nuclear translocation through both real-time PCR and Western Blot analysis.

Potential limitations of this study include not conducting a controlled trial with 5.5 mM glucose utilizing YAP/TAZ siRNA. This could have checked if YAP/TAZ siRNA knocked down proliferation in normal glucose conditions. In this case, YAP/TAZ siRNA would have knocked down proliferation in general and not only in response to high glucose concentrations.

Given the role of TG2in collagen deposition and fibrogenesis,[1,2] the impact of YAP/TAZ on ECM,[4,5] and the relationship between TG2 and YAP/TAZ in cancer cells[6]; our current study's findings explore the relationship between TG2 activity, YAP/TAZ expression and fibroblast proliferation. Thus, these studies further advance our understanding of PH pathogenic mechanisms. Furthermore, these studies suggest that TG2 and YAP/TAZ may serve as potential targets for novel therapies for patients with PH.

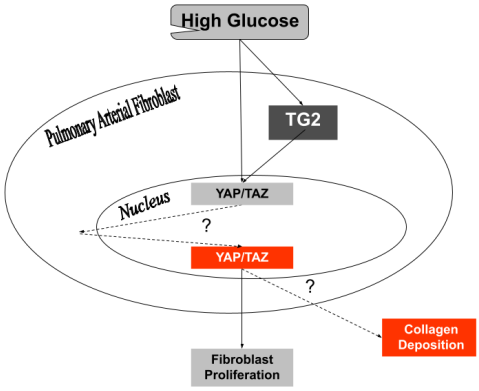

Figure 4: Schematic pathway for high glucose-mediated induction of TG2, YAP/TAZ, fibroblast proliferation, and fibrogenesis in PH. Verified pathways are denoted with filled arrows, while unverified pathways are marked with dotted arrows and (?).

Acknowledgements

The immense support and guidance from James P. Michielini of Tufts University and the Tufts Medical Center Department of Medicine/Pulmonary Division is gratefully acknowledged.

References

1. Bhedi, C. D.; Nasirova, S.; Toksoz, D.; Warburton, R. R.; Morine, K. J.; Kapur, N. K.; Galper, J. B.; Preston, I. R.; Hill, N. S.; Fanburg, B. L.; & Penumatsa, K. C. Glycolysis Regulated Transglutaminase 2 Activation in Cardiopulmonary Fibrogenic Remodeling. The FASEB Journal. 2019, 34(1), 930–944. https:// faseb.onlinelibrary wiley.com/doi/10.1096/fj.201902155R
2. Penumatsa, K. C.; Toksoz, D.; Warburton, R. R.; Kharnaf, M.; Preston, I. R.; Kapur, N. K.; Khosla, C.; Hill, N. S.; & Fanburg, B. L. Transglutaminase 2 in Pulmonary and Cardiac Tissue Remodeling in Experimental Pulmonary Hypertension. American Journal of Physiology. Lung Cellular and Molecular Physiology. 2017, 313(5), L752–L762. DOI: 10.1152/ajplung.00170.2017
3. Totaro, A.; Panciera, T.; & Piccolo, S. YAP/TAZ Upstream Signals and Downstream Responses. Nature. 2018, 20(8), 888–899. https:// journals.physiology.org/doi/full/10.1152/ajplung.00170.2017
4. Dupont, S.; Morsut, L.; Elvassore, N.; Piccolo, S.; Aragona, M.; Enzo, E.; Giulitti, S.; Cordenonsi, M., Zanconato, F.; Le Digabel, J.; Forcato, M.; & Bicciato, S. Role of YAP/TAZ in Mechanotransduction. Nature. 2011, 474(7350), 179–183. https://www.nature. com/articles/nature10137
5. Bertero, T.; Oldham, W. M.; Cottrill, K. A.; Pisano, S.; Vanderpool, R. R.; Yu, Q.; Zhao, J.; Tai, Y.; Tang, Y.; Zhang, Y.-Y.; Rehman, S.: Sugahara, M.; Qi, Z., Gorcsan, J.; III, Vargas, S. O.; Saggar, R.; Saggar, R.; Wallace, W. D.; Ross, D. J.; Chan, S. Y. Vascular Stiffness Mechanoactivates YAP/TAZ-dependent Glutaminolysis to Drive Pulmonary Hypertension. Journal of Clinical Investigation. 2016, 126(9), 3313+. https://www.jci.org/articles/view/86387
6. Fisher, M. L.; Kerr, C.; Adhikary, G.; Grun, D.; Xu, W.; Keillor, J. W.; & Eckert, R. L. Transglutaminase Interaction With α6/β4- Integrin Stimulates YAP1-Dependent ΔNp63α Stabilization and Leads to Enhanced Cancer Stem Cell Survival and Tumor Formation. Cancer Research. 2016, 76(24), 7265–7276. https://cancerres. aacrjournals.org/content/76/24/7265

Author

Jennifer Wu is a junior at Winchester High School in Winchester, Massachusetts. She has long had a passion for science and biomedical research. In college, Jennifer hopes to major in biology and pursue a medical degree.

DOI: 10.36838/v5i1.13

IJHSR
ijhighschoolresearch.org
RESEARCH ARTICLE

The Effect of Steering Effort on the Simulated Rollover Dynamics Behavior of Cars

Lee Yoonsu

George Washington University Online High School, 44983 Knoll Square, Room 153, Ashburn, VA, 20147, U.S.A.; yoonlee9302@gmail.com

ABSTRACT: This study proposes the threshold level of steering effort to reduce rollover accidents. There is much research about the causes of rollover behavior during driving. The center of gravity height, tread length of road wheels, tire properties, and ESC is among the leading causes of rollover of vehicles. An enormous amount of research was done on those factors. First, the steering effort threshold value, which leads to loss of wheel grip, was tested. Second dynamic maneuver tests were done in a virtual environment with the help of CarMaker® vehicle dynamics software. By doing that, steering effort could be measured to understand how much effort is needed in those risky situations.

KEYWORDS: Rollover; steering effort; vehicle dynamics; cars.

Introduction

Rollovers are a type of collision in which a car tips over to its side or roof, runs off the road, and has a more severe fatality rate than other crashes. SUVs and pickup trucks have a higher tendency to roll over. Many factors in vehicle design affect this phenomenon, but the center of gravity height or wheel tread length is the leading cause of this problem. A National Highway Traffic Safety Administration (NHTSA) report in 2019 describes that the rollover rate of SUVs in fatal crashes was 21.2%. This rate exceeds the rollover rates in fatal crashes of all other common types of motor vehicles: cars, pickup trucks, vans, large trucks, and buses.[1] This higher fatality rate makes rollovers the main culprit of most deadly accidents. This phenomenon occurs in two ways. One is the collision-induced rollover, and the other is the steering input-induced rollover. These two rollovers are closely related to SUV vehicles' characteristics. This propensity to rollover could be better avoided if better-designed and tuned dynamics of the vehicles are sought and developed. The usual tuning guide to deviate this propensity in vehicles is the lessening of steering effort and the ESC (Electronic Stability Control) modification, which reduces human effort and stabilizes the behavior in tipping points of rolling over. Sivinski says, "as ESC saturates the on-road fleet in the coming years, it is likely that rollovers resulting from loss of vehicle control will continue to decline. Other types of rollovers, such as those caused by an impact with another vehicle, are not likely to be affected by the spread of ESC in the population."[2] The studies about ESC and vehicle control systems are more abundant than steering ones.

On-road rollovers due to vehicle maneuvering comprise only a tiny percentage of rollover crashes. Still, despite its small percentage, significant importance is given to steering input-induced problems for safety reasons.[3] So the objective of this study is to highlight the importance of the role of the steering system in risky maneuvers like J-turn or double lane change, which are the recommended tests for rollover validation.

For this study, a special bench test was prepared with the help of Halla University's car lab. Real steering threshold effort could be measured based on this; a practical virtual method was employed to prove this threshold value.

1.1 Technological background for simulation test:

Actual tests for dynamic maneuvers are dangerous and challenging to implement on normal roads because of traffic. And most developers of vehicles use a proving ground which is specially developed roads and environments for vehicle testing. Because it is safe and efficient for this kind of test, another way of doing a dynamic maneuver test is a simulation, which uses a vehicle, road, and driver in a mathematical model and evaluates the car in various maneuvers. Mostly the simulations are done in a completely virtual environment, but a valuable way of using simulations is to combine them with physical models. This is called a HIL (Hardware In the Loop) simulation. This makes the test more reliable and realistic. Because the interesting parts are real and don't need to be modeled in mathematical form, this study used steering gear as hardware, and the signals from the gear go to the virtual car model and steer the car. And the car model calculates the road wheel force and pushes or pulls the steering gear by the Hils actuator; in this way, they interact with each other.

Pfeffer and Koegeler developed the steering system HILS test with European car makers, and by using this method, they optimized the tuning map of the steering system to get the best steering feel and characteristics.[4,5]

The research about the virtual driver model is various. Most apply to everyday situations where the vehicle doesn't skid on the path due to an unavoidable slip angle. But some research on vehicle dynamics dealt with tire dynamics and driver behavior at the limits of handling, from lane keeping to drifting.[6,7] This discussion can be expanded to vehicle safety systems to avoid accidents effectively by taking the physical limitations of

DOI: 10.36838/v5i1.14

vehicles into account. To repeatedly evaluate a vehicle control system in the same situation, simulations with a suitable driver model are needed to provide reliable analysis results and satisfy cost and safety issues, especially at the limits of handling.

Methods

Equipment for steering effort measurement:

The equipment was used to test components and systems without requiring a complete vehicle. The steering wheel was connected to the input test actuator, and steering gear ends were connected to the two output test actuators. The simulation was the same as running offline in CarMaker®, but the real components were used instead of the software's steering model. Figure 1 shows the method used to measure the effort of grip loss and its bench and equipment.

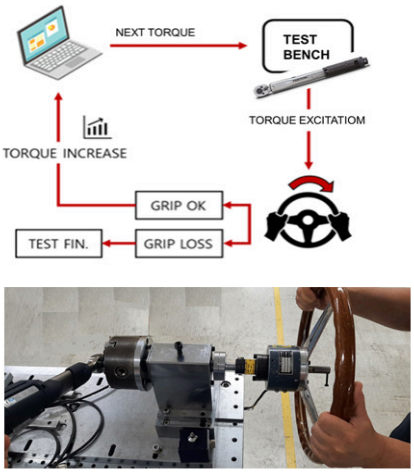

Figure 1: Schematic diagram and test equipment.

HILs dynamic maneuver test:

Rigs were used to test components and systems without requiring a complete vehicle. The steering wheel was connected to the input test actuator, and two tie rod ends were connected to the road wheel actuators. The simulation was the same as running offline in CarMaker®, but the real components were used instead of the software's steering model. And a standard SUV model was chosen for this study (Figure 2).

The steering torque is closely related to rack force, calculated by rack position, velocity, and acceleration. To control the vehicle's direction, the natural rack motion quantities were inputted to the vehicle simulation model by the rack motion feedback mechanism installed on the test bed.

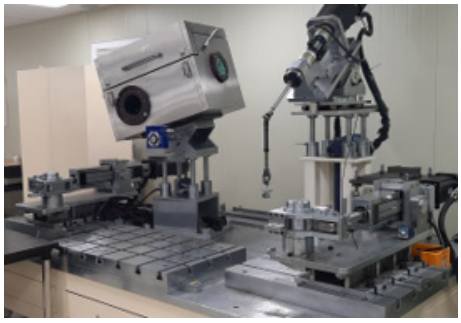

Figure 2: Steering HILS equipment (1 input /2 output actuator).

Most of the dynamic maneuver test covers open loop tests like steady state circular (ISO 4138), sine sweep (ISO 7401), and weave test, which doesn't require a driver's role in the test. But most subjective tests conducted in the proving ground were closed loop tests like ISO Lane change (ISO3888) or slalom and handling courses. The standard driver model was installed in the software to simulate the closed loop test on the HILS benches. Figure 3 shows closed loop test principles which feedback the vehicle response to the driver tasks.

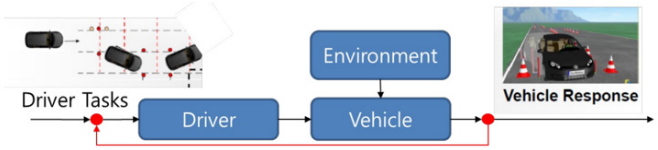

Figure 3: Closed loop test principle.

The experiment on Steering grip loss and the result:

A special test rig was devised to see the threshold of steering effort that makes a driver lose grip of a wheel. The test procedure was as follows: Evaluator generated the torque-based excitation by using a torque meter manually, and the evaluatee stood behind the wheel. The evaluator increased the torque until the evaluatee lost grip of the wheel and recorded the value. The grip loss effort was defined as the torque that makes one lose one's grip on the wheel and let the wheel rotate 60 degrees. This study selected 5 participants who could represent the age group between 18 and 60. And 20 tests were conducted for each person, and the threshold values were averaged. Figure 4 shows the distribution of these efforts and has a normal distribution.

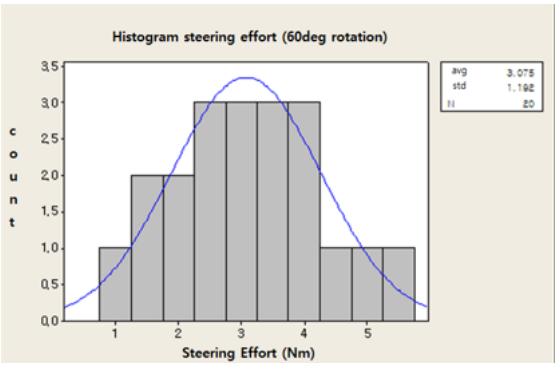

Figure 4: Histogram of grip loss effort.

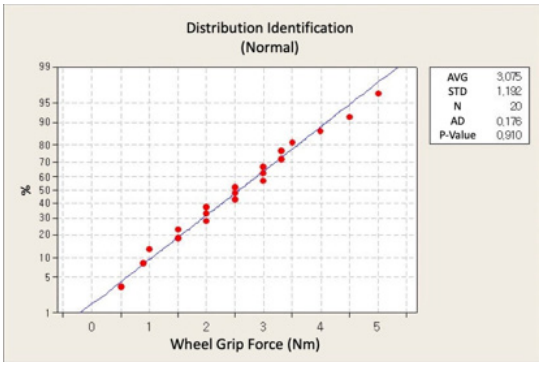

Figure 5: Distribution Identification.

DOI: 10.36838/v5i1.14

The p-value is a probability that measures the evidence against the null hypothesis. For an Anderson-Darling test, the null hypothesis is that the data follow the distribution. Therefore, lower p-values provide more substantial evidence that the data do not follow the distribution. P-values greater than 0.05 and Anderson-Darling statistic is small enough to conclude normal distribution. Most importantly, the average effort of grip loss was 3.075 Nm. And this shows that the effort that exceeds this value could make the driver lose control of the car and lead to a rollover.

High-risk dynamic maneuver test

Index development for dynamic maneuver test:

To be able to compare outputs from complete simulation and HILS tests in an objective way, key indexes were used. Indexes are effective since the behavior of the data is described in a scalar value, making it easier to compare. So, the most traditional and commonly used rollover index was defined using a 2D vehicle model as

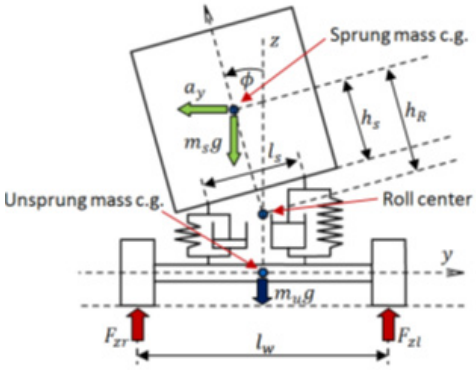

Figure 6: Rollover diagram in a 2D car model.

they are shown in Figure 6. Several researchers tried to invent a new rollover index for tripped rollover from external inputs such as forces.[8] But this study confines the rollover in the high lateral acceleration-induced rollover category. The formula is LTR (Load Transfer Ratio) in Equation (1). When the vehicle is lifted and the tire is off the ground, the vehicle could be said to have rolled over. The main parameters of the rollover index LTR are lateral acceleration a_y and roll over angle ∅ and the vehicle is said to be rolled over when LTR-value nears 1.

$$R = \frac{F_{zr}-F_{zl}}{F_{zr}+F_{zl}} = \frac{2m_s a_y h_R}{mgl_w} + \frac{2m_s h_R \tan\emptyset}{ml_w} \quad (1)$$

Where

F_{zr} F_{zl} = Left, Right-hand Tire Forces in the Z direction

M_s = sprung mass

h_R = Radius of sprung mass rotation for R.C

l_W = wheel tread distance

a_y = lateral acceleration

Test maneuvers

Double Lane Change:

Pylons were arranged as seen in Figure 7 and Figure 8. The test consisted of an entry and an exit lane with a length of 12m and a side lane with a length of 11m. The driver factor is the most influential in this test; objective results couldn't be anticipated in the past. Vehicle speed for this test ranged from 50 kph to maximum velocity, making the car roll over.

Reverse quick J-turn:

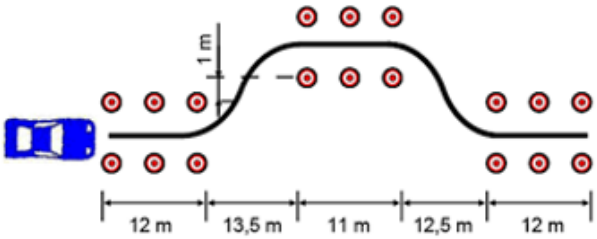

Figure 7: ISO 3888 double lane change.

This test is achieved by transferring the momentum of

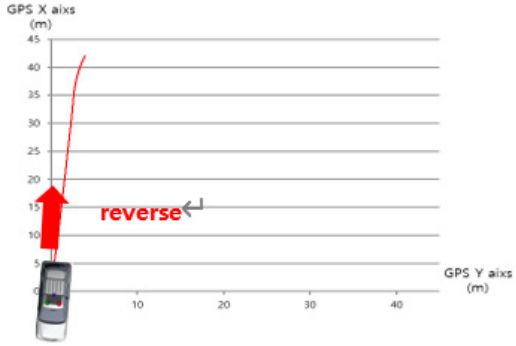

Figure 8: Reverse quick J-turn.

the car by reversing quickly in a straight line and then turning the wheel sharply while using a brake to lock the front wheels. The driver changes into a forward gear as the nose comes about. Figure 7 shows the x-y bird's eye view data used for the reverse quick J-turn test. And a virtual test run was created based on this data.

Sine with dwell:

The test has a steering input defined in terms of angle against time. It is a steering plus counter-steering maneuver that a panicked driver might apply to avoid an obstacle on the road. In this test, the possibility of unreasonable steer effort or steer lock was checked, and the performance of suspension and tires was also of interest other than steering performance. Typically vehicle speed is set to 80 kph, and steer input defined in Figure 9 should be implemented. The exact test condition is described in Table 1

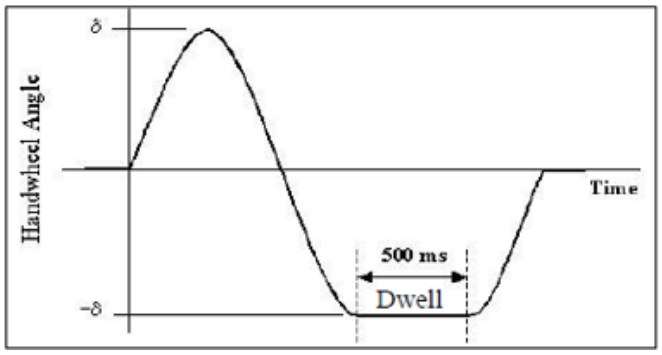

Figure 9: Sine with dwell test.

Table 1: Test mode for risky dynamic maneuvers.

Test mode	Vehicle Speed	Steer rate
reverse J turn	backward 40kph	Quick
double Lane Change	100kph	720deg/s
sine with dwell	80kph	1180deg/s

Results and Discussion

Dynamic test results and discussion

Double Lane Change:

Closed loop tests were implemented by using optimized driver models. Trials were proceeded by measuring the necessary item-related motion and feeling of the steering. Vehicle speed was increased from 50 to 100 kph (Figure 10), and whether steering effort crossed the upper threshold value of 3.07 Nm was checked during the test.

Figure 10: Simulation test for DLC.

Steering wheel angle and torque values were measured in the HILS test and simulation test, which are displayed in Figure 11. No abnormality was found until 70 kph, but the car rolled over at 80 kph, and the maximum steer torque was observed to be over 6.54 Nm which is well over the threshold value. The driver could have lost the wheel's grip and couldn't escape the rollover

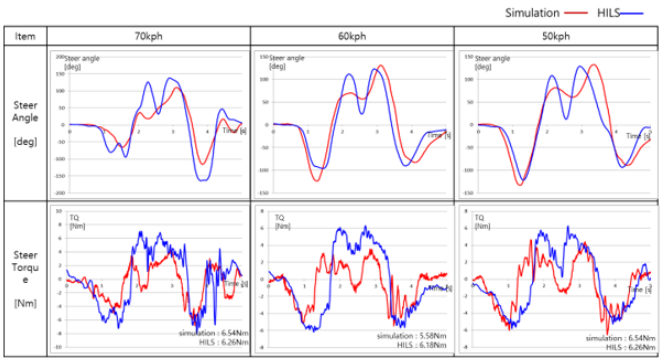

Figure 11: Dynamic maneuver test for DLC (steer angle and torque).

Reverse quick J-turn:

Putting the car in reverse, speeding up, and using a sharp steering maneuver were implemented at reasonable vehicle speed. This test doesn't require a driver model because this is an open-loop test. The test scene was captured in Figures 12-14. Forward quick J-turn is also one of the most dangerous maneuvers to implement on the road. But reverse quick J-turn is a more severe maneuver and demands lots of steering effort because this kind of turning makes a more sudden change in direction and generates a more lateral acceleration. The big difference between the simulation test and the HILS rig test derived from the fact HILS actuator was delayed slightly more than the simulation, and that caused the fluctuation in the data of the latter part.

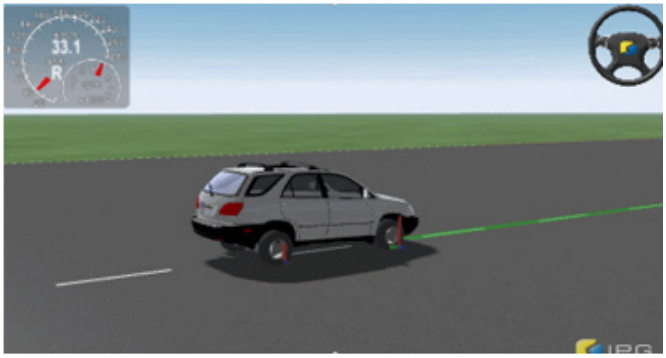

Figure 12: Simulation test for reverse J-turn.

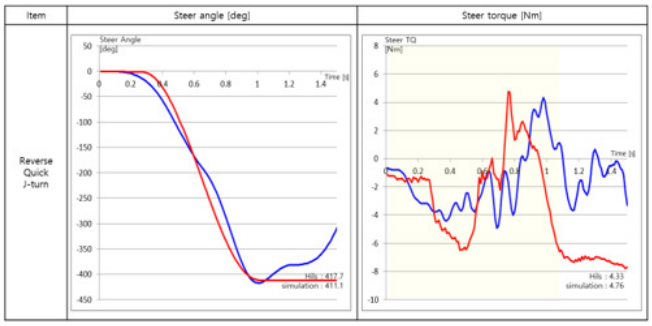

Figure 13: Test for reverse J-turn (steer angle and torque).

Sine with dwell:

This is also an open-loop test with a vehicle speed of 50-80 kph. The test result is shown in Figure 14.

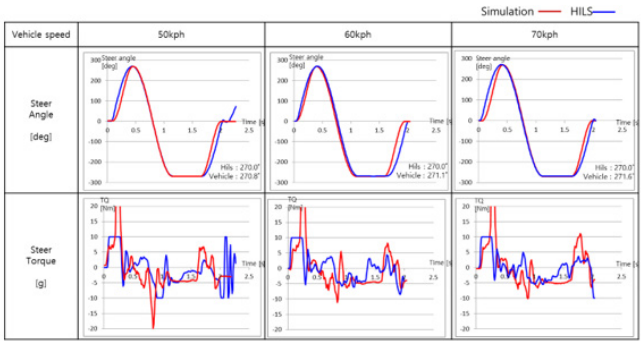

Figure 14: Test for sine with dwell (steer angle and torque).

HILS steering effort couldn't measure the maximum because of the limit of torque sensor at this high steering speed of 1500 deg/s, and test at the rate of 80 kph couldn't be completed because of instability of the vehicle, and the HILS showed the same phenomenon.

DOI: 10.36838/v5i1.14

Conclusion

Nowadays, the steering system helps the driver control the vehicle with a motor-driven intelligent assist function called an advanced driver assistance system. UN/ECE R 799 requires the steering control effort necessary to override the directional control provided by the system shall not exceed 50 N, which means 10Nm below (if the lever ratio of the wheel is 0.2m) if we compare the steering rollover control effort threshold value proposed here with that of UN/ECE R 79. This study shows that the steering wheel grip loss effort is far below the regulation. The actual bench test result specifies that the average threshold value of steering effort to lose the wheel's grip is 3.07 Nm. And the dynamic simulation tests conducted using vehicle dynamics software and HILS also shows rollover could happen below 10Nm of steering control effort. So steering control effort requirements should be changed to reduce the rollover fatality.

Even though the actual value from the real vehicle test could not correlate with the result of this study, the well-built and correlated vehicle model, which was used by the university's other project and HILS test, showed a plausible outcome. Using this simulation test on the bench, risky real vehicle tests could be covered and could have protected the real test driver from the potential fatality of the test. And most of all, the rig test could cover the lack of objectiveness of the vehicle test and give it a more repeatable and reproducible test.

Max steer effort per each test case:

Max steer efforts per each test case exceeded the threshold value (refer to Table 2) and need to be regulated for driver's safety in the future. Vehicle makers need to make the steering system easier to handle in this dynamic test and risky situation.

Table 2: Test modes and their test result.

No.	Test mode	Rollover R	Max Steer Effort (Nm)
1	Reverse Quick J_TURN	0.81	4.76
2	Double Lane Change	0.62	6.54
3	Rollover (Sine with dwell)	0.59	Over 20

The developed and utilized validation methods in this study were supported by Halla university's test lab and greatly appreciated for their help. The indicators such as rollover index and steering effort values are good metrics to investigate the impact of the stability and controllability of the SUV vehicle.

References

1. https://driving-tests.org/driving-statistics
2. Bob Sivinski, "The Effect of ESC on Passenger Vehicle Rollover Fatality Trends", NHTSA research note, DDT HS B12 031, 2014
3. Narahari Vittal Rao, "An Approach To Rollover Stability In Vehicles Using Suspension Relative Position Sensors And Lateral Acceleration Sensors", Texas A&M University master of science degree, 2005
4. P.E. Pfeffer, H.-M. Koegeler, "Model-Based Steering ECU Calibration on a Steering in the Loop Test Bench", Chassis. Tech, 2015
5. P.E. Pfeffer, M. Nigel, "Model-Based Steering ECU Application Using Offline Simulation (Software in the Loop)", AVEC 16, 2016
6. Li HZ, Li L, Song J, Yu LY. Comprehensive lateral driver model for critical maneuvering conditions. Int Journal of Automotive Technology. 2011;12(5)
7. Hindiyeh RY. Dynamic and control of drifting in automobiles [Ph.D. dissertation]. Stanford University; 2013
8. G. Phanomchoeng, R. Rajamani, "New rollover index for detection of the tripped and untripped rollover, IEEE, 2011
9. UN/ECE/TRANS/505/Rev.1/Add.78/Rev.3/Amend.2, 2018

Author

Yoonsu Lee is a Senior at George Washington University Online High School in Ashburn, VA. He loves researching mechanical engineering, AI, computer science, and cybersecurity.

IJHSR
ijhighschoolresearch.org
■ REVIEW ARTICLE

Small Molecule-Drug Conjugates: Targeted Tunable Therapy for Cancer Treatment

Lucy L. Wang

Gunn High School, 780 Arastradero Rd, Palo Alto, California, 94306, USA; lucywang860@gmail.com

ABSTRACT: Cancer is one of the leading causes of death worldwide, with over 1.6 million people affected yearly in the U.S. alone. Common treatments such as chemotherapy harm healthy cells and bring dangerous side effects. In the search for safer solutions, scientists have turned to a new field of study: targeted therapy. In the past decade, attention has shifted to the use of substances able to specifically target and identify cancer cells, minimizing harsh side effects and damage to healthy organs. With the success of targeted therapy like antibody-drug conjugates, a new area of research known as small molecule-drug conjugates has risen. A relatively new field, small molecule-drug conjugates are a more cost-effective and efficient treatment for eliminating cancer. With its unique mechanisms and potential to eliminate cancer cells quicker than previously targeted therapies, small molecule-drug conjugates present a new perspective on therapeutics. Using current preclinical and clinical data, this review examines the potential and future of small molecule-drug conjugates, emphasizing comparisons to existing treatments. In addition, this review highlights its novel scientific mechanisms while identifying critical research areas for a better understanding of targeted cancer therapy.

KEYWORDS: Chemistry; Organic Chemistry; Medicinal Chemistry; Therapeutic; Targeted Therapy.

■ Introduction

As the second leading cause of death in the world, cancer involves the rapid, uncontrollable growth of specific body cells with the ability to spread to other parts of the body.[1,2] Current treatments for cancer, such as chemotherapy, involve cytotoxic agents to prevent the rapid division of these cancerous cells.[3] While effective, these traditional chemostherapeutic agents lack both specificity and selectivity.[4] Generally, these highly toxic agents cannot distinguish between healthy and cancer cells, killing any cell that grows and divides quickly. This failure of cell distinction leads to many adverse side effects, including hair loss, fatigue, nausea, and mouth sores.[5]

In the 1900s, Paul Ehrlich, a Nobel Prize-winning German scientist, envisioned a 'magic bullet' that rationally targeted diseases with the ability to distinguish between healthy and cancer cells.[6] Now, nearly a century later, his vision has become a reality known as targeted therapy, the backbone of precision medicine. As selective alternatives, targeted therapies not only decrease unwanted toxic exposure to healthy cells but also promote the safety and efficacy of therapeutics. Modern targeted anticancer treatments include kinase inhibitors, monoclonal antibodies, antibody-drug conjugates (ADCs), small molecule-drug conjugates (SMDCs), and more.[3] In recent years, ADCs have risen in popularity and become promising sought-after research areas. With 12 ADCs on the market, such as trastuzumab deruxtecan, trastuzumab emtansine, and brentuximab vedotin, ADCs are being pursued by powerful biotechnology companies such as Genentech, Seagen, and ImmunoGen.[7,8] ADCs consist of a tumor-specific antibody attached to a potent chemotherapeutic agent via a linker. Seagen's ADC brentuximab vedotin, for example, consists of an anti-CD30 monoclonal antibody and monomethylauristatin E to treat Hodkin's lymphoma.[7] The antibody specifically targets surface proteins highly expressed on cancerous tumor cells. Once successfully internalized, the ADC and its linkers are broken by lysosomal enzymes, and the active drug is released to inhibit the assembly of microtubules essential for cell division. Because ADCs are a targeted therapy, they reduce the side effects compared to chemotherapy. ADCs are often limited by extravasation into nearby areas, premature drug release, *in vivo* selectivity, and malignant accumulation in healthy organs. Because of these properties, ADCs are not entirely without side effects either.[3]

SMDCs, although similar to ADCs, present a more cost-effective and rapid treatment with simpler synthesis processes.[9] Unlike antibodies in ADCs, SMDCs use targeting ligands, molecules that bind to a specific receptor overexpressed in cancerous cells. Because targeting ligands are both smaller and lighter than traditional antibodies, SMDCs have a drastically smaller size and molecular weight, allowing for quicker and easier penetrating tumors. SMDCs consist of 4 parts: a targeting ligand, linker or spacer, cleavable bond/bridge, and cytotoxic agent.[3,4] With a variety of SMDCs currently undergoing clinical review, SMDCs bring a new perspective to cancer treatment and targeted therapy. This review article aims to highlight distinctive mechanisms, evaluate efficacy compared to already existing therapies, and present a critical discussion of the potential of SMDCs through analysis of current conjugates under preclinical and clinical development.

■ Discussion

Targeting Ligands:

The targeting ligand is a crucial element to SMDCs as it serves a similar function to the antibodies of ADCs. Most

DOI: 10.36838/v5i1.15

targeting ligands function by attaching to a receptor overexpressed on the surface of cancerous tumors and proceed to enter the cell via an endocytosis process. Some receptors can then resurface to the cell's surface to bind to another targeting ligand. Selection of both the targeting ligand and its receptor requires extensive review because the safety, drug concentration, and SMDC success rate largely depend on the targeting ligand.[7]

The targeted receptor must be overexpressed in cancer cells compared to normal cells. An ideal minimum rate would be three times overexpression. In current SMDC development, however, most are categorized into the 2-3 times overexpression range. Furthermore, it's essential to consider both the receptor recycling rate and the nature of healthy cells compared to cancer cells.[10] A majority of normal tissues are non-mitotic, while cancer tissues are. Thus meaning that normal tissues are less sensitive to antimitotic chemotherapeutic agents. Cancer tissues also require and absorb much more nutrients to sustain their rapid growth, increasing their sensitivity to therapies and receptor recycling rate. Because the recycling rate is faster in cancerous cells than in healthy cells, SMDCs can enter cancerous cells faster, allowing more SMDCs to be absorbed by the cell in a similar amount of time.[10,11]

When selecting a targeting ligand, an essential factor to consider is the binding affinity, as it is inversely proportional to the concentration of the cytotoxic agent. The higher the binding affinity of a ligand, the lower the drug dose is needed to achieve the desired receptor saturation. High binding affinities thus simultaneously decrease the risks and toxicity to healthy cells from the cytotoxic drug.[3] From recent data on SMDC development, it has been analyzed that 10 Kd is the maximum dissociation constant value of the ligand affinity for their receptors.[10] If ligands cannot meet this requirement, ligation of multiple ligands to the same anti-cancer payload is possible and compensates for the inadequate ligand affinity. For example, the Paclitaxel conjugate has a median lethal dose of LD50 with a peptide ligand of about 2.5μM but was increased to 160nM simply by adding a second targeting peptide to the conjugate.[10] A possible downside of multiple ligands exists in the increase in molecular weight. The size of ligands is crucial as they affect permeability and excretion. The larger the molecular weight, the more strenuous it is for therapeutic drugs to diffuse into tumors. Additionally, high molecular weight therapeutics are not easily excreted from the body, resulting in adverse toxicities to healthy cells.[9] For more straightforward and more efficient conjugation, ligands also require a derivatizable functional group such as carboxylic acid, amine, alcohol, thio, etc. This permits easy attachment to the spacer via more straightforward chemical reactions. It has, however, been observed that such functional groups may interfere with interactions between the ligand and receptor and possibly obstruct the two from binding. Therefore, it's crucial to consider functional group placement and ensure it lies in an area that will not interfere with binding.[10]

A wide variety of receptors and targeting ligands undergoing clinical or preclinical trials exist, and among these, a few receptors have shown promising outcomes. A popular receptor is the folate receptor (FR), a glycosylphosphatidylinositol-linked membrane protein, and its corresponding ligand, vitamin folic acid (FA). Folic acid, known as folate, pteroyl-L-glutamic acid, and vitamin B9, is not biologically active. Its derivatives, however, perform the necessary biological functions.[7] FR is poorly expressed on most cells but overexpressed in many cancers, including breast, lung, kidney, and colon. Over 80% of the cells in epithelial ovarian cancers alone express FR.[3,10] Because of such properties, folate-linked drugs are quite common in trials.[10] Vintafolide, otherwise EC145, is a microtubule-destabilizing agent that inhibits mitosis using a water-soluble folate conjugate of desacetylvinblastine monohydrazide (DAVLBH). The DAVLBH drug moiety is linked to a hydrophilic folate-peptide compound with a cleavable disulfide bond.[4,12] Vintafolide reached a Phase 3 clinical trial before failing to demonstrate efficacy in progression-free survival in patients with ovarian cancer.[13] There exist many similar SMDCs to vintafolide with a similar folate-vinca alkaloid SMDC such as vincristine (EC0275), vindesine (EC192), vinorelbine (EC1041), vinflunine (EC1044).[4] A more well-known drug Gleevec (imatinib), is utilized as a payload such that folic acid acts as a ligand for the folate receptor. Common SMDCs with targeting ligands other than FA that are in or have been in the clinical review include glucose transporter 1 (GLUT1), aminopeptidase N (APN), and low-density lipoprotein receptor-related protein 1 (LRP1), and prostate-specific membrane antigen (PSMA or FOLH1).[3,4,14,15] Other less common and less expressed receptors, but still in sufficient quantities for use in targeted drug delivery, include somatostatin receptor 2 (SSTR2), cholecystokinin type B receptor (CCKBR), and sigma non-opioid intracellular receptor 1 (SIGMAR1).[10,16,17]

Linker:

The linker connects the targeting ligand to the therapeutic payload and contains both the spacer and cleavable bridge. If the cytotoxic drug and targeting ligand is too close in proximity, receptor binding is interfered with, and a spacer is necessary.[10] While linkers play a crucial role in receptor binding; incompatible linkers can lower binding affinity and cause undesirable intramolecular associations.[3,4] One of the most significant advantages of the linker is that it can be modified to improve the hydrophilicity of the SMDC. Both the targeting ligand and therapeutic agent are hydrophobic to maximize membrane permeability and receptor affinity.[9] This hydrophobicity caused by the targeting ligand leads to unnecessary interactions with lipoproteins, different receptors, lipids, and membranes. Water-soluble spacers such as polysaccharides, PEGs, hydrophilic amino acids, and peptidoglycans are used to combat this. First-generation spacers were composed primarily of carbohydrates, acidic residues, and saccharo-amino acids.

Second-generation spacers, however, have been improved and consist of glutamic acid and glutamine.[3] PSMA-targeted imaging agents, for example, have increased affinities when ligand 2-[3-(1,3-dicarboxy propyl)-ureido]pentanedioic acid (DUPA) is connected via an alkyl chain of a minimum of 6 atoms.[10] Linkers must be able to withstand and remain stable during circulation in the blood. Unstable linkers will

lead to premature drug release and additional toxicity. Recent research has shown hope for thio-substituted pyridazinediones as linkers for their stability to blood thiols and trigger in cleavable linker design. It undergoes substitution in the presence of glutathione (GSH), a substance found to exist in high concentrations intracellularly.[18]

Cleavable Bridge:

SMDC efficacy depends on the reliability of the cleavable bridge to release the cytotoxic payload at the right location and rate. Unstable cleavable bridges will release the drug before it reaches the tumor destination, while bridges unable to release the drug once inside the cell are less effective. There exist two popular triggering methods: the use of disulfide bond-based linkers or pH-sensitive cleavable bridges.[9]

The pH-sensitive bridges are popular because most endosomal compartments are acidic, creating a lower intracellular pH.[4] These bridges maintain stability during circulation at a pH of 7.4 but aim to cleave at the pH of endosomes (pH 5.5-6.2) and lysosomes (pH 4.5-5.0). This method has proved successful in Pfizer's Mylotarg (gemtuzumab ozogamicin) ADC. Although the success of pH-sensitive bridges, many new drugs in development are moving away from acid-cleavable bridges due to low selectivity and difficulty synthesizing accurately.[19]

On the other hand, disulfide bonds have also been applied to a vast range of drug delivery designs in SMDCs. The ADCs Mylotarg and Besponsa, both from Pfizer and a pH-sensitive hydrazine linker, also use reducible disulfides, showing great clinical success.[19] The mechanisms are activated by the enzymes thioredoxin (TRX) and glutaredoxin (GRX), which are responsible for initiating the cleavage of disulfide bonds and are generously available inside cancer cells. The downside, however, lies in the unsecure stability of such disulfide bonds. Research has also shown that disulfide linkers can become unstable due to the abundance of free thiol compounds such as GSH, cysteine, and homocysteine found outside the tumor cells, such as in red blood cells.[20]

Other successful cleavable bridges originating from use in ADCs are now also being investigated for use in SMDCs. Currently, a class of enzyme cleavable linkers has risen to become a popular research topic in ADCs known as dipeptide-containing linkers. Most ADCs in clinical trials contain some form of a dipeptide-containing linker, including FDA-approved brentuximab vedotin.[19] Valine-Citrulline (VCit) dipeptide linkers are one of the most common dipeptide linkers as they can be found in various successful ADCs, such as Adcetris. During a study on current VCit linkers Val-Cit, Ser-Val-Cit, and Glu-Val-Cit, Glu-Val-Cit demonstrated strong stability over 14 days in mouse plasma, while the other two fully hydrolyzed.[21] VCit linkers target cathepsin B, a cysteine protease overexpressed in a wide range of cancerous tumors. VCit linkers, especially Glu-Val-Cit, provide a more stable and specific option for cleavable linkers.[19]

Besides those mentioned above, other successful cleavable linkers exist, such as glutathione (GSH), peroxiredoxins, thioredoxin, NADH, and NADPH.[3] While non-cleavable bridges also exist, research has revealed that such SMDCs induce less biological activity. In a SAR study done on folate-DVLBH SMDCs, 2 SMDCs with non-cleavable thioether-based linkers, EC1142 and EC1177, showed significantly less activity compared to related SMDCs with cleavable linkers.[4]

The primary pathway for self-cleaving linkers is receptor-mediated endocytosis. Once internalized via endocytosis, the SMDC complex reaches the lysosome, where the cytotoxic drug is released via deconjugation and kills the cancerous cell. Proper deconjugation is crucial, and select SMDCs enact elimination cascades into linkers to ensure all atoms of the spacer are removed from the released drug.[3,10]

Payload:

The therapeutic payload, or in other words, an active drug, is the central fragment of the SMDC designed to kill the cancer cell. The value of a payload, however, does not simply rely on the cytotoxicity of the drug. The FDA evaluates a payload based on efficacy and safety.[3] It must thus follow strict criteria to ensure adequate elimination of cancer cells. It must be toxic enough to kill cells, avoid intracellular metabolism, and reach the intended target.[10] To meet the criterion, it's crucial to examine multiple aspects of the payload, including release rate, cell activity, intracellular stability, and binding affinity.[9]

Firstly, the potency of the payload depends on the type and number of receptors present on the surface of a single cancer cell. If the number of receptors is towards the smaller end of the spectrum, higher IC_{50} values of the payload are necessary to suffice for the loss in the amount of drug able to enter the cell. For receptors that exceed 1 million per cancer cell, a general IC50 value of 10nM is necessary. For receptors with over 100 million per cancer cell, however, a minimum IC_{50} of 1 μM is sufficient. Current and past SMDCs in trials have stayed in the low nanomolar or submicromolar ranges, such as Mitomycin C and Epothilone.[4] While the payload's efficacy can be increased by adding more warheads to the same targeting ligand, it is a unique approach as such synthesis proves to be a difficult challenge. It is much more time and cost-effective to develop a single drug with tenfold higher potency than to attach ten payloads of lower potency to the same ligand.[10] A notable exception, however, is GRN1005 (ANG1005), a peptide-drug conjugate with three molecules of paclitaxel attached to its ligand; paclitaxel is a common drug used in chemotherapy. Unfortunately, it was discontinued and never reached a Phase 3 study.[22,23]

Cytotoxic agents kill cancer cells by inhibiting the fundamental cellular functions necessary to survive, such as DNA replication, cytokinesis, anti-apoptotic processes, and protein synthesis. More rare agents aim to block essential metabolic mechanisms, such as glycolysis, glutaminolysis, and sugar transport but require a more specific design and consideration. To inhibit such biological functions, easily modifiable functional groups are necessary, such as carboxyl, amines, sulfhydryl, aldehyde, etc. It is also essential to consider the membrane permeability of payloads as released drugs must be able to escape the encapsulating endosome to begin the cancer cell elimination process. Targeted therapies have often found membrane permeability to be a difficult obstacle: Research has

DOI: 10.36838/v5i1.15

shown that peptides, oligonucleotides, antibodies, and proteins do not diffuse passively across lipid bilayers, partly due to their high molecular weights, charges, and size. Instead, alternatives such as cell-permeating peptides, pore-forming fusogenic or cationic lipids, and photothermally activated complexes have all been considered and investigated.[10] More research in this area is needed to evaluate SMDCs and their endosomal escaping abilities properly.

Conclusion

SMDCs in Comparison:

With a wide range of cancer therapies emerging, SMDCs stand out with their effective and cost-efficient approach. As a targeted treatment, SMDCs have fewer side effects than chemotherapy.[24,25] Chemotherapy involves only a cytotoxic payload, while SMDCs have targeting ligands and spacers for a more complex but targeted approach. SMDCs can reduce unwanted toxicities, a key fault in chemotherapy. Because SMDCs also contain water-soluble spacers and linkers, such as polysaccharides and hydrophilic amino acids, the hydrophilicity of SMDCs is greatly improved. For chemotherapy, however, water solubility was a limiting factor for many first-line anticancer agents such as paclitaxel (PTX) and camptothecin (CPT).[4] SMDCs also consist of different parts, permitting each section to be modified for optimal drug properties. Chemotherapy, unfortunately, is less flexible due to only consisting of a cytotoxic drug. From the ligand's type and size to the spacer's length and stability to the cleavable bridge's rate of dissociation to the strength and number of payloads, SMDCs have a variety of modifiable factors. This allows for more possibilities, research, and control over side effects.

SMDCs also have a variety of additional applications besides those previously discussed. For one, SMDCs have proven to be effective in radionuclide therapy. Targeted drug delivery therapies are used to clinically diagnose malformations and metastasized cells by combining targeting ligands with radionuclides. The first SMDC to pass clinical trials and be approved, Lu^{177}-DOTATATE, is a radioactive isotope conjugated to somatostatin used for the treatment of gastroenteropancreatic neuroendocrine tumors.[33] Results reveal Lu^{177}-DOTATATE resulted in both lowered toxicity and higher efficacy than somatostatin or radioisotope therapy alone.[3] SMDCs are also used in cancer diagnosis when conjugated with cancer-imaging agents. Such SMDCs with radio-imaging molecules or fluorescence allow scientists to inspect cancerous tumors for diagnosis and surgery. Some diagnostic strategies include an SMDC with a fluorophore conjugated to a drug, known as fluorophore-drug conjugates.[26] These technologies provide scientists with highly specific illuminated pathways of transport, real-time drug monitoring, and drug distribution.

ADCs and SMDCs are similar, with their only physical difference being an antibody versus a small molecule targeting ligand. While both serve as targeted treatments and reduce unnecessary toxicities to healthy cells, their differences lie in permeability and production. Because antibodies are much larger than small molecule targeting ligands, ADCs have a notably more considerable molecular weight and size than SMDCs. Their large size is the basis of tissue penetration being a difficult challenge to overcome.[27] SMDCs' lower molecular weights allow for easy tissue penetration.[3] In terms of production, SMDCs are composed of small molecules, which involve controllable and stable synthesis processes. These processes are not only more straightforward than ADC synthesis but also more cost-effective.

As a relatively new field of targeted treatment, SMDCs have a considerably smaller number of drugs currently in clinical trials. At the same time, ADCs' success lives in 12 available medications on the market, with more in clinical trials. Based on the statistics alone, ADCs present a more promising approach to targeted cancer treatment. However, more data, time, and research are needed to draw a firm conclusion between the two. Both are undeniably promising areas of targeted therapies that bring a new generation of advanced cancer treatments.

Current Clinical Trial Analyses:

There exists a variety of SMDCs currently in the preclinical or clinical phase. Two radionuclide SMDCs are presently approved and available on the market, Lu^{177}-Dotatate, and Lu^{177}-PSMA-617. Currently, of those SMDCs in trials, the most popular targeted receptor would be the folate receptor detailed earlier. A popular and promising SMDC with such folate targeted receptors, vintafolide (EC145), had reached a phase 3 trial but was unfortunately discontinued due to little progress shown during the study.[28] Vintafolide was a pioneer in folate receptors in SMDCs, and since then, a variety of folate-targeted conjugates have reached clinical trials.

More recently, attention has focused on a drug called PEN-866, a heat shock protein 90 (HSP90) inhibitor drug conjugate. It consists of a cleavable carbamate linker tied to the cytotoxic payload topoisomerase 1 (SN-38). HSP90 is strongly overexpressed in cancerous tumors and is a promising receptor. PEN-866 is currently in phase I/II trial with hopes for the trial to be completed within the next few years.[3]

Another novel compound, VIP236, emerged from a preclinical study with exceptionally favorable results. The SMDC consists of a stable, non-peptidic ligand $\alpha V\beta_3$ binder connected to a newly modified drug camptothecin payload (VIP126). The $\alpha V\beta_3$ binder enables the drug to target and bind to the protein $\alpha V\beta_{33}$ integrin. The two parts are linked together and can only be broken via the enzyme neutrophil elastase, which is found in high quantities in cancerous tumors. This ensures the cytotoxic payload won't be released prematurely until the SMDC reaches the target site where there is an abundance of neutrophil elastase. The treatment reduced tumor progressions and maintained healthy tolerability in all *in vivo* models tested.[29]

Different receptors, such as luteinizing-hormone-releasing hormone (LHRH) receptors, are currently being researched. It is overexpressed in various tumor types, including prostate, breast, ovarian, pancreatic, and more. The drug EP-100 is a relatively new anticancer SMDC consisting of the natural LHRH linked to a cationic membrane-disrupting peptide that has reached the phase II study. Besides EP-100, a variety of SMDCs targeting this LHRH receptor, including LHRH conjugates with RNase A and pokeweed protein.[30]

Finally, various targeted anticancer treatments are similar to SMDCs in development, such as peptide receptor radionuclide therapies (PRRT). PRRTs share similar structures to SMDCs with ligands and spacers. Currently, ^{177}Lu-edotreotide is in a phase 3 trial to investigate the effects of this radiolabeled somatostatin against gastroenteropancreatic neuroendocrine tumors.[31]

Another targeted therapy with similar mechanisms to SMDCs is proteolysis targeting chimeric (PROTAC). A very popular area of study recently, PROTAC targets protein degradation, which is crucial to several cellular processes such as gene transcription, DNA pairing, cell cycle control, and apoptosis. PROTAC molecules use the ubiquitin-proteasome system (UPS) to degrade target proteins by combining with the target protein through E3 ligase and form a ternary complex which instigates the degradation process. PROTACs bring a unique perspective as they do not inhibit proteins but degrade them. Several PROTACs have entered clinical studies and shown positive results, such as ARV-110 and ARV-471.[32] PROTACs have a similar structure to SMDCs as they contain a ligand for the target protein and a linker. The difference lies in the E3 ligase recognition moiety of the PROTAC, the cytotoxic payload of the SMDC, and the passive diffusion for PROTAC compared to the receptor-mediated endocytosis of SMDCs through cells.

Currently, a healthy amount of SMDCs presently being studied in preclinical and clinical development. With one SMDC already on the market, SMDCs quickly advance past clinical studies. Considering clinical trials for anticancer targeted treatments require more extended periods of time to study and the fact that SMDCs are a new area of research, it is understandable for there to be fewer SMDCs available on the market compared to other therapies. It is notable, however, that SMDCs and ADCs do not erase all side effects but instead provide a more tunable and adjustable therapeutic alternative. Targeted medicines that share similar mechanisms to SMDCs, such as PRRTs and ADCs, have shown positive results in clinical trials and on the market, leading to hopeful expectations for the future of SMDCs.

References

1. Cancer Statistics - NCI. https://www.cancer.gov/about-cancer/understanding/statistics (accessed 2022-06-23).
2. Cancer - Our World in Data. https://ourworldindata.org/cancer (accessed 2022-06-23).
3. Patel, T. K.; Adhikari, N.; Amin, S. A.; Biswas, S.; Jha, T.; Ghosh, B. Small Molecule Drug Conjugates (SMDCs): An Emerging Strategy for Anticancer Drug Design and Discovery. New J. Chem. 2021, 45 (12), 5291–5321. https://doi.org/10.1039/ D0NJ04134C.
4. Zhuang, C.; Guan, X.; Ma, H.; Cong, H.; Zhang, W.; Miao, Z. Small Molecule-Drug Conjugates: A Novel Strategy for Cancer-Targeted Treatment. Eur J Med Chem 2019, 163, 883–895. https://doi.org/10.1016/j.ejmech.2018.12.035.
5. Side Effects of Chemotherapy - Cancer Council Victoria. https://www.cancervic.org.au/cancer-information/treatments/treatments-types/chemotherapy/side_effects_of_chemotherapy.html (accessed 2022-06-23).
6. Valent, P.; Groner, B.; Schumacher, U.; Superti-Furga, G.; Busslinger, M.; Kralovics, R.; Zielinski, C.; Penninger, J. M.; Kerjaschki, D.; Stingl, G.; Smolen, J. S.; Valenta, R.; Lassmann, H.; Kovar, H.; Jäger, U.; Kornek, G.; Müller, M.; Sörgel, F. Paul Ehrlich (1854-1915) and His Contributions to the Foundation and Birth of Translational Medicine. JIN 2016, 8 (2), 111–120. https://doi.org/10.1159/000443526.
7. Vlahov, I. R.; Leamon, C. P. Engineering Folate–Drug Conjugates to Target Cancer: From Chemistry to Clinic. Bioconjugate Chem. 2012, 23 (7), 1357–1369. https://doi.org/10.1021/bc2005522.
8. Tong, J. T. W.; Harris, P. W. R.; Brimble, M. A.; Kavianinia, I. An Insight into FDA Approved Antibody-Drug Conjugates for Cancer Therapy. Molecules 2021, 26 (19), 5847. https://doi.org/10.3390/molecules26195847.
9. Small Molecule-Drug Conjugates (SMDCs): Novel Targeted Therapy | Biopharma PEG. https://www.biochempeg.com/article/196.html (accessed 2022-06-23).
10. Principles in the design of ligand-targeted cancer therapeutics and imaging agents | Nature Reviews Drug Discovery. https://www.nature.com/articles/nrd4519 (accessed 2022-06-23).
11. Rana, A.; Bhatnagar, S. Advancements in Folate Receptor Targeting for Anti-Cancer Therapy: A Small Molecule-Drug Conjugate Approach. Bioorg Chem 2021, 112, 104946. https://doi. org/10.1016/j.bioorg.2021.104946.
12. Li, J.; Sausville, E. A.; Klein, P. J.; Morgenstern, D.; Leamon, C. P.; Messmann, R. A.; LoRusso, P. Clinical Pharmacokinetics and Exposure-Toxicity Relationship of a Folate-Vinca Alkaloid Conjugate EC145 in Cancer Patients. J Clin Pharmacol 2009, 49 (12), 1467–1476. https://doi.org/10.1177/0091270009339740.
13. Novartis wins FDA OK for radiopharmaceutical drug, cashing in on Endocyte deal. BioPharma Dive. https://www.biopharmadive.com/news/novartis-fda-approval-pluvicto-prostate-cancer-endocyte/620973/ (accessed 2022-06-23).
14. Corti, A.; Pastorino, F.; Curnis, F.; Arap, W.; Ponzoni, M.; Pasqualini, R. Targeted Drug Delivery and Penetration into Solid Tumors. Med Res Rev 2012, 32 (5), 1078–1091. https://doi.org/10.1002/med.20238.
15. Ciuleanu, T. E.; Pavlovsky, A. V.; Bodoky, G.; Garin, A. M.; Langmuir, V. K.; Kroll, S.; Tidmarsh, G. T. A Randomised Phase III Trial of Glufosfamide Compared with Best Supportive Care in Metastatic Pancreatic Adenocarcinoma Previously Treated with Gemcitabine. Eur J Cancer 2009, 45 (9), 1589–1596. https://doi.org/10.1016/j.ejca.2008.12.022.
16. Huo, M.; Zou, A.; Yao, C.; Zhang, Y.; Zhou, J.; Wang, J.; Zhu, Q.; Li, J.; Zhang, Q. Somatostatin Receptor-Mediated Tumor-Targeting Drug Delivery Using Octreotide-PEG-Deoxycholic Acid Conjugate-Modified N-Deoxycholic Acid-O, N-Hydroxyethylation Chitosan Micelles. Biomaterials 2012, 33 (27), 6393–6407. https://doi.org/10.1016/j.biomaterials.2012.05.052.
17. Brabez, N.; Nguyen, K. L.; Saunders, K.; Lacy, R.; Xu, L.; Gillies, R. J.; Lynch, R. M.; Chassaing, G.; Lavielle, S.; Hruby, V. J. Synthesis and Evaluation of Cholecystokinin Trimers: A Multivalent Approach to Pancreatic Cancer Detection and Treatment. Bioorg Med Chem Lett 2013, 23 (8), 2422–2425. https://doi.org/10.1016/j.bmcl.2013.02.022.
18. Fine-tuning thio-pyridazinediones as SMDC scaffolds (with intracellular thiol release via a novel self-immolative linker)- Chemical Communications (RSC Publishing). https://pubs.rsc.org/en/content/articlelanding/2020/cc/c9cc08744c (accessed 2022-06-23).
19. Bargh, J. D.; Isidro-Llobet, A.; Parker, J. S.; Spring, D. R. Cleavable Linkers in Antibody-Drug Conjugates. Chem Soc Rev 2019, 48 (16), 4361–4374. https://doi.org/10.1039/c8cs00676h.
20. Catalytic Cleavage of Disulfide Bonds in Small Molecules and Linkers of Antibody–Drug Conjugates | Drug Metabolism & Disposition. https://dmd.aspetjournals.org/content/47/10/1156 (accessed 2022-06-23).
21. Anami, Y.; Yamazaki, C. M.; Xiong, W.; Gui, X.; Zhang, N.; An,

DOI: 10.36838/v5i1.15

Z.; Tsuchikama, K. Glutamic Acid–Valine–Citrulline Linkers Ensure Stability and Efficacy of Antibody–Drug Conjugates in Mice. Nat Commun 2018, 9 (1), 2512. https://doi.org/10.1038/s41467-018-04982-3.
22. Kurzrock, R.; Gabrail, N.; Chandhasin, C.; Moulder, S.; Smith,C.; Brenner, A.; Sankhala, K.; Mita, A.; Elian, K.; Bouchard, D.; Sarantopoulos, J. Safety, Pharmacokinetics, and Activity of GRN- 1005, a Novel Conjugate of Angiopep-2, a Peptide Facilitating Brain in Penetration, and Paclitaxel, in Patients with Advanced Solid Tumors. Mol Cancer Ther 2012, 11 (2), 308–316. https://doi.org/10.1158/1535-7163.MCT-11-0566.
23. Erez, R.; Segal, E.; Miller, K.; Satchi-Fainaro, R.; Shabat, D. Enhanced Cytotoxicity of a Polymer-Drug Conjugate with Triple Payload of Paclitaxel. Bioorg Med Chem 2009, 17 (13), 4327–4335. https://doi.org/10.1016/j.bmc.2009.05.028.
24. Small molecules in targeted cancer therapy: advances, challenges, and future perspectives | Signal Transduction and Targeted Therapy. https://www.nature.com/articles/s41392-021-00572-w (accessed 2022-06-23).
25. Beekman, A. M.; Cominetti, M. M. D.; Cartwright, O. C.; Boger, D. L.; Searcey, M. A Small Molecule Drug Conjugate (SMDC) of DUPA and a Duocarmycin Built on the Solid Phase. Med. Chem. Commun. 2019, 10 (12), 2170–2174. https://doi.org/10.1039/C9MD00279K.
26. Lang, W.; Yuan, C.; Zhu, L.; Du, S.; Qian, L.; Ge, J.; Yao, S. Q. Recent Advances in Construction of Small Molecule-Based Fluorophore-Drug Conjugates. Journal of Pharmaceutical Analysis 2020, 10 (5), 434–443. https://doi.org/10.1016/j. jpha.2020.08.006.
27. Cazzamalli, S.; Corso, A. D.; Neri, D. Linker Stability Influences the Anti-Tumor Activity of Acetazolamide-Drug Conjugates for the Therapy of Renal Cell Carcinoma. J Control Release 2017, 246, 39–45. https://doi.org/10.1016/j.jconrel.2016.11.023.
28. Carbohydrate-Based Synthetic Approach to Control Toxicity Profiles of Folate–Drug Conjugates | The Journal of Organic Chemistry. https://pubs.acs.org/doi/10.1021/jo100448q (accessed 2022-06-23).
29. Lerchen, H.-G.; Stelte-Ludwig, B.; Kopitz, C.; Heroult, M.; Zubov, D.; Willuda, J.; Schlange, T.; Kahnert, A.; Wong, H.; Izumi, R.; Hamdy, A. A Small Molecule-Drug Conjugate (SMDC) Consisting of a Modified Camptothecin Payload Linked to an AVß3 Binder for the Treatment of Multiple Cancer Types. Cancers (Basel) 2022, 14 (2), 391. https://doi.org/10.3390/cancers14020391.
30. Curtis, K. K.; Sarantopoulos, J.; Northfelt, D. W.; Weiss, G. J.; Bar-nhart, K. M.; Whisnant, J. K.; Leuschner, C.; Alila, H.; Borad, M. J.; Ramanathan, R. K. Novel LHRH-Receptor-Targeted Cytolytic Peptide, EP-100: First-in-Human Phase I Study in Patients with Advanced LHRH-Receptor-Expressing Solid Tumors. Cancer Chemother Pharmacol 2014, 73 (5), 931–941. https://doi.org/10.1007/s00280-014-2424-x.
31. Pivotal phase III COMPOSE trial will compare ^{177}Lu-edotreotide with best standard of care for well-differentiated aggressive grade 2 and grade 3 gastroenteropancreatic neuroendocrine tumors. Journal of Clinical Oncology. https://ascopubs.org/doi/abs/10.1200/JCO.2022.40.4_suppl.TPS514 (accessed 2022-06-23).
32. Qi, S.-M.; Dong, J.; Xu, Z.-Y.; Cheng, X.-D.; Zhang, W.-D.; Qin, J.-J. PROTAC: An Effective Targeted Protein Degradation Strategy for Cancer Therapy. Frontiers in Pharmacology 2021, 12.
33. Research, C. for D. E. and. FDA Approves Lutetium Lu 177 Dotatate for Treatment of GEP-NETS. *FDA* 2019

Author

Lucy Wang is a current senior at Gunn High School located in the Bay Area. She has a deep interest in medicinal chemistry and is looking forward to pursuing a career in organic chemistry. She plans on majoring in chemistry in the future.

IJHSR
ijhighschoolresearch.org
RESEARCH ARTICLE

AI-Based Power Demand Forecasting of California Counties

Maxwell Y. Chen, Shourya Bose, Yu Zhang

Department of Electrical and Computer Engineering, University of California, 1156 High Street, Santa Cruz, California 95064, USA; maxwellyhchen@gmail.com

ABSTRACT: Electricity is an indispensable form of energy in almost every aspect of our life. Balancing power supply and demand is critical in maximizing energy efficiency and preventing power outages. Towards this end, the ability to make reliable power demand predictions represents a key step, and artificial intelligence and machine learning are emerging tools. In this study, the power demands of selected counties in California are analyzed for the past 30 years by various models, including linear regression, polynomial regression, and autoregressive integrated moving averages (ARIMA). The simulation results show that ARIMA is an effective tool in predicting future power demand, with performance noticeably enhanced compared with those by linear and polynomial regressions.

KEYWORDS: Systems Software; Algorithms; Power Demand; ARIMA; Prediction.

Introduction

Electrical energy is a major engine that drives the economy and plays a critical role in almost every aspect of our life. Currently, the world consumes about 2.7 terawatts (TW) of electricity a year, which accounts for ca. 15% of the total energy consumption, including natural gas, oil, coal, and alternative energy sources like solar, wind, hydropower, etc.;[1] in the United States alone, approximately 0.4 TW of electricity is used in a year.[2] With such a huge demand, it is essential to develop effective strategies to minimize the waste of electricity by balancing supply and demand since it is costly and challenging to develop viable technologies for large-scale electricity storage. Towards this end, making sound predictions of power demand represents a crucial step. Yet conventional technologies for power demand forecasts are primarily empirical in nature, which compromises the accuracy and reliability of the results. The development of smart grid technology is a key building block in a sustainable economy.

Within this context, artificial intelligence (AI) has emerged as an attractive tool that can be used to make predictions of power demand in the future based on past usage patterns. AI is a computer science technology that renders it possible for the computer to perform tasks that traditionally require human intelligence. For instance, in a recent study,[3] Awalin and coworkers developed a machine learning platform based on Microsoft Azure cloud to predict energy consumption. The models were constructed with an algorithm based on three methods, i.e., Support Vector Machine (SVM), Artificial Neural Network (ANN), and k-Nearest Neighbor (k-NN). Data from two tenants in a commercial building were used for model training and testing, and the results show that energy consumption characteristics varied between the tenants. In another study, four random forest algorithms are used in a big data environment to make accurate and feasible predictions of household energy demand, where the consumer's socioeconomic status is found to play a key role in energy use. Wang *et al.* proposed a stacking model by integrating various base-prediction algorithms into "meta-features" such that the resultant model can analyze the data from different structural and spatial perspectives.[5] The results show an improved performance of the stacking method compared to conventional ones, such as Random Forest, Gradient Boosted Decision Tree, Extreme Gradient Boosting, SVM, and k-NN, in terms of accuracy, generalization, and robustness.

Autoregressive integrated moving average (ARIMA) represents another effective method in data analysis and trend prediction of power demand.[6] ARIMA is a time series technique with an implicit assumption that the future will follow the past pattern. Thus it can predict future values based on past values by smoothing time-series data using lagged moving averages. In the present study, the power demand in six select counties in California is analyzed from 1990 to 2019, three in Northern California (Alameda, Santa Clara, and San Mateo) and the other three in Southern California (Los Angeles, Riverside, and San Diego). Compared to linear and polynomial regressions, ARIMA exhibits markedly enhanced fitting to the actual data and can predict future power demand in the counties.

Methods

The power demand data were obtained from the California Energy Commission for the period of 1990 to 2019,[7] and the corresponding population data were retrieved from the Census Bureau.[8-10]

Three tools were used in this study, including (a) Pycharm is, an integrated development environment (IDE) used to write and execute code in Python, (b) NumPy, a plugin for Python that adds math functions and other useful tools, and (c) Matplotlib, which is, a plugin for Python and a library for the numerical mathematics extension NumPy that allows the ability to plot graphs.

DOI: 10.36838/v5i1.16

Results and Discussion

Table 1: Average power consumption (Watts, W) per capita per year within 1990-2019 in six select counties in California.

Santa Clara	Alameda	San Mateo	Los Angeles	Riverside	San Diego
610 ± 26	812 ± 53	604 ± 63	3383 ± 388	1972 ± 420	4930 ± 360

Based on the power demand and population data, we first analyzed the average power consumption (Watts, W) per capita per year from 1990 to 2019. From Table 1, it can be seen that the per-capita power consumption varies rather markedly from one county to another and that the Southern California counties consume far more electricity per person than the Northern California counties, probably because of the drastically more extensive use of air-conditioning in the former. For instance, in the three northern counties, each person consumes 600- 800 W per year compared to 2000 - 5000 W in the southern counties. However, the variation within a specific county is mostly under 10% over the past 30 years. This suggests that per-capita electricity consumption is unlikely to be a significant factor in determining the power demand for these six counties.

Therefore, the study focused on a specific county's total power demand. Figure 1 shows the total power demand (gigawatts, GW) in these six counties over the past 30 years (red symbols). The data were first fitted with linear regression, y = mx + c, with m being the slope and c being the intercept. It can be clearly seen that while linear regression roughly captures the general trends of Alameda, Santa Clara, Riverside, and San Diego, drastic deviations can be seen for several data points, in particular, in the most recent years. For San Mateo and Los Angeles, linear regression is clearly not a good fit for the data.

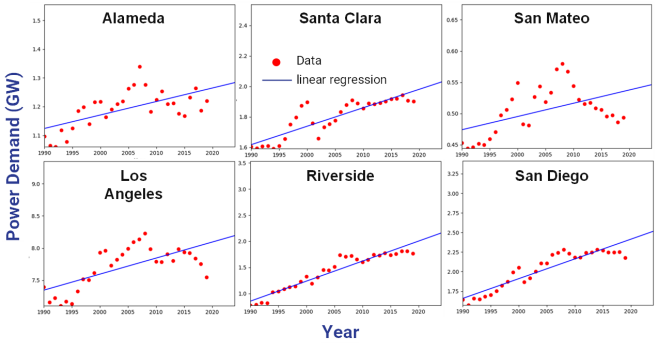

Figure 1: Power demands in six counties in California from 1990 to 2019. Symbols are actual data, and lines are linear regressions.

Further analysis was then carried out with a more complicated fitting model based on polynomial fitting. The datasets were divided into two parts to test the model's validity. Data points from the first 20 years were used as the fitting data for polynomial regression, and data points in the last ten years were used as the comparison data to assess the accuracy of the polynomial fits. In Figure 2, the red symbols are the training data, green symbols are the comparison data, and solid lines are the corresponding polynomial fits. One can see that of the six counties, the polynomial model over-predicted the power demand in comparison to the actual data for Alameda and Santa Clara counties. In contrast, it clearly failed to reflect the actual data trends for the other four counties. This suggests that polynomial modeling is not a reliable tool for predicting power demand, either.

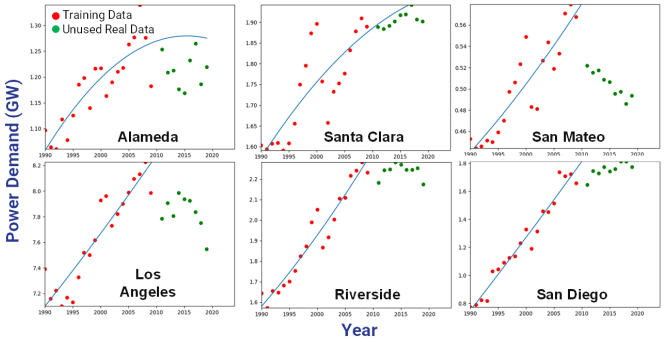

Figure 2: Power demands in six counties in California from 1990 to 2019. Red symbols are the actual data in the first 20 years for training, green symbols are the actual data in the last ten years for comparison, and blue lines are polynomial regressions.

In sharp contrast, a significant improvement in data prediction was achieved by using ARIMA models. Santa Mateo, Alameda, and Los Angeles were chosen as the illustrating examples as their power demand patterns were the most complicated in the series. As depicted in Figure 3, their actual datasets were divided into two parts: the first 25 years' data were used as the training data (red symbols), and the remaining five years' data were used as the comparison data. The ARIMA prediction data are shown in green, which can be seen to exhibit good agreement with the actual data for these three counties, suggesting that ARIMA indeed can be used as a reliable tool in making predictions about power demands.

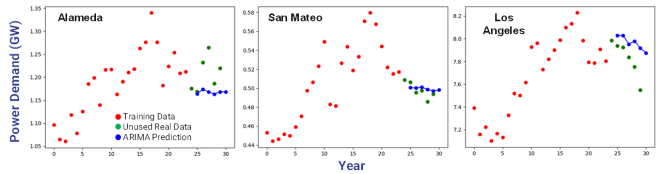

Figure 3: Power demands in three counties in California from 1990 to 2019. Red symbols are the actual data in the first 25 years for training, green symbols are the actual data in the last five years for comparison, and blue symbols/lines are ARIMA predictions.

Therefore, a further analysis was performed where the entire datasets were used as the training data to make predictions about the future. Figure 4 depicts the ARIMA power demand predictions for the next five years. For Alameda County, the power demand is expected to remain relatively steady, whereas it increases slightly for San Mateo and Los Angeles counties. In addition, all counties show moderate fluctuations in power demand in the next five years.

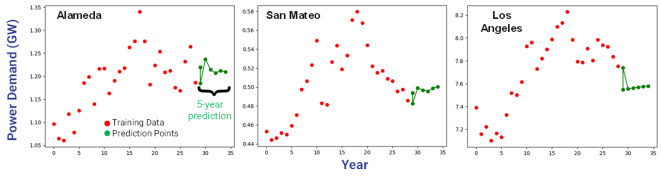

Figure 4: Power demands in three counties in California from 1990 to 2019. Red symbols are the actual data for the entire time period, and green symbols/lines are ARIMA predictions for the next five years.

Conclusions

Power demand varies from one county to another, and ARIMA was demonstrated to be an effective tool in modeling and predicting power demand for various counties in California. The ARIMA performance is markedly better than linear and polynomial regressions. Based on the ARIMA predictions, the three select counties of Alameda, San Mateo, and Los Angeles are anticipated to see a moderate increase in power demand, with slight fluctuations, in the next five years. This study's results highlight ARIMA's unique significance in power demand forecasting, where additional variables may be included to provide a more comprehensive socioeconomic context. Further research is underway, and results will be reported in due course.

Acknowledgments

M.Y.C. would like to thank UCSC for the opportunity to participate in the research project.

References

1. https://www.statista.com/statistics/280704/world-power-consumption/
2. https://www.statista.com/statistics/201794/us-electricity-consumption-since-1975/#:~:text=Electricity%20consumption%20in%20the%20United,of%20electricity%20by%20power%20plants.
3. Shapi, M. K. M.; Ramli, N. A.; Awalin, L. J. Energy consumption prediction by using machine learning for smart building: Case study in Malaysia, *Dev. Built Environ.*, 2021, 5, 100037.
4. Caceres, L.; Merino, J. I.; Diaz-Diaz, N. A Computational Intelligence Approach to Predict Energy Demand Using Random Forest in a Cloudera Cluster, *Appl. Sci.*, 2021, 11, 8635.
5. Wang, R.; Lu, S.; Feng, W. A novel improved model for building energy consumption prediction based on model integration, *Appl. Energy*, 2020, 262, 114561.
6. Jahanshahi, A.; Jahanianfard, D.; Mostafaie, A.; Kamali, M. An Auto Regressive Integrated Moving Average (ARIMA) Model for prediction of energy consumption by household sector in Euro area, *AIMS Energy*, 2019, 7, 151-164.
7. http://www.ecdms.energy.ca.gov/elecbycounty.aspx
8. https://www.census.gov/data/tables/time-series/demo/popest/1990s-county.html
9. https://www.census.gov/data/tables/time-series/demo/popest/intrcensal-2000-2010-counties.html
10. https://www.census.gov/data/tables/time-series/demo/popest/2010s-counties-total.html

Author

Maxwell Y. Chen is a junior at the Georgiana Bruce Kirby Preparatory School. He wants to pursue a computer science major in college and is very interested in modern technological advancements. In his spare time, he likes to experiment with software and hardware.

Shourya Bose is a graduate student pursuing a Ph.D. in the Department of Electrical and Computer Engineering (ECE) at UCSC under the supervision of Prof. Yu Zhang.

Yu Zhang received his Ph.D. degree in ECE from the University of Minnesota and worked as a postdoctoral fellow at the University of California Berkeley and Lawrence Berkeley National Laboratory before joining UCSC as an assistant professor of ECE. His research interests span the spectrum from theory to real-world applications.

DOI: 10.36838/v5i1.16

IJHSR
ijhighschoolresearch.org
RESEARCH ARTICLE

Novel Multipurpose Air Purification and Distribution Robot with AI-Based Anomaly Detection

Mikul Saravanan

Cranbrook Schools, Michigan, USA; mikulsaravanan@gmail.com

ABSTRACT: Maintaining optimal indoor air quality (IAQ), humidity, and household safety are critical to improving overall health. Poor IAQ and improper humidity have adverse health effects. To a limited extent, stationary air purifiers and humidifiers address these issues. I experimented with multiple humidities and air quality sensors placed throughout a room, which showed that a standalone air purifier or humidifier could not distribute air evenly within the space. I solved the uneven distribution and household safety with an innovative robot containing an air purifier, humidifier/ dehumidifier, Ultraviolet C (UVC) lamp (disinfects air by killing most bacteria and viruses such as COVID-19), cameras, and microphones. My custom-built robot uses a Jetson Nano, LiDAR, cameras, microphones, and air quality and humidity sensors. The robot and the air handling system were modeled in Computer-Aided Design (CAD), analyzed with Computational Fluid Dynamics (CFD) to find various components' optimal design, and built with 3D printed parts. AI-based environmental anomaly detection uses the microphone to detect unusual events, such as a glass breaking, smoke alarm, etc., and a camera for human fall detection. The robot was programmed using the Robot Operating System (ROS) to navigate a mapped room to avoid obstacles or until it detects poor air conditions or household safety anomalies. A LiDAR sensor, visual odometry, and an AI-based object detection algorithm accomplish navigation and obstacle detection. My experiment shows that the robot can humidify and purify the air in a room more evenly than standalone devices and detect environmental anomalies.

KEYWORDS: Robotics and Intelligent machines; Air quality; robot; distribution; Environmental anomaly detection.

Introduction

Poor indoor air quality (IAQ) increases heart rate, discomforts such as headaches and sleeplessness (insomnia), eye irritation, and illnesses like asthma.[1-3] Low humidity causes dehydration and dryness and leads to an increased chance of eczema and infection due to virus survival.[4] Dry air irritates the airways, leads to worse sleep, and affects asthma, among others. Low humidity also causes damage to wood furniture and hardwood floors.

An improvement of 10 parts per million (PPM) of Particulate Matter (PM) 2.5 in the air led to a life expectancy of up to 22 months longer for people aged 30 years.[5] Reductions in air pollution accounted for as much as 15% of the increase in life expectancy.[6] In addition, better air quality has been related to improvements in overall health aspects, including child lung growth, reduced chance of asthma, and lowered heart rate.[7]

Air purifiers with High-Efficiency Particulate Air (HEPA) and Carbon filters are effective.[8] HEPA filters are proven to help reduce the pollutants in the air by trapping the particles. Typically, the HEPA filters trap pollen, pet dander, dust, micro-organisms, and allergens such as mold and tobacco smoke.[9] The activated carbon filter removes smells, Volatile Organic Compounds (VOC), gases, fumes, and chemicals. The combined use of both filters leads to cleaner air and even better sleep.

Air circulation is vital for keeping air cleaner everywhere. However, not all places are created equal, so air circulation may not be even. As a result, some parts of an occupied room may not have the same air quality as others. Therefore, air distribution is critical to have improved air quality in a room.[10]

Humidifiers increase humidity in a room to keep the range between 40% and 60% for people's comfort. Humidity outside of this range can affect people's physical and emotional well-being. The two major types of humidifiers are evaporation-based and ultrasonic-based. Ultrasonic humidifiers add humidity by breaking up the water into tiny droplets. Evaporation humidifiers humidify the air by evaporation from a sponge. Optimal moisture helps to maintain the health of the people in a room.

Higher humidity content is also a problem, as too much humidity can cause people to feel hot and drive mold growth. A dehumidifier removes humidity from the air and converts it to water, which can be drained.

COVID-19 and other bacteria and viruses threaten many people in schools, homes, hospitals, etc. Ultraviolet -C (UVC) LEDs deactivate and disinfect these microbes.

Additionally, many households have medical accidents or intruder break-ins that injure or kill occupants. Microphones and cameras can monitor and detect potential hazards to notify people of dangers. The house is one of the most used buildings, and its safety is essential. In addition, many injuries happen to elders, and security can help provide peace of mind for them and their well-wishers.

DOI: 10.36838/v5i1.17

Therefore, improving IAQ, maintaining humidity at a certain level, removing bacteria and viruses, and detecting household anomalies, such as break-ins and fall detection, are essential for healthy and safe living.

The current development is to resolve all the above issues mentioned. This was done through the creation of a smart novel robot using AI and machine learning that can:

- Purify the air and remove pollutants
- Disinfect the air to remove viruses and bacteria
- Humidify or dehumidify the air
- Detect environmental audio and video anomalies to protect residents
- Perform all these tasks in a smart robot that can distribute air evenly and navigate between rooms

Some air purifiers are bigger than others. Small ones (about 1.5'x0.5'x2') are not particularly good for cleaning the air of a big room because they are not powerful enough. In these instances, periodically moving the small air purifier is required to clean the air in a large room. Even though the larger air purifiers (about 2'x1'x2') are better for larger spaces, they cannot clean the air in every part of the room. This is due to poor airflow caused by a lack of air circulation and stagnant air in a few pockets of the room. One solution is to use multiple air purifiers. However, they would occupy more space, and the cost would be much higher. Whole-house air purifiers, such as those installed within HVAC systems, are very good at bringing in clean air. However, many pollutants do not come from within these systems and cannot solve the abovementioned issues. The pollution can come from people, windows, chemicals used in the room, or others. A novel smart moving local purifier is a solution to resolve the previously discussed limitations.

Air purifiers containing high-efficiency particulate absorbing (HEPA) air filters and carbon filters are good at removing pollutants, but their ability to remove viruses from the air is very minimal. Due to this limitation of being inefficient with viruses, it takes many passes to remove large numbers of viruses from the air. The alternative is to use Ultraviolet C (UVC) lamps that can remove almost all viruses, including COVID-19, from the air, increasing people's safety in that area. There are three forms of Ultraviolet (UV) light: UVA (315–400 nm), UVB (280–315 nm), and UVC light (200–280 nm).[11] UVC is the shortest wavelength of the three forms of UV, and it is a more harmful type of UV radiation. UVA and UVB come from the sun but have limited germ-killing ability. UVC can kill bacteria and viruses without harming humans with low direct contact with people. Hospitals use UVC lights to disinfect their rooms.

Humid air rises, so it gets replaced by less humid air. Humidity takes a while to travel from one side of the room to another. Usually, the area around a humidifier is very humid compared to the rest of the room. Due to the many benefits of optimal humid air, humidifiers need to be moved around a large space to get more evenly distributed humidity. Alternatively, many small humidifiers are required to humidify a large room more uniformly.

Each component, the air purifier, humidifier, and UVC lamp, is essential to people's benefit and safety, but they may not be as efficient on their own. Most air purifiers and humidifiers need to move around for maximum efficiency. This is especially true for huge rooms. A device that moves would increase effectiveness and uniform distribution.

When a person living alone enters a medical emergency, they can make efforts to call 911 or their family or friends using a land phone or a cell phone. However, when people fall and become severely injured or unconscious, making a phone call becomes difficult. Also, when there are window break-ins or deafening noises like gunfire, the person attempts to hide and may not have a phone device to make an emergency call.

Various devices with special functions are needed in different rooms to solve multiple issues. This project attempts to solve a novel smart artificial intelligence (AI) based moving air purifier, sanitizer, and humidifier/ dehumidifier with the emergency alert system.

Methods

Robot Optimal Design for maximum performance:

This project aimed to develop a robot that not only cleans, purifies, and humidifies the air but also detects visual and audio anomalies. For this to happen, it needs a subsystem for each task and a navigation stack to control the movement. The functional block diagram of various modules, components, and devices (Figure 1) illustrates a data processing and AI environmental anomaly detection configured to improve air quality and provide emergency alerts. To get started with multiple design ideas, Computer-Aided Design (CAD) software was used to design the robot to create a blueprint for visualization and placement of the required electronics.

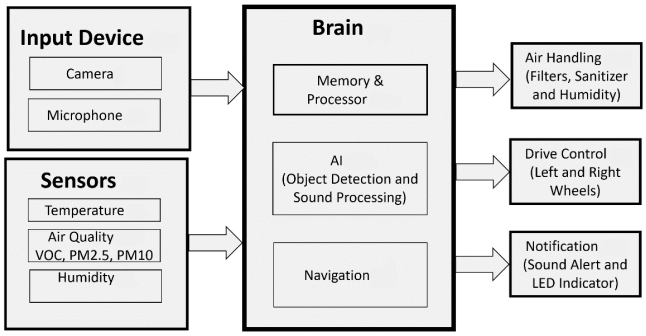

Figure 1: Functional block diagram of various subsystems.

Robot Modeling using Computer-Aided Design:

There are many possible designs for a robot. Since the most significant aspect of the robot is the air purification system, it was designed first, and then all the other systems were designed around it. Two significant fan designs include a blower fan that draws air from the front and blows it to the top and a radiator fan that pulls air from the front and blows it to the top. HEPA filters are used since it is the industry standard for air filtering. A UVC lamp is included in the design to deactivate viruses and kill bacteria. Various design ideas were thought through, and finally, the two main air chamber designs were narrowed down. Design 1 pulls air through a cylindrical filter and blows it to the top (Figure 2), while Design 2 uses a blower fan to pull air from the front of a rectangular filter and blow air to the top (Figure 3). The two designs were

DOI: 10.36838/v5i1.17

analyzed further to pick the best design. The approach to using Computational Fluid Dynamics (CFD) analysis as the next step from CAD design was followed to select the model with the highest efficiency.

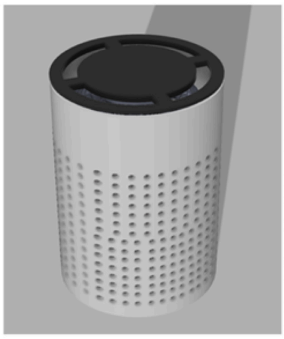

Figure 2: Design 1.

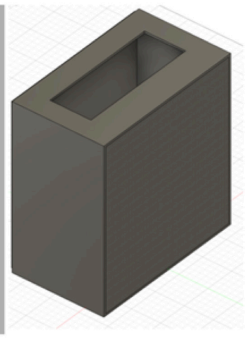

Figure 3: Design 2.

Optimal Design through Computational Fluid Dynamics:

Computational Fluid Dynamics (CFD) is mathematically modeling a physical phenomenon involving fluid flow and solving it numerically using computational prowess. The Navier-Stokes (N-S) equations are specified as the mathematical model of the physical case. A CFD software analysis examines fluid flow in accordance with its physical properties, such as velocity, pressure, temperature, density, and viscosity. The main structure of thermo-fluids examination is directed by governing equations based on the conservation law of fluid's physical properties. These principles state that mass, momentum, and energy are stable constants within a closed system. Everything must be conserved. Model establishment followed the basic four procedural steps:

Step 1: Specify the problem parameters, including boundary and initial conditions.

Step 2: Build the CFD model.

Step 3: Calculate a solution.

Step 4: Examine the results.

CFD analysis was conducted on these two designs to check peak velocity. Both designs were set up using the respective CAD models. Design 1 had a higher peak velocity (Figure 4) at around 2200 cm/sec than Design 2's 1800 cm/sec (Figure 5). As a result of the higher airflow, Design 1 was selected for the robot (Figure 6).

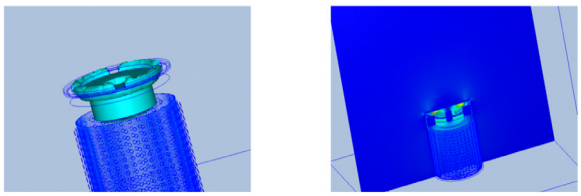

Figure 4: Design 1. CFD analysis with cylindrical HEPA air filter.

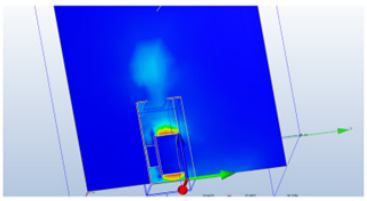

Figure 5: Design 2 CFD analysis with rectangular HEPA air filter.

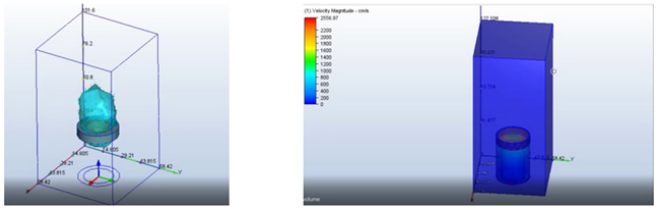

Figure 6: Final design analysis.

Final CAD design:

After choosing the first design, the CAD model was further expanded to include all aspects of a finished robot (Figure 7). The UVC chamber rests on top of the fan, and the humidification system is on top. Originally an ultrasonic humidifier was used, but it was changed to a vaporization humidifier by using a cloth wick that soaks up water, evaporating as the purified air blows through the sponge. The dehumidifier can optionally be placed on top instead of the humidifier if humidity is higher than normal. The Light Detection and Ranging (LiDAR) is located at the top. The Intel tracking camera for Visual Simultaneous Localization and Mapping (vSLAM) is placed at the front, along with the Intel depth camera used for AI object detection. The rest of the electronics are placed on the bottom.

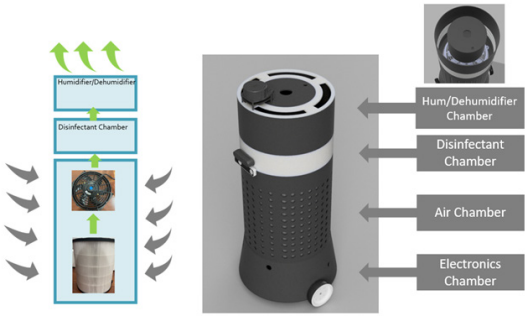

Figure 7: Robot design and render.

Physical Prototype Development:

The robot consists of hardware and software portions. The hardware consists of the physical structure that operates on two wheels, processors, sensors, batteries, etc. The software includes the Robot Operating System (ROS) with a set of libraries that performs various functions.

Hardware:

Once the detailed CAD design was completed, the robot was 3D printed using Poly Lactic Acid (PLA) filament and assembled. The electronics were attached and wired up. The various stages of the prototype process are shown (Figure 8).

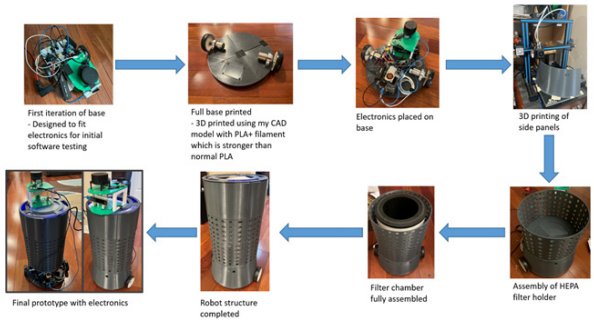

Figure 8: Robot prototyping stage.

The brain and sensors are all part of electronics and sit inside the electronics chamber. The electronics are all mounted on the base and bottom of the air handling system. The brain contains memory and a processor which receives data from the sensor system, camera, and microphone to perform multiple operations, including AI to process the data for navigation of the smart robot. The block diagram shows these components (Figure 9).

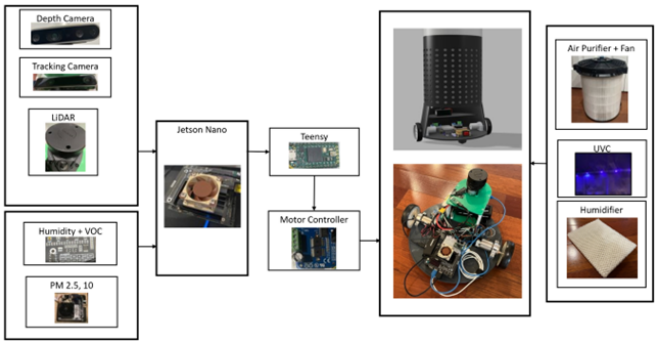

Figure 9: Diagram of electronic components.

The drive controller mounted on the base receives instruction from the navigation module of the brain. In turn, the drive controller provides instructions for the speed and direction change for the left and right motors. The two wheels mounted on either side of the base move with power and control from two individual motors. The two motors independently drive their wheels. Two metal ball bearings are mounted at the two ends to keep the robot stable.

A sensor system has multiple sensors mounted inside the electronics chamber to obtain real-time air quality data and other surrounding metrics.

As part of air quality, volatile organic compound (VOC) sensors are used to measure a wide range of VOC intended for indoor air quality monitoring of the environment. The sensor can measure total VOC concentration within 20 to 1000 parts per billion (ppb) with about 2% to 5% error. It can detect alcohols like benzene, toluene, and formaldehyde. It also detects aldehydes, ketones, organic acids, amines, organic chloramines, and aliphatic and aromatic hydrocarbons.

The particulate matter sensors PM2.5 and PM10 are used to detect smoke particles from 0.10μm to 1.0μm diameter, dust particles from 0.50 μm to 3.0μm diameter, and pollen particles with sizes from 5.0μm to 11μm in diameter. The particulate matter per 100ml air is categorized into 0.3um, 0.5um, 1.0um, 2.5um, 5.0um, and 10um size bins. The PM sensors are mounted on the base.

The humidity sensor is used to measure humidity levels between 10 and 90% with a 2% error. The temperature sensor is used to measure reading between -40˚F and 150˚F with ±0.5˚F accuracy. This sensor is mounted alongside the humidity sensor. A microphone is used to capture audio in the environment. The frequency response range is from 15Hz to 20kHz. This microphone can capture the glass-shattering waves, which are roughly 556 hertz. A camera is mounted on one side of the air handling system.

Lithium Polymer (LiPo) batteries power all electronics on board. A power supply and adapter are used to charge the LiPo batteries when the robot is turned off and docked to the regular wall power supply. The fans, humidity module, brain, and drive controller are all powered by LiPo batteries. The VOC sensor, the PM2.5, and PM10 sensors, the humidity sensor, and the temperature sensor are powered by the brain and in operable communication with the brain. The two input devices for audio and video: the microphone and the camera, are powered by the brain and in operable communication with the brain. The drive controllers power the motors, which rotate the wheels for the smart robot to traverse the floor. The sound and LED indicators are powered by the brain and are connected to the side of the air purification system.

Software:

The multiple aspects of the robot were connected by using Robot Operating System (ROS). Each sensor has its own ROS topic to publish its data, to which the main program then subscribes to (Figure 10) as per the pub-sub model of ROS. The robot has an environment module that contains temperature, humidity, and VOC values. The PM2.5 and ten sensors also publish their values onto their respective ROS topics. The AI algorithms send their data through their own ROS topics as well. The LiDAR and tracking camera are used to map and navigate the data generated. The navigation uses the navigation stack, takes a 2D nav goal as input, and outputs a cmd_vel that gets sent to the Teensy, a small microcontroller that drives the motors and the robot. The data from the air quality and humidity sensors also control the fan speed through the Teensy based on the set thresholds. There are motor controllers that take in the battery power and the data from the Teensy, which power the motors of the wheels and fan.

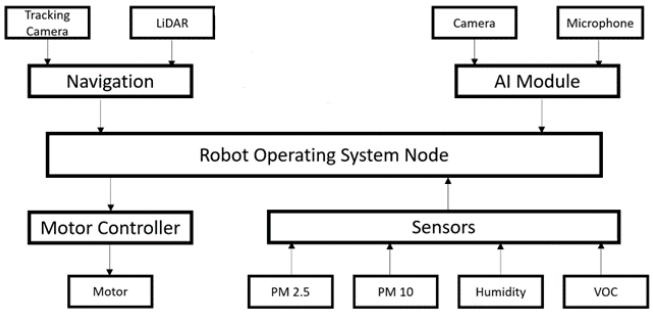

Figure 10: ROS communication diagram.

The navigation module uses air quality data from sensors, humidity data, and an AI object detection algorithm for people recognition with inputs through the camera, as shown in the flow chart (Figure 11). It also uses the stored map for its path planning algorithm (Figure 12).

DOI: 10.36838/v5i1.17

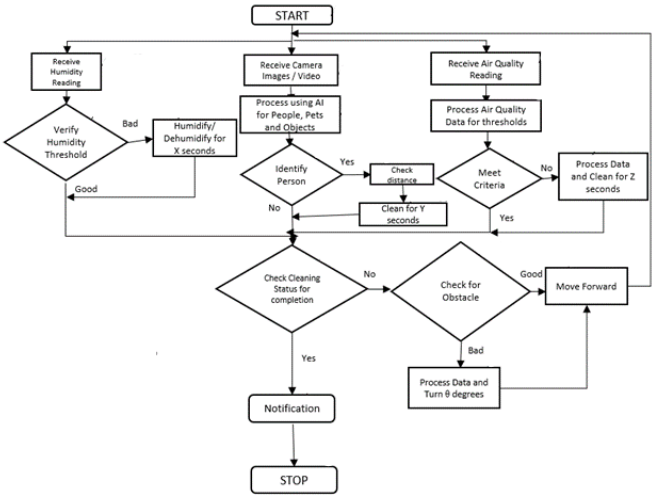

Figure 11: Navigation of the robot.

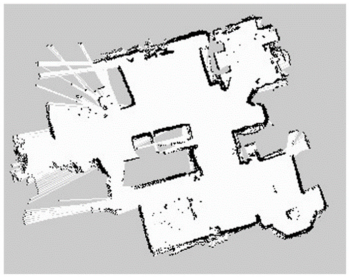

Figure 12: Robot-generated map.

The humidity sensor provides the humidity reading. This data is checked to see if they are within the humidity threshold. An ideal humidity range between 40% and 60% is used as a default. When the humidity level is either low or high, then the humidifier or dehumidifier runs for a certain amount of additional seconds at this location based on the logic programmed inside the navigation module. After this, or when the humidity threshold is good, then the navigation system flags internally that this area is at a satisfying level and would continue into the next step, waiting for the cleaning status of air quality.

Inside the navigation module, the camera feed is received images and videos as a parallel process. The data is processed using AI for people, pets, and objects. The program calculates the additional cleaning time at this location based on the data. After this, when no person is identified, then the navigation system flags internally that this area is clean and would continue into the next step, waiting for the cleaning status on the humidity and air quality.

The air quality reading is received from air quality sensors. This data is processed to see if they meet various air quality metrics criteria thresholds. One criterion for the particle sizes per volume is below 15.0 $\mu g/m^3$ or 12.0 $\mu g/m^3$ for smoke particles, dust particles, pollen particles, etc. The maximum allowable air concentration of total VOC is below 0.50mg/m^3. When the air quality threshold is not met, based on the air quality data, the navigation module determines the need to run the smart robot at this location for more time after this or when no person is identified, then the navigation system flags internally that this area's level is satisfied and continues into the next step, waiting for cleaning status on the humidity and person detection.

The navigation module calculates and uses the maximum of X, Y, or Z seconds to stay in one location. This cleaning time calculation can be overwritten with a fixed value by the user setting. This maximum time for one location is limited to about 30 seconds, after which the smart robot operates in default autonomous mode.

AI components: Audio & Video:

The environmental anomaly detection is powered by a sound classification system and an image classification system. The flow chart shows the logic used (Figure 13).

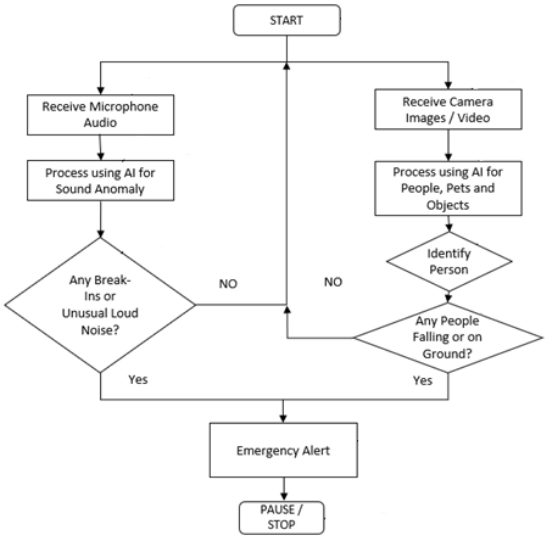

Figure 13: AI system flow diagram.

The camera provides a video feed to the AI-based object detection module of the brain. This model is a TensorFlow object detection algorithm trained on the COCO dataset and based on the YOLO (You Only Look Once) framework. Transfer learning was then used to make the model more lightweight to work on lower-powered devices. As in Figure 16, the data is received, and the AI module is processed to detect people, pets, and objects. When a person is detected with data from the camera and by the AI module, it then checks the person's orientation to determine if the person has fallen. If so, the smart robot sends the medical emergency alert to a smart device notification.

The detection of sound was done using a PyTorch model. A custom dataset was created to include samples from baby crying, glass breaking, gunshots, smoke alarms, someone falling, and background sounds (for control). This new dataset was used to train a Support Vector Machine (SVM), Random Forest, and K-Nearest Neighbors (KNN) using the framework to find the best-performing one.[12] Ultimately, the Random Forest model was selected for its second-fastest response time and highest accuracy.

Results and Discussion

Initial Experiment Research:

Preliminary experiments were conducted to validate the issue of air quality and humidity distribution. Since a standalone

device is usually placed in one corner of a room, it may not be able to have an equal overage of said room. A typical single-bedroom home (Figure 14) with an office room could be a two-bedroom home. The initial experiment was conducted with a humidifier in one corner of the 15' x 18' room. Five trials were conducted with two sensors that logged the humidity, PM2.5, PM10, and VOC values. For the trial, one group of sensors was placed near the device, and the other group of sensors was placed farther away on the other side of the room.

Figure 14: The layout of the rooms was tested.

The graph (Figure 15) shows the change in humidity over time for both sensors. The sensor close to the humidifier rose steadily over time and reached the safe 40% threshold, but the device further away did not rise as much and did not reach the 40% threshold. The humidifiers used for this test were ultrasonic humidifiers. As the test was conducted, the observations were that the overall air quality dropped. We noted this as the water is not pure since there are minerals in the water and possibly mold. As a result, we decided that the robot should use vaporization-based humidifiers since those humidifiers do not release any pollutants.

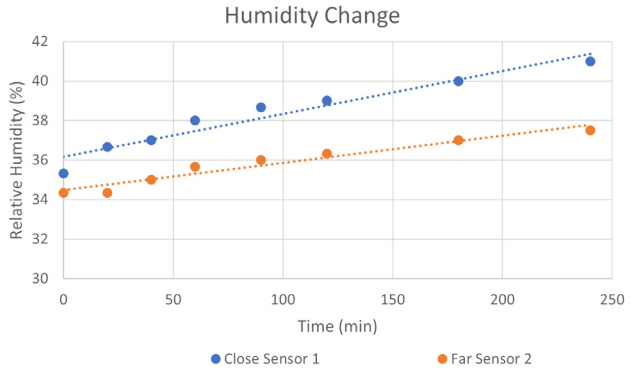

Figure 15: Humidity measurement with one humidifier at a fixed location.

Air quality was retested next with an ultrasonic humidifier providing the pollutants for the air. The change in air quality for the two locations with a standalone air purifier was uneven (Figure 16). Similar to humidity, the air quality improvement rate is based on the closeness to air purifiers, with only the close sensor reaching a safe level of particulates.

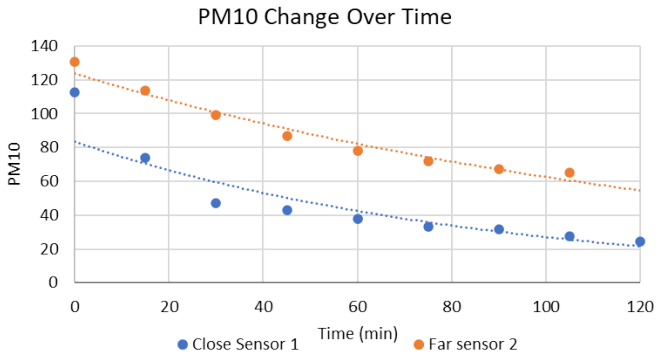

Figure 16: PM10 changes over time with one air purifier.

Further experimental trials were conducted to see the impact of two humidifiers and two air purifiers distributed in the same size, 15' x 18'. Similarly, the air purifier was placed further apart in an attempt for distribution. The trial and data, as in the above experiment, were conducted. The result was much more encouraging, as the humidity and air quality are much more uniform.

Robot Evaluation and Data Analysis:

The evaluation experiments were repeated, except the robot was used instead of the standalone devices. When humidity was tested, both the near and far sensors noticed similar increases in humidity over time, reaching the 40% threshold of safe humidity (Figure 17). On the other hand, air quality still performed, with both sensors displaying similarly decreasing values (Figure 18). They both approached the safe level of 30-40ppm. This shows that the robot is effective at distributing clean air evenly. On top of this, the AI modules were evaluated with good results. The robot effectively performed the even distribution throughout the room for both air quality and humidity. This would be an excellent device to use, especially in this pandemic, as many people are staying indoors, and the removal of COVID-19 with this robot using the UVC LEDs. This product can benefit those who need it even during normal times.

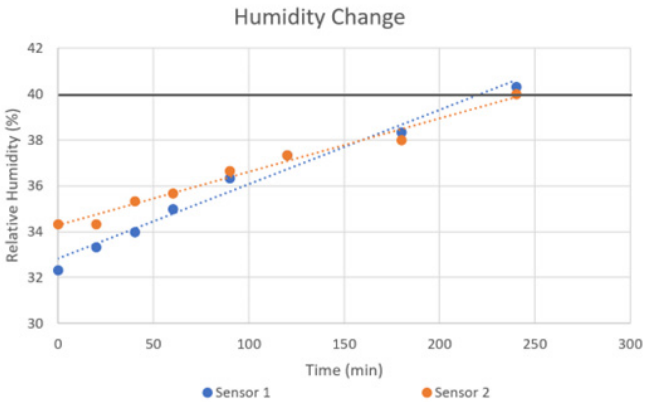

Figure 17: Humidity change over time with robot for close and far sensors, respectively.

DOI: 10.36838/v5i1.17

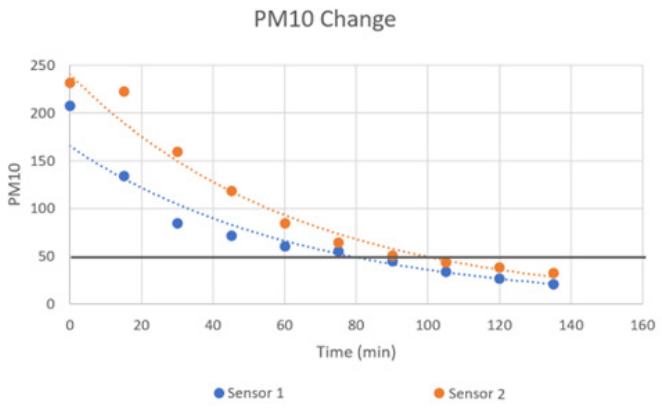

Figure 18: PM10 changes over time with the robot.

Conclusion

This project constructed a smart robot to purify, humidify, dehumidify, and disinfect the air evenly. The mobile robot automatically removes dust and pathogens and maintains stable humidity evenly across the chosen space. Additionally, the robot detects environmental anomalies, keeping people safe in its operating space.

The ability of the robot to travel between rooms reduces the time needed to move multiple devices manually and eliminates the need for these devices. The environmental anomaly detection, comprised of video fall detection and audio anomaly detection, was able to detect falls and anomalies in the real world during testing.

The robot was able to improve on the existing standalone devices. People will not have to get multiple devices to perform various functions as outlined at the beginning. The robot should be commercialized in schools, homes, hospitals, offices, and nursing homes to provide cleaner air and a safer environment.

Acknowledgments

Thanks to the JSHS Momentum Grant for the funding for this project.

References

1. Sattar, S. A., Bhardwaj, N., & Ijaz, M. K. (2016). *Airborne viruses. Manual of environmental microbiology,* 3-2.
2. Wolkoff, P. (2018). Indoor air humidity, air quality, and health–An overview. *International journal of hygiene and environmental health*, 221(3), 376-390.
3. Schraufnagel, D. E., Balmes, J. R., De Matteis, S., Hoffman, B., Kim, W. J., Perez-Padilla, R., ... & Wuebbles, D. J. (2019). Health benefits of air pollution reduction. *Annals of the American Thoracic Society*, 16(12), 1478-1487.
4. Pope III, C. A., Ezzati, M., & Dockery, D. W. (2009). *Fine particulate air pollution and life expectancy in the United States. New England Journal of Medicine,* 360(4), 376-386.
5. Lelieveld, J., Pozzer, A., Pöschl, U., Fnais, M., Haines, A., & Münzel, T. (2020). Loss of life expectancy from air pollution compared to other risk factors: a worldwide perspective. *Cardiovascular Research*, 116(11), 1910-1917.
6. Cooper, E., Wang, Y., Stamp, S., Burman, E., & Mumovic, D. (2021). Use of portable air purifiers in homes: Operating behavior, effect on indoor PM2. 5 and perceived indoor air quality. *Building and Environment*, 191, 107621.
7. Memarzadeh, F., Olmsted, R. N., & Bartley, J. M. (2010). Applications of ultraviolet germicidal irradiation disinfection in health care facilities: effective adjunct, but not stand-alone technology. *American journal of infection control*, 38(5), S13-S24.
8. Mackenzie, D. (2020). Ultraviolet light fights new viruses. *Engineering* (Beijing, China), 6(8), 851.
9. Buonanno, M., Welch, D., Shuryak, I., & Brenner, D. J. (2020). Far-UVC light (222 nm) efficiently and safely inactivates airborne human coronaviruses. *Scientific Reports*, 10(1), 1-8.
10. Yao, J., Zhong, J., & Yang, N. (2022). Indoor air quality test and air distribution CFD simulation in hospital consulting room. *International Journal of Low-Carbon Technologies*, 17, 33-37.
11. Ma, B., Gundy, P. M., Gerba, C. P., Sobsey, M. D., & Linden, K. G. (2021). UV inactivation of SARS-CoV-2 across the UVC spectrum: KrCl* excimer, mercury-vapor, and light-emitting-diode (LED) sources. A*pplied and environmental microbiology*, 87(22), e01532-21.
12. Giannakopoulos, T. (2015). pyaudioanalysis: An open-source python library for audio signal analysis. *PloS one*, 10(12), e0144610.

Author

My name is Mikul Saravanan, and I am passionate about engineering and computer science, especially robotics and AI. He will be entering college in Fall 2023.

IJHSR
ijhighschoolresearch.org
RESEARCH ARTICLE

The Association of the 'Hide Like and View Counts' Feature with Disordered Eating, Self Esteem, and Self Image

Naisha Agarwal

The Cathedral and John Connon School, 6, Purshottamdas Thakurdas Marg, Fort, Mumbai, Maharashtra, 400001, India; naishaagarwal30@gmail.com

ABSTRACT: The 'hide like and view counts' feature is a recently implemented feature on the Instagram app, designed to depressurize people's experience and give users more control. This cross-sectional survey study examines if the use of this feature is associated with higher levels of self-esteem and body satisfaction and lower levels of disordered eating symptoms. We conducted a survey (N=116) to analyze if there was a significant difference between the self-esteem, self-image, and disordered eating risk of Instagram users who use the feature and users who do not. The participants that used the feature demonstrated significantly lower scores on the Eating Attitudes Test, thus at a lower risk for developing an eating disorder. This is consistent with our hypothesis.

Contrary to our hypothesis, the two groups had no significant difference in self-esteem and body dissatisfaction. Our findings show that the feature is indeed associated with some positive psychological outcomes. Future research should study how the social media experience can be altered to suit one's needs and support positive health.

KEYWORDS: Social Psychology; Clinical Psychology; Social Media; Disordered Eating; Self-Esteem.

Introduction

The popularity of social media has escalated massively in recent years.[1] In 2022, social networking sites are estimated to reach 3.96 billion users, and these numbers are expected to increase as mobile device usage, and social networks gain more attention.[2] Due to the COVID-19 pandemic, social media use has grown immensely to stay in touch with friends and family in the face of lockdown restrictions and social distancing measures. According to a survey of U.S. social media users, 29.7 percent of respondents used social media for 1-2 additional hours per day during the pandemic.[3] Instagram is a particularly popular social networking site. A forecast from October 2020 estimates that there will be nearly 1.2 billion Instagram users worldwide in 2023.[4] Media use is constantly changing, and the Internet and social networking sites are quickly becoming the primary media source young adults use.[5,6] In 2015, 90% of all young adults used social media, compared with 12% in 2005, a 78-percentage point increase.[7] It is evident that social media significantly impacts many people, so it is crucial to study its effects on users.

There is much-mixed research on social media and mental health. The use of social networking sites (SNS) comes with many risks. Some studies show that online technologies have harmful effects like increased exposure to social isolation, depression, and cyberbullying.[8-10] One study showed that limiting social media usage on a mobile phone to 10 minutes per platform per day for a full three weeks significantly impacted well-being and decreased loneliness and depression.[11] Additionally, more time spent using social media is significantly associated with more significant symptoms of anxiety.[12] On the other hand, some studies show that communication through platforms such as Facebook, Twitter, Instagram, and Snapchat provides ways to keep in touch with family and friends and other social interactions that can mitigate depression and anxiety.[13,14] Social media is vital to the lives of many people. We use it to communicate, spread awareness, socialize, collaborate, and share content. Owing to the mixed research, there is no clear association between social media use and well-being.

Social media can heavily influence body dissatisfaction and disordered eating. According to the DSM-5, eating disorders include intense fear of gaining weight even though underweight, body image disturbance, recurring inappropriate compensatory behavior (vomiting, laxatives, exercise, diet pills), and restriction of energy intake, leading to significantly low body weight.[15] Eating disorders can cause significant health consequences and may even result in death if left untreated. Up to 13% of youth may experience at least one eating disorder by the age of 20.[16] Eating disorders can cause unhealthy eating habits to develop. They might start with an obsession with food, body weight, or body shape. Those with eating disorders can have various symptoms like severe food restriction, food binges, or purging behaviors like vomiting or over-exercising.[17] It was found that some patients with severe eating disorders report dissociative symptoms, including depersonalization, trance-like states, out-of-body experiences, and amnesias.[18] In one meta-analysis, it was found that the crude mortality rate due to all causes of death for subjects with anorexia nervosa was 5.9% (178 deaths in 3,006 subjects). The aggregate mortality rate was estimated to be 0.56% per year or approximately 5.6% per decade.[19] Several studies show that social media use is consistently and positively associated with negative body image.[20-21] Mass media is considered the most influential and

DOI: 10.36838/v5i1.18

prevalent cause of body dissatisfaction.[22] Spending more time on social networking sites (SNS) like Facebook is positively associated with disordered eating, increased body surveillance, and obsessing over one's appearance.[23] A study showed that young girls with more Facebook friends reported higher levels of body surveillance, and sharing more photos on Facebook led to a greater likelihood of basing self-worth on appearance.[23] Mass media is filled with images of the thin ideal, which is highly unrealistic for most women. Research has shown that mass media contributes to developing and maintaining eating disorders.[24] However, research has also shown that online worlds can be mindfully constructed to support positive health and well-being. In one study, social media actually aided female weightlifters during their recovery from eating disorders. It was able to offer opportunities to feel connected to the outside world from a distance that felt safe and manageable.[25] The social media experience can be altered to suit one's needs via 'Digital Pruning,' unfollowing triggering or unhelpful content.[25]

Social Media is pervasive and omnipresent in society. Since SNS are here to stay, instead of focusing on the various negative impacts of SNS on well-being, we should try to understand how to use them effectively. Research should focus on how technology can adapt depending on user needs and how SNS can be changed to provide a better user experience. Instead of promoting the thin ideal, it may be beneficial if social media conveys positive and self-esteem-building messages to counteract the harmful effects of SNS and improve body satisfaction and self-esteem.

Giving and receiving feedback and 'likes' is a fundamental part of users' experiences on social media. A 2017 study showed that receiving a more significant number of likes reliably predicted greater self-esteem.[26] Research shows that the intensity of positive social feedback experienced (increased number of likes received) from users' audience is positively associated with current happiness and increased self-esteem. Receiving likes can boost self-esteem and consequently produce a state of happiness.[27] In another study, adolescents reported significantly greater feelings of rejection when they were randomly assigned to receive few likes relative to when they received many likes.[28] Women placing greater importance on receiving "likes" are more likely to compare their photos to friends' posted photos and report the highest levels of disordered eating symptoms.[29] It is apparent that the number of likes a user gets can impact their well-being significantly, and thus, it is essential to conduct future research on this aspect.

In May 2021, Instagram introduced a new feature to the app: the 'hide like and view counts' feature. Instagram announced that this feature was to help depressurize people's experience on Instagram and give users more control over their experience.[30] This feature enables users to hide the number of likes they get on any images shared. Users are still able to see the number of likes they themselves receive. This feature is optional, allowing users to alter their Instagram experience according to their own needs.

Hypotheses:

Hypothesis 1: Use of the "Hide Like and View Counts" Feature will be associated with higher levels of self-esteem.

Hypothesis 2: Use of the "Hide Like and View Counts" Feature will be associated with higher levels of body satisfaction.

Hypothesis 3: Use of the "Hide Like and View Counts" Feature will be associated with lower levels of disordered eating symptoms.

Methods

Procedure:

We used an online survey to collect data to specifically examine the association between the 'hide like and view counts' feature on the Instagram app and behaviors and cognitions associated with disordered eating, body dissatisfaction, and self-esteem. Following approval of our study procedures by an Ethics Board, the optional survey was administered electronically to all participants via Amazon Mechanical Turk. The survey was made on Google Forms and took about 5-7 minutes to complete. All participants provided informed consent at the onset of the study. The date of collection of the data is 1st March 2022. All participants were recruited from Amazon Mechanical Turk.

Participants:

Participants (N=116) were recruited through Amazon Mechanical Turk and were paid 25 cents for completing the survey. The criteria for inclusion of participants included using Instagram at least once a week and being between the ages of 15 and 25. We chose this age range as we believed that social media use is the most common.

Measures:

The survey incorporated five key measures:

1. RSES (Rosenberg Self-Esteem Scale): The 10-item Rosenberg Self-Esteem Scale (RSES)[31] was used to measure global trait self-esteem (SE). Items are measured on a 4-point scale ranging from 1 (strongly agree) to 4 (strongly disagree), with reverse scoring when appropriate and then summed. Higher scores indicate more excellent global trait SE. A sample question is, " I feel that I'm a person of worth, at least on an equal plane with others." Cronbach's alpha for the ten items was acceptable (α = .75).

2. BSQ-8d (Body Shape Questionnaire): The 8-item Body Shape Questionnaire (BSQ-8d)[32] measured body shape preoccupations typical of bulimia nervosa and anorexia nervosa. Each item is scored 1 to 6 with "Never"= 1 and "Always"= 6, and the overall score is the total across the 8 items, a theoretical score ranging from 8 to 48. Higher scores indicate greater body dissatisfaction. A sample question is, "Have you avoided situations where people could see your body (e.g., communal changing rooms or swimming baths)?" Cronbach's alpha for the eight items showed excellent internal consistency (α= .95).

3.EAT-26 (The Eating Attitudes Test): The 26-item Eating Attitudes Test (EAT-26)[33] was used to measure self-reported symptoms and concern characteristics of eating disorders. Items were scored on a 6-point Likert scale ranging from 1 (always) to 6 (never). For questions 1-25, points 1-3 have a

score of 0, while point 4 has a score of 1, point 5 has a score of 2, and point 6 has a score of 3. The scoring is reversed for question 26. Items are then summed to obtain a total score, with any score of 20 or higher considered at risk. A sample question is, "I particularly avoid food with a high carbohydrate content (bread, rice, potatoes, etc.)." Cronbach's alpha for the 27 items demonstrated acceptable internal consistency ($\alpha = .75$).

4. Instagram Usage: Participants were asked to fill in the number of days on average they use Instagram per week. This item was scored on a 7-point Likert scale from 1 (once a week) to 7 (every day).

5. Hide Like and View Counts' Feature Usage: Participants were asked if they knew the feature and if they used it. Both questions were answered yes/no.

Analysis:

Analyses were conducted using Google Sheets and R. We used Welch's t-test to account for unequal group sizes and variances. The Welch's t-test is a nonparametric adaptation of a Student's t-test, which measures group mean differences. The nonparametric test allows us to conduct analyses on unequal sample sizes. Any missing values in data were considered null values.

Results and Discussion

The average participant age was 22.73 years (SD = 3.11). 48.28% of participants were male, while 51.72% were female. On average, participants used Instagram 6.13 times per week.

Self-Esteem Comparison:

There was no significant effect for self-esteem, t (37.56) = 0.96, p = 0.35, despite the group that does use 'hide like and view counts' feature (M = 26.50, SD = 4.48) attaining higher scores than the group that does not use the feature (M = 24.97, SD = 8.63). Figure 1 compares the mean self-esteem score of the two groups.

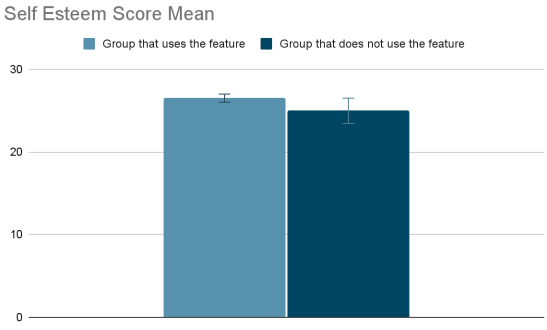

Figure 1: Mean self-esteem score of the two groups.

Body Dissatisfaction Comparison:

There was no significant effect for body dissatisfaction, t (51.64) = 1.85, p = 0.07, despite the group that does use 'hide like and view counts' feature (M = 33.58, SD = 10.47) attaining higher scores than the group that does not use the feature (M = 29.25, SD = 11.53). Figure 2 compares the mean body dissatisfaction score of the two groups.

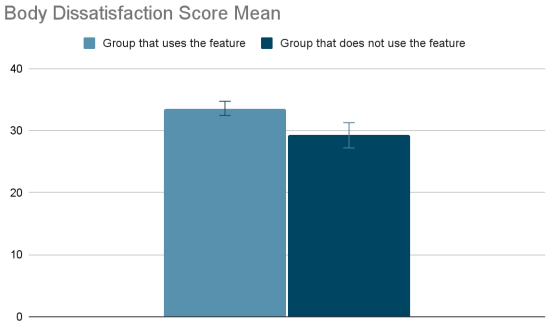

Figure 2: Mean body dissatisfaction score of the two groups.

Eating Disorder Risk Comparison:

The 84 participants in the group that did use the 'hide like and view counts' feature (M = 26.08, SD = 4.48) compared to the 33 participants in the group that did not use the feature (M = 34.44, SD = 8.63) demonstrated significantly lower scores on the EAT, thus being at a lower risk for developing an ED, t (60.41) = -2.06, p = 0.04. Figure 3 compares the two groups' mean risk of developing an eating disorder score.

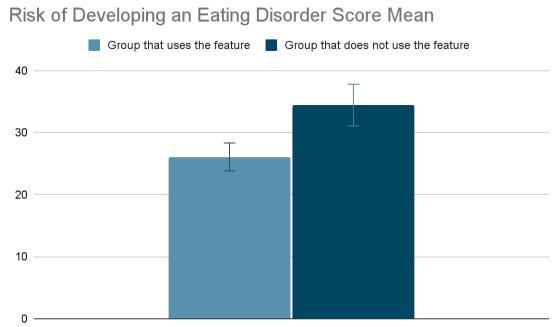

Figure 3: The mean risk of developing an eating disorder score of the two groups.

Gender-Based Comparison:

After we found these significant results, we decided to do an exploratory analysis based on gender differences. Since disordered eating is more common in women, we thought this would be beneficial.

There were no significant differences in males and females, using and not using the feature for the Body Shape Questionnaire and the Self Esteem Scale. However, there was a significant difference for the Eating Attitudes Test in males only.

The 38 male participants in the group that did use the 'hide like and view counts' feature (M = 25.13) compared to the 18 male participants in the group that did not use the feature (M = 38.33) demonstrated significantly lower scores on the EAT, thus being at a lower risk for developing an ED, t (36.87) = -2.46, p = 0.019. Figure 4 compares the two male groups' mean risk of developing an eating disorder score.

DOI: 10.36838/v5i1.18

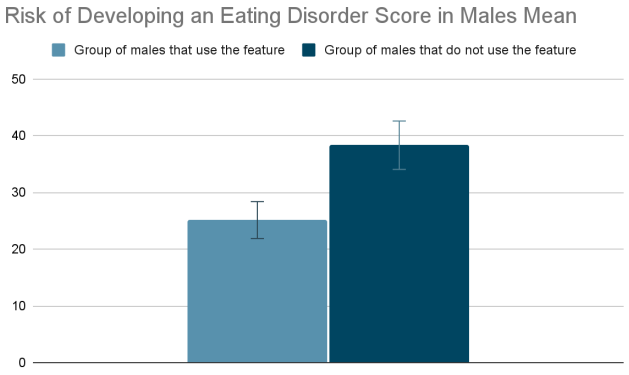

Figure 4: The mean risk of developing an eating disorder score of the two male groups.

Discussion

This study sought to determine whether the 'hide like and view counts' feature is associated with the self-esteem, body dissatisfaction, and disordered eating of Instagram users. The group that used the feature scored significantly lower on the EAT-26, indicating a lower risk of developing an eating disorder than the group that did not. This suggests that the feature may be related to positive rather than negative psychological outcomes. This finding is consistent with our predictions. Contrary to our predictions, the two groups had no significant difference in self-esteem and body dissatisfaction. A subsidiary finding is that 71.79% of the participants, a vast majority, said that they use the 'hide like and view counts' feature, indicating that this feature is slowly gaining popularity.

There could be several reasons why the use of this feature is linked to disordered eating behavior. Someone at a lower risk for developing an eating disorder could be more drawn toward using the feature for reasons currently unknown and requiring further exploration. On the other hand, using the feature may lead individuals to experience fewer triggers for disordered eating.

While we do not know for sure, people could have the notion that the number of likes they receive is a measure of their beauty. For instance, if someone posts a picture of themselves and does not receive many likes, they may think they look ugly, too fat, or too thin in the picture they posted. This could make them more likely to indulge in unhealthy eating patterns. However, if they can't see the number of likes they received, they would not have the opportunity to feel bad about the picture at all. This could be associated with people who use the "hide likes and view counts" feature experiencing lower levels of disordered eating behavior. On the other hand, someone who is already at a lower risk for developing an eating disorder may be more inclined to use the feature. These individuals may place less emphasis on receiving external validation for their appearance and may feel indifferent toward their number of likes, making them more likely to use the feature.

Several other factors could influence the link between the use of this feature and disordered eating behavior. One example could be the number of followers a user has. An instance of this could be someone having a large following feeling more pressured to look perfect on social media. They may feel the need to live up to unrealistic beauty standards and receive many likes. They may compare the number of likes they are getting with others and feel the need to get more. These unhealthy expectations could, in turn, be related to an increase in disordered eating behavior. They may feel that looking a certain way or having a perfect body would help them get more likes. However, if they decide to hide their likes and use the feature, then they could be rid of that stress. Once they cannot see the number of likes they receive, they would not be able to compare themselves with others or be unsatisfied with their likes. This could ease the pressure they may feel from having a flawless body, which could be related to lower levels of disordered behavior. Another factor that could influence the link between the feature and disordered eating is anxiety. In one study, social appearance anxiety predicted body dissatisfaction, bulimic symptoms, shape concern, weight concern, and eating concern.[34] Someone with anxiety may feel judged by others based on the number of likes they receive, so they could decide to hide their likes. Their use of the feature could be related to lower levels of disordered eating.

Interestingly, we did not see any relationship between the feature and self-esteem or body dissatisfaction. One reason for this could be because having the choice of whether to use the feature or not is more beneficial than actually using it. They have the freedom to make this choice could be helpful in many ways. Some users may feel that likes create a competitive environment and feel less anxious when they do not know how many likes they receive on a post. However, other users may want to see the number of likes so they can get a sense of what is 'trending' or popular. Having the option to pick and choose between these alternatives allows a variety of Instagram users to tailor the experience to their needs.

While we did not see a significant difference in females, it was surprising to see a significant difference in males who use the feature and males who do not. The prevalence of eating disorders is more commonly seen in women, so this was interesting. Future research should consider gender differences to find more concrete results.

Limitations and Future Research:

Since this is a correlational study, determining the causality of results is uncertain. Since we could not assign groups, one limitation is the significant difference in the sample sizes of the two groups: the group that uses the feature (n= 84) and the group that does not (n= 33). Future research should try an experimental manipulation study and randomly assign participants to test the causation.

Future research should also consider other influential factors that could affect the impact of the feature on mental health. The content that the user's posts could be a factor. Someone who posts pictures and videos of themselves rather than images of others, their surroundings, or their pets may be more conscious of the number of likes they get. So, they may choose to have their likes hidden. Other factors, like the amount of time they spend on Instagram, could also affect if they decide to use the feature or not. Future directions could include intervention studies. One such study could measure mental health before and after the study, after having participants use the feature for a certain period of time.

Since we used MTurk to recruit our participants, we cannot be sure if each participant actually read every question asked or if they randomly chose any answers. One aspect of our data that denotes concern is that the mean score on the EAT-26 was 26.08 (SD= 4.48) for the group that uses the feature and 34.44 (SD= 8.63) for the group that does not use the feature. The mean scores of both groups fall above the clinical cutoff of 20. This suggests that most sample participants are considered at risk for an eating disorder, which is surprising given the prevalence of eating disorders in the general population. This makes the validity of the results questionable. However, to minimize this risk, we asked participants to manually fill in the words 'I am not a robot in the answer box to ensure that they read the questions asked. The responses of the 2 participants who incorrectly answered this question were discarded.

Conclusion

The popularity of social media has escalated massively in recent years,[1] with Instagram being particularly popular. Several studies have found that social media positively correlates with depression, anxiety, and low self-esteem.[8-12] Studies have shown that it is apparent that the number of likes a user gets can impact their well-being significantly.[26-29] Instagram recently introduced a new feature to the app to help counteract the ill effects of social media: the 'hide like and view counts' feature. This feature enables users to hide the number of likes they receive on shared images. Instagram announced that the feature was to depressurize users' experiences on the app.[31] This study sought to examine whether the feature was indeed associated with positive psychological factors. We hypothesized that using this feature is associated with higher self-esteem and body satisfaction levels and a lower risk of developing an eating disorder. We used a survey to collect data to specifically examine the association between the 'hide like and view counts' feature on the Instagram app and behaviors and cognitions associated with disordered eating, body dissatisfaction, and self-esteem.

While we found no significant differences between the self-esteem and body dissatisfaction of the group that uses the feature and the group that does not, a significantly lower risk of disordered eating was found for the group that uses the feature, which indicates that this feature is associated with positive factors, however, we cannot determine causality; our results suggest that the 'hide like and view counts' feature may be a step in the right direction. What one person wants from their Instagram experience is different from the next. Instagram has recently used several other features to help create a benevolent community and make users feel satisfied with their time on the Instagram app. For instance, Instagram has announced new tools to allow people to filter offensive content and give people ways to control what they see on the app. These efforts are vital in making social media a place where users are welcome to alter their experience to support positive health. Future research should study how technology use can adapt depending on user needs and how social media sites can make conscious interface changes to promote well-being.

Acknowledgments

I would like to express my earnest gratitude to Olivia Losiewicz, Tyler Moulton, and Rithika Abraham for their continuous assistance and feedback throughout this process. I would also like to thank Lumiere Education for providing me with the necessary resources to write this paper.

References

1. Boulianne, S. (2015). Social media use and participation: A meta-analysis of current research. *Information, Communication & Society*,18(5),524–538.https://doi.org/10.1080/1369118X.2015.1008542
2. *Most used social media* 2021. (2022, January 28). Statista. https://www.statista.com/statistics/272014/global-social-networks-ranked-by-number-of-users/
3. *U.S. increased time spent on social media due to coronavirus* 2020. (2021, January 28). Statista. https://www.statista.com/statistics/1116148/more-time-spent-social-media-platforms-users-usa-coronavirus/
4. Instagram users worldwide 2023. (2022, January 28). Statista. https://www.statista.com/statistics/183585/instagram-number-of-global-users/
5. Bair, C. E., Kelly, N. R., Serdar, K. L., & Mazzeo, S. E. (2012). Does the Internet function like magazines? An exploration of image-focused media, eating pathology, and body dissatisfaction. *Eating Behaviors*, 13(4), 398–401. https://doi.org/10.1016/j.eathbeh.2012.06.003
6. Tiggemann, M., & Slater, A. (2013). NetGirls: The Internet, Facebook, and body image concern adolescent girls. *International Journal of Eating Disorders*, 46(6), 630–633. https://doi.org/10.1002/eat.22141
7. Perrin, A. (2015, October 8). Social Media Usage: 2005-2015 65% *of adults now use social networking sites – a nearly tenfold jump in the past decade*.
8. Best, P., Manktelow, R., & Taylor, B. (2014). Online communication, social media and adolescent wellbeing: A systematic narrative review. *Children and Youth Services Review*, 41, 27–36. https://doi.org/10.1016/j.childyouth.2014.03.001
9. Labrague, L. (2014). Facebook use and adolescents' emotional states of depression, anxiety, and stress. *Health Science Journal*, 8, 80-89.
10. Lin, L. yi, Sidani, J. E., Shensa, A., Radovic, A., Miller, E., Colditz, J. B., Hoffman, B. L., Giles, L. M., & Primack, B. A. (2016). Association Between Social Media Use and Depression Among U.s. Young Adults. *Depression and Anxiety,* 33(4), 323–331. https://doi.org/10.1002/da.22466
11. Hunt, M. G., Marx, R., Lipson, C., & Young, J. (2018). No More FOMO: Limiting Social Media Decreases Loneliness and Depression. *Journal of Social and Clinical Psychology,* 37(10), 751–768. https://doi.org/10.1521/jscp.2018.37.10.751
12. Vannucci, A., Flannery, K. M., & Ohannessian, C. M. (2017). Social media use and anxiety in emerging adults. *Journal of Affective Disorders*, 207, 163–166. https://doi.org/10.1016/j.jad.2016.08.040
13. *Does Posting Facebook Status Updates Increase or Decrease Loneliness? An Online Social Networking Experiment—Fenne große Deters, Matthias R. Mehl, 2013*. (2012, December 20). https://journals.sagepub.com/doi/abs/10.1177/1948550612469233
14. Lenhart, A., Smith, A. W., Anderson, M., Duggan, M., & Perrin, A. (2015). *Teens, technology and friendships* (Australia) [Report]. Pew Research Center. https://apo.org.au/node/56457
15. McCallum Place. (2020, February 5). *McCallum place | DSM 5 diagnostic criteria for eating disorders.* McCallum Place Eating Disorder Center. https://www.mccallumplace.com/admissions/dsm-5-diagnostic-criteria/
16. Eric Stice, C Nathan Marti, Paul Rohde. (2012, November 12). *Prevalence, incidence, impairment, and course of the proposed DSM-5 eating disorder diagnoses in an 8-year prospective*

DOI: 10.36838/v5i1.18

community study of young women. PubMed. https://pubmed.ncbi.nlm.nih.gov/23148784/
17. American Psychiatric Association. (2013). *DIAGNOSTIC AND STATISTICAL MANUAL OF MENTAL DISORDERS FIFTH EDITION DSM-5*. Welcome to Repository Poltekkes Kemenkes Kaltim - Repository Poltekkes Kemenkes Kaltim. https://repository.poltekkes-kaltim.ac.id/657/1/Diagnostic%20and%20 statistical%20manual%20of%20mental%20disorders%20_%20 DSM-5%20%28%20PDFDrive.com%20%29.pdf
18. Kim E. McCallum. M.D. James Lock, M.D. Mar) Kulla, M.D. Marcia Rorty, M.A. Richard D. Wetzel, Ph.D. (1992, January 1). *Symptoms and disorders in patients with eating disorders.* Academia.edu - Share research. https://www.academia.\edu/2085455/Symptoms_and_disorders_in_patients_with_ eating_disorders
19. Patrick F. Sullivan. (1995, July). *Mortality in Anorexia Nervosa*. CiteSeerX. https://citeseerx.ist.psu.edu/viewdoc/ download?doi=10.1.1.462.2442&rep=rep1&type=pdf
20. Jasmine Fardouly, Lenny R. Vartanian. (2016, June). S*ocial media and body image concerns: Current research and future directions*. ScienceDirect.com | Science, health and medical journals, full text articles and books. https://www.sciencedirect.com/science/article/pii/S2352250X15002249
21. Saiphoo, A. N., & Vahedi, Z. (2019). A meta-analytic review of the relationship between social media use and body image disturbance. *Computers in Human Behavior*, 101, 259–275. https://doi.org/10.1016/j.chb.2019.07.028
22. Gemma López-Guimerà, Michael P. Levine, David Sánchez-carracedo, Jordi Fauquet. (2010, December 15). *Influence of mass media on body image and eating disordered attitudes and behaviors in females: A review of effects and processes.* Taylor & Francis. https://www.tandfonline.com/doi/abs/10.1080/15213269.2010.525737
23. Holland, G., & Tiggemann, M. (2016). A systematic review of the impact of the use of social networking sites on body image and disordered eating outcomes. *Body Image*, 17, 100–110. https://doi. org /10.1016/j.bodyim.2016.02.008
24. Spettigue, W., & Henderson, K. A. (2004). Eating Disorders and the Role of the Media. *The Canadian Child and Adolescent Psychiatry Review,* 13(1), 16–19.
25. Hockin-Boyers, H., Pope, S., & Jamie, K. (2021). Digital pruning: Agency and social media use as a personal political project among female weightlifters in recovery from eating disorders. *New Media & Society*, 23(8), 2345–2366. https://doi.org/10.1177/1461444820926503
26. Burrow, A. L., & Rainone, N. (2017). How many likes did I get?: Purpose moderates links between positive social media feedback and self-esteem. *Journal of Experimental Social Psychology,* 69, 232–236. https://doi.org/10.1016/j.jesp.2016.09.005
27. Davide Marengo, Christian Montag, Cornelia Sindermann, Jon D. Elhai, Michele Settanni. (2020, November 9). *Examining the links between active Facebook use, received likes, self-esteem and happiness: A study using objective social media data*. ScienceDirect.com | Science, health and medical journals, full text articles and books. https://www.sciencedirect.com/science/article/abs/pii/S0736585320301829
28. Lee, H. Y., Jamieson, J., Reis, H., Beevers, C., Josephs, R., Mullarkey, M., O'Brien, J., & Yeager, D. (2020). Getting Fewer "Likes" Than Others on Social Media Elicits Emotional Distress Among Victimized Adolescents. *Child Development*, 91. https://doi. org/10.1111/cdev.13422
29. *Hungry for "likes": Frequent Facebook use linked to eating disorder risk, study finds*. (2014, March 5). EurekAlert! https://www.eurekalert.org/news-releases/528189
30. *Giving People More Control on Instagram and Facebook*. (2021, May 26). https://about.instagram.com/blog/announcements/giving-people-more-control
31. Rosenberg, M. (1965). Society and the adolescent self-image. Princeton, NJ: Princeton University Press.
32. Cooper, P., Taylor, M., Cooper, Z., & Fairburn, C. G. (1987). The development and validation of the Body Shape Questionnaire. *International Journal of Eating Disorders,* 6, 485–494.Garner, D. M., Olmsted, M. P., Bohr, Y., & Garfinkel, P. E. (1982).
33. The Eating Attitudes Test: psychometric features and clinical correlates. Psychological Medicine, 12, 871–878
34. Cheri A. Levinson, Thomas L. Rodebaugh. (2012, January). Social anxiety and eating disorder comorbidity: *The role of negative social evaluation fears*. ScienceDirect.com | Science, health and medical journals, full text articles and books. https://www.sciencedirect.com/science/article/abs/pii/S1471015311001097

Author

Naisha Agarwal is a senior student at The Cathedral and John Connon School, Mumbai, India. She co-founded 'Bodily Safe Space,' a body positivity movement to spread awareness about eating disorders. She hopes to pursue an undergraduate degree in behavioral economics in college.

IJHSR
ijhighschoolresearch.org
RESEARCH ARTICLE

Skin Disease Classification Using Privacy-Preserving Federated Learning

Brian J. Nam

Westwood High School, 12400 Mellow Meadow, Austin, TX, 78750, USA; brian.janghoon.nam@gmail.com

ABSTRACT: Skin diseases, being one of the most common diseases worldwide, can occur to people of all ages and are caused by bacteria, infections, etc. Currently, skin diseases are initially diagnosed visually, which is often prone to errors. Skin diseases unable to be identified through inspection are identified using a biopsy process that uses dermoscopic analysis and is prescribed manually by physicians. However, a biopsy has its safety and accessibility issues, and manual inspection requires long periods of time. Therefore, this paper uses machine learning for image-based classification techniques for skin disease diagnosis. However, to be trained and tested, machine learning generally requires access to a dataset to be stored in a centralized server, which often raises many concerns regarding security and privacy. In a medical environment especially, maintaining the security and confidentiality of patients' records is very important. Therefore, with the increase in awareness of user privacy, this paper builds a federated learning system where data is decentralized. Using a dataset of more than 10,000 images, the federated learning system initially shows an overall accuracy rate of classifying skin diseases of about 79%. Since the original dataset has class imbalance problems, a data balancing technique is applied to enlarge the dataset and balance the samples per class in the dataset. After balancing the dataset, the performance of the classifier is improved significantly in that it achieves the classification accuracy of 95%. This system is shown to be effective for classifying the type of skin disease using image-based classification techniques, while also keeping user-sensitive information secure.

KEYWORDS: Skin Disease Classification; Machine Learning; Federated Learning; Skin Disease Diagnosis.

Introduction

Skin diseases are one of the most common diseases worldwide. Despite this, diagnosing skin diseases accurately is a challenging task. The prevalence of skin diseases is common in which 26.98% of the world population or 1.6 in 4 people are infected.[1] Particularly, skin cancer has been the most common cancer in the United States and research has shown that one-fifth of Americans suffer from skin cancer during their lifetimes.[2] Most people ignore early symptoms of skin diseases, which can cause various damages on the skin and will continue to spread overtime. Therefore, it is important to identify these diseases as soon as possible to control their potential spread.

Currently, skin diseases are initially diagnosed by doctors visually. Diagnosing a skin disease correctly is challenging since a variety of visual clues, such as the individual lesion morphology, the body site distribution, color, scaling, and arrangement of lesions should be utilized to facilitate the diagnosis. When the individual components are analyzed separately, the diagnosis process can be complex.[3] Skin diseases unable to be identified through inspection are identified using a biopsy process that uses dermoscopic analysis and is prescribed manually by physicians. However, differentiating a skin disease with dermoscopy images may be inaccurate or irreproducible since it depends on the experience of dermatologists. In practice, the diagnostic accuracy of melanoma from the dermoscopy images by an inexperienced specialist is between 75% to 84%.[4]

By contrast, image-based classification techniques can improve the accuracy of skin disease diagnosis. Using images of infected areas of the skin as input, features are extracted from the images to be suitable for the classifier model to classify the type of disease. By utilizing features, traditional machine learning systems for skin disease classification can achieve excellent performance in certain skin disease diagnosis tasks.[5,6] However, with technology continuing to develop and growing more powerful, issues involving privacy concerns also emerge. Machine learning, to be trained and tested, generally requires access to a dataset stored in a centralized server. In a medical environment, maintaining the security and confidentiality of patients' records is very important. Because of strict regulations regarding data privacy, it is usually considered not practical to gather and share consumers' data within a centralized location. This challenges traditional machine learning algorithms because they require huge quantities of data training examples to learn.[7]

Motivated by the aforementioned privacy issues of traditional machine learning, this paper uses the federated learning (FL) system where data is decentralized. A federated learning system consists of a server and several local devices where users can input their own local data into the local network using local devices.[8] Each local network model is then trained using its local data, not through a server network with risk of exposing private data. The devices then send the local networks, not the user data, to the server. The server then is able to update the global network by aggregating the local networks. The federated learning approach is very advantageous for utilizing

DOI: 10.36838/v5i1.19

low-costing machine learning models on devices such as cell phones and sensors.[9]

The main contributions of this paper include:

• A convolutional neural network (CNN)-based federated learning model is proposed to classify skin disease while preserving data privacy.

• A data balancing technique is used to resolve the data imbalance problem of the skin disease dataset and also increase the size of the training dataset, which improves overall classification accuracy by more than 15%.

This paper is organized as follows. Section 2 briefly summarizes the related existing work. Section 3 explains the proposed federated learning method, while the dataset used in the learning method is discussed in Section 4. The results are presented in Section 5 followed by the conclusions.

Related Work:

Recently, machine learning methods have become popular in feature detecting and have achieved excellent performances in various tasks, including image classification.[10,11] A variety of research showed that deep learning methods were able to surpass humans in many computer vision tasks.[12-14] One thing behind the success of machine learning is its ability to extract features automatically from large amounts of datasets. In particular, there have been many works on applying machine learning methods to skin disease diagnosis.[14-17] For example, Esteva *et al*. propose a universal skin disease classification system based on a pre-trained convolutional neural network (CNN).[14] Rezvantalb *et al*. also developed multiple CNNs with classification accuracies of 94.4%, which significantly outperforms the performances of human specialists.[17] Traditionally, CNN is one of the earliest machine learning models proposed for image classification. For instance, Yuan *et al*.[18] proposed a framework based on convolutional neural networks to automatically segment skin lesions in dermoscopy images. The method was tested on the ISIC dataset and resulted in an index of 78.4% on the validation dataset. Al-Masni *et al*.[19] developed a method via full resolution convolutional neural networks. The method was able to directly learn the full resolution result of each input image without the need for preprocessing operations. The method resulted in an index of 77.1% and overall accuracy of 94.03% on the ISIC dataset, respectively.

Deep neural networks can deal with the large variations included in the images of skin diseases by extracting features with multiple layers. Despite these technological advances, however, these traditional systems cannot secure user-sensitive information, making federated learning the more practical option. Federated learning has been employed in a variety of applications, with plenty of research relating to its applications, one example being in the healthcare sector.[20] This application of Federated Learning (FL) also covered medical imaging where it was used for brain tumor segmentation. While methods such as Deep Neural Networks have illustrated notable findings, they can be problematic because the needed training data may not be available due to having low incident rates of particular diseases and a low number of people. Therefore, a dataset that contained MRI scans of almost 300 people with brain tumors is used for an application of FL.[21] They then compared their methods with data-based training where the results showed the effectiveness of the authors' proposed method. Another use for FL is an anomaly detection system using FL to detect various IoT devices.[22] Aledhari *et al*. demonstrate the usage of a federated learning system within a healthcare sector.[23] Each hospital acts as a local client where patients input local data. Then the local networks of each hospital are aggregated by a central cloud server which can be used by doctors to act as a powerful tool. The autonomous system can effectively operate without human intervention or labeled data. Their system was able to achieve a 95% detection rate with no false positives. Additionally, their system can withstand new and unknown attacks. Many different industries and companies are beginning to implement FL into their own works and products. As a result, Federated Learning is becoming one of the most innovative technologies to date.

Methods

Dermatology is termed as a visual specialty wherein most diagnoses can be performed by visual inspection of the skin. Equipment-aided visual inspection is important for dermatologists since it can provide crucial information for precise early diagnosis of skin diseases. Subtle features of skin diseases need further magnification such that experienced dermatologists can visualize them clearly.[24] In some cases, a skin biopsy is needed which provides the opportunity for a microscopic visual examination of the lesion in question. However, with the development of machine learning, there have been many studies using images obtained by digital cameras or smartphones for skin disease diagnosis.[25] Though the quality of these images is not as high as those obtained with professional equipment, excellent diagnosis performance can be achieved with advanced image processing and analysis methods.

HAM10000 Dataset:

Training a machine learning system requires a large amount of labeled data. Therefore, high-quality skin disease data with reliable labels is significant for the development of advanced algorithms. The dataset used in this paper is the HAM10000 ("Human Against Machine with 10000 training images"). The dataset is publicly available through the ISIC archive and was collected by Hospital Universitario de Caracas in Caracas, Venezuela. The dataset consists of 10,015 dermatoscopic images which are released as a training set for academic machine learning purposes.[26] The images of the dataset are collected from various ages, genders, and locations of skin disease. This benchmark dataset can be used for machine learning and for comparisons with human experts. There are seven different skin disease types including Melanocytic nevi, Melanoma, Benign keratosis-like lesions, Basal cell carcinoma, Actinic keratoses, Vascular lesions, and Dermatofibroma. The diagnoses of all melanomas were verified through histopathological evaluation of biopsies, while the diagnosis of nevi is made by either histopathological examination (24%), expert consensus (54%), or another diagnosis method, such as a series of images that showed no temporal changes (22%).[27] Figure 1(a) shows a frequency distribution of the seven skin disease types in the dataset. As shown in

the figure, the number of images for each skin disease type is uneven such that the akiec skin disease takes up about 65% of the whole dataset which causes the machine learning network to be biased when trained. This is a common problem occurring in skin disease diagnosis causing an imbalance in datasets. Many datasets contain significant disparities in the number of data points among different skin classes and can be heavily dominated by certain data. Training deep learning models with imbalanced data may result in biased results. Although HAM10000 does not seem like a good option for the dataset, acquiring a large dataset of skin disease images can be difficult. The HAM10000 dataset is available publicly online and is easy to access. Additionally, many other studies have used the same dataset; For example, Srinivasu *et al*. use the HAM10000 dataset in order to classify skin diseases using deep learning neural networks.[28]

Data Preprocessing and Balancing:

Data preprocessing is a crucial step for a classifier model to achieve high performance. Since there is a huge variation in image resolutions within the skin disease dataset, it is necessary to crop or resize the images from these datasets to adapt them to deep learning networks. It should be noted that resizing and cropping images directly into required sizes might introduce object distortion or substantial information loss.[29] The original high-resolution images of the HAM10000 dataset are resized to 28x28 for training the FL network.

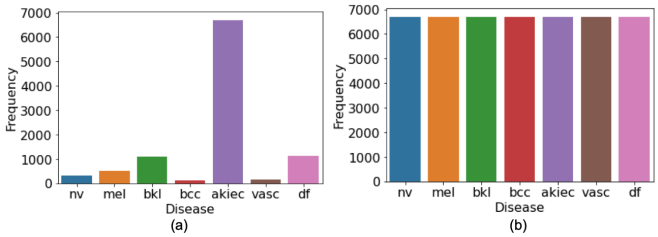

Figure 1: Frequency distribution of skin disease classes of (a) the original HAM10000 dataset that shows an imbalanced class problem and (b) the HAM10000 dataset after applying data balancing by SMOTE.

As shown previously, the HAM10000 image dataset has data class imbalance, which results in a biased trained network. Generally, an imbalanced dataset problem can be solved by several approaches as described as follows: 1) weighted class approach, 2) under-sampling approach, 3) data augmentation for minority class, and 4) synthetic minority over-sampling technique (SMOTE). In the weighted class approach, each class is assigned a weight based on the ratio of occurrence of each class, but this technique does not perform well. The under-sampling method selects the same number of samples for both majority and minority classes, which often reduces the size of the training dataset. Data augmentation is very popular when dealing with image datasets, in which the dataset can be enlarged by adding more images by applying various image transformation techniques such as mirroring, rotating, sheering, cropping, translating, zooming, noise injection, color space transformation, random erasing, mixing images, etc.[30] Since data augmentation can artificially transform the original data, it is important for the algorithm to have scalability. It must be flexible enough to allow changes in size or topology to be handled easily. Additionally, it is important to prioritize which resources need to be done beforehand for better equal provision for the dataset. Another technique, used in this manuscript, is SMOTE (synthetic minority over-sampling technique), in which new samples are generated by over-sampling in terms of an interpolation of the original data. It is an over-sampling technique that generates synthetic samples from minority classes.[31] After numerous tests for those various techniques, this paper uses SMOTE to resolve the imbalanced distribution of the dataset, in which the number of samples in the dataset is increased to 46,935 images. Figure 1(b) illustrates the frequency distribution of classes after applying SMOTE to the HAM10000 dataset, which shows the equal number of image samples for each class. It shows in the later section that the classification accuracy is improved by more than 15% by balancing the dataset.

Federated Learning Methods:

Figure 2 shows the structure of a federated learning system, where it consists of a cloud server and N users with local clients. Each user can input the local data to train its local network and then send the local network, the results of the local data, to the server.[8,32] After receiving the local networks from the users, the cloud server then updates its global network by aggregating the local networks and further distributing the global network back down to the users. Each user then updates the global network by further training it with its local data to construct the local network, which is again reported to the server. These steps of interaction repeat as many as they can or until a certain performance target is met. Note that the users only transmit the trained local network to the server without the risk of exposing private local data. By utilizing this system, not only does it provide an accurate skin disease diagnosis, but it is also able to secure user-sensitive information, making it more accessible and safer for people to use. Unfortunately, there are still some crucial obstacles for FL to be fully incorporated in other settings, especially regarding the data. For our models and algorithms to learn effectively to obtain optimal results, it requires a lot of data in order to ensure our models will be as accurate as possible.[33] Therefore, despite FL's promising potential, FL is still not widely understood regarding some of its technical components such as platforms, hardware, software, and others regarding data privacy and data access.[23]

A Federated Learning framework centered around privacy comes with many challenges. Local network to global network transmission can be expensive and may not be stable. An FL was implemented using python language on a Jupyter notebook under a virtual environment by anaconda. A Colab server was used to train and test the dataset. There are some FL examples on Kaggle.com and one of those examples is used and modified to build my FL implementation. The aggregation of the local networks to create a global network at the FL server is done by averaging all the local networks, which is the FedAvg algorithm.

Model:

This paper demonstrates the application of a federal learning system to skin disease diagnosis. The dataset was divided into two groups as the training and testing groups randomly. The

DOI: 10.36838/v5i1.19

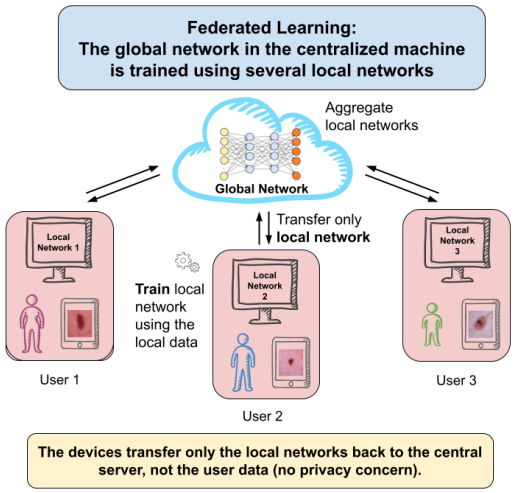

Figure 2: Privacy-preserving federated learning system structure.

dataset is split into 90% of the dataset as the training dataset and the remaining 10% as the test dataset. A loss function is used in the network to calculate the loss, where the network is always trained to minimize the loss. There was also a validation procedure to avoid overfitting while training. In the federated learning system considered in this paper, 10 different clients (N = 10 in Figure 2) are created where the images are randomly divided equally between each client. Each client has a local network where it trains using its own local dataset. Once the local networks are done training the server receives and aggregates all the local networks together to create a global network. The global network then is distributed down back to the clients. From there, the clients use the global network as a new starting point, then trains its local network again using its local dataset. The client's local network updates and the cycle repeats 100 times. In this paper's model, it is assumed that the communication between the server and clients has no issues. However, in the real world, a local network to global network transmission can be expensive and unstable, making it prone to errors. The impact of such erroneous communications between the server and clients on the performance is difficult to analyze and is an active ongoing research area. Like most of the federated learning papers, this manuscript also assumes perfect communication with no error. The dataset is distributed randomly over the clients, each with similar amounts of samples.

Global and Local Networks:

A convolutional neural network (CNN) model is used for the global network and local networks. Figure 3 demonstrates the structure of the CNN model used in the federated learning system in this paper. Both the global and the local networks use the same CNN structure.

A CNN generally consists of multiple layers of convolution and pooling. The CNN structure used in this paper has 4 such layers, in which features are extracted from the skin disease image dataset. For each convolution layer, a number of kernels are deployed to extract the features. The first layer uses 64 kernels, and the later layers increase the number to achieve the best performance. For max pooling, the image sizes are reduced by taking 4 neighboring pixels and choosing the largest pixel to represent it. The last step in the structure is a fully

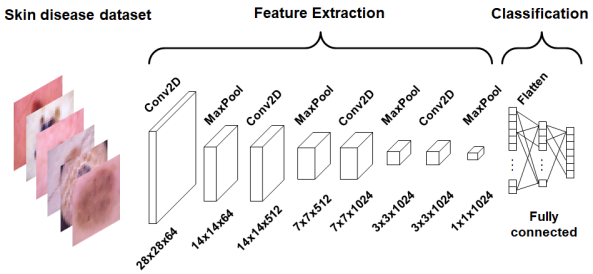

Figure 3: Privacy-preserving federated learning system.

connected layer to classify what type of skin disease the image belongs to. To accomplish the task of classification, using the extracted features, a fully connected layer has 1024 features flattened and arranged in one row of 1x1x1024. Each feature is then connected to each of the 7 output nodes through over 7000 weight values. The training dataset is used to repeat this process to train the network until the weight values saturate. Then the test dataset is used for the trained network to analyze the results.

The CNN architecture shown in Figure 3 consists of two stages: feature extraction and classification. The hyper-parameters of the architecture were selected based mainly on the input image size (28x28) and max-pooling steps. The number of kernels for each convolution layer was determined experimentally after numerous simulations. Some CNN network examples for image classification in the public domain were also useful for hyper-parameter selection.

Results and Discussion

Simulations and Evaluation:

An extensive number of simulations are performed to evaluate the performance of the federated learning-based classifier. For a development environment, Jupyter lab and Anaconda tools are used on an Intel Core(TM) i7-1165G7 CPU @ 2.80GHz accelerated by GPU Nvidia RTX 3090. A cloud GPU server Google Colab was also utilized. During the implementation process, training the model with a large dataset requires a considerable amount of time for an ordinary CPU to execute. Therefore, a GPU is commonly used to build and run the model to save a large amount of time. The in-depth learning approach in this paper is built using Tensorflow 2.0 and Python 3.

Classification Accuracy:

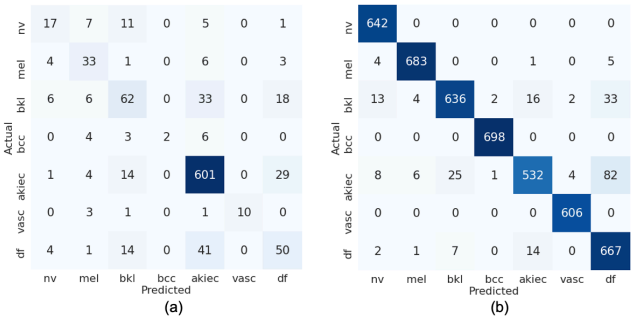

Figure 4: Confusion matrices for skin disease classification for (a) the FL system with the original HAM10000 dataset and (b) the FL system with the HAM10000 dataset balanced by SMOTE.

To evaluate the effectiveness of data balancing, two federated learning systems with identical structures are trained each with a different dataset. One with the original HAM10000 dataset and the other with the balanced HAM10000. Figure 4 illustrates confusion matrices to show the classification accuracy of the two Federated Learning (FL) systems, one with the original HAM10000 dataset, which has a data imbalance problem, and the other with the HAM10000 dataset after applying a data balancing by SMOTE. For classification problems, a confusion matrix is generally a popular way to show performance. As shown in Figure 4(a), the FL system with the original dataset has an overall accuracy rate of about 79% overall, but it exhibits a heavily biased performance result: 93% accuracy for akiec detection (dark squares), whereas only 20% accuracy for bcc detection due to the imbalanced dataset. The problem of a high accuracy rate for akiec but not as high of an accuracy for the other diseases occur because the akiec skin disease images take up about 65% of the whole dataset which causes the learning system to be biased, as shown in Figure 1(a). Limited data are common in the field of medical image analysis due to the rarity of the disease, patient privacy, the requirement of labeling by medical experts, and the high cost to obtain medical data. Training deep learning models with imbalanced data often results in biased results. On the other hand, Figure 4(b) clearly depicts that all the skin disease types have high accuracy (80% or higher) with an overall accuracy of 95% thanks to the data balancing technique, which artificially transforms or over-samples the original data to increase the amount of available training data. By enhancing the size and quality of the available training data, the network can learn more significant properties. Although it may not be a fair performance comparison between those two FL systems given above due to the different number of samples in the two datasets, the figures clearly indicate that the classification performance of the federated learning system is greatly improved by balancing the dataset.

Conclusion

Skin disease diagnoses with machine learning methods has had promising progress in recent years. This paper proposes a federated learning system for skin disease diagnosis. Not only does federated learning provide an accurate skin disease diagnosis, but it is also able to secure user-sensitive information, making it safer for people of all ages to use. Although the classification accuracy of 79% for the FL system with the original dataset may not seem practical at first, the FL system along with a data balancing technique improves the accuracy significantly up to 95%. This model should be helpful for doctors, those who cannot diagnose visually with high accuracy, and act as extra evidence for more experienced doctors. It is worth noting that machine learning is always evolving as time goes on, the accuracy may go higher in the future. Although machine learning systems will never replace doctors, instead they can be used as powerful tools. This can be taken advantage of to provide doctors with useful information to help them make a final intelligent decision while also keeping patients' medical data secure. The potential benefits of automated diagnosis of skin diseases with machine learning are tremendous. However, accurate diagnosis increases the demand for a reliable automated process that can be utilized by doctors and clinicians. It should be understood that a computer-aided skin disease diagnosis system should be critically tested before it is utilized for real-life clinical diagnosis tasks.

Acknowledgments

I would like to thank Seong-Hyo Ahn, University of Texas at Austin for helping to guide me throughout the entire of conducting my research. In addition, I would like to thank Jeffery Mickel, Westwood high school, for deepening my understanding of computer science and machine learning.

References

1. Lim et al., "The Burden of Skin Disease in the United States," *Journal of the American Academy of Dermatology*, 1 May 2017, https://www.jaad.org/article/S0190-9622(17)30016-6/fulltext.
2. R. S. Stern, "Prevalence of a history of skin cancer in 2007: results of an incidence-based model," *Archives of dermatology*, 146 (3) (2010) 279–282.
3. T. P. Habif, M. S. Chapman, J. G. Dinulos, and K. A. Zug, "Skin disease e-book: diagnosis and treatment," *Elsevier Health Sciences*, 2017.
4. A.-R. A. Ali and T. M. Deserno, "A systematic review of automated melanoma detection in dermatoscopic images and its ground truth data, Medical Imaging 2012: Image Perception, Observer Performance, and Technology Assessment," Vol. 8318, *International Society for Optics and Photonics*, 2012, p. 83181.
5. J. L. G. Arroyo and B. G. Zapirain, "Automated detection of melanoma in dermoscopic images," *Computer vision techniques for the diagnosis of skin cancer,* Springer, 2014, pp. 139–192.
6. A. S´aez, B. Acha, and C. Serrano, "Pattern analysis in dermoscopic images," *Computer vision techniques for the diagnosis of skin Cancer, Springer*, 2014, pp. 23–48.
7. D. B. Larson, D. C. Magnus, M. P. Lungren, N. H. Shah, and C. P. Langlotz, "Ethics of using and sharing clinical imaging data for artificial intelligence: A proposed framework," *Radiology,* vol. 295,no. 3, 2020, Art. no. 192536.
8. T. Li, M. Sanjabi, A. Beirami, and V. Smith, "Fair resource allocation in federated learning," 2019, arXiv:1905.10497. [Online]. Available: http://arxiv.org/abs/1905.10497
9. R. Doku, D. B. Rawat, and C. Liu, "Towards federated learning approach to determine data relevance in big data," Proceedings of IEEE 20th International Conference Information Reuse Integration for Data Science (IRI). Los Alamitos, CA, USA, Jul. 2019, pp. 184–192, doi: 10.1109/iri.2019.00039
10. K. He, X. Zhang, S. Ren, and J. Sun, "Deep residual learning for image recognition," *Proceedings of the IEEE conference on computer vision and pattern recognition*, 2016, pp. 770–778
11. A. Krizhevsky, I. Sutskever, and G. E. Hinton, "Imagenet classification with deep convolutional neural networks," *Advances in neural information processing systems*, 2012, pp. 1097–1105.
12. W. Ouyang, X. Wang, X. Zeng, S. Qiu, P. Luo, Y. Tian, H. Li, S. Yang, Z. Wang, and C.-C. Loy, "Deepid-net: Deformable deep convolutional neural networks for object detection," *Proceedings of the IEEE conference on computer vision and pattern recognition*, 2015, pp. 2403–2412.
13. P. Sermanet, D. Eigen, X. Zhang, M. Mathieu, R. Fergus, and Y. LeCun, "Overfeat: Integrated recognition, localization and detection using convolutional networks," arXiv preprint arXiv:1312.6229.
14. A. Esteva, B. Kuprel, and S. Thrun, "Deep networks for early stage skin disease and skin cancer classification," Project Report, Stanford University.
15. A. Esteva, B. Kuprel, R. A. Novoa, J. Ko, S. M. Swetter, H. M. Blau,

DOI: 10.36838/v5i1.19

and S. Thrun, "Dermatologist-level classification of skin cancer with deep neural networks," *Nature* 542 (7639) (2017) 115.
16. H. Liao, Y. Li, and J. Luo, "Skin disease classification versus skin lesion characterization: Achieving robust diagnosis using multi-label deep neural networks," *23rd International Conference on Pattern Recognition (ICPR)*, IEEE, 2016, pp. 355–360.
17. Rezvantalab, Amirreza, et al. "Dermatologist Level Dermoscopy Skin Cancer Classification Using Different Deep Learning Convolutional Neural Networks Algorithms." *ArXiv.org*, Cornell University, 21 Oct. 2018, https://arxiv.org/abs/1810.10348.
18. Y. Yuan, M. Chao, and Y.-C. Lo, "Automatic skin lesion segmentation using deep fully convolutional networks with jaccard distance, " IEEE transactions on medical imaging, 36 (9) (2017) 1876-1886.
19. M. A. Al-Masni, M. A. Al-antari, M.-T. Choi, S.-M. Han, and T. -S. Kim, "Skin lesion segmentation in dermoscopy images via deep full resolution convolutional networks," *Computer methods and programs in biomedicine*, 162 (2018) 221–231.
20. A. Stoian, R. Ivan, I. Stoian, and A. Marichescu, "Current trends in medical imaging acquisition and communication," *Proceedings of IEEE International Conference on Automation, Quality and Testing, Robotics*, vol. 3. May 2008, pp. 94–99.
21. W. Li, F. Milletari, D. Xu, N. Rieke, J. Hancox, W. Zhu, M. Baust, Y. Cheng, S. Ourselin, M. J. Cardoso, and A. W. Feng, "Privacypreserving federated brain tumour segmentation," in Proc. MLMI@M ICCAI, 2019, pp. 133–141.
22. T. D. Nguyen, S. Marchal, M. Miettinen, H. Fereidooni, N. Asokan, and A.-R. Sadeghi, "DÏoT: A federated self-learning anomaly detection system for IoT," *Proc. IEEE 39th Int. Conf. Distrib. Comput. Syst. (ICDCS)*, May 2019, pp. 756–767.
23. M. Aledhari, R. Razzak, R. M. Parizi and F. Saeed, "Federated Learning: A Survey on Enabling Technologies, Protocols, and Applications," *IEEE Access*, vol. 8, pp. 140699-140725, 2020.
24. A. Alexander, A. Jiang, C. Ferreira, and D. Zurkiya, "An intelligent future for medical imaging: A market outlook on artificial intelligence for medical imaging," *Journal of the American College of Radiology,* vol. 17, no. 1, pp. 165–170, Jan. 2020.
25. A. Marghoob and R. Braun, *An atlas of dermoscopy*, CRC Press, 2012.
26. E. Chao, C. K. Meenan, and L. K. Ferris, "Smartphone-based applications for skin monitoring and melanoma detection," *Dermatologic clinics*, 35 (4) (2017) 551–557.
27. P. Tschandl, C. Rosendahl, and H. Kittler, "The ham10000 dataset, a large collection of multi-source dermatoscopic images of common pigmented skin lesions," *Scientific data*, 5 (2018) 180161
28. Srinivasu PN, SivaSai JG, Ijaz MF, Bhoi AK, Kim W, Kang JJ. Classification of Skin Disease Using Deep Learning Neural Networks with MobileNet V2 and LSTM. Sensors (Basel). 2021 Apr 18;21 (8):2852.
29. L. Zheng, Y. Zhao, S. Wang, J. Wang, and Q. Tian, "Good practice in cnn feature transfer," arXiv preprint arXiv:1604.00133.
30. C. Shorten and T. M. Khoshgoftaar, "A survey on image data augmentation for deep learning," Journal of Big Data, 6 (1) (2019) 60.
31. N. V. Chawla, K. W. Bowyer, L. O. Hall, W. P. Kegelmeyer, "SMOTE: Synthetic Minority Over-sampling Technique," Journal Of Artificial Intelligence Research, Volume 16, pages 321-357, 2002
32. H. Zhu, Z. Li, M. Cheah, and R. Siow Mong Goh, "Privacy-preserving weighted federated learning within oracle-aided MPC framework," 2020, arXiv:2003.07630. [Online]. Available: http://arxiv.org/abs/2003.07630
33. R. Shao, H. He, H. Liu, and D. Liu, "Stochastic channel-based federated learning for medical data privacy preserving," 2019, arXiv: 1910.11160. [Online]. Available: http://arxiv.org/abs/1910.11160

Author

Brian Nam is currently a senior at Westwood High School in Austin, TX. With interests in computer programming, mathematics, and science, he plans to continue to pursue his passions in college.

IJHSR
ijhighschoolresearch.org
■ REVIEW ARTICLE

Helmet Modifications and Policy Changes to Mitigate Chronic Traumatic Encephalopathy in Professional Football

Nikhil H. Vallikat

Thomas Jefferson High School for Science and Technology, 6560 Braddock Rd, Alexandria, VA, 22312, USA; nikhil@raddhigroup.com

ABSTRACT: Chronic Traumatic Encephalopathy (CTE) is a neurodegenerative disease caused by repetitive brain trauma, which can have symptoms of aggression, depression, and progressive dementia. Concussions, referred to as mild traumatic brain injury, happen when contact or whiplash causes the brain to shake inside the head and contact with the skull, which has been linked to the development of CTE. There are around 3.8 million sports-related concussions annually. CTE can only be definitively diagnosed (beyond limited imaging) postmortem through an analysis of the abnormal tau proteins in the brain. Unfortunately for the afflicted, there is no known cure for CTE. Preventative measures are thus paramount in reducing the incidence and severity of CTE. We present current measures being researched, including helmet modifications and neck strengthening methods and a potential policy alteration to football to reduce and/or prevent concussions (and more severe injuries such as neck fractures) and thereby mitigate CTE.

KEYWORDS: Translational Medical Sciences, Disease Prevention, Chronic Traumatic Encephalopathy, Concussions, Football.

■ Introduction

Chronic Traumatic Encephalopathy (CTE) is a neurodegenerative disease caused by repeated traumatic brain injuries (TBIs) or general trauma.[1] Its effects include memory loss, impaired judgment, impulse control problems, aggression, depression, suicidality, Parkinson's syndrome, and, eventually, progressive dementia.[2] The effects of CTE are progressive and are divided into four stages. Stage 1 represents the earliest signs of CTE; symptoms often include memory loss. Stage 2 has symptoms of decreased concentration and cognition and sometimes impulse control issues. Stage 3 can cause impulsive violent reactions, paranoia, and further memory loss. Stage 4 leads to symptoms like dementia. This progression of CTE from stage 1 is estimated to take around thirteen years; a high proportion of those over 60 with CTE is found to have stage 3 or stage 4.[3] CTE can only be definitively diagnosed postmortem through an analysis of the abnormal tau proteins in the brain.[4] Its signs, however, can be observed through Magnetic Resonance Imaging (MRI) testing, showing brain shrinkage in certain areas.[5] This limitation prevents the prevalence of individuals with CTE from being known. Unfortunately for the afflicted, there is no known cure for CTE at this point in time.

Preventative measures are thus paramount in reducing the incidence and severity of CTE. In professional sports, this can be achieved by preventing head trauma. Concussions are the most common mild traumatic brain injury (mTBI) in the United States of America and are the most diagnosable form of head trauma in professional sports. There are around 3.8 million sports-related concussions annually.[6] A concussion results from an impact to the head or body or a whiplash effect that jolts the brain causing damage to brain cells.[7] Symptoms include headaches, confusion, nausea, light sensitivity, ringing in the ears, and trouble understanding and/or concentrating. Concussions are diagnosed through a neurological exam that tests thinking abilities, memory/concentration, hearing, light sensitivity, vision, and eye movement.[8] Repeated concussions and traumatic brain injuries are believed to be the cause of CTE, but not all individuals who experience multiple traumatic brain injuries will be diagnosed with CTE.[6] The primary prevention strategy involving CTE must involve mitigating concussions or concussive blows by focusing on decreasing the forces involved in traumatic brain injuries. Reducing the magnitude of these impacts through policy change could also affect concussion incidence and CTE development.

■ Discussion

Effects of CTE on Football:

The effects of CTE on former professional players sprung into national attention after its discovery by Bennet Omalu (a Nigerian American physician, forensic pathologist, and neuropathologist). In the early 2000s, he discovered CTE after examining the head of a former professional football player. It has been diagnosed in many people, from former professional athletes to ex-military personnel.[9] It became increasingly significant after the tragic suicide of Junior Seau. He played in the National Football League (NFL) for twenty years as a linebacker and died in May 2012 of a self-inflicted gunshot. Seau was posthumously diagnosed with CTE.[10] A former teammate commented on Seau's difficulty sleeping over the years, which indicates the progressive nature of CTE. Furthermore, two years before he passed, he also owed massive debts to casinos after repeatedly playing high-stakes blackjack, potentially indicating impulsive decisions, another symptom of CTE.[11] More recently, Phillip Adams, who played six years in the NFL as a cornerback, died in April of 2021 after shooting and killing six people and then taking his own life. Adams was also posthumously diagnosed with CTE. Dr. Ann McKee, who

DOI: 10.36838/v5i1.20

analyzed the brain of Phillip Adams, diagnosed him with Stage 2 CTE. She also believed that he was suffering from paranoia and impulsive behavior symptoms.[12]

It is interesting that Gary Plummer, a former NFL player and Junior Seau teammate, said, "In the 1990s, I did a concussion seminar. They said a Grade 3 concussion meant you were knocked out, and a Grade 1 meant you were seeing stars after a hit, which made me burst out in laughter. As a middle linebacker in the NFL, if you don't have five of these each game, you were inactive the next game." This repeated onset of concussions, while mild, would be a factor in the development of CTE.[13]

These stories are examples of how CTE is not only a danger to the health of professional football players but also to the health of college and high school football players who experience repeated mild traumatic brain injuries or concussions. Over 1 million high school and seventy thousand college football athletes and CTE has already been observed in these groups. A retrospective study published in the Journal of Medical Association (JAMA) in 2017 found CTE in 3 out of 14 high school football players and 48 out of 53 college football players.[14] These statistics show that CTE is a growing public health issue and must be studied more closely, along with policies being enacted in football to mitigate concussions due to their link to CTE.

The Different Forces involved in Concussions and an Assessment of the Current Helmet :

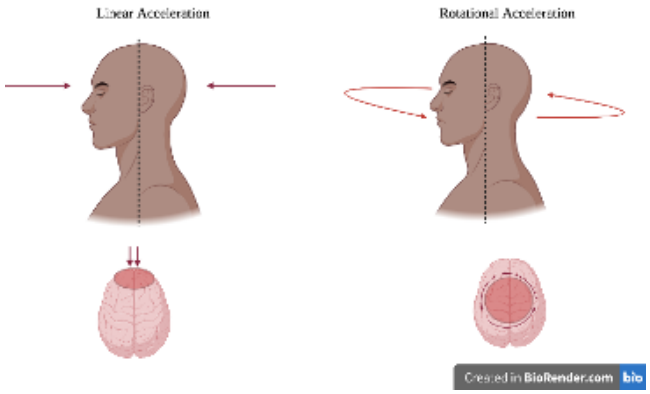

Figure 1: Visual differentiating between the linear and rotational acceleration.

During a concussion, the brain is jolted around, which stretches and damages brain cells.[7] This can damage the protectional tissue around the brain, which prevents direct contact between the brain and the skull. This can lead to bruising of the brain.[15] The main forces involved in a concussion are linear acceleration and rotational acceleration, as seen in Figure 1. Linear acceleration includes head-on impact, and injuries include intracranial hemorrhaging and skull fractures.[2] An example is when a car brakes too hard, and the passenger's head jolts forward, contacting the front of the vehicle's interior. Rotational acceleration involves the unrestricted movement of the head asynchronously to the neck and body.[2] An example would be a boxer getting punched in the side of the face, causing their neck to twist. Injuries affect the brain stem, and rotational acceleration is thought to be the leading cause of concussions. Brain stem injuries can lead to momentary paralysis and affect bodily functions and memory.[16] Most modern helmets sufficiently protect against linear acceleration but do not adequately protect against rotational acceleration. While the brain can withstand rotational acceleration up to a duration of 5 ms, typical impacts in professional football last 10-15 ms.[2] Furthermore, the rotational acceleration is dependent on the frictional coefficient. A greater frictional coefficient value would result in a greater rotational acceleration, which indicates an increased strain on the brain. The frictional coefficient represents the frictional forces between 2 objects to prevent motion; the higher the frictional coefficient, there will be less motion/slide between 2 objects. By decreasing the frictional coefficient in helmets, when contact is made, the helmets will slide on each other. Preventative measures need to limit rotational acceleration through modifications of the helmet or by decreasing the frictional coefficient of the helmet by using a different material.

Current preventative measures currently researched:

The Impact Diverting Mechanism (IDM) is a decal meant to be placed on the exterior of a football helmet.[2] The IDM Decal decreases the friction coefficient between the decal on the helmet and the impacting surface. The decal comprises four layers: the outermost layer decreases the rotational acceleration during high-speed collisions, the middle layers reduce friction between the four layers, and the innermost layer attaches to the helmet's exterior. The researchers tested this decal by comparing it to a control group (no decal). The researchers dropped helmets with decals and without and compared the rotational acceleration and velocity at a speed of 5.5 m/s.

The helmet was dropped at three impact angles at each location (15, 30, and 45 degrees) to account for the variety of hits a football player can take. They found that the decal successfully reduced rotational acceleration by amounts ranging from 27% to 77%, and rotational velocity was reduced by amounts ranging from 20% to 74%. Statistics on the durability of the IDM were not provided, and further research should investigate its feasibility. In addition, it should be noted that the researchers in this study had a conflict of interest, indicating the need for more testing to minimize the effects of bias. If the IDM consistently gets damaged, then the cost required to replace the IDM could make it impractical. This is because the IDM causes the impact to slide on the helmet, decreasing the overall magnitude of the impact by reducing the forces involved. By decreasing the frictional coefficient, the magnitude of the frictional forces involved is also reduced. Because the overall magnitude is decreased, the overall impact/jolt experienced will also be decreased, thus reducing the shock experienced by the brain. In addition, linear acceleration was also reduced (7% - 39% reduction).

Further study should go into expanding the size of the decal as the size of the decal was limited to the size of conventional decals. If the IDM covers the whole helmet, greater protection can be ensured. However, the IDM could be a great addition to a football helmet due to its ability to decrease

rotational acceleration, mitigating concussion prevalence and reducing CTE risk.

Liquid Shock Absorption:

The fluid-based shock absorber concept is the idea of applying a constant force to the head to minimize the risk of a concussion or an mTBI.[17] Applying a constant force to the head is optimal as it would minimize the jolt/blow to the head and therefore reduce the amount/degree that the brain shakes inside the head and contacts the skull. The researchers believe that by mitigating this effect, traumatic brain injuries would be prevented from occurring. The researchers used computational simulations to evaluate the effectiveness of this concept. While it doesn't perfectly encapsulate the conditions of an *in vivo* test, it provides a simulated outcome that can approximate the tested conditions, offering an accurate prediction/test of the model. The simulation accounted for collisions at a speed of 9.3 m/s and found that the average brain tissue strain is reduced by 27.6% (± 9.3) compared to the conventional helmet padding. The study did not explore whether this reduced moderate brain tissue strain would prevent a traumatic brain injury. However, the decreased brain tissue strain does indicate the success of the concept of the model. Thus, the model shows that it can, at the very least, mitigate the risk of a traumatic brain injury and the risk of the development of CTE.

Outer Shell Model:

The researchers in this study tested if an outer shell would decrease linear and rotational acceleration by reducing the overall forces transmitted to the brain.[18] They tested Sorbothane as the material for the outer shell due to its non-Newtonian properties. The property observed is the change in viscosity of the substance when under stress. Essentially, this is beneficial as the original impact/force from one player would cause the material in the helmet to "become more solid" and thus act as a harder shell. This shell was compared to the conventional helmet using a pneumatic ram test. A pneumatic ram test involves an air-powered ram that hits the helmet at several locations and angles. Both helmets were impacted five times at 3 locations (the front boss, the side, and the back). The shell reduced linear acceleration (5.8% at one location and 10.8% at another) and reduced rotational acceleration (49.8% at one location). Since the rotational and linear acceleration is decreased, then the overall jolt to the brain will decrease. The cost and durability of Sorbothane were not mentioned and are key when assessing the pros and cons of this model. However, the model may reduce the risk of a traumatic brain injury and thus decrease the risk of CTE by successfully reducing the forces acting upon the brain.

Ranking of Preventative Measures:

All three mechanisms successfully decrease the forces which act upon the brain and could be successful additions to the modern helmet. The IDM stands out for its ability to not only reduce rotational and linear acceleration but also to decrease the frictional coefficient. The Outer Shell model also decreases rotational and linear acceleration but only at specific locations on the helmet. The Liquid Shock Absorption Model decreased brain strain, but the concept was not physically tested, decreasing its potential compared to the other two options.

Role of Neck Muscles in Head Injuries:

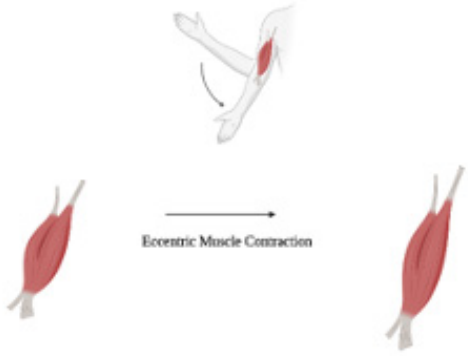

Figure 2: Visual demonstrating eccentric contraction.

Another method to prevent CTE (by preventing mTBI) would be strengthening the neck muscles. This would be beneficial as it would increase stability and minimize the jolt to the head. The researchers in this study created a musculoskeletal model of the head and neck to analyze the role of muscles in the neck and posture.[19] They looked at isometric muscle strength (muscle contracts without movement), eccentric (muscle lengthens as it contracts) multiplier - athlete's ability to apply greater muscle force during eccentric contractions (See Figure 2), muscle activation patterns, and impact properties.

The researchers were interested in the effects of active neck muscles on the outcome of a head injury. By doubling the neck strength and increasing the eccentric multiplier from 1.2 to 1.8, there would be reductions of roughly 10%, 5%, and 8% for HIC (Head Injury Criterion), BrIC (Brain Injury Criterion), and HIP (Head Impact Power), respectively. HIC is a metric that focuses on linear accelerations of the skull, BrIC is a metric that focuses on peak rotational accelerations of the skull, and HIP is a metric that accounts for all movement in all six degrees of freedom of the head. However, doubling neck strength is hard and near impossible for some athletes, which makes this idea less feasible. Interestingly, the researchers found that posture was the most critical factor in head injuries, as changing the impact direction can change angular velocity by up to 30%. This shows that training athletes to "brace" or assume specific postures would better mitigate head injuries. However, it is essential to note that this training would only be effective in impacts the player sees coming; neck muscular strength would not play a significant role in mitigating injuries for unexpected impacts.

Possible Policy changes (HS→NFL) (Kickoff/Protect Position groups):

In one study, researchers attached sensors to football players' helmets on two Canadian university teams to evaluate head accelerations.[20] Only helmet-to-helmet collisions were recorded in this study. Out of all the different play types, they found the accelerations to be the highest in kickoffs and kick returns. On kickoff coverage plays, the tackling player experienced greater linear acceleration, rotational velocity, and rotational acceleration. Meanwhile, on kickoff return plays, the player

DOI: 10.36838/v5i1.20

being tackled experienced higher experienced greater linear acceleration, rotational velocity, and rotational acceleration. For example, the linear acceleration observed in struck players on kick returns was around 53g (g is around 10 m/sec^2).

In comparison, the next highest value observed in struck players is about 22g in pass plays (highest non-kick return/cover play). Similarly, the rotational velocity and acceleration observed (34 rad/sec, 4000 rad/sec^2 (angular acceleration)) also have much higher values in kick returns than the highest non-kick return/cover play (16 rad/sec in run plays, 1500 rad/sec^2 in pass plays). The interesting thing to note is that for both kickoff coverage plays and kick return plays, these values were much higher than for any play type, indicating the potential impact of head trauma from these plays.

Concussion protocol has seen vast improvements over the past twenty years. The protocol offers a 5-step procedure for players to return to action.[21] This is positive as it provides a more personalized treatment method for players accounting for the variance in severity of concussions rather than assigning an arbitrary time restraint. The player must then be cleared by an unaffiliated neurological consultant approved by the NFL. While a player/team can bypass the evaluations and methodical procedures, the system is still a success compared to past years. Thom Mayer, the NFLPA's longtime medical director, said that "fully 50% of concussions had some element of player reporting".[21] This can be attributed to the CBA (collective bargaining agreement) in the NFL, which states that a team is obligated to continue to pay players who are rehabbing from an injury for the year in which the injury was sustained.[23]

Another triumph of concussion detection during games is the role of a UNC (Unaffiliated Neurotrauma Consultants).[24] UNCs can stand on either sideline and look for any symptoms of concussions – if they happen to see a symptom, they will diagnose if the player has a concussion or not and consequently will rule if they can continue to play in the game or not. At the same time, another UNC re-watches the game film for any signs of injury and reports back to other UNCs and team physicians if the player can play or not.

The system, however, can only help players that seek help/report their symptoms. If a player receives a concussive blow and doesn't explicitly show any symptoms, it would be up to the player to report it and get diagnosed. This system's limitation is nearly irreparable, as many players could stay in the game because of limited opportunities or competitive spirit (finishing out/winning the game).

One policy change that could be considered that can reduce the number of concussions in football would be the removal of kickoffs or altering them. The NFL has already limited the dangerous nature of kickoffs in the past by eliminating players on the kicking team from getting a running start before the ball is kicked. This decreases the possible acceleration on kickoffs, thus making it safer. However, even after these changes, the play still has the potential for severe head trauma with little game value. From 2016-2020, 60% of kickoffs resulted in touchbacks – the offense starts at the 25-yard line.[25] This means that in 3 out 5 kickoffs, nothing essential occurs. In fact, in the 2018-2019 season, there was a touchdown on a kickoff 0.02% of the time.[26] This shows that while the kickoff is one of the most dangerous plays in the game, it also has an essentially negligible impact on the final outcome. Alteration to the current rules related to kickoffs has the potential benefit of making the game safer for the players with negligible effect on the overall game.

Future studies:

For future studies, the different helmet models should continue to be tested, specifically in a game environment. This is important as it would provide the most accurate results and feedback on each helmet model. In addition, different plays should continue to be analyzed for the game's value and to see how dangerous they are. This can show if a specific type of play is too dangerous for its overall impact. These preventative measures should also be expanded to college and high school football players as they include a greater number of athletes affected by CTE and concussions.

■ Conclusion

To mitigate the effects of CTE on professional football players, traumatic brain injuries and concussions must be limited. This can be achieved in multiple ways, such as modifying the helmet, improving technique and gains in strength, and changing/altering the current rules to help make the games safer. Certain helmet modifications, such as the IDM, should continue to be tested and include some element of testing in the real game setting. This model adequately decreases the forces (rotational acceleration, frictional constant, and linear acceleration) involved in concussions and can be practically applied to the current helmet. Further testing should also assess the durability of the decal. Increasing neck muscular strength can also decrease the concussive forces on the brain, but more training on technique and posture (how to tackle) can also result in fewer concussions. Kick return plays have been found to exhibit greater rotational acceleration and velocity values indicating the increased likelihood of a concussion. Further studies are noted to examine the benefit to player health by altering the current rules on kickoff, including but not limited to starting the offense at the 25-yard line. Even though there is no known cure at this time, CTE incidence can be largely reduced in football, making it a safer American pastime.

■ References

1. Chronic traumatic encephalopathy. https://www.nhs.uk/conditions/chronic-traumatic-encephalopathy/ (accessed Feb 14, 2022).
2. Abram, D. E.; Wikarna, A.; Golnaraghi, F.; Wang, G. G. A Modular Impact Diverting Mechanism for Football Helmets. *Journal of Biomechanics* 2020, 99. https://doi.org/10.1016/j. jbiomech.2019.109502.
3. Shpigel, B. What to know about C.T.E. in football. https://www.nytimes.com/article/cte-definition-nfl.html (accessed Feb 14, 2022).
4. Resource center. https://concussionfoundation.org/CTE-resources/what-is-CTE (accessed Feb 14, 2022).
5. MRI may spot concussion-linked NFL CTE in living patients. https://www.upi.com/Health_News/2021/12/09/mri-may-spot-cte-from-concussion/8821639002455/ (accessed Feb 14, 2022).
6. Talavage TM; Nauman EA; Breedlove EL; Yoruk U; Dye AE; Morigaki KE; Feuer H; Leverenz LJ; Functionally-detected cognitive impairment in high school football players without

clinically-diagnosed concussion. https://pubmed.ncbi.nlm.nih.gov/20883154/ (accessed Feb 14, 2022).
7. Harmon, Kimberly G, et al. "American Medical Society for Sports Medicine Position Statement on Concussion in Sport." *British Journal of Sports Medicine*, vol. 53, no. 4, 2019, pp. 213–225. https://doi.org/10.1136/bjsports-2018-100338.
8. Traumatic brain injury (TBI): What is it, causes, types. https://my.clevelandclinic.org/health/diseases/8874-traumatic-brain-injury (accessed Feb 14, 2022).
9. How the discovery of CTE shifted thinking behind concussion protocol. https://www.brainandlife.org/articles/when-bennet-omalu-md-identified-a-degenerative-brain-disease-in/ (accessed Feb 14, 2022).
10. Junior Seau suffered chronic brain damage, NIH study finds. https://www.pbs.org/wgbh/frontline/article/junior-seau-suffered-chronic-brain-damage-nih-study-finds/ (accessed Feb 14, 2022).
11. Smith, S. Lives after junior. https://www.espn.com/nfl/story/_/id/9410051/a-year-later-one-junior-seau-close-friends-comes-forward-recount-version-descent (accessed Feb 14, 2022).
12. Press, A. Autopsy of ex-NFL player Phillip Adams, accused of killing six people, shows 'unusually severe' CTE. https://www.espn.com/nfl/story/_/id/32866344/autopsy-ex-nfl-player-phillip-adams-accused-killing-six-people-shows-unusually-severe-cte-damage (accessed Feb 14, 2022).
13. Josh Katzowitz. On May 4th, Gary Plummer, former teammate, says junior Seau could have had 1,500 concussions. https://www.cbssports.com/nfl/news/gary-plummer-former-teammate-says-junior-seau-could-have-had-1500-concussions/ (accessed Feb 14, 2022).
14. Emanuel, D. CTE found in 99% of studied brains from deceased NFL players. https://www.cnn.com/2017/07/25/health/cte-nfl-players-brains-study/index.html (accessed Feb 14, 2022).
15. Understanding concussions - what happens when brain is injured. https://sunnybrook.ca/content/?page=bsp-understanding-concussion (accessed Feb 14, 2022).
16. Brain Stem injury: Symptoms and causes explained. https://valientemott.com/blog/brain-stem-injury-symptoms-and-causes-explained/ (accessed Feb 14, 2022).
17. Alizadeh, H. V.; Fanton, M. G.; Domel, A. G.; Grant, G.; Camarillo, D. B. A Computational Study of Liquid Shock Absorption for Prevention of Traumatic Brain Injury. *Journal of Biomechanical Engineering* 2021, 143 (4). https://doi.org/10.1115/1.4049155.
18. Zuckerman, S. L.; Reynolds, B. B.; Yengo-Kahn, A. M.; Kuhn, A. W.; Chadwell, J. T.; Goodale, S. E.; Lafferty, C. E.; Langford, K. T.; McKeithan, L. J.; Kirby, P.; Solomon, G. S. A Football Helmet Prototype That Reduces Linear and Rotational Acceleration with the Addition of an Outer Shell. *Journal of Neurosurgery* 2019, 130 (5). https://doi.org/10.3171/2018.1.JNS172733.
19. Mortensen, J. D.; Vasavada, A. N.; Merryweather, A. S. Sensitivity Analysis of Muscle Properties and Impact Parameters on Head Injury Risk in American Football. *Journal of Biomechanics* 2020,100. https://doi.org/10.1016/j.jbiomech.2019.109411.
20. Brooks, J. S.; Redgrift, A.; Champagne, A. A.; Dickey, J. P. The Hammer and the Nail: Biomechanics of Striking and Struck Canadian University Football Players. *Annals of Biomedical Engineering* 2021, 49 (10). https://doi.org/10.1007/s10439-021-02773-4.
21. NFL Website. Concussion protocol & return-to-participation protocol: Overview. https://www.nfl.com/playerhealthandsafety/health-and-wellness/player-care/concussion-protocol-return-to-participation-protocol (accessed Feb 14, 2022).
22. Under the Blue Tent: How the NFL's concussion protocol went from a 'joke' to the gold standard. https://sports.yahoo.com/under-the-blue-tent-how-the-nf-ls-concussion-protocol-went-from -a-joke-to-the-gold-standard-162147691.html?guccounter=1&guce_referrer=aHR0cHM6Ly93d3cuZ29vZ2xlLmNvbS8&guce_referrer_sig=AQAAAIVkDjyl2QRzZcHwHntX3utBCpgoXkobm50w_CyAvr61qJtGaB-pt7WPuZ0MhuT66f75lvj52I7bnglI4SK7ahKaQZFIJEjSmyCsaRAznh0a01up0VIkO8Qkg-qa1Yme-YZoHJue-Uqt5XhzmBRtEXm8ThFGnyHCRjQldaZCMuWYL (accessed Feb 14, 2022).
23. Alikpala, G. Do NFL players get paid when they are injured? who pays for the Players' medical bills? https://en.as.com/en/2021/11/05/nfl/1636111487_338373.html (accessed Feb 14, 2022).
24. Mack C; Sendor RR; Solomon G; Ellenbogen RG; Myers E; Berger M; Sills A; Enhancing concussion management in the National Football League: Evolution and initial results of the unaffiliated Neurotrauma Consultants Program, 2012-2017. https://pubmed.ncbi.nlm.nih.gov/31792503/ (accessed Feb 14, 2022).
25. Malinowski, T. Kickoffs deserve the boot: Why the NFL needs to eliminate the kickoff. https://hcctimes.org/2021/05/kickoffs-deserve-the-boot-why-the-nfl-needs-to-eliminate-the-kickoff/ (accessed Feb 14, 2022).
26. Ruiz, S. The NFL needs to just get rid of the kickoff already. https://ftw.usatoday.com/2019/03/nfl-onside-kick-rule-change-kickoffs (accessed Feb 14, 2022).
Note - Diagrams in the paper were created using BioRender.com https://biorender.com/ (accessed Feb 14, 2022).

Author

Nikhil H. Vallikat is a high school senior at the Thomas Jefferson High School for Science and Technology (TJHSST) in Alexandria, Virginia. He plans to pursue a career in medicine. He has been a passionate sports lover from first grade, and this paper is a result of combining both his academic and love for sports.

DOI: 10.36838/v5i1.20

IJHSR
ijhighschoolresearch.org
RESEARCH ARTICLE

The Aggregation of Tau Protein in Alzheimer's Disease

Tanvi Chichili

The Athenian School, 2100 Mt Diablo Scenic Blvd, Danville, CA, 94506, U.S.A; tanvilimegreen@gmail.com

ABSTRACT: Currently, neurodegenerative diseases affect approximately 50 million people and are a significant cause of death and disability worldwide. One of the most well-known neurodegenerative diseases is Alzheimer's Disease. Alzheimer's Disease (AD) is characterized by the presence of neurofibrillary tangles made up of filamentous Tau aggregates and ß- amyloid depositions and is a relatively common cause of dementia in older adults. AD is known as a tauopathy, a family of neurodegenerative diseases characterized by tau neurofibrillary tangles. Neurofibrillary tangles are thought to be toxic aggregates of Tau protein that occur after tau disengages from microtubules. In neurons, microtubules are responsible for transporting substances to different parts of the cell. They exhibit dynamic instability, meaning they constantly grow and shrink. Under normal physiological conditions, Tau protein, a neuronal microtubule-associated protein, promotes microtubule self-assembly and stabilizes microtubules. Tau's intracellular interactions and functioning is regulated by phosphorylation, a post-translational modification. However, Tau undergoes hyperphosphorylation and aggregation under pathological conditions to form neurofibrillary tangles, leading to neurotoxicity. This synaptic dysfunction and loss of microtubule stability eventually lead to the neurodegeneration characteristic of tauopathies. To find new therapeutic targets, the loss of normal tau function and gain of toxic tau function must be investigated. This review will discuss the current models of Tau aggregation, the Tau pathology that causes Alzheimer's Disease, and current therapeutic strategies to treat tauopathies.

KEYWORDS: Biomedical and health sciences, genetics and molecular biology of disease, Tau, tauopathies, aggregation.

Introduction

In addition to toxic Tau pathology, AD can also be caused by beta-amyloid aggregates that form deposits in the brain leading to neurodegeneration. Because beta-amyloid is still considered causative, it has been the target of several therapeutics. However, at least four anti-amyloid antibodies have failed in phase III trials in different Alzheimer's disease settings. Three BACE inhibitors and two γ-secretase inhibitors, which act on amyloid processing, have also failed. In some cases, these treatments were even associated with worsening cognition.[1] After failed therapy for amyloid, Tau became an alternative target for therapeutics to treat AD as it is a proximal mediator of neurodegeneration and causative of cognitive decline. Nonetheless, the key to understanding Tau's pivotal role in AD begins with its regular function in neurons to stabilize microtubules.

Microtubules are part of the cytoskeleton, a structural network within the cell's cytoplasm. In neurons, microtubules transport materials from the cell body to the axon terminals at the synapse, and they also define axons and dendrites.[2] They are composed of alpha- and beta-tubulin subunits assembled into approximately thirteen linear strands called protofilaments; these protofilaments bind together to form the hollow, tube-like structure of the microtubule.[2] Microtubules are constantly growing and shrinking, which happens when the alpha and beta tubulin subunits associate and dissociate from the plus end (the end that grows more rapidly) of the protofilament. This phenomenon is known as "dynamic instability."[3] Dynamic instability is a useful biological mechanism because it allows the microtubules to reorganize the cytoskeleton when necessary quickly.[4] In neurons, the dynamic instability of microtubules upon which axonal transport occurs is suppressed by the microtubule-associated protein Tau. Tau protein promotes microtubule self-assembly and stabilizes microtubules that have already formed.[5] Tau's other functions include neuronal cell signaling, nuclear function, and maintenance of the neuronal cytoskeleton.[5] However, an essential facet of Tau that places it at the center of research surrounding tauopathies and neurodegenerative disorders is the insoluble lesions it forms in disease.

Tau can undergo several post-translational modifications to regulate its functioning through the brain. A critical post-translational modification to analyze is phosphorylation, the addition of a phosphate group to serine, threonine, and tyrosine residues. Phosphorylation regulates Tau functioning under normal conditions; however, under pathological conditions, hyperphosphorylation can occur. As this happens, Tau loses its normal physiological function and aggregates, resulting in toxicity, for example, causing synaptic dysfunction. According to Goedert *et al.*,[6] hyperphosphorylation results in the reduced ability of tau to interact with microtubules, which is most likely necessary for its ordered assembly into oligomers, proto-fibrils, fibrils, tangles, paired helical filaments, and neurofibrillary tangles. Most importantly, neurofibrillary tangles, made up of fibrils of hyperphosphorylated tau, are a biomarker of Alzheimer's disease and other related tauopathies. This review paper will summarize the literature that aims to address the mechanisms of Tau aggregation and seeding, and current therapeutic strategies that target tauopathies will be described.

DOI: 10.36838/v5i1.21

Discussion

Structure of Tau:

Tau assembles and stabilizes microtubules by interacting with the tubulin subunits in the microtubules at various microtubule binding regions. The repeat region is a region of Tau which is tightly and specifically bound in the core of the paired helical filament and is believed to be the microtubule binding domain. The microtubules binding regions differ across the six Tau isoforms in the human brain by having varying three or four repeats in the C-terminal region.[7] Furthermore, the N-terminal inserts may help regulate Tau's dynamic behavior and function during axonal transport.[8]

When investigating Tau's primary structure, it is crucial to note that Tau's primary structure can, in fact, cause disease. For example, Tau isoforms containing either three (3R) or four (4R) microtubule binding regions usually are in a one-to-one ratio. But, there are splicing defects in familial tauopathies such as frontotemporal dementia or corticobasal degeneration, which skew the ratio of 3R to 4R, either increasing the amount of 3R or 4R.[9] Furthermore, missense and silent tau primary structure mutations cause frontotemporal dementia with parkinsonism-chromosome 17 type by affecting multiple alternative RNA splicing regulatory elements.[10]

In addition to examining Tau's primary structure, the secondary and tertiary structures are equally important in understanding Tau's significance in neurodegenerative disorders. Tau is an intrinsically disordered protein, meaning that it lacks a well-defined three-dimensional structure. Yet, a secondary structure exists; it retains a flexible conformation important to its role in cellular processes.[11] Furthermore, intrinsically disordered proteins undergo order-to-disorder or disorder-to-order transitions as part of their normal biology. Their structure and function may be modulated by protein chaperones, post-translational modifications, and degradation processes. Tau's secondary structure is largely transient but consists of α-helices, β-pleated sheets, and a polyproline II helix.[8]

A "paper-clip" structure for some molecules of Tau monomers may have been indicated through nuclear magnetic resonance and small-angle X-ray scattering. A "paper-clip" structure may suggest that the N and C termini work together closely.[12] However, when Tau is bound to microtubules, the two terminals are disjointed, with the N-terminal facing away from the microtubules.[13] The presence of a "paper-clip" structure may suggest the presence of intramolecular interactions between at least two different regions of the Tau protein. If one of those regions is involved in Tau self-interaction, the opening of the "paper-clip" structure could be what facilitates self-aggregation in Tau pathology.[13]

Furthermore, the elastic and bendable structure of the Tau protein enables interaction with multiple partners, implying its involvement in many signaling pathways.[14] However, being intrinsically disordered allows tau to interact with other Tau molecules to form oligomers and filaments, which are the root cause of the gain of toxic function.[14] These neurofibrillary tangles cause degeneration of neurons and glial cells, displaying as a group of neurodegenerative disorders termed 'tauopathies.'

Phosphorylation of Tau:

An important feature of Tau is the presence of various types of post-translational modifications that it can undergo. These modifications include phosphorylation, acetylation, deamidation, methylation, O-Glycylation, and ubiquitination.[15] Of these modifications, a critical one to investigate is phosphorylation. The phosphorylation of proteins involves adding a phosphate group to three types of amino acids: serine, threonine, and tyrosine. Phosphorylation regulates tau's functioning by neutralizing its positive charge, reducing its affinity for microtubules, thereby detaching Tau from microtubules.[16] In an intact cell, Tau is constantly phosphorylated and dephosphorylated to regulate microtubule assembly.[16] There are eighty-five potential phosphorylation sites (45 serine, 35 threonine, and five tyrosine residues) scattered on the longest Tau isoform; specifically, they are located in regions around the repeat microtubule-binding regions on the C-terminal region.[17] According to Bramblett *et al*,[18] Tau's ability to stabilize microtubules inversely correlates with its phosphorylation, meaning that the more Tau gets phosphorylated, the less it can stabilize microtubules.

Furthermore, the amount of phosphorylation in Tau is directly tied to the amount of active protein kinase. This enzyme catalyzes the chemical reaction between ATP and Tau protein and phosphatase. This enzyme removes a phosphate group from a protein.[19] In addition, O-linked glucosamine modifications occur on serine and threonine residues and block phosphorylation. When glucosamine is removed, tau can be phosphorylated, making the enzymes that remove O-linked glucosamines a regulator of tau phosphorylation and a target in clinical trials.[20] Lastly, an enzyme called Glycogen synthase kinase 3 (GSK3β) is the most effective Tau kinase in the human brain, and it is directly linked to phosphorylation levels in Tau.[21] In other words, as GSK3β increases, so does the amount of Tau phosphorylation. This can have potentially detrimental effects on the brain, such as the onset of tauopathies.

In tauopathies, Tau is hyperphosphorylated at specific sites, forming aggregates and neurofibrillary tangles and making it a potential target for therapy. Changes in Tau conformation could result in (1) increased phosphorylation because of altered binding to kinases and (2) decreased binding to microtubules. Both of these can cause tau-mediated neurodegeneration.[22]

According to Hanger *et al.*,[21] Tau hyperphosphorylation occurs when there is an increased activity of Tau kinases (specifically GSK3β) and a decreased activity of Tau phosphatases. Another study has shown that hyperphosphorylation can occur when Tau is exposed to proteins such as β-amyloid, Fyn kinase, Pin1, heat shock cognate Hsc70, and heat shock protein Hsp90, immunophilins FKBP51 and FKBP52, α-synuclein or actin interacting protein PACSIN1.[22] Moreover, hyperphosphorylation causes many complications regarding tau's functional capabilities. When Tau gets hyperphosphorylated, the affinity of Tau to microtubules is lessened, causing microtubule instability and disassembly and then promoting Tau self-aggregation, which leads to neurofibrillary tangles

DOI: 10.36838/v5i1.21

made up of paired helical filaments.[6] Therefore, hyperphosphorylation is the critical event at the onset of Tau pathology.

Moreover, according to Goedert *et al.*,[23] stress-activated protein kinases also contribute to tau phosphorylation. They may also explain several observations demonstrated in a study on rat brains. Cold-water stress induces a relatively spontaneous (30–90 min) two to three times increase in Tau phosphorylation.[24]

Several animal models depict the influence of hyperphosphorylation in tauopathies. For instance, Ishihara *et al.*,[25] designed a transgenic mouse model in which three wild-type Tau transgenic mouse lines expressing different levels of the shortest tau isoform were used. Ishihara and colleagues found clusters of phosphorylated tau at several phospho-epitopes where there was an increased level of the Tau kinase, GSK-3β.[25] Furthermore, the authors found a substantial correlation between the specific phosphorylation changes and the aggregation levels of tau. In the *hTau* strain mice specifically, there were increased levels of Tau kinases such as p38, p35, and p25, which later caused an increase in phosphorylated tau. Changes in Tau kinases in the *hTau* mice were directly linked with how much Tau was present as toxic, insoluble aggregates.[25] In summary, this illustrates that Tau is subject to varying levels of phosphorylation with respect to the differential activities of kinases.

Tau Seeding and Aggregation:

Evidence suggests that hyperphosphorylated tau can spread through the brain in the form of "seeds" that contaminate neurons in a prion-like fashion, meaning they can transmit their misfolded shape onto the normal variant of the same protein. This causes Tau to lose its normal function and gain a toxic function model (Figure 1). In specific animal models, Tau aggregates are shown to actively spread from neuron to neuron, illustrating Tau seeding and how that causes Tau aggregates to propagate.

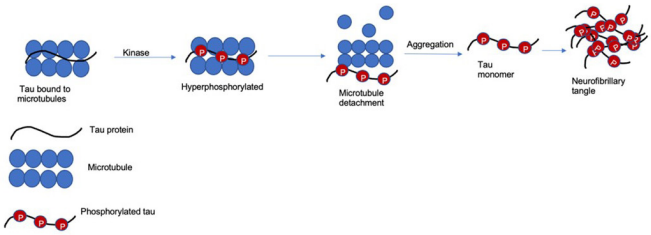

Figure 1: Tau aggregation and loss of microtubule affinity.

Braak *et al.*,[26] and colleagues used transgenic mouse models with localized Tau expression to express mutant Tau in the entorhinal cortex. After the Tau protein was injected into the mice, it demonstrated similar behaviors as it does in humans, such as hyperphosphorylation, abnormal Tau folding, and accumulation of aggregates. They found that Tau progressively spreads across the brain to neuroanatomically connected regions, demonstrating the possibility that this spreading could be due to Tau seeding. However, this study did not provide conclusive evidence that Tau seeding was causing aggregation to occur.[26]

In 2009, Clavaguera *et al.*,[27] conducted a vital experiment with respect to Tau seeding and spreading, which eventually paved the way for studies that utilized patient-derived Tau by injecting it into mouse models. They injected Tau filament containing Tau fibrils from a Transgenic mouse model that expressed the 0N4R human Tau isoform with the FTD-linked P301S mutation into the hippocampus and overlying cerebral cortex of Transgenic mice overexpressing a single WT human Tau isoform (2N4R). Through their results, this study contributed the first evidence that injected Tau fibrils induce the onset of pathological Tau aggregates, which progressively propagate to parts of the brain anatomically associated with the injection sites. Tau pathology was observed in different cell types, with aggregates present in the form of neurofibrillary tangles and neuropil threads. Moreover, further analysis suggested that the induced aggregates were composed of insoluble, phosphorylated tau.[27]

Similar to Clavaguera and colleagues, Ahmed *et al.*,[28] injected brain extracts of five-month-old transgenic mice for seeding into the brain of two-month-old mice from the same line. The result was an exponentially more rapid and immediate Tau pathology initiation than that demonstrated in the study performed before. They found the development of neuronal inclusions in the form of neuropil threads and neurofibrillary tangles beginning two weeks after the injection in the ipsilateral region and one month after in the contralateral region. Most notably, this series of experiments corroborated the hypothesis that pathological Tau can spread through connections between the synapses. These findings were additionally verified by the formation of Tau pathology in the white matter tracts linking regions with abundant toxic Tau aggregates.[28] To sum up, these studies demonstrate that Tau seeding is a mechanism that explains why Tau aggregation propagates throughout the brain.

Therapeutic Strategies to Treat Tauopathies:

A plenitude of Tau antibodies and vaccines have been tested in preclinical studies in the last two decades. Currently, eight Tau antibodies and two Tau vaccines have entered clinical trials for various tauopathies. Considering the failure of the clinical trials with amyloid targeting drugs, Tau therapy is manifesting as the frontrunner in the search for an effective treatment for Alzheimer's Disease. One such therapeutic is monoclonal antibodies (mABs) which are laboratory-produced molecules that act as substitute antibodies that can restore, enhance, or mimic the immune system's attack on cells. Since seeding mechanisms are driven by the passage of tau fibrils from cell to cell, antibodies are being designed to recognize these objects. Various mABs are being designed to target different Tau protein domains, demonstrating fruitful laboratory results.

It is well-known that Tau fibrils are hyperphosphorylated. Therefore, some mAbs have been designed to bind specific phosphorylation residues scattered along the Tau protein specifically. Research shows that using some mABs can successfully decrease the amount of Tau seeding when injected in transgenic AD Tau seeding mouse models. On a similar note, Dai *et al.*,[29] administered transgenic mice with injections of an mAB that targets the N-terminal region of Tau. The results

showed a decreased level of hyperphosphorylation and Tau seeding.

More recently, Courade *et al.*,[30] invented a screening tool to help classify the mAB that would be most effective against human Tau seeds and found mAB targeting the Tau mid-region to display the highest activity. This mAB was later shown to successfully halt the progression of Tau pathology following injection of human AD brain extracts in Tg mice expressing the human Tau P301L mutation. However, a concern that the authors of this paper had was that the specific mABs tested in their study after the screening tool did not thoroughly neutralize the seeding activity of the fibrillar tau in the AD extracts. This may be due to the conformation of Tau changing as it is being hyperphosphorylated, making it difficult for the mABs to bind to them. Furthermore, Gibbons *et al.*,[31] later identified two additional mABs, recognizing the abnormal conformation of tau fibrils, which can inhibit Tau pathology induced upon human AD brain extract inoculation in an aggressive amyloid pathology model (5xFAD mice). Confirming the efficacy of these treatments in models with better translational value, such as humanized Tau models injected with patient-derived Tau fibrils, is a crucial next step.[31]

Lastly, another potential therapeutic strategy to treat tauopathies is inhibiting Tau kinases from preventing hyperphosphorylation of tau. However, there is still uncertainty about which kinases are most relevant to Tau phosphorylation in neurons. Some ser/thr kinases have been proposed, such as glycogen synthase kinase-3β (GSK-3β), cell cycle-dependent kinase 5 (CDK5), MT-affinity regulated kinases (MARKs), protein kinase A (PKA), mitogen-activated kinases (MAPKs) and others.[32] Among these, the most well-studied and most endorsed are the GSK-3β and CDK5 kinases. Furthermore, there are convincing data demonstrating that changing the expression of GSK-3β or p25, an activator of CDK5, affects Tau pathology in transgenic mouse models. Lithium chloride and specific small synthetic molecules, which are inhibitors of the Tau kinase GSK-3β, have been shown to lower the amount of Tau phosphorylation and Tau deposits in transgenic mouse models of tauopathy.

Moreover, lithium chloride started to be clinically tested in AD patients. Unfortunately, no improvements in cognitive outcomes were observed in Phase 2 clinical study. Additionally, a non-competitive GSK-3β inhibitor (tideglusib) was recently evaluated in Phase 2 testing in PSP and AD patients, but it also failed to improve clinical outcomes.

The tertiary structure of a protein determines its function and what it can interact with. Because Tau in solution is a highly disordered protein and does not exhibit a stable tertiary structure, it remains a challenging protein target for structural analysis. The lack of Tau structure in the solution is not a barrier to understanding its function, just a barrier to being amenable to structure-function-based intervention. The lack of structural information about Tau limits the progress in neurodegeneration research and the development of effective therapeutic strategies. Some progress has been made in identifying a three-dimensional structure for Tau, such as the "paper clip" structure that was previously mentioned. However, this still does not provide sufficient information to design a therapeutic method because the "paper clip" structure was only briefly explored as a model for the Tau protein. Despite challenges regarding tau's tertiary structure, progress has been made in limiting Tau seeding and eventual aggregation through the use of monoclonal antibodies, refinement of antibody types through screening methods, and tau kinase inhibitors (see Table 1). This illustrates that novel strategies to overcome the gap in knowledge with respect to tau's structure are on the horizon.

Table 1: Pros and Cons of Recent Tauopathy Therapeutic Strategies.

Therapeutic Strategy	Pros	Cons
Monoclonal Antibodies (mAbs)	Decreased hyperphosphorylation and tau seeding in transgenic mouse models	Tau's structural changes as it gets hyperphosphorylated make it difficult for the mABs to neutralize the phosphorylation
Screening Tool	Classified the monoclonal antibody (mAB) that would be most effective against human tau seeds	
Tau Kinases Inhibitors	Certain tau kinases have been shown to decrease the amount of phosphorylation and tau deposits in transgenic mouse models	The tau kinase GSK-3β failed to improve clinical outcomes during Phase 2 clinical trials.

Conclusion

Hyperphosphorylation and fibrillization are linked to neurodegeneration and cognitive dysfunction in Alzheimer's Disease. Through the studies described in this paper, it is evident that Tau seeding makes aggregation more prevalent because the aggregates can spread from neuron to neuron through connections between the synapses. This demonstrates how one hyperphosphorylated Tau aggregate can propagate and spread throughout the brain. These discoveries have paved the way for new therapeutic strategies for neurodegenerative diseases that are primarily Tau targeted. For instance, by using monoclonal antibodies, phosphorylation sites on Tau can be specifically targeted to reduce Tau seeding. Another therapeutic strategy is using Tau kinase inhibitors to reduce phosphorylation. However, unfortunately, many of these strategies have not made it past Phase 2 clinical trials. Some argue that therapies that fail to demonstrate efficacy do so because it is too late to intervene when a patient has shown enough cognitive dysfunction to warrant inclusion in a tau therapy trial. Therefore, if the disease can be detected earlier, it would allow for earlier intervention and perhaps greater efficacy. Nevertheless, it is estimated that currently, 30 million people live with tauopathies, so it is incredibly pertinent to continue studying Tau aggregation and hyperphosphorylation to develop a therapeutic strategy that will hopefully advance the treatment and prevention of tauopathies in the future.

Acknowledgments

I want to thank my mentor Erika Beyrent (Cornell University), for her assistance and guidance when writing this paper.

References

1. Yiannopoulou, K. G.; Anastasiou, A. I.; Zachariou, V.; Pelidou, S.-H. Reasons for Failed Trials of Disease-Modifying Treatments for Alzheimer Disease and Their Contribution in Recent Research. *Biomedicines* **2019**, 7 (4), 97. https://doi.org/10.3390/biomedicines7040097.
2. Howard, J.; Hyman, A. A. Dynamics and Mechanics of the Microtubule plus End. *Nature* **2003**, 422 (6933), 753–758. https://doi.org/10.1038/nature01600.
3. Mitchison, T.; Kirschner, M. Dynamic Instability of Microtubule Growth. *Nature* **1984**, 312 (5991), 237–242. https://doi. org/10.

DOI: 10.36838/v5i1.21

38/312237a0.
4. Liu, Z.; Huang, Y. Advantages of Proteins Being Disordered. *Protein Sci. Publ. Protein Soc.* **2014**, 23 (5), 539–550. https://doi.org/10.1002/pro.2443.
5. Breuzard, G.; Hubert, P.; Nouar, R.; De Bessa, T.; Devred, F.; Barbier, P.; Sturgis, J. N.; Peyrot, V. Molecular Mechanisms of Tau Binding to Microtubules and Its Role in Microtubule Dynamics in Live Cells. *J. Cell Sci.* **2013**, 126 (Pt 13), 2810–2819. https://doi.org/10.1242/jcs.120832.
6. Goedert, M.; Spillantini, M. G.; Serpell, L. C.; Berriman, J.; Smith, M. J.; Jakes, R.; Crowther, R. A. From Genetics to Pathology: Tau and α-Synuclein Assemblies in Neurodegenerative Diseases. *Philos. Trans. Biol. Sci*. **2001**, 356 (1406), 213–227.
7. Lee, G.; Neve, R. L.; Kosik, K. S. The Microtubule Binding Domain of Tau Protein. *Neuron* **1989**, 2 (6), 1615–1624. https://doi. org/10.1016/0896-6273(89)90050-0.
8. Zabik, N. L.; Imhof, M. M.; Martic-Milne, S. Structural Evaluations of Tau Protein Conformation: Methodologies and Approaches. *Biochem. Cell Biol. Biochim. Biol. Cell.* **2017**, 95 (3), 338–349. https://doi.org/10.1139/bcb-2016-0227.
9. Goedert, M.; Spillantini, M. G.; Crowther, R. A. Cloning of a Big Tau Microtubule-Associated Protein Characteristic of the Peripheral Nervous System. *Proc. Natl. Acad. Sci. U. S. A.* **1992**, 89 (5), 1983 –1987. https://doi.org/10.1073/pnas.89.5.1983.
10. D'Souza, I.; Poorkaj, P.; Hong, M.; Nochlin, D.; Lee, V. M.-Y.; Bird, T. D.; Schellenberg, G. D. Missense and Silent Tau Gene Mutations Cause Frontotemporal Dementia with Parkinsonism-Chromosome 17 Type, by Affecting Multiple Alternative RNA Splicing Regulatory Elements. *Proc. Natl. Acad. Sci. U. S. A*. **1999**, 96 (10), 5598–5603.
11. Dyson, H. J.; Wright, P. E. Intrinsically Unstructured Proteins and Their Functions. *Nat. Rev. Mol. Cell Biol.* **2005**, 6 (3), 197–208. https://doi.org/10.1038/nrm1589.
12. Qi, H.; Cantrelle, F.-X.; Benhelli-Mokrani, H.; Smet-Nocca, C.; Buée, L.; Lippens, G.; Bonnefoy, E.; Galas, M.-C.; Landrieu, I. Nuclear Magnetic Resonance Spectroscopy Characterization of Interaction of Tau with DNA and Its Regulation by Phosphorylation. *Biochemistry* **2015**, 54 (7), 1525–1533. https://doi.org/ 10.1021/bi5014613.
13. Andronesi, O. C.; von Bergen, M.; Biernat, J.; Seidel, K.; Griesinger, C.; Mandelkow, E.; Baldus, M. Characterization of Alzheimer's-like Paired Helical Filaments from the Core Domain of Tau Protein Using Solid-State NMR Spectroscopy. *J. Am. Chem. Soc.* **2008**,130 (18), 5922–5928. https://doi.org/10.1021/ja7100517.
14. Shammas, S. L.; Garcia, G. A.; Kumar, S.; Kjaergaard, M.; Horrocks, M. H.; Shivji, N.; Mandelkow, E.; Knowles, T. P. J.; Mandelkow, E.; Klenerman, D. A Mechanistic Model of Tau Amyloid Aggregation Based on Direct Observation of Oligomers. *Nat. Commun*. **2015**, 6, 7025. https://doi.org/10.1038/ncomms8025.
15. Martin, L.; Latypova, X.; Terro, F. Post-Translational Modifications of Tau Protein: Implications for Alzheimer's Disease. *Neurochem. Int.* **2011**, 58 (4), 458–471. https://doi.org/10.1016/j.neuint.2010.12.023.
16. Jho, Y. S.; Zhulina, E. B.; Kim, M. W.; Pincus, P. A. Monte Carlo Simulations of Tau Proteins: Effect of Phosphorylation. *Biophys. J.* **2010**,99 (8),2387–2397.https://doi.org/10.1016/j.bpj.2010.06.056.
17. Hanger, D. P.; Gibb, G. M.; de Silva, R.; Boutajangout, A.; Brion, J.-P.; Revesz, T.; Lees, A. J.; Anderton, B. H. The Complex Relationship between Soluble and Insoluble Tau in Tauopathies Revealed by Efficient Dephosphorylation and Specific Antibodies. *FEBS Lett.* **2002**, 531 (3), 538–542. https://doi.org/10.1016/s0014-5793(02)03611-6.
18. Bramblett, G. T.; Goedert, M.; Jakes, R.; Merrick, S. E.; Trojanowski, J. Q.; Lee, V. M. Abnormal Tau Phosphorylation at Ser396 in Alzheimer's Disease Recapitulates Development and Contributes to Reduced Microtubule Binding. *Neuron* **1993**, 10 (6), 1089-1099. https://doi.org/10.1016/0896-6273(93)90057-x.
19. Yoshida, H.; Ihara, Y. Tau in Paired Helical Filaments Is Functionally Distinct from Fetal Tau: Assembly Incompetence of Paired Helical Filament-Tau - PubMed. *J Neurochem* **1993**, 61 (3). https://doi.org/10.1111/j.1471-4159.1993.tb03642.x.(1)
20. Hart, G. W.; Slawson, C.; Ramirez-Correa, G.; Lagerlof, O. Cross Talk Between O-GlcNAcylation and Phosphorylation: Roles in Signaling, Transcription, and Chronic Disease. *Annu. Rev. Biochem.* **2011**, 80, 825–858. https://doi.org/10.1146/annurev-biochem-060608-102511.
21. Hanger, D. P.; Byers, H. L.; Wray, S.; Leung, K.-Y.; Saxton, M. J.; Seereeram, A.; Reynolds, C. H.; Ward, M. A.; Anderton, B. H. Novel Phosphorylation Sites in Tau from Alzheimer Brain Suppor a Role for Casein Kinase 1 in Disease Pathogenesis. J. *Biol. Chem*. **2007**, 282 (32), 23645–23654. https://doi.org/10.1074/jbc.M703269200.
22. Mietelska-Porowska, A.; Wasik, U.; Goras, M.; Filipek, A.; Niewiadomska, G. Tau Protein Modifications and Interactions: Their Role in Function and Dysfunction. *Int. J. Mol. Sci*. **2014**, 15 (3), 4671-4713. https://doi.org/10.3390/ijms15034671.
23. Goedert, M.; Cuenda, A.; Craxton, M.; Jakes, R.; Cohen, P. Activation of the Novel Stress-Activated Protein Kinase SAPK4 by Cytokines and Cellular Stresses Is Mediated by SKK3 (MKK6); Comparison of Its Substrate Specificity with That of Other SAP Kinases. *EMBO J*. **1997**, 16 (12), 3563–3571. https://doi.org/10.1093/emboj/16.12.3563.
24. Phosphorylation of microtubule-associated protein tau by stress-activated protein kinases - Goedert - 1997 - FEBS Letters - *Wiley Online Library*. https://febs.onlinelibrary.wiley.com/doi/ full/10.1016/S0014-5793%2897%2900483-3 (accessed 2022-06-24).
25. Ishihara, T.; Hong, M.; Zhang, B.; Nakagawa, Y.; Lee, M. K.; Trojanowski, J. Q.; Lee, V. M.-Y. Age-Dependent Emergence and Progression of a Tauopathy in Transgenic Mice Overexpressing the Shortest Human Tau Isoform. *Neuron* **1999**, 24 (3), 751–762. https://doi.org/10.1016/S0896-6273(00)81127-7.
26. Braak, H.; Alafuzoff, I.; Arzberger, T.; Kretzschmar, H.; Del Tredici, K. Staging of Alzheimer Disease-Associated Neurofibrillary Pathology Using Paraffin Sections and Immunocytochemistry. *Acta Neuropathol. (Berl.)* **2006**, 112 (4), 389–404. https://doi. org/10.1007/s00401-006-0127-z.
27. Clavaguera, F.; Hench, J.; Lavenir, I.; Schweighauser, G.; Frank, S.; Goedert, M.; Tolnay, M. Peripheral Administration of Tau Aggregates Triggers Intracerebral Tauopathy in Transgenic Mice. A*cta Neuropathol. (Berl.)* **2014**, 127 (2), 299–301. https://doi.org/10.1007/s00401-013-1231-5.
28. Ahmed, Z.; Cooper, J.; Murray, T. K.; Garn, K.; McNaughton, E.; Clarke, H.; Parhizkar, S.; Ward, M. A.; Cavallini, A.; Jackson, S.; Bose, S.; Clavaguera, F.; Tolnay, M.; Lavenir, I.; Goedert, M.; Hutton, M. L.; O'Neill, M. J. A Novel in Vivo Model of Tau Propagation with Rapid and Progressive Neurofibrillary Tangle Pathology: The Pattern of Spread Is Determined by Connectivity, Not Proximity. *Acta Neuropathol. (Berl.)* **2014**, 127 (5), 667–683. https://doi.org/10.1007/s00401-014-1254-6.
29. Dai, C.-L.; Hu, W.; Tung, Y. C.; Liu, F.; Gong, C.-X.; Iqbal, K. K. Tau Passive Immunization Blocks Seeding and Spread of Alzheimer Hyperphosphorylated Tau-Induced Pathology in 3 x Tg-AD Mice. *Alzheimers Res. Ther.* **2018**, 10 (1), 13. https://doi.org/10.1186/s13195-018-0341-7.
30. Courade, J.-P.; Angers, R.; Mairet-Coello, G.; Pacico, N.; Tyson, K.; Lightwood, D.; Munro, R.; McMillan, D.; Griffin, R.; Baker, T.;

Starkie, D.; Nan, R.; Westwood, M.; Mushikiwabo, M.-L.; Jung, S.; Odede, G.; Sweeney, B.; Popplewell, A.; Burgess, G.; Downey, P.; Citron, M. Epitope Determines Efficacy of Therapeutic Anti-Tau Antibodies in a Functional Assay with Human Alzheimer Tau. *Acta Neuropathol. (Berl.)* **2018**, 136 (5), 729–745. https://doi.org/10.1007/s00401-018-1911-2.

31. Gibbons, G. S.; Kim, S.-J.; Wu, Q.; Riddle, D. M.; Leight, S. N.; Changolkar, L.; Xu, H.; Meymand, E. S.; O'Reilly, M.; Zhang, B.; Brunden, K. R.; Trojanowski, J. Q.; Lee, V. M. Y. Conformation-Selective Tau Monoclonal Antibodies Inhibit Tau Pathology in Primary Neurons and a Mouse Model of Alzheimer's Disease. *Mol. Neurodegener.* **2020**, 15 (1), 64. https://doi.org/10.1186/s13024-020-00404-5.
32. Lovestone, S.; Hartley, C. L.; Pearce, J.; Anderton, B. H. Phosphorylation of Tau by Glycogen Synthase Kinase-3 Beta in Intact Mammalian Cells: The Effects on the Organization and Stability of Microtubules. *Neuroscience* **1996**, 73 (4), 1145–1157. https://doi.org/10.1016/0306-4522(96)00126-1.

Author

Tanvi Chichili is currently a senior at The Athenian School. She is interested in studying neuroscience with a focus on tauopathies such as Alzheimer's Disease.

DOI: 10.36838/v5i1.21

IJHSR
ijhighschoolresearch.org
REVIEW ARTICLE

Therapeutic Potential Targeting Cancer Stem Cells to Treat Breast Cancer

Tianyue Yu

Shanghai Starriver Bilingual School, 2588 Jindu Lu, Shanghai, 201108, China; yutianyue2005@126.com

ABSTRACT: Breast cancer has become the most common type of cancer worldwide since 2021. Despite recent advances in therapies, many patients with breast cancer experience tumor relapse and drug resistance, which are believed to attribute to breast cancer stem cells (CSCs), a small population of cells within breast cancer. Therefore, eradicating breast CSCs represents a promising therapeutical strategy to prevent cancer reoccurrence and drug resistance. Current studies have shown that breast CSCs arise from normal mammary stem cells/progenitor cells or differentiated mammary cells. Multiple key signaling pathways have been discovered and implicated in breast CSCs' self-renewal and differentiation, including Wnt/β-catenin signaling. In this article, I review the recent progress in breast CSC's biological studies and therapeutics by targeting breast CSCs' biomarkers and the Wnt/β-catenin signaling pathway.

KEYWORDS: breast cancer; cancer stem cells; Wnt; β-catenin; treatment; signaling pathway.

Introduction

According to the World Health Organization, breast cancer became the most prevalent cancer worldwide as of 2021, accounting for 12% of all new annually diagnosed cancer.[1] Based on the expression of estrogen receptor (ER), progesterone receptor (PR), and human epidermal growth factor receptor-2 (HER2), breast cancer is generally classified into four subtypes: luminal A (ER+/PR+/Her2-), luminal B (ER+/PR+/Her2+), Her 2+ enriched (ER-/PR-/Her2+) and triple negative (ER-/PR-/Her2-).[2] Among the four subtypes, luminal A breast cancer is the most prevalent but the least aggressive, whereas triple-negative breast cancer (TNBC) is the most aggressive and challenging to treat.[3] Distinct therapies have been devised for each subtype of breast cancer; however, many breast cancer patients eventually experience tumor relapse and drug resistance.

CSCs are a very small subpopulation of cells within a tumor, and they can self-renew and differentiate into heterogeneous cancer cells.[4] The CSCs, first reported in acute myeloid leukemia, play a significant role in the advancement of cancer research.[5] Accumulative studies have demonstrated that CSCs account for tumor initiation, progression, and recurrence.[6-8] Recently, intensive efforts have been made to research breast CSCs with the hope of treating breast cancer by eradicating breast CSCs. Here, I summarize the recent progress in breast CSCs' studies and drug development to treat breast cancer, focusing on targeting the Wnt/β-catenin signaling.

Discussion

Current Models of Breast CSCs' Origin:

Breast CSCs play a fundamental role in breast cancer initiation, progression, reoccurrence, and drug resistance, and the cellular origin of breast CSCs remains controversial. Two well-accepted models, namely the hierarchical and stochastic models, have been proposed (Figure 1). In the hierarchical model, breast CSCs are believed to originate from mammary stem cells/progenitor cells that acquire sequential genetic mutations.[9] For example, Liu *et al*. demonstrated that the CD44+/CD24− cell markers expressed on normal mammary progenitor cells resemble the CD44+/CD24− lineage found on breast CSCs, suggesting that breast CSCs arise from the mammary stem cells/progenitor cells.[10] In contrast, it is postulated in the stochastic model that breast CSCs are derived from the differentiated mammary cells, which undergo de-differentiation and gain stem-like properties with enrichment of breast CSCs when exposed to damaging environmental factors such as chemotherapy and radiotherapy, leading to genetic alterations.[11,12] Those two CSCs' models can explain cancer recurrence and chemoresistance well, and currently, it remains unknown which model represents the true biological origin of CSCs.

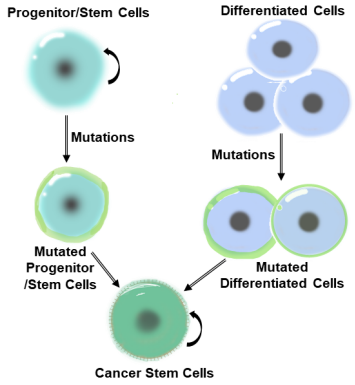

Figure 1: Current Models for the Origin of CSCs: (A) Hierarchical Model and (B) the Stochastic Model. In the hierarchical model, mutations occur in the normal stem/ progenitor cells, and the mutated stem/progenitor/ cells take advantage of the self-renewal ability to become the CSCs. Conversely, the differentiated cells acquire mutations in the stochastic model and then dedifferentiate into the CSCs.

DOI: 10.36838/v5i1.22

Breast CSC Specific Markers:

Identifying breast CSC-specific markers has dramatically helped the characterization and isolation of breast CSCs. To date, several significant markers have been found to be associated with breast CSCs, including CD44, CD24, and aldehyde dehydrogenase 1 (ALDH1), and combinatorial expression of these markers has been proven to characterize breast CSCs better. In 2003, Al-Hajj *et al*. reported the isolation of breast CSCs expressing cell-surface markers CD44+/CD24-/low from human breast cancer patients, and this cell subpopulation displays great tumorigenic ability.[7] In this study, they showed that approximately 100 cells with CD44+/CD24-/low markers formed tumors in mice, whereas 20,000 cells with alternative markers failed to generate tumors.[7] In addition, the breast CSCs with CD44+/CD24-/low markers can be serially passaged without losing their tumorigenic ability in mice.[7] Subsequently, Ginestier, and colleagues identified a distinct subpopulation of breast CSCs with the expression of the ALDH1+ marker. These cells are capable of self-renewal and generating breast tumors.[13] To figure out the relationship between the two subgroups of breast CSCs (CD44+/CD24-/low cells and ALDH1+ cells), their gene expression profiles were compared, and the result showed that the CD44+/CD24-/low subgroup cells are a mesenchymal and quiescent type of breast CSCs whereas ALDH1+ subgroup cells are an epithelial and proliferative type of breast CSCs.[10,14] These two subgroups of breast CSCs are believed to be two dynamic states of breast CSCs, and one subgroup can be transited to the other subgroup by appropriate signaling regulation.[15,16]

Wnt/β-catenin Signaling in Breast CSCs:

Among multiple signaling pathways implicated in the breast CSCs functions, Wnt/β-catenin signaling is critical (Figure 2). In the absence of Wnt ligands, the cytoplasmic β-catenin is phosphorylated by a "destruction complex" consisting of axin, adenomatous polyposis coli (APC), glycogen synthase kinase 3β (GSK3β) and casein kinase Iα (CKIα).[17] The phosphorylated β-catenin is then degraded by the proteasome, leading to the inactivation of the Wnt/β-catenin signaling pathway.[17] In contrast, Wnt/β-catenin signaling can be activated when Wnt ligands bind to the receptor Frizzled (FZD) and the low-density receptor-related protein 5/6 (LRP5/6).[17] The "destruction complex" with phosphorylation function for β-catenin is then decomposed, and the unphosphorylated β-catenin accumulates and translocates into the nucleus to regulate target gene expression.[4] A recent study has shown that Wnt/β-catenin signaling is highly active in the ALDH+ breast CSCs population and silencing the Wnt in the ALDH+ breast CSCs dramatically decreases their tumor-initiating potential.[18] In addition, the Wnt/β-catenin signaling activation has been reported in various subtypes of breast cancer, including TNBC.[19] The overexpression of Wnt/β-catenin signaling has also resulted in breast tumor formation in transgenic mice and an increased number of stem cells in precancerous mammary glands.[20,21] Vice versa, blocking the Wnt/β-catenin signaling suppresses breast cancer metastasis by inhibiting breast CSCs.[22]

Targeting Breast CSCs' Markers:

As illustrated previously, those common breast CSCs markers CD44, CD133, and ALDH1 are phenotypically and functionally crucial for preserving breast CSCs. Thus, therapeutically targeting these markers may effectively eliminate breast CSCs.

CD44 is a vital breast CSC marker, and direct knockdown

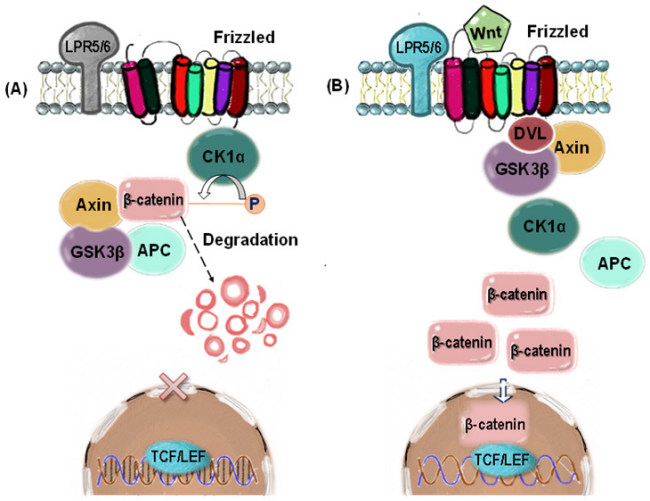

Figure 2: Scheme of the Wnt/β-catenin pathway: (A) In the absence of the Wnt ligand, the signaling process will not get initiated as the cytoplasmic β-catenin is phosphorylated by a "destruction complex" consisting of Axin, APC, GSK3β, and CKIα followed by subsequent proteasome-mediated degradation (Wnt off). (B) In contrast, in the presence of the Wnt ligand, the Wnt binds to the Frizzled family receptors, the signaling pathway is turned on (Wnt on), and a DVL (disheveled) molecule is liberated from the WNT receptor complex. The DVL molecule induces the β-catenin to be detached from the AXIN bound to CK1a, GSK3β, and APC. The β-catenin is then transduced, arrives in the nucleus, and adheres to the TCF/LEF transcription factor protein.

of CD44 effectively reduces breast CSC stemness and increases breast cancer susceptibility to anti-cancer drugs.[23,24] Pham et al. knocked down CD44 with lentivirus particles in breast CSCs, which resulted in the loss of their stemness.[23] The breast CSCs with the CD44 knockdown showed lower tumorigenic potential, altered the cell cycle, and similar gene expression profiles to the non-breast CSCs. For instance, expression of crucial genes related to stemness, metastasis, and anti-tumor drug resistance in breast CSCs, such as Myc and EGFR genes, have sharply reduced in breast CSCs with CD44 knockdown.[23]

In addition, as CD44 is a major cell membrane receptor for hyaluronic acid (HA), multiple anti-tumor drugs take advantage of such interaction between CD44 and HA by coating anti-tumor drugs with HA nanoparticles so that they can effectively bind to and kill the breast cancer cells expressing CD44.[25, 26] Lapatinib and rapamycin coated with HA nanoparticles, for example, can be effectively delivered to CD44+ breast CSCs, leading to dramatic breast CSC apoptosis.[25,27]

Moreover, ALDH1 is another breast CSC marker in Her 2+ enriched and triple negative (ER-/PR-/Her2-) breast cancer cells. The activity of ALDH1 is positively correlated to stemness in breast CSCs.[28] Hence, targeting ALDH1

DOI: 10.36838/v5i1.22

can be a promising therapy to kill breast CSCs for cancer treatment. Withaferin A, derived from the roots of Withania somnifera plants, has been reported to lower ALDH1 activities, inducing the death of the breast CSCs and shrinking breast tumor size.[29]

Targeting Wnt/β-catenin Signaling:

As Wnt signaling activation is implicated in breast CSCs' self-renewal and tumorigenesis, targeting Wnt signaling represents a potential therapy for breast cancer by targeting breast CSCs. Recently, numerous Wnt signaling inhibitors have been identified, some of which have gone into clinical trials.[30]

In a high-throughput screening of Wnt signaling inhibitory molecules, Liu and colleagues identified that LGK974 (also known as WNT974), a small molecular chemical, dramatically inhibits Wnt/β-catenin signaling by targeting porcupine, a Wnt pathway associated acyltransferase.[31] The preclinical result has demonstrated that LGK974 is well-tolerated and displays strong efficacy in rat breast cancer models, and later LGK974 was moved into clinical trial.[31] In 2011, an open-label phase I clinical trial of LGK974 was initiated to treat a variety of malignancies, including breast cancer (NCT01351103), and the preliminary result was recently released, showing that LGK974 was generally well tolerated but exhibited a limited anti-tumor activity.[32]

Vantictumab (OMP18R5) is a humanized monoclonal antibody targeting the Frizzled receptor to inhibit the Wnt/β-catenin.[33] The Phase I clinical trial of Vantictumab in 37 breast patients, was recently completed, and the final result has not been released yet (NCT01973309). Two additional Phase I studies of Vantictumab in patients with solid tumors have revealed that Vantictumab suppressed target gene expression of the Wnt/β-catenin pathway and was tolerated at 2.5 mg/kg for one intravenous injection every three weeks. In contrast, a clinical trial with further dose escalation is ongoing (NCT01345201).[33]

Disheveled (DVL) plays a decisive role in the transduction of Wnt signals from the Frizzled receptor to the downstream of Wnt signaling. Therefore, it is a feasible target to modulate Wnt signaling. Shan *et al*. identified a small molecular compound, NSC668036, which binds to the Dvl to inhibit Wnt/β-catenin signaling by interrupting the interaction between Frizzled receptor and Dvl.[34] In a succeeding study, Shan *et al*. identified six new compounds exhibiting improved binding affinity over NCS668036.[35]

Tankyrase is an important enzyme involved in the Wnt/β-catenin signaling, and it stimulates Axin degradation for Wnt/β-catenin activation through the ubiquitin-proteasome pathway.[36,37] So far, several small-molecule Tankyrase inhibitors have been developed to inhibit the Wnt/β-catenin signaling. Chen *et al*. testified that a Tankyrase inhibitor, IWR-1, stabilizes Axin to block the Wnt/β-catenin signaling.[38] Subsequently, another Tankyrase inhibitor, XAV939, is discovered, and it functions similarly to IWR-1.[36] Recently, several new Tankyrase inhibitors have been identified, including WIKI4 and G007-LK.[39,40]

Wnt/β-catenin signaling can also be regulated by microRNAs (miRNAs). Isobe *et al*. reported that one miRNA, miR-142, dramatically activated the Wnt/β-catenin signaling through decomposing the "destruction complex" and knockdown of miR-142, effectively suppressed formation by breast CSCs, and slowed down breast cancer growth *in vivo*.[41] Furthermore, Liu *et al*. reported that another miRNA, miR-1, can down-regulate breast CSC stemness, proliferation, and migration by binding to the Frizzled seven receptor and Tankyrase-2 to inhibit Wnt/β-catenin signaling.[42]

In summary, considerable efforts and advances have been made to develop drugs by targeting the Wnt/β-catenin signaling pathway with small molecules, antibodies, and miRNAs which have shown beneficent effects on the treatment of breast cancer. However, to date, no Wnt signaling-related drugs have been officially approved by FDA for clinical usage.

■ Conclusion

Years of scientific research have revealed that breast CSCs play vital roles in cancer relapse and drug resistance. Thus far, several breast CSCs markers have been identified, including CD44, CD133, and ALDH1, and therapeutically targeting these markers have been shown to induce breast CSC apoptosis and shrink tumor growth.[23-27] The Wnt/β-catenin signaling is one of the key pathways involved in breast CSCs self-renewal and differentiation. Several potential drugs have been developed to target the abnormal activation of the Wnt/β-catenin signaling at multiple levels with small molecules, antibodies, and miRNAs. Preclinical studies and clinical trials have indicated that targeting the Wnt/β-catenin pathway represents a promising strategy for treating breast cancer. However, as Wnt/β-catenin signaling is also essential to normal cell proliferation and tissue homeostasis, it remains challenging to effectively fix the dysregulated Wnt/β-catenin pathway in breast CSCs, while being safe enough not to damage the normal cell functions and tissue homeostasis. Nevertheless, our understanding of the Wnt/β-catenin pathway continues to improve in both physiology and pathology, and several potential drugs are under clinical trials. Therapeutic agents targeting Wnt/β-catenin signaling may be developed to treat breast cancer in the near future effectively.

■ Acknowledgments

I want to thank my mentor, Dr. Jay Hao, for his guidance and valuable feedback. In addition, I want to thank my parents for their endless support, and I would not be anywhere without them.

■ References

1. www.breastcancer.org/facts-statistics (accessed on 03/01/2022)
2. Song, K.; Farzaneh, M., Signaling pathways governing breast cancer stem cells behavior. *Stem Cell Res Ther* **2021**, 12 (1), 245.
3. Yersal, O.; Barutca, S., Biological subtypes of breast cancer: Prognostic and therapeutic implications. *World J Clin Oncol* **2014**, 5 (3), 412-24.
4. Koury, J.; Zhong, L.; Hao, J., Targeting Signaling Pathways in Cancer Stem Cells for Cancer Treatment. *Stem Cells Int* **2017**, 2017, 2925869.
5. Bonnet, D.; Dick, J. E., Human acute myeloid leukemia is organized as a hierarchy that originates from a primitive hematopoietic cell. *Nat Med* **1997**, 3 (7), 730-737.

6. Lapidot, T.; Sirard, C.; Vormoor, J.; Murdoch, B.; Hoang, T.; Caceres cortes, J.; Minden, M.; Paterson, B.; Caligiuri, M. A.; Dick, J. E., A Cell Initiating Human Acute Myeloid-Leukemia after Transplantation into Scid Mice. *Nature* **1994**, 367 (6464), 645-648.
7. Al-Hajj, M.; Wicha, M. S.; Benito-Hernandez, A.; Morrison, S. J.; Clarke, M. F., Prospective identification of tumorigenic breast cancer cells. *P Natl Acad Sci USA* **2003**, 100 (7), 3983-3988.
8. Reya, T.; Morrison, S. J.; Clarke, M. F.; Weissman, I. L., Stem cells, cancer, and cancer stem cells. *Nature* **2001**, 414 (6859), 105-11.
9. Lindeman, G. J.; Visvader, J. E., Insights into the cell of origin in breast cancer and breast cancer stem cells. *Asia-Pac J Clin Onco* **2010**, 6 (2), 89-97.
10. Liu, S. L.; Cong, Y.; Wang, D.; Sun, Y.; Deng, L.; Liu, Y. J.; Martin-Trevino, R.; Shang, L.; McDermott, S. P.; Landis, M. D.; Hong, S.; Adams, A.; D'Angelo, R.; Ginestier, C.; Charafe- Jauffret, E.; Clouthier, S. G.; Birnbaum, D.; Wong, S. T.; Zhan, M.; Chang, J. C.; Wicha, M. S., Breast Cancer Stem Cells Transition between Epithelial and Mesenchymal States Reflective of their Normal Counterparts. *Stem Cell Rep* **2014**, 2 (1), 78-91.
11. Lagadec, C.; Vlashi, E.; Della Donna, L.; Dekmezian, C.; Pajonk, F., Radiation-Induced Reprogramming of Breast Cancer Cells. *Stem Cells* **2012**, 30 (5), 833-844.
12. Koren, S.; Reavie, L.; Couto, J. P.; De Silva, D.; Stadler, M. B.; Roloff, T.; Britschgi, A.; Eichlisberger, T.; Kohler, H.; Aina, O.; Cardiff, R. D.; Bentires-Alj, M., PIK3CA(H1047R) induces multipotency and multi-lineage mammary tumours. *Nature* **2015**, 525 (7567), 114-+.
13. Ginestier, C.; Hur, M. H.; Charafe-Jauffret, E.; Monville, F.; Dutcher, J.; Brown, M.; Jacquemier, J.; Viens, P.; Kleer, C. G.; Liu, S. L.; Schott, A.; Hayes, D.; Birnbaum, D.; Wicha, M. S.; Dontu, G., ALDH1 is a marker of normal and malignant human mammary stem cells and a predictor of poor clinical outcome. *Cell Stem Cell* **2007**, 1 (5), 555-567.
14. Mani, S. A.; Guo, W.; Liao, M. J.; Eaton, E. N.; Ayyanan, A.; Zhou, A. Y.; Brooks, M.; Reinhard, F.; Zhang, C. C.; Shipitsin, M.; Campbell, L. L.; Polyak, K.; Brisken, C.; Yang, J.; Weinberg, R. A., The epithelial-mesenchymal transition generates cells with properties of stem cells. *Cell* **2008**, 133 (4), 704-15.
15. Brabletz, T., EMT and MET in metastasis: where are the cancer stem cells? *Cancer Cell* **2012**, 22 (6), 699-701.
16. Stankic, M.; Pavlovic, S.; Chin, Y.; Brogi, E.; Padua, D.; Norton, L.; Massague, J.; Benezra, R., TGF-beta-Id1 signaling opposes Twist1 and promotes metastatic colonization via a mesenchymal-to-epithelial transition. *Cell Rep* **2013**, 5 (5), 1228-42.
17. Clevers, H., Wnt/beta-catenin signaling in development and disease. *Cell* **2006**, 127 (3), 469-80.
18. Cui, J.; Li, P.; Liu, X.; Hu, H.; Wei, W., Abnormal expression of the Notch and Wnt/beta-catenin signaling pathways in stem-like ALDH(hi)CD44(+) cells correlates highly with Ki-67 expression in breast cancer. *Oncol Lett* **2015**, 9 (4), 1600-1606.
19. Pohl, S. G.; Brook, N.; Agostino, M.; Arfuso, F.; Kumar, A. P.; Dharmarajan, A., Wnt signaling in triple-negative breast cancer. *Oncogenesis* **2017**, 6 (4), e310.
20. Li, Y.; Welm, B.; Podsypanina, K.; Huang, S. X.; Chamorro, M.; Zhang, X. M.; Rowlands, T.; Egeblad, M.; Cowin, P.; Werb, Z.; Tan, L. K.; Rosen, J. M.; Varmus, H. E., Evidence that transgenes encoding components of the Wnt signaling pathway preferentially induce mammary cancers from progenitor cells. *P Natl Acad Sci USA* **2003**, 100 (26), 15853-15858.
21. Liu, B. Y.; McDermott, S. P.; Khwaja, S. S.; Alexander, C. M., The transforming activity of Wnt effectors correlates with their ability to induce the accumulation of mammary progenitor cells. *P Natl Acad Sci USA* **2004**, 101 (12), 4158-4163.
22. Jang, G. B.; Kim, J. Y.; Cho, S. D.; Park, K. S.; Jung, J. Y.; Lee, H. Y.; Hong, I. S.; Nam, J. S., Blockade of Wnt/beta-catenin signaling suppresses breast cancer metastasis by inhibiting CSC-like phenotype. *Sci Rep-Uk* **2015**, 5.
23. Pham, P. V.; Phan, N. L.; Nguyen, N. T.; Truong, N. H.; Duong, T. T.; Le, D. V.; Truong, K. D.; Phan, N. K., Differentiation of breast cancer stem cells by knockdown of CD44: promising differentiation therapy. *J Transl Med* **2011**, 9, 209.
24. Van Phuc, P.; Nhan, P. L.; Nhung, T. H.; Tam, N. T.; Hoang, N. M.; Tue, V. G.; Thuy, D. T.; Ngoc, P. K., Downregulation of CD44 reduces doxorubicin resistance of CD44CD24 breast cancer cells. *Onco Targets Ther* **2011**, 4, 71-8.
25. Agrawal, S.; Dwivedi, M.; Ahmad, H.; Chadchan, S. B.; Arya, A.; Sikandar, R.; Kaushik, S.; Mitra, K.; Jha, R. K.; Dwivedi, A. K., CD44 targeting hyaluronic acid coated lapatinib nanocrystals foster the efficacy against triple-negative breast cancer. *Nanomedicine* **2018**, 14 (2), 327-337.
26. Spadea, A.; Rios de la Rosa, J. M.; Tirella, A.; Ashford, M. B.; Williams, K. J.; Stratford, I. J.; Tirelli, N.; Mehibel, M., Evaluating the Efficiency of Hyaluronic Acid for Tumor Targeting via CD44. *Mol Pharm* **2019**, 16 (6), 2481-2493.
27. Zhao, Y.; Zhang, T.; Duan, S.; Davies, N. M.; Forrest, M. L., CD- 44-tropic polymeric nanocarrier for breast cancer targeted rapamycin chemotherapy. *Nanomedicine* **2014**, 10 (6), 1221-30.
28. Ricardo, S.; Vieira, A. F.; Gerhard, R.; Leitao, D.; Pinto, R.; Cameselle-Teijeiro, J. F.; Milanezi, F.; Schmitt, F.; Paredes, J., Breast cancer stem cell markers CD44, CD24 and ALDH1: expression distribution within intrinsic molecular subtype. *J Clin Pathol* **2011**, 64 (11), 937-946.
29. Kim, S. H.; Singh, S. V., Mammary Cancer Chemoprevention by Withaferin A Is Accompanied by In Vivo Suppression of Self-Renewal of Cancer Stem Cells. *Cancer Prev Res* **2014**, 7 (7), 738-747.
30. Zhang, X.; Hao, J., Development of anticancer agents targeting the Wnt/beta-catenin signaling. *Am J Cancer Res* **2015**, 5 (8), 23-44-60.
31. Liu, J.; Pan, S. F.; Hsieh, M. H.; Ng, N.; Sun, F. X.; Wang, T.; Kasibhatla, S.; Schuller, A. G.; Li, A. G.; Cheng, D.; Li, J.; Tompkins, C.; Pferdekamper, A.; Steffy, A.; Cheng, J.; Kowal, C.; Phung, V.; Guo, G. R.; Wang, Y.; Graham, M. P.; Flynn, S.; Brenner, J. C.; Li, C.; Villarroel, M. C.; Schultz, P. G.; Wu, X.; McNamara, P.; Sellers, W. R.; Petruzzelli, L.; Boral, A. L.; Seidel, H. M.; McLaughlin, M. E.; Che, J. W.; Carey, T. E.; Vanasse, G.; Harris, J. L., Targeting Wnt-driven cancer through the inhibition of Porcupine by LGK974. *P Natl Acad Sci USA* **2013**, 110 (50), 20224-20229.
32. Rodon, J.; Argiles, G.; Connolly, R. M.; Vaishampayan, U.; de Jonge, M.; Garralda, E.; Giannakis, M.; Smith, D. C.; Dobson, J. R.; McLaughlin, M. E.; Seroutou, A.; Ji, Y.; Morawiak, J.; Moody, S. E.; Janku, F., Phase 1 study of single-agent WNT974, a first -in-class Porcupine inhibitor, in patients with advanced solid tumours. *Br J Cancer* **2021**, 125 (1), 28-37.
33. Smith, D. C.; Rosen, L. S.; Chugh, R.; Goldman, J. W.; Xu, L.; Kapoun, A.; Brachmann, R. K.; Dupont, J.; Stagg, R. J.; Tolcher, A. W.; Papadopoulos, K. P., First-in-human evaluation of the human monoclonal antibody vantictumab (OMP-18R5; anti-Frizzled) targeting the WNT pathway in a phase I study for patients with advanced solid tumors. *J Clin Oncol* **2013**, 31 (15).
34. Shan, J.; Shi, D. L.; Wang, J.; Zheng, J., Identification of a specific inhibitor of the dishevelled PDZ domain. *Biochemistry* **2005**, 44 (47), 15495-503.
35. Shan, J.; Zhang, X.; Bao, J.; Cassell, R.; Zheng, J. J., Synthesis of potent dishevelled PDZ domain inhibitors guided by virtual screening and NMR studies. *Chem Biol Drug Des* **2012**, 79 (4), 376-

DOI: 10.36838/v5i1.22

-83.
36. Huang, S. M. A.; Mishina, Y. M.; Liu, S. M.; Cheung, A.; Stegmeier, F.; Michaud, G. A.; Charlat, O.; Wiellette, E.; Zhang, Y.; Wiessner, S.; Hild, M.; Shi, X. Y.; Wilson, C. J.; Mickanin, C.; Myer, V.; Fazal, A.; Tomlinson, R.; Serluca, F.; Shao, W. L.; Cheng, H.; Shultz, M.; Rau, C.; Schirle, M.; Schlegl, J.; Ghidelli, S.; Fawell, S.; Lu, C.; Curtis, D.; Kirschner, M. W.; Lengauer, C.; Finan, P. M.; Tallarico, J. A.; \Bouwmeester, T.; Porter, J. A.; Bauer, A.; Cong, F., Tankyrase inhibition stabilizes axin and antagonizes Wnt signalling. *Nature* **2009**, 461 (7264), 614-620.
37. Lehtio, L.; Chi, N. W.; Krauss, S., Tankyrases as drug targets. *Febs J* **2013**, 280 (15), 3576-3593.
38. Chen, B. Z.; Dodge, M. E.; Tang, W.; Lu, J. M.; Ma, Z. Q.; Fan, C. W.; Wei, S. G.; Hao, W. N.; Kilgore, J.; Williams, N. S.; Roth, M. G.; Amatruda, J. F.; Chen, C.; Lum, L., Small molecule-mediated disruption of Wnt-dependent signaling in tissue regeneration and cancer. *Nat Chem Biol* **2009**, 5 (2), 100-107.
39. James, R. G.; Davidson, K. C.; Bosch, K. A.; Biechele, T. L.; Robin, N. C.; Taylor, R. J.; Major, M. B.; Camp, N. D.; Fowler, K., Martins, T. J.; Moon, R. T., WIKI4, a Novel Inhibitor of Tankyrase and Wnt/beta-Catenin Signaling. *Plos One* **2012**, 7 (12).
40. Voronkov, A.; Holsworth, D. D.; Waaler, J.; Wilson, S. R.; Ekblad, B.; Perdreau-Dahl, H.; Dinh, H.; Drewes, G.; Hopf, C.; Morth, J. P.; Krauss, S., Structural Basis and SAR for G007-LK, a Lead Stage 1,2,4-Triazole Based Specific Tankyrase 1/2 Inhibitor. *J Med Chem* **2013**, 56 (7), 3012-3023.
41. Isobe, T.; Hisamori, S.; Hogan, D. J.; Zabala, M.; Hendrickson, D. G.; Dalerba, P.; Cai, S.; Scheeren, F.; Kuo, A. H.; Sikandar, S. S.; Lam, J. S.; Qian, D. L.; Dirbas, F. M.; Somlo, G.; Lao, K. Q.; Brown, P. O.; Clarke, M. F.; Shimono, Y., miR-142 regulates the tumorigenicity of human breast cancer stem cells through the canonical WNT signaling pathway. *Elife* **2014**, 3.
42. Liu, T.; Hu, K.; Zhao, Z.; Chen, G.; Ou, X.; Zhang, H.; Zhang, X.; Wei, X.; Wang, D.; Cui, M.; Liu, C., MicroRNA-1 down-regulates proliferation and migration of breast cancer stem cells by inhibiting the Wnt/beta-catenin pathway. *Oncotarget* **2015**, 6 (39), 41638-49.

Author

Yu Tianyue is G11, a high school student from Shanghai, China. For her future career, she wants to be a pharmacist who produces the most economical drugs to rescue people's lives. Hence, through this review article, she dives deep into a highly promising medical solution to the breast cancer.

GENIUS OLYMPIAD

"Let's build a better future together"

www.geniusolympiad.org

International Environment Project Fair For Grades 9-12

Rochester, New York

Hosted by Rochester Institute of Technology

RIT Rochester Institute of Technology

@GeniusOlympiad

terra science and education

IJHSR International Journal of High School Research

is a publication of

terra science and education

N.Y. based 501.c.3 non-profit organization
dedicated for improving K-16 education